On Thin Ice: Experimental Spectroscopy and Ice Mechanics in Support of Ocean World Exploration

by

Vishaal Singh

A Dissertation Presented in Partial Fulfillment
of the Requirements for the Degree
Doctor of Philosophy

Approved April 2021 by the
Graduate Supervisory Committee:

Steven J. Desch, Co-Chair
Alyssa R. Rhoden, Co-Chair
James F. Bell
Mark S. Robinson
Murthy S. Gudipati

ARIZONA STATE UNIVERSITY

May 2021

ABSTRACT

Water ice is a fundamental planetary building block and ubiquitous in the outer solar system. On Ocean worlds like Europa, convecting ice may transport material from a subsurface ocean (a potential habitat) to the surface, depositing ices and salts. Evaluating the habitability of Ocean Worlds, requires either unraveling the history of ice on the surface to contextualize biosignatures, or probing the ocean for direct access. There are, however, challenges to both exploration strategies. How can recent exposures of subsurface ice be identified? How can a probe penetrate beneath an ice shell and still communicate with the surface?

I have developed techniques to address these questions, and pose new ones, using a two-part approach to exploration of Ocean Worlds, viewed as both remote sensing targets, and sites for in-situ analysis. First, I combined investigations using laboratory spectroscopy and Hapke modeling to identify the diagnostic limits of existing datasets, collected optical and spectral measurements of candidate ices at relevant conditions, and identified the effects of grain size, sample thickness, and thermal cycling on water ice absorption features. I designed this dataset to enable better interpretation of Galileo and upcoming Europa Clipper mission spectra, with a focus on characterization of surface properties. To demonstrate its efficacy, I determined the bulk crystallinity of Europa's leading hemisphere, the environmental conditions required to meet current age estimates, and developed a criterion for selection of regions of recent exposure. Second, I simulated conditions in Europa's interior and ice shell faults using cryogenic shear experiments, to evaluate the mechanical behavior of ice and explore the limitations of communication

tethers for deployment by a melt probe transiting the ice shell. Surprisingly, I find that these tethers are robust across the range of temperature and velocity conditions expected on Europa and offer capabilities as potential science instruments to detect ice-quakes and characterize the thermal profile of the ice shell.

Together, these studies improve the ability to probe the thermomechanical and compositional properties of dynamic ice shells, characterize the environments likely to be encountered by landed missions, and guide future technology development for assessing the habitability of Ocean Worlds.

DEDICATION

For my mother, Vijita, and my partner, Malvika, who are strong, clever, kind, and caring. Thank you for guiding me, and adding meaning and happiness to my life. For my brother, Vaibhav, who is my archenemy and my closest friend. You have always inspired me and taught me how to lead a better life over a week in Mumbai. For my father, Sushil Kumar, who is meticulous. Thank you for encouraging us from a very young age.

For my grandparents, M.N. Singh and Lata, who are honorable and kind. I hope to one day be as learned, patient and caring as you were for me.

ACKNOWLEDGMENTS

This work is the culmination of an interdisciplinary effort with many scientists and engineers, conducted at three research institutions over the past five years. My gratitude goes first to the mentors without whom I would not have begun my research career: Partho Bhattacharya, who taught me the principles of critical thinking, and my M.S. thesis advisor, Saibal Gupta, for giving me a chance to work with him and changing my life. Thank you to my dissertation committee members, Jim Bell and Mark Robinson, and qualifying exam members, Paul Scowen and Patrick Young, for their critical feedback and continued encouragement. You have molded how I approach and communicate science, and I am a better scientist because of you. I am also grateful to the faculty, staff and administrators of the School of Earth and Space Exploration (SESE) for their support.

Alyssa Rhoden's kindness, patience, insightful advising and mentorship have been central to the success of this work. Thank you for taking a chance on an unknown international student after a handful of emails and being the best Ph.D. advisor. I am grateful to Steve Desch for taking me under his wing early on at ASU – I have since come to realize that his selflessness is a constant state of being. Murthy Gudipati taught me how to approach a research problem, develop a proposal, and acquire the lab skills which will prove essential in the future. Thank you to Christine McCarthy, for letting me tear down instruments in her lab to learn a new technique, and for her mentorship, editing, and transportation services. Early on, Paul Scowen took me on to work on an astronomy project – thank you for helping me develop an aptitude for fieldwork and instrument development.

Ted Koczynski had an enduring impact on my time in New York City, with his spiritual and technical guidance, his friendship, and the unrivalled exposure to Italian

cuisine. Thank you to the postdocs and students of Icebox and Deschcoveries, and to everyone I have met along the way, and been on adventures with. You have made this journey much more bearable and a lot more fun.

The research ideas behind this dissertation were first conceptualized together with Alyssa Rhoden and Murthy Gudipati (Chapters 2 through 5), and by Kate Craft, Christine McCarthy, and the Europa Signals Through the Ice (STI) team (Chapters 6 and 7). *Chapters 2 through 5:* My gratitude to Murthy Gudipati and Bryana Henderson for access to the instrumentation, and for teaching me the fundamentals of laboratory spectroscopy and data analysis. Many thanks to Christine McCarthy for her advice on ice sample preparation, and to Jodi Berdis for performing the time-consuming band area and crystallinity calculations. Eleonora Ammannito performed the transmission spectroscopy experiments in 2010 at ISL, and her measurements and meticulous notes were invaluable for identifying the dependence of water ice spectral features on thickness. The spectroscopic work was carried out in the Ice Spectroscopy Laboratory at the Jet Propulsion Laboratory, California Institute of Technology, under the JPL Visiting Student Research Program (JVSRP) from 2017 to 2020. *Chapters 6 and 7:* I am grateful to the grant PI Kate Craft and the STI team for the opportunity to work on this project. Many thanks to Christine McCarthy, Mike Jakuba, Matt Silvia, and Ted Koczinski for their guidance in this project, particularly in sample preparation, shear testing, and tether handling. This research was conducted as a laboratory associate in the Rock and Ice Mechanics Lab at Lamont-Doherty Earth Observatory, Columbia University. The project was funded by the NASA Scientific Exploration Subsurface Access Mechanism for Europa (SESAME) technology development opportunity at Applied Physics Laboratory, Johns Hopkins University.

TABLE OF CONTENTS

Page

CHAPTER Page

CHAPTER Page

CHAPTER Page

CHAPTER Page

LIST OF TABLES

Table Page

LIST OF FIGURES

Figure Page

Figure Page

Figure Page

Figure Page

CHAPTER 1

OVERVIEW AND SUMMARY

Life as we know it, requires three ingredients: water, a source of energy, and a suite of essential bioavailable nutrients (CHNOPS, Hand *et al*., 2009 and references therein). Since the days of the life-searching Viking Landers (Soffen and Snyder, 1976), a key driver for exploration is the likelihood of assessing the habitability of a planetary body. Flash forward to the 1990s, and the discovery of a deep, subsurface ocean with "*potential suitability for life",* Jupiter's moon Europa became "*one of the most important targets in all of planetary science"* (National Research Council, 2011). In addition to a global ocean (Pappalardo *et al*., 1999), where nutrients may potentially be available, interaction between liquid water and the silicate bedrock could provide energy through redox cycles (Vance *et al*. 2016), and the overlying insulating ice shell is ideal for geologically short-time surface and subsurface exchange. Hence, the potential of icy ocean worlds like Europa to be abodes of life is tantalizing.

In 2016, the Congressional Commerce, Justice, Science, and Related Agencies Appropriations Bill directed NASA ''*to create an Ocean World Exploration Program whose primary goal is to discover extant life on another world*'' (H. Rept. 114-130, 2015). The NASA Roadmap to Ocean Worlds (ROW) group was formed, and in 2019, they defined the overarching goal of an Ocean Worlds Program: to identify ocean worlds, characterize their oceans, and evaluate their habitability prior to the search for life, and understanding any life we find (Hendrix *et al*., 2019). Following that framework, this

dissertation focuses on the preceding stages in the search for life, with characterization of planetary surfaces and interiors, and technological developments that enable (or restrict) evaluation of potential habitability.

1.1 Scope, Relevance, and Structure of This Dissertation

In the upcoming decade, with the NASA Europa Clipper and Dragonfly missions and ESA's L-class JUICE mission designed to assess the relative habitability of multiple Ocean Worlds, there is now great momentum and support for exploration of Ocean Worlds like Europa, from the United States Congress, the planetary science community, and the public. The recently established NASA Astrobiology Program Research Coordination Network (RCN) The *Network for Ocean Worlds* (NOW) recently recommended two critical flagship missions to: (1) land on Europa or Enceladus in the decade 2023-2032, and (2) access a planetary ocean in the decade 2033-2042 (Howell *et al*., 2020). *How do we prepare for these future missions, which may soon be feasible?* One approach is to identify the limitations of our diagnostic capabilities and find the right tools to enhance them, thus maximizing science return from these and future missions – this approach constitutes the common thread of this dissertation, revolving around the theme of target characterization with enhanced analysis capabilities and instrument development (Figure 1.1).

I studied the exploration of Ocean Worlds in two parts: laboratory measurements to enhance remote characterization of icy bodies and technology development to enable in situ exploration. In Part I (Chapters 3-5), I investigated the processes controlling the present-day behavior of icy bodies in the outer solar system, to provide a geologic context

for exploration and develop a criterion to identify high science interest localities at the scale of a remote sensing target. This part is directly aligned with the goals of NASA's Planetary Science Division (PSD) within the Science Mission Directorate (SMD), specifically to "*seek a deep understanding of the chemical and physical processes that have shaped planetary interiors and surfaces ... through time*" (National Research Council, 2011), and is traceable to multiple science objectives for Europa Clipper (Geology / Ocean and Ice Shell, Pappalardo *et al*., 2017).

In Part II (Chapters 6-7), I developed and reduced the technical risk of technology to enable communication through many kilometers of ice, so that these technologies may eventually be incorporated into future flight missions at the scale of a lander and in the depths of the ice shell. This part addresses one of the priorities of NASA's *Science 2020-2024: A Vision for Scientific Excellence*, to "*Challenge assumptions about what is technically feasible and enable revolutionary scientific discovery through a deliberate focus on innovation, experimentation, and cross-disciplinary research*" (NASA 2020).

Tables 1.1 to 1.3 highlight the goals, science objectives and investigations, techniques and tools, and the findings of this dissertation with a science traceability matrix.

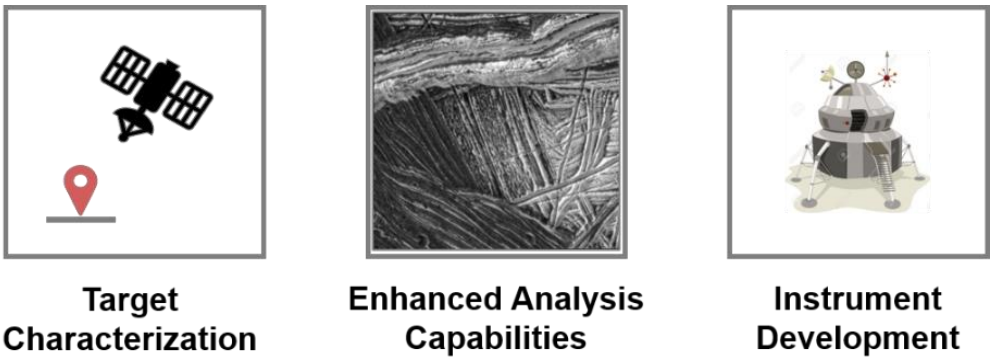

Figure 1.1: This dissertation is designed to support future exploration with 3 major themes.

Table 1.1: Science Traceability Matrix (Age) for this dissertation.

Goals / Questions	Objectives and Investigations	Techniques / Tools	Findings	Ch.
How do we find recent exposures of oceanic materials?	Develop a framework to identify sites of young, oceanic material based on surface properties	▪ Results combined from Chapters 4, 5 and literature	▪ Crystallinity, grain size, composition, and optical albedo identified as key parameters; combined with geomorphological context	5
What is the surface age of Europa?	Evaluate limitations of current age estimates due to image resolution	▪ Resolution Analysis	▪ Diameter and image resolution limit detections of craters	5
	Crystallinity as an indicator of surface age ▪ Compare crystallinity vs cratering age estimates ▪ Investigate variation with thermal evolution, particle flux, and resurfacing	▪ Reflection Spectroscopy ▪ 1.65/1.5 μm Band Area Ratio ▪ Age / Amorphous Fraction Equation	▪ Age estimates need better constraints on surface conditions ▪ Higher temperature (~ 110 K) and lower particle flux than current predictions required for age of 60 Ma, consistent with cratering record.	5
Goals are identified from various NASA reports in the past decade: [1] Vision and Voyages for Planetary Science in the Decade 2013-2022 (National Research Council 2011); [2] 2014 Science Plan; [3] Europa Clipper (Pappalardo *et al*., 2017); [4] Europa Lander SDT Report; [5] 2015 Astrobiology Strategy, [6] Roadmap to Ocean Worlds (Hendrix *et al*., 2019).				

Table 1.2: Science Traceability Matrix (Surface Processes) for this dissertation.

Goals / Questions	Objectives and Investigations	Techniques / Tools	Findings	Ch.
How do surface processes modify ice on Europa? *(global vs local predictions)*	Determine crystallinity and age of leading hemisphere ▪ Evaluate for a broad range of surface conditions ▪ Quantify the role of thermal annealing and particle flux	▪ Planetary Analog Preparation ▪ 1.65/1.5 μm Band Area Ratio ▪ Age / Amorphous Fraction Equation	▪ ~ 47-52% crystallinity ▪ Age from <1 to 104 Ma, based on equation inputs (varies with location) ▪ Crystallinity evolves with formation mechanism and thermal evolution (frost, irradiation, cryovolcanism)	4, 5
How can we improve future classification of icy surface properties?	Investigate dependence of spectral band areas (planetary surface interpretation) on changing properties ▪ Effect of sample thickness and grain size on NIR spectra	▪ Hapke Spectra Modeling ▪ Reflection and Transmission Spectroscopy ▪ Thermal Annealing	▪ Grain size dependent laboratory spectra will alter interpretation of surface properties ▪ Band shape and depth vary for model and lab spectra	3, 4
Goals are identified from various NASA reports in the past decade: [1] Vision and Voyages for Planetary Science in the Decade 2013-2022 (National Research Council 2011); [2] 2014 Science Plan; [3] Europa Clipper (Pappalardo *et al*., 2017); [4] Europa Lander SDT Report; [5] 2015 Astrobiology Strategy, [6] Roadmap to Ocean Worlds (Hendrix *et al*., 2019).				

Table 1.3: Science Traceability Matrix (Interior) for this dissertation.

Goals / Questions	Objectives and Investigations	Techniques / Tools	Findings	Ch.
How do we explore the ice shell and ocean of Europa?	Evaluate robustness of Tethers in Europa subsurface ice while maintaining communication ▪ Identify surface / subsurface conditions; simulate in a lab ▪ Shear tests of Tethers in ice ▪ Identify science capabilities	▪ Sample Preparation (develop protocols) ▪ Instrument Development ▪ Cryogenic Double-Direct Shear Tests ▪ Optical Transmission and Strain Analysis	▪ Tethers may survive in a water ice shell ▪ Sample properties are representative of ice behavior (strength, sliding) ▪ Strain & Temperature measurement are feasible	6, 7
Goals are identified from various NASA reports in the past decade: [1] Vision and Voyages for Planetary Science in the Decade 2013-2022 (National Research Council 2011); [2] 2014 Science Plan; [3] Europa Clipper (Pappalardo *et al*., 2017); [4] Europa Lander SDT Report; [5] 2015 Astrobiology Strategy, [6] Roadmap to Ocean Worlds (Hendrix *et al*., 2019).				

1.1.1 Enabling Remote Sensing Exploration

Predicted transport of potentially biosignature rich oceanic material to the surface may manifest as a variety of icy compositions (e.g., with salts) and geologic features (e.g., plumes, chaos terrains, bands, etc.). In the short term, the selection of a target site for exploration is therefore dependent on unraveling the history of ice on Europa or any other icy worlds. Chapter 2 focuses on the presence and evolution of water ice in the outer solar system. Chapters 3 and 4 investigate the current limitations of spectroscopy for characterization of planetary surfaces. For those investigations, I have used reflection spectroscopy to collect a new dataset and analyzed previously acquired transmission spectra to evaluate the capabilities of both techniques. I further investigated how surface processes and sample properties influence the NIR spectrum and evolution of water ice using an integrated band area approach.

Chapter 5 focuses on the application of this approach and the new spectroscopic dataset to Europa. I determined the surface crystallinity of Europa's leading hemisphere using new end members for 100% pure amorphous and crystalline ice, which is key to understanding the role of physical processes such as thermal annealing and cryovolcanism in surface evolution, and on the chemistry of the ocean. The calculated crystallinity provides an inkling into age of the surface, and the conditions required to meet cratering age estimates (a warmer surface or the presence of localized hotspots; lower particle flux with shallow penetration depth). Finally, a criterion is suggested for selection of regions of interest based on these findings, our understanding of surface properties, and their evolution over time.

1.1.2 Enabling In-Situ Exploration

Characterizing the interior conditions in the ice shells of Ocean Worlds will provide key engineering and design constraints for ice and ocean access technologies (Howell *et al*., 2020). In Chapters 6 and 7, I focus on improving the mission readiness of an ice-ocean probe, with a test case of exploring Europa's interior. Chapter 6 investigates the heritage of communication tethers (wires connecting a surface lander to a probe) for subsurface exploration on Earth, and constrains the expected conditions in a seismically active (and/or chemically hostile) ice shell. In Chapter 7, I simulate these environmental and fault conditions in the laboratory and test how various tethers frozen inside ice blocks behave under a range of shear velocity and temperature conditions. I use these tests to characterize the optical performance of the tether and determine the maximum shear stress it can sustain in an ice fault on Europa before failure (i.e., identify viable versus unviable regimes for deployment). The sliding or frictional behavior of the ice, and the brittle to ductile transition is also identified and evaluated for application to Europa.

Our tests successfully demonstrate that optical tethers could potentially survive shearing across 'ice-faults' in the water-ice shell conditions expected on Ocean Worlds like Europa and Enceladus. However, despite surviving the range of creeping strike-slip and 'ice-quake' shear events, at the coldest temperatures (~100 K), I noticed some damage to the outer jackets of the tethers and stretching of fibers. This indicates a need for further tether development which I discuss in Chapter 8.

CHAPTER 2

WATER ICE IN THE OUTER SOLAR SYSTEM

~ 4.5 billion years ago, during the formation of planets from the solar nebula, water ice was able to condense in the colder reaches of space beyond the asteroid belt, or in other worlds, at a radial distance from the proto-Sun (*snowline*) as close as 2 AU but no further than 5 AU (Lunine 2006; ~ 2.7–3.1 AU from Martin and Livio 2012, and references therein). Consequently, the outer solar system (> 5 AU) is characterized by the presence of H_2O ice on or near the surface of planetary bodies, often found in combination with other ices (like CO_2, CH_4) or impurities (e.g., salts like NaCl) (Hand *et al*., 2015). In fact, H_2O ice is the most prevalent frozen volatile in our solar system, and it has been detected (or, inferred) in the Jovian and Saturnian Systems (including Ocean Worlds like Ganymede, Europa, Enceladus, etc.), the moons of Uranus and Neptune, Pluto, Charon and KBOs, and Asteroids and Comets (Figure 2.1). In Table 2.1, I have updated previous estimates of the distribution of water ice in the outer solar system with recent results, demonstrating both its ubiquitous detection and the compositional heterogeneity within systems.

Table 2.1: Distribution of Water Ice and other frozen volatiles ('ices') in the Outer Solar System (modified from Table 1.1 in Mastrapa 2008 to include present day understanding; Data from Clark *et al*. (2013), Cruikshank *et al*. (1993) and references therein).

Planets	**Satellites**	**Ices**
Jupiter	Io	SO_2, HS, H_2S
	Europa	H_2O, NaCl, $MgSO_4$
	Ganymede	H_2O
	Callisto	H_2O
Saturn	Titan	C_6H_6, ~ HC_3N, ~ C_7H_8, ~ H_2O, ~ CH_4, ~ NH_3
	Mimas	H_2O, CO_2
	Enceladus	H_2O, NH_3
	Tethys	H_2O, CO_2
	Dione	H_2O, CO_2
	Rhea	H_2O, CO_2
	Hyperion	H_2O, CO_2
	Iapetus	H_2O, CO_2
	Rings	H_2O, CO_2
Uranus	Miranda	H_2O, ~ NH_3
	Ariel	H_2O, CO_2
	Umbriel	H_2O, CO_2
	Titania	H_2O, CO_2
	Oberon	H_2O
Neptune	Triton	CH_4, N_2, H_2O, CO, CO_2
Dwarf Planets / Kuiper Belt Objects / Small Bodies	Ceres	H_2O, $MgSO_4$
	Pluto	CH_4, N_2, CO
	Charon	H_2O, NH_3
	Haumea	H_2O
	Arrokoth	CH_3OH, ~ H_2O
Comets		H_2O, CO, CO_2

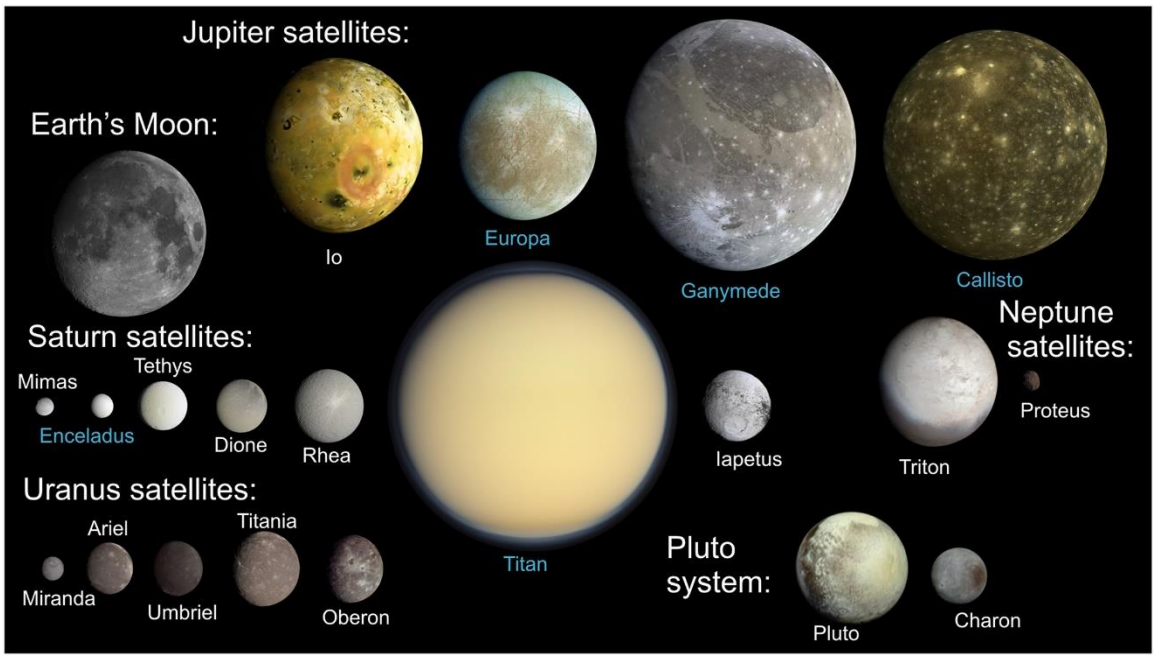

Figure 2.1: Icy Worlds in the Outer Solar System, highlighted in blue (Courtesy of Emily Lakdawalla / Planetary Society and modified from Nimmo and Pappalardo 2016).

2.1 Structure and Phases of Water Ice

Serving as a fundamental building block, water ice exists in three distinct solid (and stable) configurations at the low pressures and low-temperatures observable on the surfaces of icy objects (Mastrapa *et al*., 2013, Grundy and Schmitt, 1998):

1. Vapor phase condensation at low temperatures (< 110 K) leads to formation of an amorphous, disordered, fully bonded, random network of H_2O molecules frozen in place, with a density of 0.94 gm/cm^3 (low-density phase). At temperatures below 30 K, a high-density phase of amorphous ice is expected to form (Narten *et al*., 1976; Jenniskens and Blake, 1994).

2. On heating to a temperature between 110 K and 150 K, amorphous ice and metastable crystalline cubic (I_c) ice phases initially coexist (above 120 K), based on the thermal history and temperature of the ice, before transforming irreversibly to the cubic crystal structure at higher temperatures (density of 0.9197 gm/cm^3) (Jenniskens *et al*., 1996; Petrenko and Whitworth, 1999; Mastrapa *et al*., 2013). The specific temperature of transition from amorphous to crystalline water-ice depends on the style of deposition, the deposition rate, and the presence of impurities, with the phase change detected at temperatures between 135-160 K (Sugisaki *et al*., 1969; Jenniskens and Blake 1994, 1996; Hagen *et al*., 1981). The transition time is temperature dependent – 10^5 years at 90 K versus a few years at 115 K (Kouchi *et al*., 1994).
3. Further heating results in an irreversible phase change from cubic to hexagonal crystalline ice, occurring at temperatures between 160 K and 200 K (Jenniskens *et al*., 1998). However, at these temperatures and ultra-high vacuum conditions (pressures less than 10^{-5} mbar) of outer solar system airless bodies, ice sublimation sets in around 155 K and is significant above 170 K (Gudipati and Allamandola, 2006), resulting in competing mechanisms of formation and loss of ice. Alternatively, freezing ice from liquid water on these surfaces results in crystallization with the hexagonal structure, and it maintains that structure even when cooled to cryogenic temperatures. Figure 2.2 highlights the phase diagram of water.

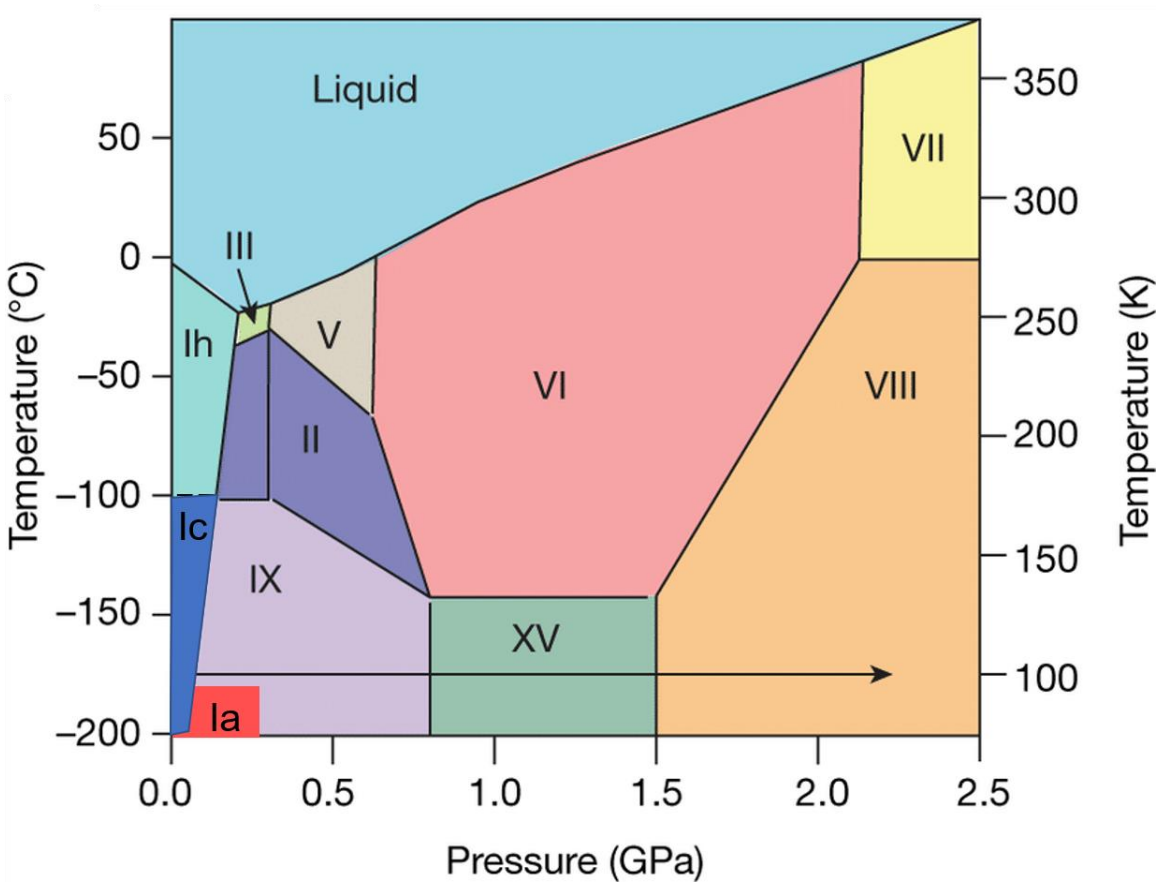

Figure 2.2: The phase diagram of H_2O at relevant temperature conditions. Figure modified from Tulk *et al*. (2019) to include approximate locations of cubic crystalline ice (I_c) and amorphous ice (I_a). Phase boundary lines indicate historical approximations of where transformations are thought to occur.

2.2 Phase Transition Processes Operating in the Outer Solar System

In the outer solar system, crystalline phase of water ice is currently interpreted to dominate water ice abundances (in the collected spectra), even beyond Saturn where the temperatures are less than 90 K (Clark *et al*., 2013). This predominance suggests a potential transition of amorphous ice post deposition to crystalline ice (at least for the top sub mm of detection). To evaluate the role of physical processes in enabling such a transition, the

amount of the crystalline water ice is compared to that of total abundance of both the crystalline and amorphous phases of ice, referred to here as the ‘‘crystallinity’’ of a surface (C). Crystallinity can be key to understanding the environmental history (including present-day conditions) and surface evolution of planetary surfaces, and provides estimates of surface age, independent of the cratering record. Several processes can affect a change in crystallinity, operating on timescales of a few hours to millions of years, some of which are studied in this dissertation (Table 2.2):

1. Thermal relaxation of amorphous water ice to crystalline ice (Jeniskens *et al*., 1998; Kouchi *et al*., 1994)
2. Particle flux dependent disruption and disorder of crystalline ice structure to amorphous-like structure due to magnetospheric particle bombardment (Baragiola *et al*., 2013; Cooper *et al*., 2001)
3. Micrometeorite annealing of amorphous ice to crystalline ice (Porter, Desch, and Cook, 2010)
4. Galactic Cosmic Rays, and Solar UV radiation convert crystalline ice to amorphous ice (Cook 2007)
5. Vapor-deposition of amorphous water ice onto a cold surface below T =120 K as plume material (Kouchi *et al*. 1994)
6. Cryovolcanic activity (or localized heating) to convert amorphous ice to crystalline ice (Collins & Nimmo 2009; Pappalardo *et al*. 1999).

Table 2.2: Active Processes in the Outer Solar System for phase transitions of ice, and associated timelines of transition.

Surface Process	Timeline
Thermal relaxation of *amorphous* to *crystalline* [Jeniskens *et al*. 1998; Kouchi *et al*. 1994; Ligier *et al*. 2016; Berdis *et al*. 2020]	<1 day to 10-100 Myr
Conversion of *crystalline* ice to *amorphous* ice due to magnetospheric particle bombardment [Baragiola 2003; Cooper *et al*. 2001, Fama *et al*. 2010]	~ 0.6 to 600 years (depending on ion flux) ~ 3 to 9 years for Europa's Leading Hemisphere
Micrometeorite Impact Annealing of ice to *crystalline* [Porter, Desch, and Cook 2010]	~2,300 years (Europa) 7900 years (Enceladus) 364,000 years (Triton)
Galactic cosmic rays (GCRs), and Solar UV radiation convert *crystalline* ice to *amorphous* ice [Cook 2007]	1500 kyr for (GCRs) 50 kyr for UV amorphization at 40 AU
Vapor-deposition of *amorphous* water ice as plume material [Kouchi *et al*. 1994]	Present-Day Process
Cryovolcanic activity (or impact events) could convert *amorphous* to *crystalline* (localized heating) [Collins & Nimmo 2009; Pappalardo *et al*. 1999]	Present-Day Process

Europa is likely affected by all these aforementioned ice transformation processes, and the timescales and temperatures over which these transformations occur suggests that the water ice there should primarily exist in the crystalline form (Table 2.2). However, the surface bombardment by charged particles induced by Jupiter's magnetic field, and vapor deposition of water ice from Europan plumes, can produce amorphous water ice surface deposits on short timescales (Berdis *et al.*, 2020). This can potentially result in spatially and temporally varying amounts of crystalline water ice on the surface and can provide insight into the active processes that affect its surface. Current predictions of crystallinity of Europa's leading hemisphere range from ~27% to 37% using band area estimates (Berdis *et al*., 2020), ~40-60% from spectral unmixing (Ligier *et al*., 2016), and ~80-95% from thermophysical modeling (Berdis *et al*., 2020). So, there is clearly a disconnect in estimates based on different calculation techniques, and therefore a need for a more comprehensive understanding of water ice, and ice phase transitions on the surface.

Part I of this dissertation focuses on developing techniques for characterization of the crystallinity (and age) of planetary surfaces in the outer solar system, prior to application to Europa. I intend to quantitatively unravel the contributions of thermal annealing and charged particle bombardment and make predictions for steady state conditions on Europa.

PART I ENABLING REMOTE SENSING EXPLORATION

CHAPTER 3

CRYOGENIC NEAR INFRARED SPECTROSCOPY OF WATER ICE

Spectroscopy is a useful tool for investigation of the physical and compositional properties of planetary surfaces, based on their interaction with light at different wavelengths in the electromagnetic spectrum, and under various illumination geometries. It has been broadly used for over five decades to characterize planetary surfaces (at the upper sub-mm depths) using ground-based and spacecraft measurements, redefining our understanding of the outer solar system and its ability to host life.

In this chapter, I build on past research and focus on water ice, which has been extensively studied in the laboratory for the near-infrared region (Table 3.1 and references therein), using the two prominent techniques of reflection and transmission spectroscopy. For a sample placed in the path of light (or an infrared source for NIR spectroscopy), reflection spectroscopy is a method of collecting the light that reflects off the sample in a detector, while in transmission spectroscopy the light passes through the sample and is then collected. The diagnostic capabilities of each approach are identified, including their limitations, and new approaches are devised to overcome these limitations.

3.1 Water Ice Spectral Features and Associated Uncertainties

The water molecule has three fundamental vibrations in the infrared: an O-H symmetric stretching band at ~3.18 μm (ν_1), an H-O-H bending transition at ~6.1 μm (ν_2), and an O-H asymmetric stretching band at ~3.08 μm (ν_3) (Figure 3.1). Overtones and combination bands produce characteristic signals at shorter wavelengths. Further, molecular translations (ν_T) or librations (ν_L or ν_R) produce bands at ~45 μm and ~12.5 μm, respectively (Moore and Hudson, 1992). In this chapter, I focus on the 1.5 μm combination band, caused by $\nu_1 + \nu_3$, and the 1.65 μm band, caused by combinations of $\nu_2 + \nu_3 + \nu_L + \nu_T$ (fundamental bending mode, fundamental asymmetric stretch mode, librational and translational excitations) (Ockman 1958; Petrenko and Whitworth, 1999; Mastrapa 2008 and references therein).

In the near-infrared spectrum of water ice, the 1.5 μm and 1.65 μm band features are considered indicative of ice phase (Clark *et al*., 1981). Mastrapa *et al*. (2008) found the 1.65/1.5 μm integrated band area ratio to be one of the best metrics for distinguishing between crystalline and amorphous water ice. Amorphous ice is characterized by the presence of generally weak and broad band features due to their structural disorder, while crystalline ice displays stronger, narrower features (Figure 3.2). Cubic and hexagonal crystalline ice spectra are, however, relatively indistinguishable in near and mid-IR wavelengths (Bertie *et al*., 1969, and references therein). The 3.1 μm absorption peak (or 'Fresnel Peak') is another indicator of phase transitions, appearing for crystalline ice, and is broader and weaker for amorphous & warm ice.

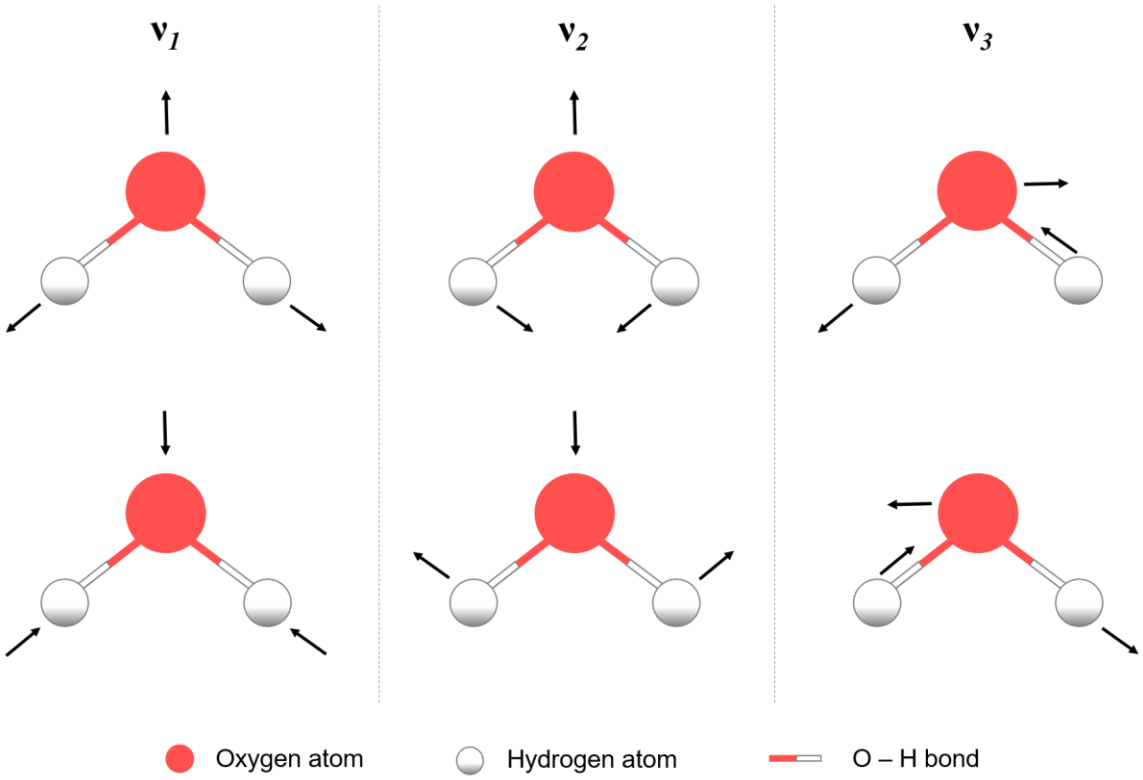

Figure 3.1: Fundamental vibration modes for water ice, ν_1 (left), ν_2 (middle), and ν_3 (right), which produce spectral features at short wavelengths (image modified from Schroeder 2002).

It is important to note that these spectral features can be dependent on, and thus representative of, various processes in the sample's history and its physical properties, which can complicate interpretation as amorphous or crystalline ice. Any such interpretation needs to be made within the context of the thermal and radiation history of the ice, its thickness, grain size, and sintering or molecular rearrangements, apart from the illumination conditions and observation geometry of the measurements. Distinctions in ice phase are less evident in the spectra based on (1) Temperature, (2) Grain Size, (3) Sample Thickness, and (4) Radiation, as detailed below.

3.1.1 Temperature versus Phase Transitions

Both amorphous and crystalline ice show variability in spectral properties depending on their temperature history. Grundy and Schmitt 1998 found that features at 1.50, 1.57, 1.65, and 2 μm shift to shorter wavelength with temperature, with the 1.57 and 1.65 μm features lose intensity with increasing temperature. In fact, high temperature, crystalline ice spectra in the NIR region look very similar to lower temperature, amorphous water ice spectra, exhibiting softer and shallower features. On cooling crystalline ice to 10 K, these bands recover their sharpness and display deeper features. Amorphous ice does not display this reversible trend. Once heated beyond 70 K (low density amorphous to high density amorphous transition) and/or 135 K (phase transition to cubic crystalline ice), it cannot recover its original absorption features on cooling (Mastrapa, 2008).

The spectral dependence on the ice phase complicates our understanding of the contribution of temperature to changes in absorption features. Bands increase in depth (greater band areas) and shift to longer wavelengths (by as much as 0.05 μm) as the crystalline ice fraction increases (Grundy and Schmitt, 1998; Mastrapa and Brown, 2006; Mastrapa *et al*., 2008). For example, the band near 1.65 μm (6050 cm^{-1}) can range in location from 1.643 μm (6087 cm^{-1}) in amorphous H_2O-ice to 1.661 μm (6020 cm^{-1}) in 20 K, crystalline H_2O-ice. Simultaneous presence of two phases complicates interpretation further. Relative amounts of each phase need to be deduced from the positions of the broad 1.5 and 2.0 μm bands and the strength of the 1.65 μm band, before unraveling the role of temperature.

These temperature and associated phase dependent spectral changes can be assigned to changes in molecular and lattice vibrations, due to the two major processes of thermal expansion and reduction of atomic motion (Mastrapa, 2008).

- The lattice contracts between 10 and 100 K, resulting in O-O space becoming smaller, the H atoms moving away from the O atoms, lengthening the O-H bond and strengthening the H-H bonds. The frequency of O-H vibration is reduced, while the frequency of lattice vibrations is increased (due to increased restoring forces from stronger hydrogen bonds acting on molecules). The bond lengths are similar and most of the molecular vibrations are in phase, sharpening the vibrational spectral features.
- When the temperature increases above 100 K, the lattice expands (Petrenko and Whitworth, 1999) with the displacement of individual atoms in the lattice increasing in size. The size of individual O-H bonds in the lattice varies, leading to a distribution of molecular vibrational frequencies broadening the spectral features.

Owing to their dependence on temperature and phase, the 1.5 μm and the 1.65 μm bands are often used in combination (using integrated band area ratios or B) as a measure of ice crystallinity, and as a thermometer for the outer solar system (e.g., Grundy *et al*., 1999; Jewitt and Luu, 2004; Cook *et al*., 2007, etc.).

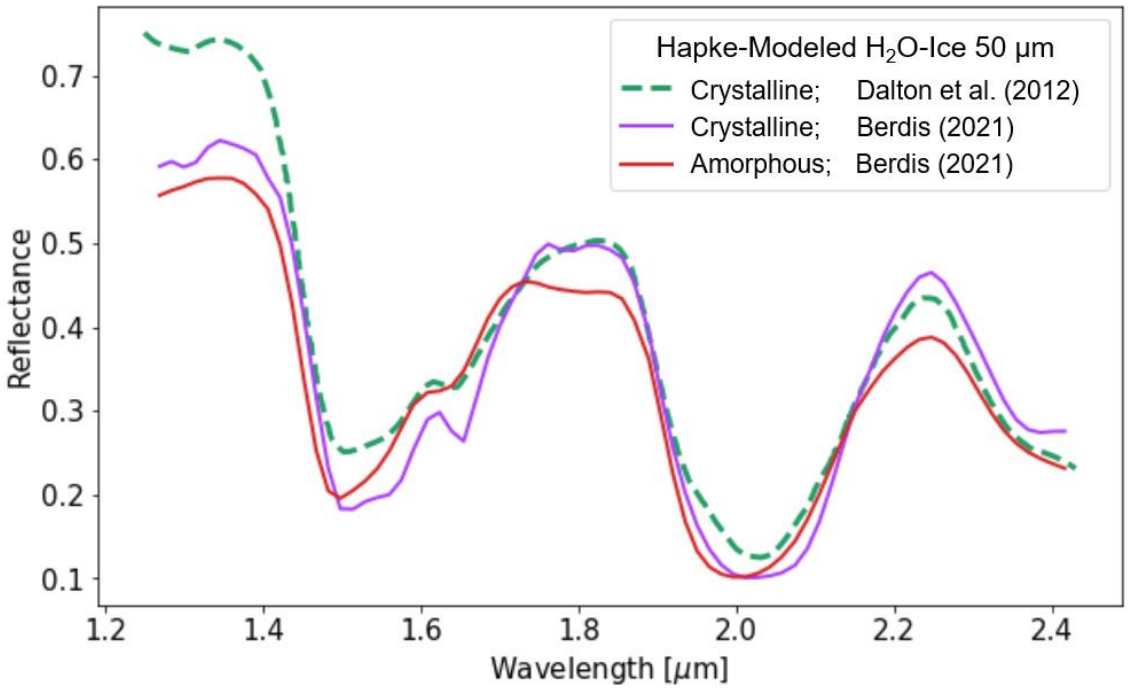

Figure 3.2: Hapke synthetic spectra of amorphous and crystalline water ice at temperatures >70 K from Berdis (2021) (using Mastrapa *et al*. (2008) optical constants), highlight the characteristic 1.25, 1.5, 1.65, and 2.0 μm band features for both ice phases.

3.1.2 Grain Size

As the grain size increases to ~240 μm, the shapes of the 1.5 and 1.65 μm infrared bands produced by water ice samples: (1) grow deeper with increased band depth, (2) broaden with change in position of band center to longer wavelengths as reported by Taffin *et al*. (2012), and (3) exhibit an overall reduced spectral reflectance (Clark, 1981). This can be explained by considering the path of light through the water ice sample. Scattering off the surface, at the grain boundary interfaces or due to imperfections in the crystal, controls the amount of incident light reflected back to the detector. For a surface composed of large grain sizes, with a longer path length through the sample, some of the incident light penetrates through the grains instead of undergoing reflection at the prominent grain boundaries, resulting in a decrease in overall reflectance signal. This behavior is consistent with a large, continuous block of ice, where the reflected signal is very low due to the block acting like a transparent medium. For smaller sized grains, the light undergoes single scattering reflection at the interfaces and a higher reflectance is recorded.

Constraining the role of grain size on NIR band features will enhance interpretation of planetary surfaces, including composition with spectral unmixing techniques, the relative age of features using spatial variation in sizes, and eventually identifying regions of interest for future missions.

3.1.3 Thickness

The thickness of water ice samples is known to influence spectral band features and their band areas in the 1.5-1.65 μm region. A thickness of >5 μm is required for sufficient path length through the sample to see the infrared bands between 1 and 3 μm. Thickness >15 μm is required to avoid distortion of infrared bands by interference fringes caused by light reflecting from substrate on which ice is deposited under laboratory conditions. This is not an issue under planetary surface conditions unless the layer beneath is a smooth reflecting surface. An increase in thickness of the samples during water vapor deposition therefore results in a nearly linear increase in absorption band depths until saturation (Berdis, 2021). Beyond a thickness of 50 μm, scattering increases which can lower the signal to noise ratio (SNR) and lower the absorption depths (Mastrapa, 2008).

Laboratory spectroscopy of " thick" water ice is directly relevant to interpretation of spectra collected from real planetary surfaces in the outer solar system, which have a thickness far beyond 50 μm. It has also been proposed that the top layer of an amorphous ice sample can crystallize due to a warming effect of the subsurface layer ice with an increase in thickness (or deposition). In such a case, NIR spectra will resemble that of crystalline ice, disguising the underlying amorphous ice on the surface. Similarly, condensation of residual water vapor in the chamber on crystalline ice could result in the formation of thin layer of amorphous ice on the crystalline ice at temperatures well below the amorphous to crystalline transition, which can subdue the signal of underlying crystalline ice. Both cases have significant implications for crystallinity calculations in regions with fresh, plume deposits.

3.1.4 Radiation

Near infrared spectra of radiation-altered crystalline water ice and vapor-deposited amorphous ice show similarities, which often leads to interpretation as ‘‘amorphization of crystalline ice’’ due to radiation. However, to date there exists no direct evidence indicating that the crystalline structure is completely destroyed during irradiation (Mastrapa, 2008). Instead, irradiation is predicted to cause disorder in the crystal lattice that broadens band features and decreases intensity. The variations in the 1.65 μm band feature are assigned to either (1) breaking of hydrogen bonds due to ion interaction, (2) moving/breaking of O-H bonds, or (3) disruption of the water molecules contributing to vibrational modes (Mastrapa, 2008). Previous irradiation experiments on crystalline ice identified a temperature dependence for the 1.65 μm feature, which decreases with increase in dosage at 50 K but changes only slightly at 100 K (which is the average surface temperature of Europa) and shifts to longer wavelengths. The 1.5 μm feature is weaker than in the amorphous ice spectrum at 50 K, but becomes stronger on irradiation at 100 K.

Irradiation experiments on amorphous ice are extremely rare but expected to sever the molecular bonds in the ice and change the strength of spectral features. Hudson and Moore 1992 reported a temperature dependence with little to no changes observed on irradiation between 27 K and 125 K, but observed a crystallization of ice with increased radiation dose below 27 K. Rise in temperature post (UV-) irradiation is reported to change the shape of amorphous ice, implying a liquid-like state for the ice between ~ 60 K and 150 K (Tachibana *et al*., 2017) (Figure 3.3).

Incorrect interpretation of planetary surface ices as amorphous due to subdued band features post irradiation is a valid concern, with implications for Galilean satellites, while changes in spectra for amorphous ice has astrochemical implications. The role of high radiation dosage (~ MeV) for electrons, protons, and ions thus needs to be constrained.

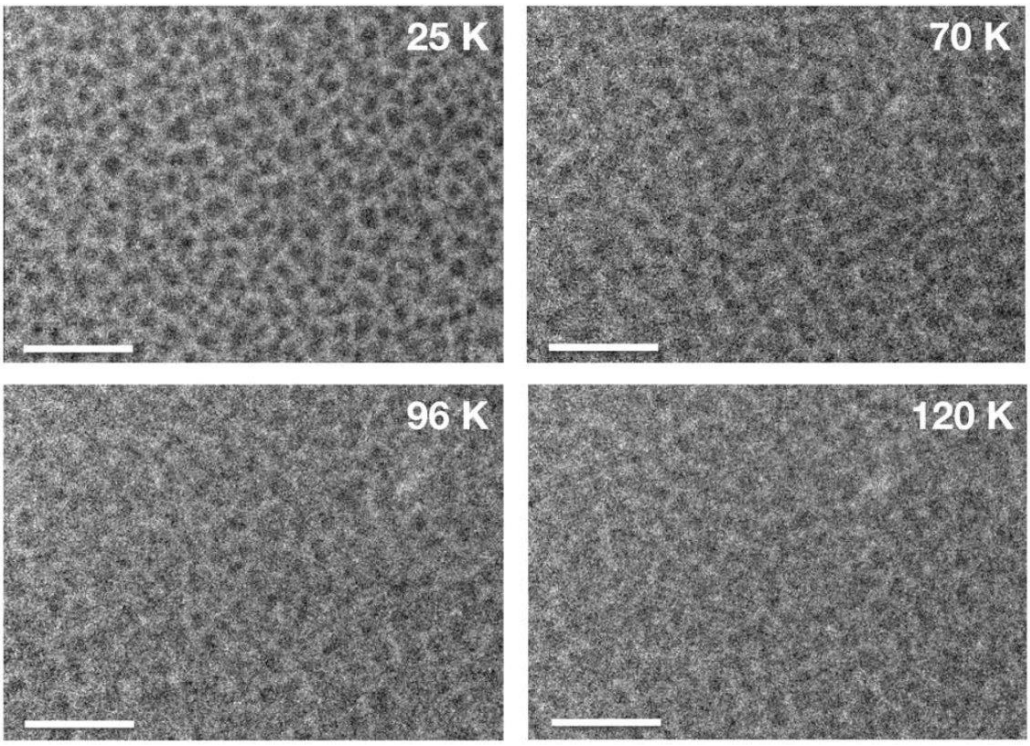

Figure 3.3: Effects of temperature rise on (UV-irradiated) amorphous ice observed by a transmission electron microscope. Islands of amorphous water ice (represented by dark areas in the photos) change shape and spread over the substrate like liquid, which is indicated by the blurring of the images. Scale bars=0.5 micrometers. Figure from Tachibana *et al*. (2017).

3.2 Current State of Laboratory Spectroscopy Data and Limitations

Radiative transfer models (e.g., for spectral unmixing analysis of observed spectra of Solar System objects) require accurate optical constants, describing the spectral character of the absorption and refraction of light, as inputs. Water ice spectral properties have been extensively studied in the past (Irvine and Pollack 1968, Wiscombe and Warren 1980), and absorption coefficients of relatively warm ice have been published (Kou *et al*., 1993, Grundy and Schmitt, 1998; Clarke and Roush, 1984; Mastrapa *et al*., 2008, 2009). However, as highlighted in Section 3.1, there is a need to characterize water ice absorption bands in the near-infrared region using (1) reflection spectroscopy, (2) within the context of the thermal and irradiation histories, and (3) physical properties (grain size and thickness) of the material.

Several research groups are currently working on understanding the properties of ice grains (Pommerol and Schmitt 2008; Gundlach *et al*., 2011, 2018; Hand *et al*., 2015; Hibbits *et al*., 2017; Poston *et al*., 2017, 2018; Johnson *et al*., 2019; Table 3.1 and references therein). Models have been developed to study the temperature dependence of water ice and generate synthetic spectra to identify grain size dependence (Grundy and Schmitt, 1998; Mastrapa *et al*., 2009; Nolin and Dozier, 2000). These studies provide a starting point for understanding the surface spectra of icy satellites, but the short wavelength coverage and lack of constraints on the physical parameters add uncertainty to our interpretations (Hansen and McCord, 2004; Jaumann *et al*., 2008; Dalton, 2008; Dalton *et al*. 2013). For example, the variability of water ice spectra as a function of grain size

have been modeled but laboratory measurements are rare (Clark *et al*., 1980, 1983), while cryogenic reference spectra for hydrated salts of varying grain sizes are not yet available.

Berdis *et al*. (2020) and references therein highlighted the current state of knowledge for optical constants and the available laboratory spectra of pure crystalline and amorphous water ice which act as end members for spectral interpretation. In Table 3.1, I have expanded on their work to incorporate the recent history of laboratory spectral studies conducted for various grain sizes, compositions, and temperature conditions, and importantly the wavelength regime over which these studies were conducted. While this table is not an exhaustive list, it demonstrates that there are knowledge gaps (in red) that still need to be addressed.

Table 3.1: Laboratory spectroscopy for water ice (+salts) in the last three decades, highlighting the wavelength coverage, along with grain size, composition, and temperature constraints.

Study (Wavelength)	Grain Size	Composition	Temperature
Clark *et al*. 1980a (0.65-2.5 μm)	Fine to Coarse (50; 0.4-2 mm)	Water Frost	110-170 K
Clark *et al*. 1980b (0.325-2.5 μm)	<= 125 μm	Montmorillonite, Kaolinite, Beryl, Mauna Kea red Cinder, and Black Charcoal	177-293 K
Clark *et al*., 1983	-	Water Ice	-
Grundy and Schmitt 1998	-	Water Ice	20-270 K
Carlson *et al*. 1999 (1 – 2.5 μm)	Between ~5 to 50 μm	Hydrated Sulfuric Acid	140 K

Study (Wavelength)	Grain Size	Composition	Temperature
Dalton *et al*. 2003-2012 (0.3 – 2.5 μm)	-	Hydrated Sulfate Salts, Brines	100-140K
Mastrapa *et al*. 2008 (1 – 2.5 μm)	-	Water Ice	20-150 K
ISL 2010 (unpublished) (1.25 – 8 μm)	-	Water Ice (Few μm thick)	10-150 K
Taffin *et al*. 2012 (~ 1 – 2 μm)	80 – 700 μm	Water Ice & Frost (5 mm thick)	80-140 K
Hanley *et al*. 2015 (1 – 25 μm)	63 μm	Chlorates	290-400 K
Poston *et al*. 2017 (0.35 – 1.1 μm)	300 μm	NaCl	100-290 K
Thomas *et al*. 2017 (1 – 2.7 μm)	Fine powder	NaCl, KCl, $CaCl_2$, $MgCl_2$	80-233 K
Hibbits *et al*. 2019 (0.2 – 1.3 μm)	13 mm diameter Pellets	NaCl, KCl, Na_2SO_4, $MgSO_4$, $FeSO_4$, Na_2CO_3, $CaCO_3$	300 K
Johnson *et al*. 2019 (1 – 2.7 μm)	Fine powder	Hydrated Salts	100 K
Loeffler *et al*. 2020	-	Water Ice	10-100 K
This work (1.25 – 8 μm)	10 to >250 μm Every 25 μm	Water Ice (2 mm thick, Crystalline & Amorphous)	10-150K

3.3 New Measurements: Rationale and Scope of This Work

Observational ground-based and spacecraft datasets for planetary bodies such as Europa are collected as reflectance spectra, which are evaluated using laboratory datasets. With the Europa Clipper mission scheduled to launch in 2024, and Dragonfly scheduled in ~2027, detailed surface characterization of Europa and Titan (alongside other icy worlds) may soon be feasible. Among the suite of instruments on board Europa Clipper, the Mapping Imaging Spectrometer for Europa (MISE) (Blaney *et al*., 2019) could help reveal the surface distribution of organics, salts, water ice phases and other materials on Europa. However, our interpretation will be contingent on the availability of lab spectra over the full spectral range of the MISE instrument (0.8 to 5 μm), in addition to the spectral range of the Galileo Near Infrared Mapping Spectrometer (NIMS) (0.7 to 5.2 μm).

Table 3.1 highlights the need for new measurements as existing datasets were collected either as transmission spectra or as reflectance spectra of thin, vapor deposited samples (e.g., Clark *et al*., 1980; Schmitt *et al*., 1998; unpublished ISL measurements; Mastrapa *et al*., 2008, 2009), and they do not cover the requisite spectral range (confined to 1-2.5 μm). UV-VIS-NIR laboratory spectroscopy measurements of multiple icy satellite candidate materials of appropriate sample thickness, under cryogenic temperatures and realistic irradiation conditions are required. I attempt to address some of these needs with experimental reflection spectroscopy over the wavelength range of 1.25 to 8.0 μm, using thick water ice samples with controlled grain sizes, over a range of cryogenic temperatures.

Broadly, three components of laboratory spectroscopy identified for improvement are detailed below, along with the approaches developed to achieve these improvements:

1. Differences in the methods of acquiring reflectance spectra from a real planetary surface and transmission spectra from thin films of water ice may contribute to inaccurate calculations of the integrated band areas for the 1.5 and 1.65 μm bands (despite conversions made to account for the differences in acquisition methods, such as $\text{Absorbance}_\lambda = \log_{10}(1/\text{Reflectance}_\lambda)$.

   In particular, laboratory samples of amorphous and cubic ice have only been prepared by direct condensation from the vapor phase, and there is no reported way of preparing thick, optical quality samples of amorphous H_2O ices (Clark, 1981). Previous work like Mastrapa 2008 used thin films with thicknesses of 8 ± 1.5 μm. I attempt to prepare thick samples of amorphous and crystalline water ice in the lab, at 77 K and 250 K respectively. I performed reflection spectroscopy and optical microscopy to record variations in band features, including any perceived phase transitions on heating between 100-150 K. Using experimental procedures described in Chapter 4, I adopt two techniques to prepare ice samples, and determine whether it is possible to create amorphous ice samples in the laboratory by ex-situ deposition.

2. Previously acquired crystalline and amorphous end-member laboratory spectra (and the ratio of 1.65 and 1.5 μm band areas: defined here as B_{cryst} and B_{amorph} respectively for crystalline and amorphous ice) of pristine water ice do not capture the thermal history of the ice. Calculation of crystallinity or surface composition for icy solar system bodies using these end members can be problematic, as the shapes and positions of the bands, and their band areas evolve significantly with temperature. It was previously reported by Mastrapa (2008) that the heating history of a sample has no effect on its spectral features, barring a phase change. For example, they report that a crystalline

H_2O-ice sample deposited at 150 K, cooled to 20 K, and heated to 50 K looked the same as a sample deposited at 150 K, and cooled directly to 50 K**.** This claim is investigated in Chapter 4, where I have used laboratory measurements to study the effects of thermal cycling on water ice grains and their collected infrared spectra, with a focus on the temperature sensitive 1.65 μm and 1.5 μm bands. New laboratory end-members are calculated for amorphous and crystalline water ice (B_{cryst} and B_{amorph}) and compared with Mastrapa *et al*. (2008) values (shown in Figure 3.4). Evolution of band area ratios and phase changes with temperature are also determined using a new ratio B_{TH} to track the change in band area (and spectral features) with evolution of thermal history of the ice. In other words, does a crystalline ice sample at 100 K have the same spectral features as a sample cooled to 10 K and then heated to 100 K?

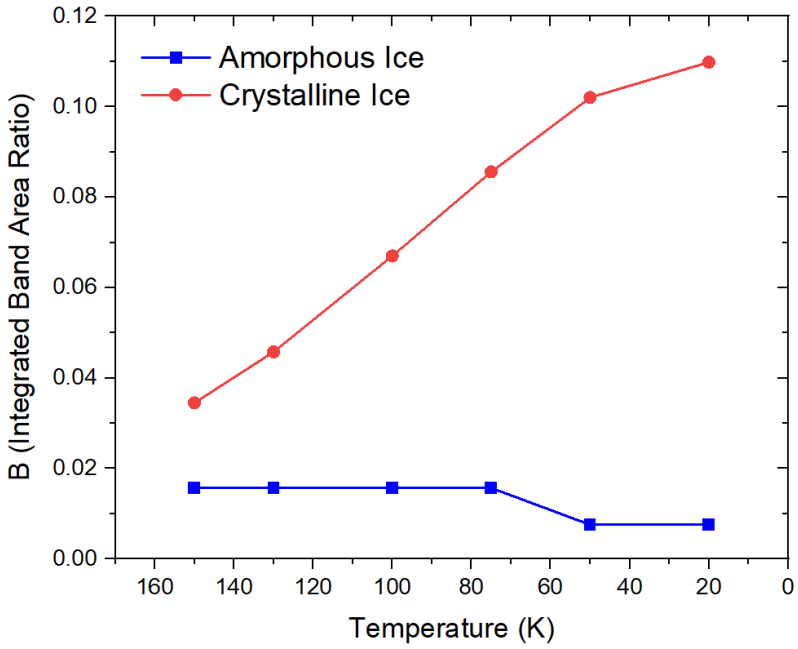

Figure 3.4: Mastrapa *et al*. (2008) laboratory end members for 100% crystalline and amorphous ice at different temperatures relevant to the outer solar system.

3. Expected variations in grain size for water ice across the surfaces of planetary bodies like Europa (Prockter *et al.*, 2017) can impact crystallinity and composition calculations, due to associated changes in band depths (e.g., Clark 1981; Jaumann *et al.*, 2008). Current grain size estimates for Europa vary from 5 μm to a few mm for the remotely sensed layer (Dalton *et al.*, 2012, Shirley *et al.*, 2010; Hansen and McCord, 2004), with larger grains (75-100 μm) expected in older, higher albedo regions, and smaller grains more abundant in younger, lower albedo regions (Prockter *et al.*, 2017). Grain size can thus be used as a tool to determine the relative exposure age of observed materials if accurately characterized. However, there are only a handful of laboratory studies with grain size controls.

   To investigate the impact of grain size on the 1.5 and 1.65 μm band features, I have used two temperature-dependent protocols to create controlled grain size samples of water ice in the laboratory. I have assessed the accuracy of using these bands in interpreting the crystallinity and evolution of surface ices on icy bodies in the outer solar system, and Europa in particular: to differentiate between cold, "*fresh*" ice and thermally altered, "*old*" ice using measured signal strength.

In Chapter 4, I will address spectral feature variations arising due to (a) temperature, (b) grain size, and (c) thickness. Radiation experiments (d) are not included in this dissertation, but remain a strong focus for future work, as described in Chapter 8. In Chapter 5, I will identify the limitations of our new reflection spectra and the integrated band area ratio technique (Chapter 4) in application to Europa. This will result in a deeper understanding of the physical properties of the surfaces of outer solar system icy bodies.

CHAPTER 4

CONSTRAINING THE ROLE OF THERMAL HISTORY, THICKNESS, AND GRAIN SIZE OF WATER ICE IN PLANETARY REFLECTION SPECTROSCOPY

To understand the influence of crystal phase, environmental conditions, and sample physical properties on water ice spectral features, I undertook a laboratory effort that included preparing relatively thick (> 15 μm), optical-quality, grain size-controlled samples of ice by ex-situ deposition at cryogenic temperatures (77 K) as well as relatively warm temperatures (~250 K). A new instrument was custom built in the Ice Spectroscopy Lab at the Jet Propulsion Laboratory, to collect reflection spectra of samples deposited on a copper sample holder inside a vacuum chamber. Here, I report on the thermal cycling, thickness, and grain size experiments at conditions relevant to ocean worlds, though the complete setup enables an even broader suite of future experiments involving irradiation and various chemistries (e.g., ice and salts, sulfuric acid, etc.).

4.1 Materials and Methods

4.1.1 ISL Experimental Setup:

Experimental ice research requires specific equipment and facilities to work at low temperatures, and special care to handle and characterize icy material without modifying its properties. Some challenges include (1) preserving consistent grain sizes within each sample, (2) avoiding thermal alteration of the sample and preventing contamination from other particles (including frost) due to exposure to nominal atmospheric conditions, and (3) ensuring collected spectra is representative of the samples.

4.1.1.1 Ice Deposition Setup

New infrastructure was custom-built to produce pristine samples of ices of various chemistries, while reducing contamination due to frosting from the air. This instrument consists of an ice deposition and sieving dry box with continuous N_2 purge (see Figure 4.1). The setup includes an air gun / mister with ultrapure water which is sprayed into a dewar filled with liquid nitrogen (LN) to form small droplets of ice in solution. Details are described in the ice preparation subsection below. This ice-LN solution is transferred to precooled sieves in a LN bath to control the grain size of the sample in the range of 10 to >200 μm. Sieved grains are transferred to a 1 inch copper sample holder in an LN bath using precooled spatulas, maintaining a uniform ~2 mm layer on the surface of the holder.

Figure 4.1: An ice deposition setup has been developed at ISL to prepare samples of controlled grain size (with sieving in liquid nitrogen at 77K), composition, and crystal structure at different temperatures.

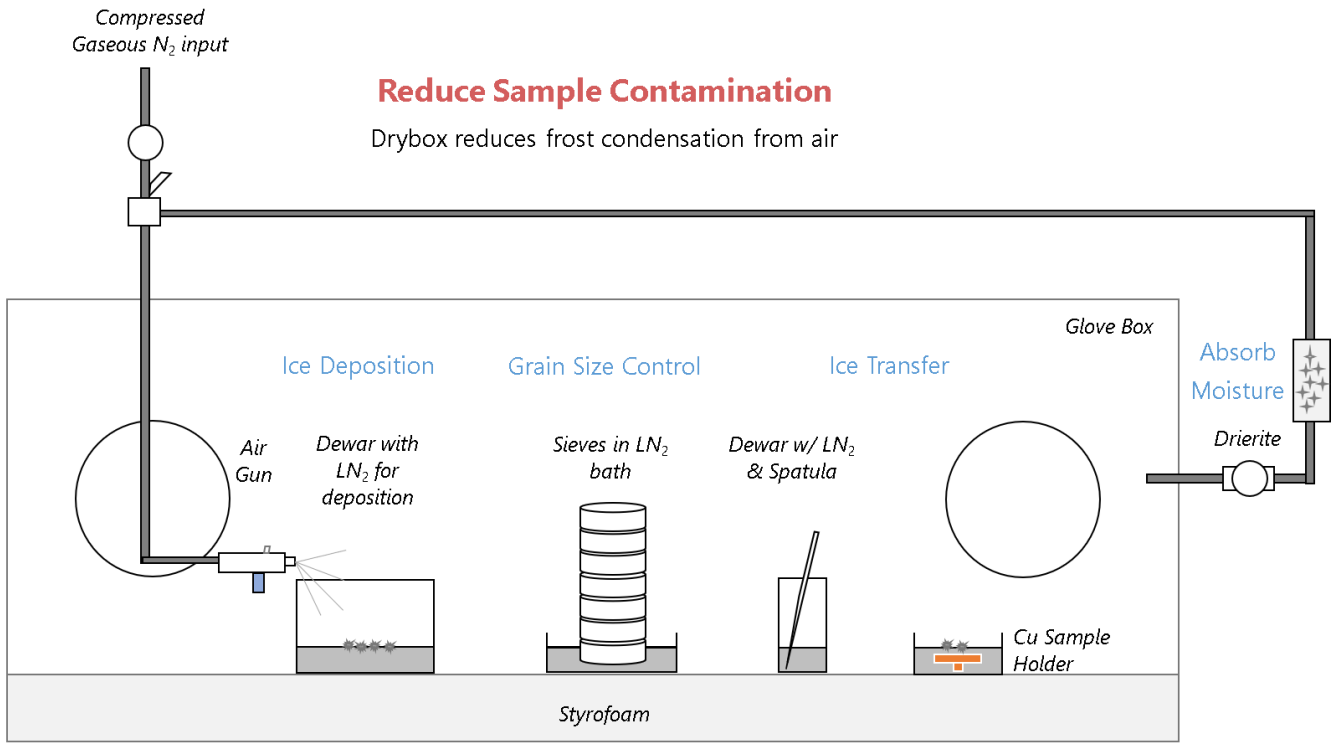

4.1.1.2 Vacuum Chamber

The sample holder with ice grains is transferred to a high-vacuum chamber (titled 'Apollo') with a closed-cycle helium cryostat, to maintain the Cu substrate at a specific temperature between 10 K–300 K, which is connected to a turbomolecular pump assuring an ultrahigh vacuum of $<10^{-8}$ mbar as measured by an inverted magnetron gauge at room temperature. A heater on the cryostat, controlled by a Lakeshore temperature controller, was used to regulate the temperature and perform thermal cycling with a precision of ± 0.01 K. The chamber also includes UV-VIS-NIR reflection spectrometers with a custom mirror assemblage and closed with a sapphire window mounted on stainless-steel flanges with O-ring seals, and a remote microscope setup, as depicted in Figure 4.2. 4.3. I have spent the past two years designing, fabricating, and calibrating instrumentation, to enable the types of experiments described here. This setup allows collection of spectra at a range of pressure and temperature conditions from 5-300 K, covering the spectral range of 0.2 to 8 μm (spectral resolution of 1 cm^{-1}), which overlaps with both Galileo NIMS (0.7 to 5.2 μm) and future Europa Clipper MISE observations (0.8 to 5.0 μm).

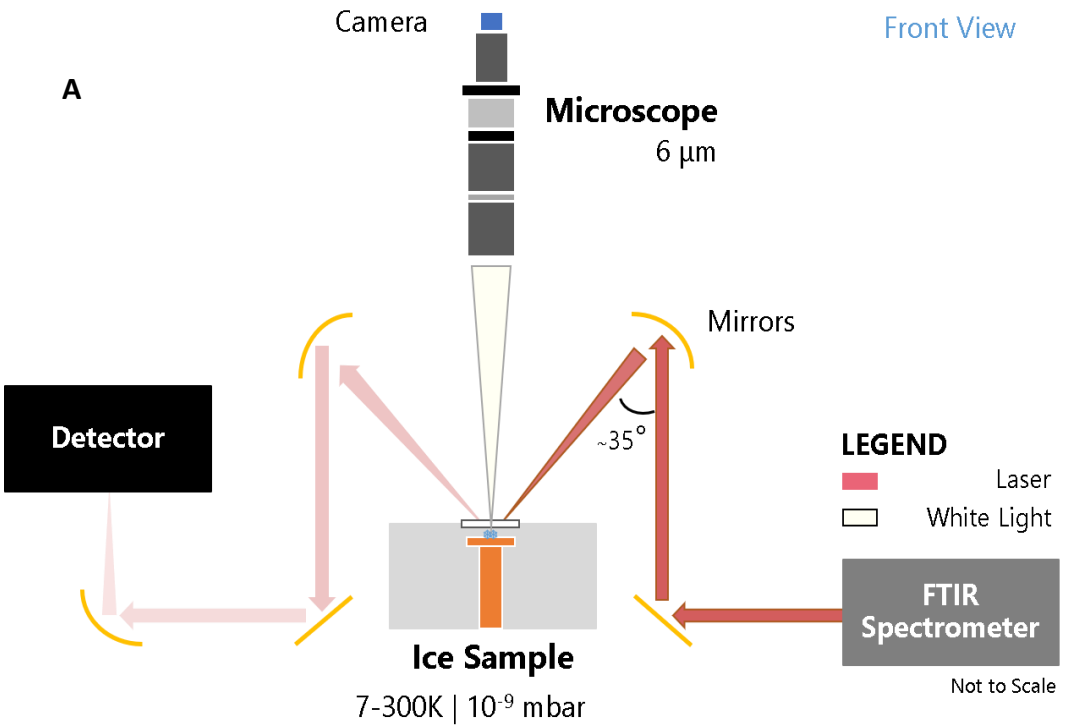

Figure 4.2: The ISL-developed instrument incorporates an ice deposition setup, an FTIR spectrometer with an MCT detector, and a remote microscope, as depicted here, to conduct spectroscopic studies on grain-size specific Europa surface ice analogs.

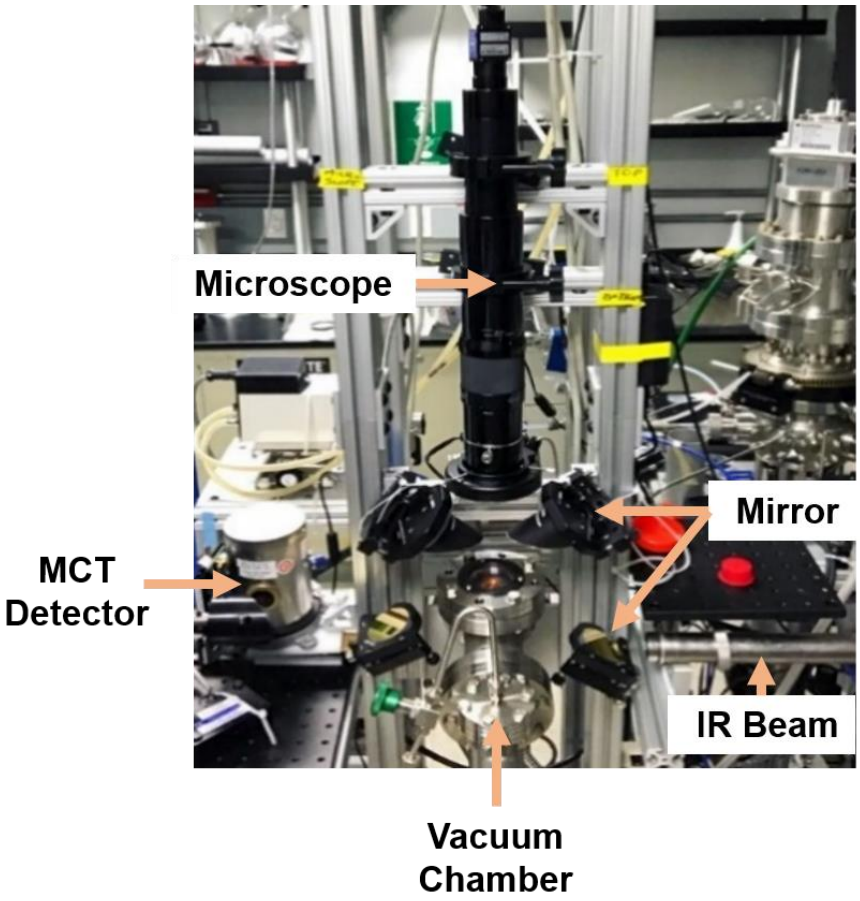

Figure 4.3: Apollo experimental setup used for reflectance spectroscopy.

4.1.2 Sample Preparation for pure H_2O Ice

In this dissertation, I focus primarily on water ice samples, prepared at different temperatures using two separate protocols, which were developed for preparation of grains of controlled size, with varying ice composition at 77-250 K. These protocols were undertaken to further investigate the role of ice crystallinity in the observed spectral features as well as changes observed over the timeline of the thermal cycling experiments. Overall, the characteristics of the ice samples were selected based on the current consensus of Europa's surface materials in the literature.

Pure water-ice samples (referred to as Mist Ice or MI) are produced through droplet condensation, by misting ultrapure H_2O into a clean dewar filled with liquid nitrogen (LN) (Goldsby and Kohlstedt, 2001; McCarthy *et al*., 2011). For pure crystalline water ice (referred to as Freezer Ice or FI), we slowly freeze ultrapure water overnight in capped aluminum cylinders, with ~1 mm wall thickness, placed inside 253 K (-20°C) ice chests. This creates a column of ice, or core, which is immersed in liquid nitrogen to equilibrate the sample. All ice cores are frozen in a vertical configuration and are fully dense, with no visible air pockets. The ice cores are subsequently ground with a mortar and pestle in liquid nitrogen. Grain size is divided into sets, based on availability of commercial sieves, by sieving in liquid nitrogen (Figure 4.4).

The grains are sieved into seven different ranges:

(i) Less than 25 μm

(ii) Between 25 and 53 μm

(iii) Between 53 and 75 μm

(iv) Between 75 and 106 μm

(v) Between 106 and 153 μm

(vi) Between 153 and 212 μm

(vii) Greater than 212 μm

Ice grains are transferred to a sample holder (circular well of ~ 2 cm) inside a high vacuum chamber (Bekaert *et al*., 2017), which is pumped down to 10^{-9} mbar and cryogenically cooled to 100 K to replicate Europa's surface conditions, specifically equatorial dayside temperatures (Spencer *et al*., 1999).

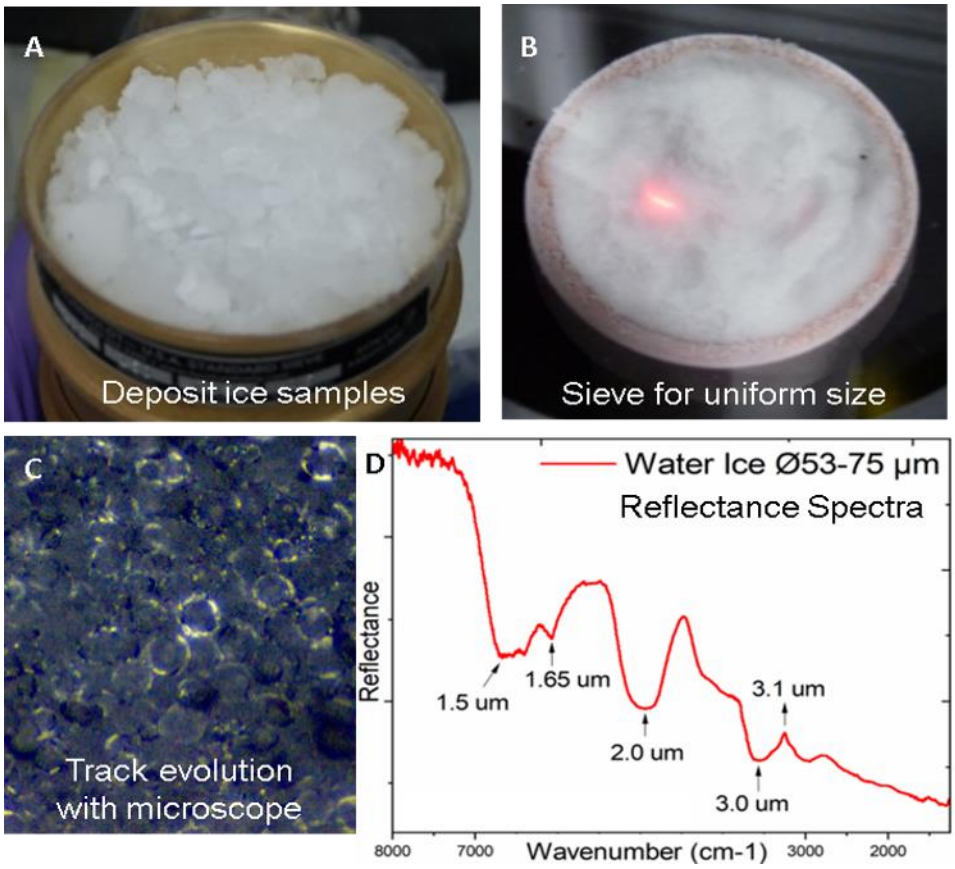

Figure 4.4: Our lab study uses the approach demonstrated here to deposit ices (A), sieve to relevant size (B), track the evolution (C), and collect reflectance spectra (D) in the 1.25-8 µm spectral range, required to interpret both Galileo NIMS (past) and Europa Clipper MISE data (future).

4.1.3 Infrared Reflection and Absorption Spectroscopy

Single beams near infrared spectra of prepared ice samples are collected using a Thermo Scientific Nicolet 6700 Fourier Transform Infrared Spectrometer (FTIR), and processed to obtain absorption spectra by choosing appropriate background spectrum as reference. As shown in Figure 4.2, the FTIR collimated beam (a few millimeters in diameter) is focused onto the sample inside the chamber, using a plane mirror and an off-axis parabolic mirror, and enters the chamber through a sapphire window. The beam goes back out the window, diverges post reflection, and is inverted back to a collimated beam by another parabolic mirror, before being focused onto the Mercury Cadmium Telluride (MCT) detector, cooled to 77 K by liquid nitrogen. Infrared spectra were recorded between 1,600 cm^{-1} (the sapphire window absorption limit) and 12,500 cm^{-1} at a resolution of 1 cm^{-1} by averaging 200 scans. Multiple measurements for all ice samples are collected to ensure "*photometric precision*" or reproducibility of data. Background pressure during the collection is stable in the range of 10^{-7} to 10^{-8} mbar (depending on temperature).

Future Capabilities: The current mirror assemblage allows us to provide realistic reflection data for a given phase angle (i.e., incidence (i) = 35º, emission (e) = 35º, phase (g) = 70º). In future, this range will be extended to cover all phase angles relevant to Galileo NIMS and Europa Clipper MISE instruments.

4.1.4 Transmission Spectroscopy of Thin, Water Ice Samples

The 'Acquabella' experimental setup at ISL includes a cryogenic vacuum chamber, cooled by a closed-cycle helium cryostat, capable of simulating the surface conditions of outer solar system objects (as low as 10 K). Inside the chamber, ice samples are vapor-deposited from degassed ultrapure water (from J.T. Baker / Fischer Scientific) at a constant flow rate of ~ 8.5 nm minute^{-1} (Barnett *et al*., 2012) through a spray nozzle onto a sapphire window (Gudipati and Allamandola, 2004). Deposition is performed at a pressure of 10^{-8} mbar and at constant temperatures (100 K or 120 K, depending on experiment). The sapphire sample holder is rotated 45º from perpendicular to the infrared beam, and kept in position throughout the experiment. It can be rotated toward one of the spectrometers for measurements (Figure 4.5, 4.6). Single beam transmission spectra were continuously collected during the experiments using a Nicolet 6700 FTIR Spectrometer with a quartz beam splitter, and a Mercury Cadmium Telluride (MCT) infrared detector.

Various other instruments were also incorporated in the setup for future testing, including ultraviolet-visual spectrometers, a mass spectrometer (MS), and an Optical Parametric Oscillator (OPO) laser (at wavelengths between 410 – 2400 nm) to irradiate samples if desired (Dubois, 2018).

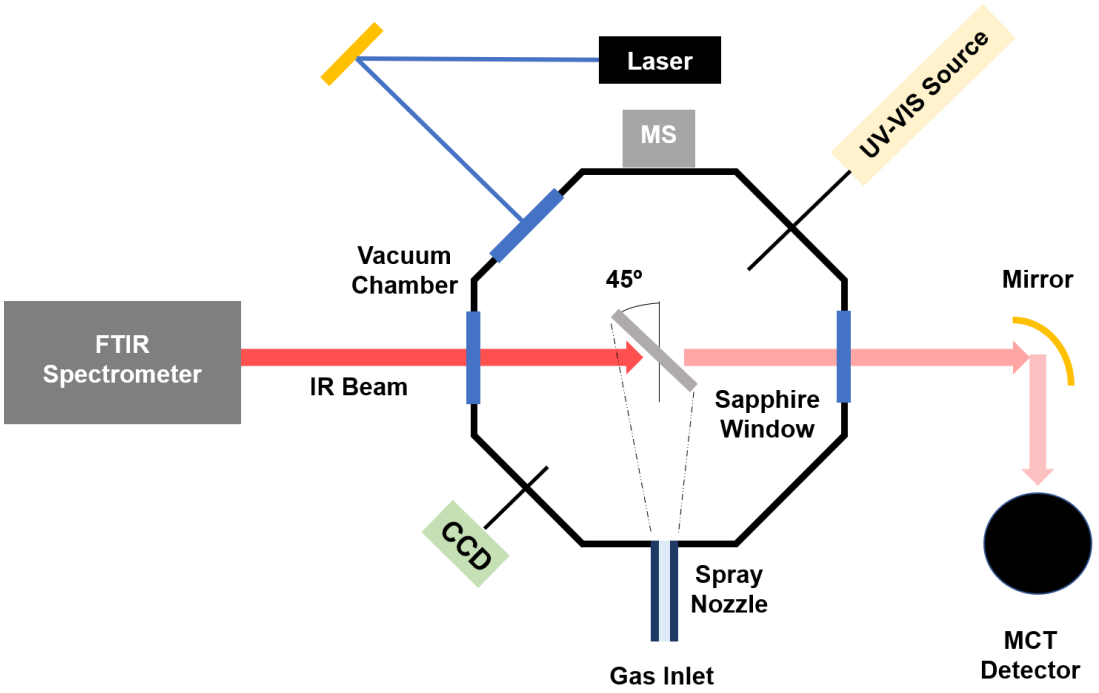

Figure 4.5: The Acquabella instrument at ISL used for collection of transmission spectra for water ice samples of varying thickness. Experiments conducted in 2010 are evaluated in this dissertation (acknowledgement of researchers is included in Section 4.4).

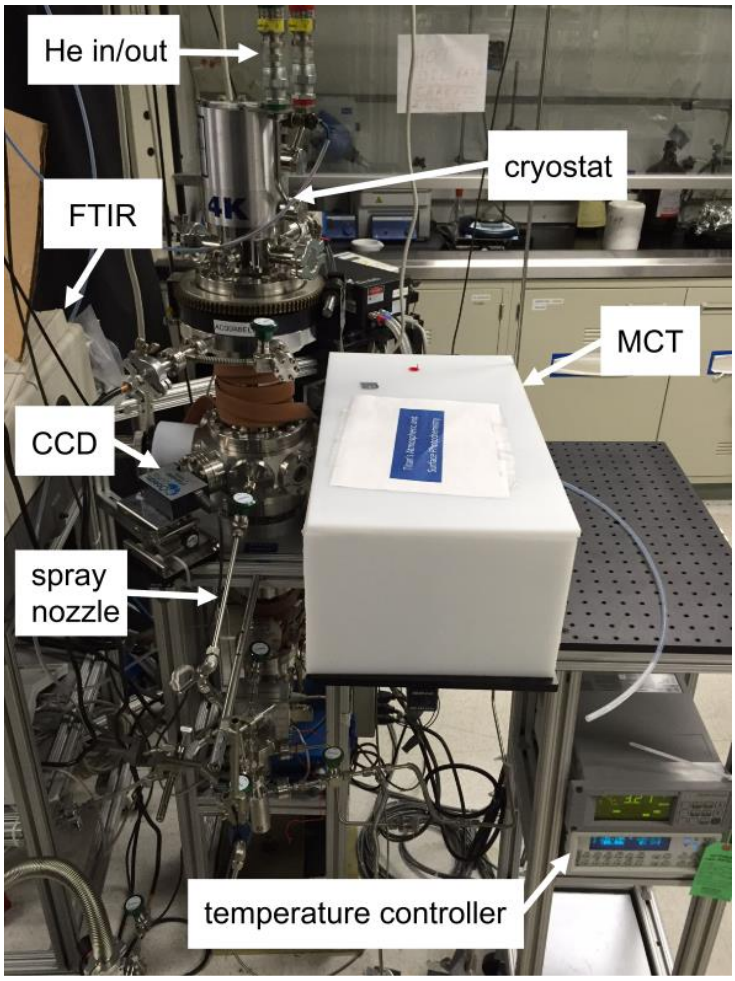

Figure 4.6: Labeled image of the Acquabella experimental setup at ISL. Image courtesy of Dubois 2018 and Berdis 2021 figure 2.3.

4.1.5 Variation of Temperature

Thermal cycling of the ice samples inside the vacuum chamber is performed, post placement in three separate stages, namely cooling – heating – cooling. At multiple temperatures during this cycle, reflectance spectra and optical images are collected to observe the evolution of the ice and its spectral features.

First, the samples placed at 100 K are cooled in steps of 25 K, down to 50 K, and then cooled to a minimum temperature of 10 K (to increase signal to noise ratio), collecting spectra at each step between 10-100 K. The temperature adjustment or ramp rate is maintained at ~3 K per minute between each data collection step, and the pressure is recorded to ensure high vacuum during the entire experiment. The sample is allowed to thermally equilibrate at each temperature by letting it sit for at least 10 minutes – until the collected infrared spectra shows minimal changes, and the chamber pressure has stabilized. There is a possibility that the temperature displayed in the controller is not identical to the temperature of the sample, owing to the placement of the thermocouple at the base of the cryostat. Allowing thermal equilibration is a means of overcoming this limitation. In the second stage of the experiment, the sample is heated up from 10 K, in steps of 25 K with thermal equilibration, up to a maximum temperature of 150 K, collecting spectra and images. Finally, the sample is cooled back down to 10 K using the same procedure as in the first stage. During this entire cycle, the temperature range of 50-150 K (and 10 K) (Figure 4.7) is covered, which overlaps with the expected diurnal/seasonal range of surface temperatures (considering both equatorial and polar regions) for ocean worlds like Europa, Enceladus, Triton, etc., thus ensuring applicability of collected spectra to these bodies.

In a few experiments, the heating range was extended to 250 K, far beyond the generally studied 150 K. The goal was to identify any further transitions in the ice crystal structure, apparent in the spectral band variations, from crystalline to hexagonal crystalline ice, as reported by Grundy and Schmitt 1998. An additional set of experiments were pursued with an additional stage of thermal equilibration of the loaded ice at 100 K for 24-72 hours. They are described in detail in Section 4.3.2.1.

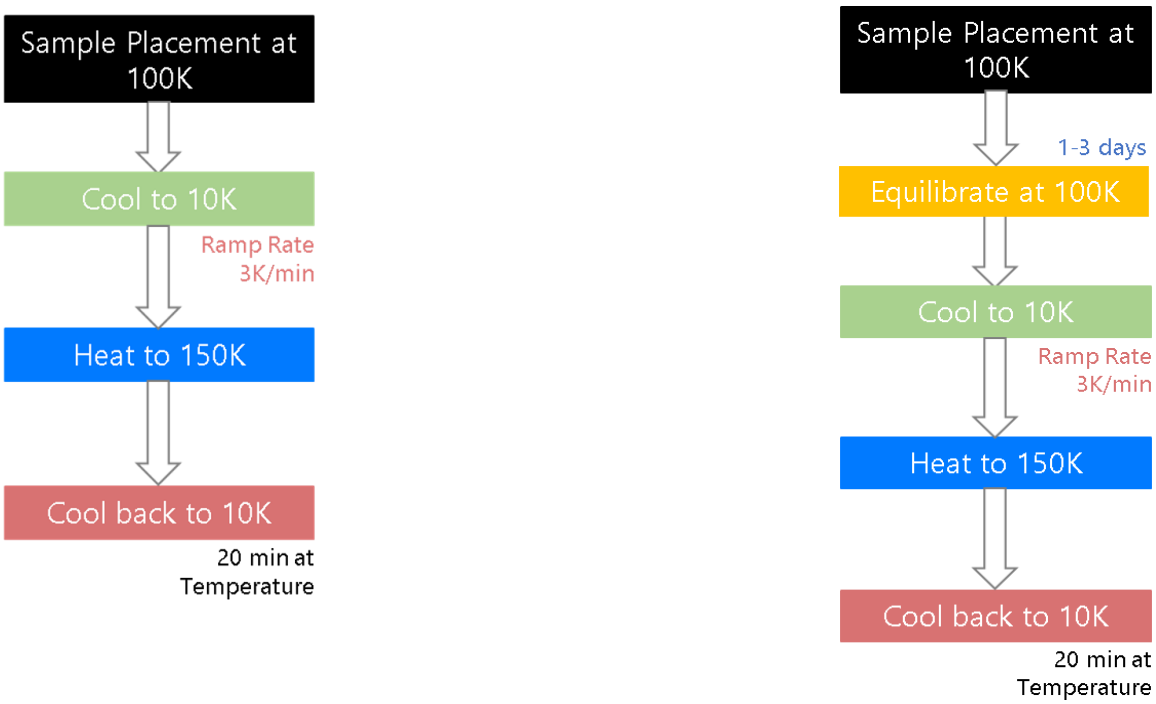

Figure 4.7: Thermal cycling procedure for samples (left). For overnight tests (right), the procedure is modified to include equilibration at 100 K for 1 to 3 days.

4.1.6 Grain Size Evolution with Microscopy

Optical images of ice grains inside the copper sample holder, mounted vertically inside the chamber, are collected using an INFINITY K-2 DistaMax Microscope with a CF-2 objective (resolution: 2 µm at 10 cm vertical distance), and a Zeiss Axiocam digital camera with a C-Mount adapter (resolution: 6 µm). The Zeiss camera allows continuous video recording and imaging. Images are collected during each experiment along with each spectra collection, and analyzed qualitatively to observe any changes in shape or structure of ice grains (e.g., pore formation).

ImageJ software is used for image processing, to determine grain size distribution of samples inside the chamber and verify sieving efficiency. At the end of experiments, the final images are analyzed to quantitatively estimate the evolution of grain size.

4.2 ISL Laboratory Reflection Spectra

Reflectance spectra of laboratory samples of "thick" pristine water-ice grains was collected in the near infrared (NIR) wavelength range, with grain-size ranging from 25 μm to greater than 212 μm at temperatures of 10-170 K for direct comparison to spectra of Solar System objects. Samples display spectral signatures of water ice, both crystalline and amorphous based on temperature and formation protocols. In Figure 4.8, the modeled reflectance spectra for 20 μm grains by Jaumann *et al*. (2008) are shown as a reference for the expected band features of crystalline water ice in the near infrared region. Two spectral band regions are identified here for analysis, and I will refer to the bands near 6600 cm^{-1} as 1.5 μm, and 6050 cm^{-1} as 1.65 μm. An ISL sample spectra from this work (Figure 4.8), collected at 10 K (to enhance signal / noise ratio) for 53–75 μm crystalline water ice grains successfully displays these characteristic band features. Both the 1.50 μm and 1.65 μm band features are observed, along with 2.0 μm, 3.0 μm bands, and 3.1 μm Fresnel peak.

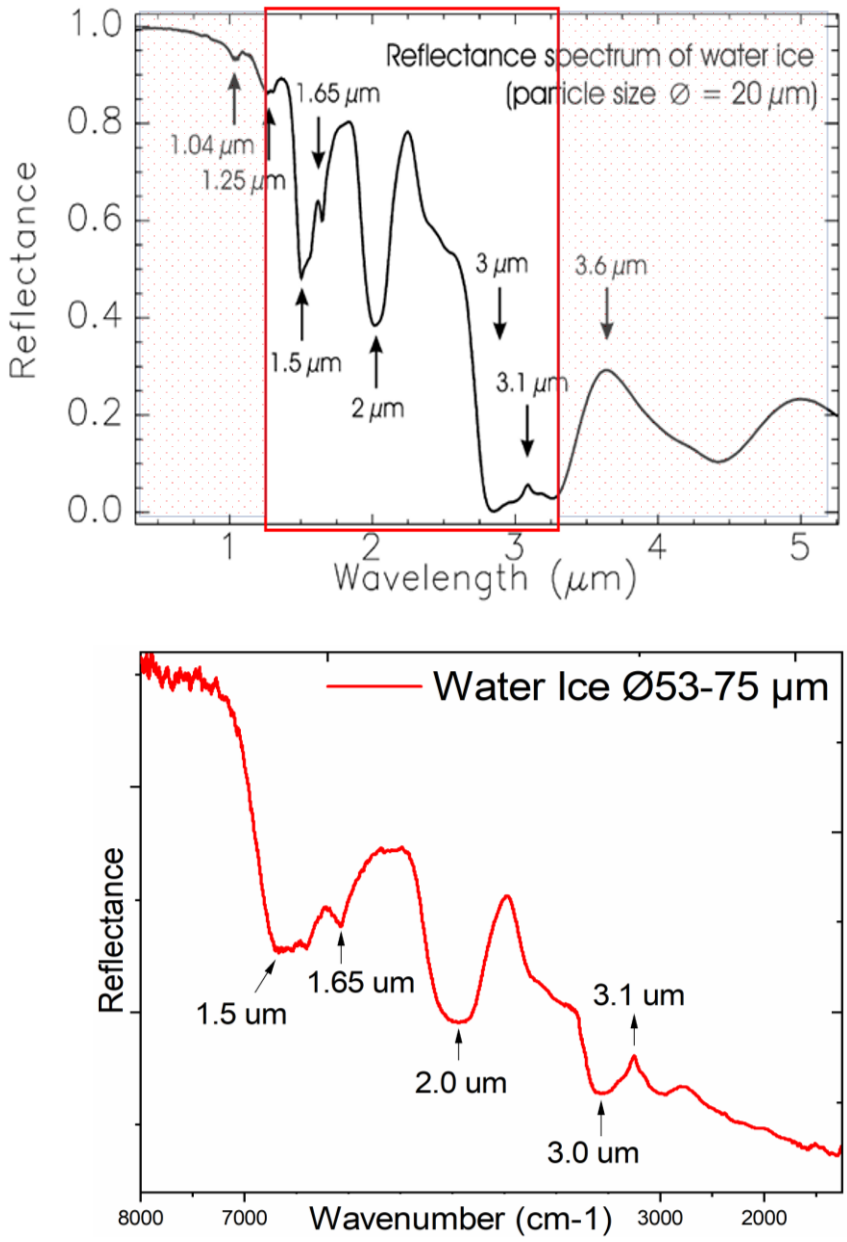

Figure 4.8: Theoretical modeled spectra of crystalline water ice from Jaumann *et al*., 2008 (top) are compared to ISL laboratory reflection spectra of water ice grains from this study (bottom). The relevant part of the NIR region used for comparison is highlighted with a red box.

4.2.1 Comparison to Previous Laboratory Measurements

After removing polynomial continua, normalized reflectance spectra of pure crystalline and amorphous water ice with controlled grain size of 25-53 μm, at 100 K are calculated for this work. Details of experiments and spectral variations are investigated later in this chapter, but in this section, I compare our normalized curves to previous laboratory measurement (with no grain size controls). In particular, I consider:

1. Crystalline water ice transmission spectra at 100 K, formed by freezing liquid water with a seed crystal (thickness 100 μm to 1 cm), from Grundy and Schmitt (1998)
2. Thin film, crystalline and amorphous water ice transmission spectra at 100 K and greater than 70 K respectively, from Mastrapa *et al*. (2008)
3. Thin film, crystalline and amorphous water ice at 105 K and 100 K respectively, from unpublished ISL transmission spectra acquired in 2010.

Transmission spectra were converted to absorbance by removing the background, and then converting to reflectance using: Reflectance = $10^{-Absorbance}$. Details of experimental conditions are provided in Section 4.4.

Figure 4.9 shows the comparison between the spectra collected in this study and the previous datasets. Qualitatively, our spectra appears to have a higher reflectance but lower band areas for the 1.5 and 1.65 μm regions, with shallower depths but broader bounds. All thin film measurements of crystalline ice (previous work) have comparable band strength and signals to one another, but noticeable variations for amorphous ice. These differences in strength and band position could be due to differences in laboratory acquisition methods, but may also represent variability due to thermal history, thickness

and grain size controls, which I will investigate in this chapter. In the next section, I perform a quantitative comparison of our spectra with Mastrapa *et al*. (2008) measurements, which are widely used to characterize water ice in planetary spectroscopy.

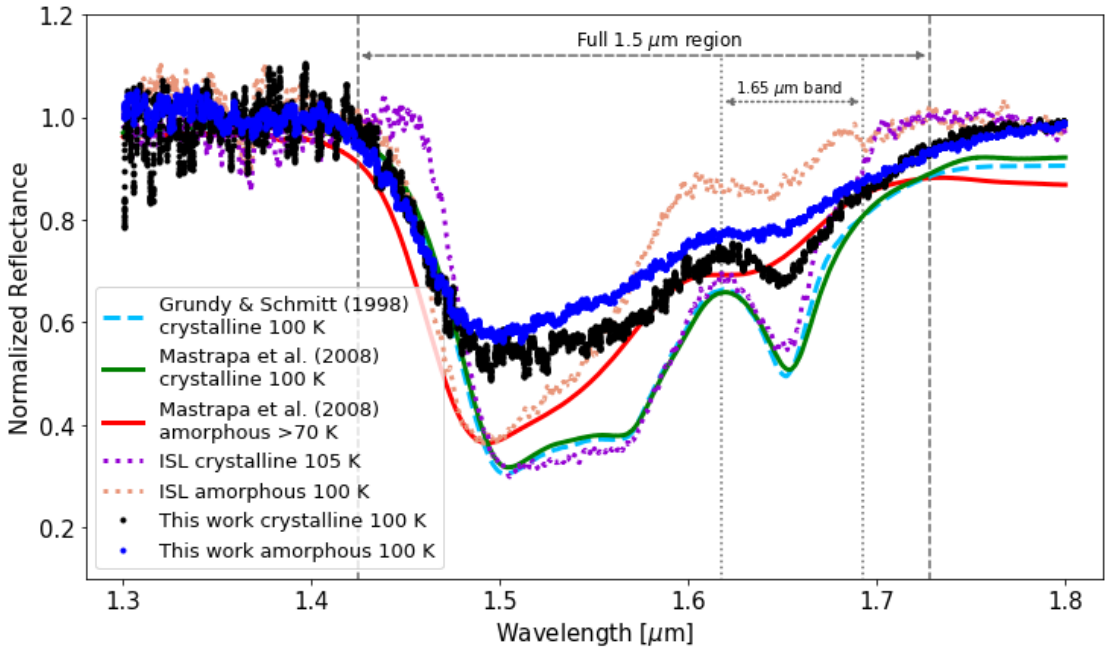

Figure 4.9: Laboratory spectra of pure amorphous and crystalline water ice from this work at ISL (blue, black solid lines) are compared to pure crystalline water ice from Grundy and Schmitt (1998) (blue dashed lines), Mastrapa *et al*. (2008) crystalline and amorphous ice (red and green solid lines), and previous ISL transmission measurements (orange and purple dotted lines). Dark gray vertical dashed lines indicate the bounds of integration for the 1.5 μm region, and light gray vertical dotted lines indicate the bounds of integration for the 1.65 μm region.

4.2.2 Calculation of 1.65/1.5 μm Integrated Band Area Ratios (B)

For our suite of collected reflectance spectra, the 1.65 μm and 1.5 μm integrated band areas are calculated at various temperatures similar to the surface of Europa and other ocean worlds. Mastrapa *et al*. (2008) defined the integration boundaries of band depths as 1.424 – 1.731 μm (5770-7020 cm^{-1}) for the 1.5 μm region, and 1.618 – 1.695 μm (5900-6180 cm^{-1}) for the 1.65 μm region. As mentioned in the previous section, our spectra extend beyond these predefined regions. The boundaries for our integration of band depths are defined as 1.407 – 1.783 μm (5610-7110 cm^{-1}) for the 1.5 μm region, and 1.616 – 1.712 μm (5840-6190 cm^{-1}) for the 1.65 μm region. For consistency, the Mastrapa *et al*. (2008) boundaries have been redefined to match the boundaries selected for this work, and their band areas were recalculated.

Cubic spline interpolation was performed on all spectra to remove interference patterns. Straight lines are fit to the data within ±10 cm^{-1} (±6.3 x 10^{-4} μm) in the wavenumber of each of the above integration bounds, or approximately 20 data points at each edge of the bounds. Absorption profile under the straight-line fit is integrated (using methodology in Berdis (2021) (Figure 4.10). The integrated band area ratio (*B*) was calculated as the integrated area of the 1.65 μm region over these bounds, divided by the integrated area of the 1.5 μm region (Equation 4.1).

$$B = \frac{\text{Area in the 1.65 μm region}}{\text{Area in the 1.5 μm region}} \tag{4.1}$$

This ratio is used to differentiate between amorphous and crystalline ice on the surface, with a larger *B* corresponding to a higher crystallinity, while also attempting to remove some of the effects of grain size dependency in our calculations.

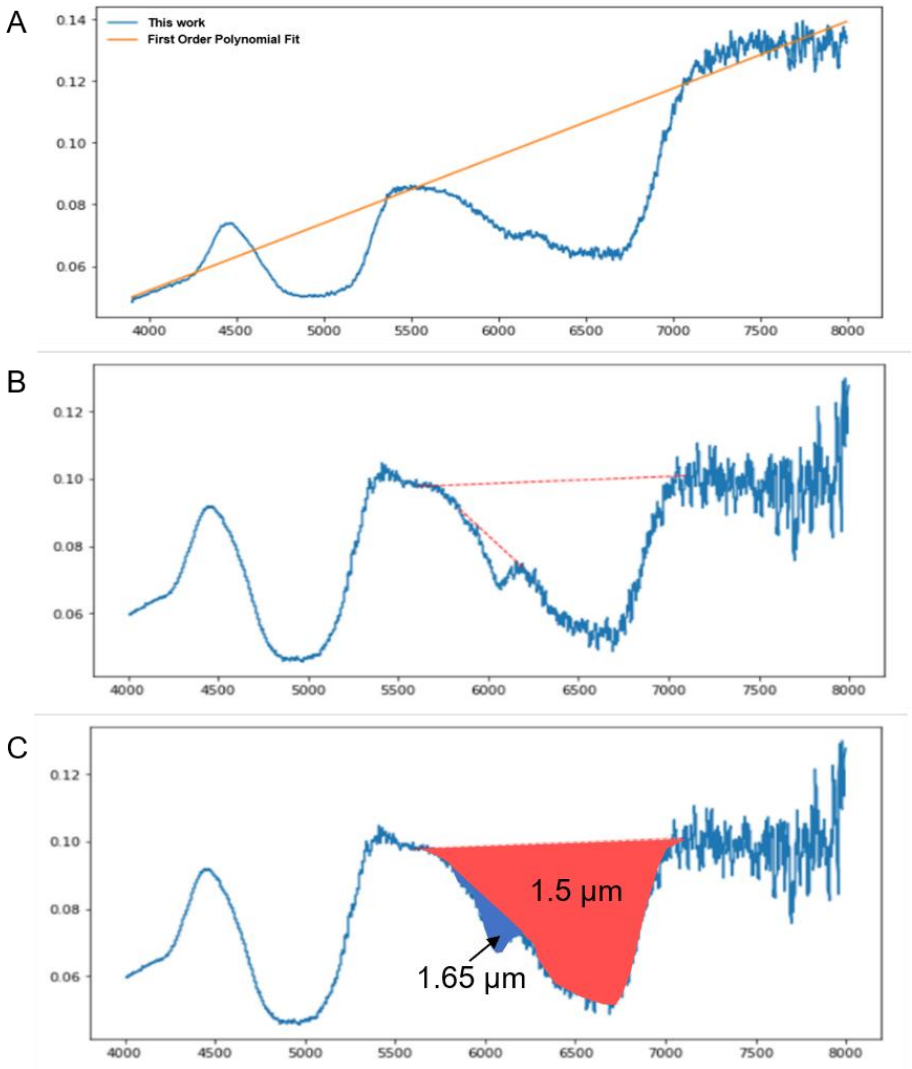

Figure 4.10: Band areas were determined by (A) removing the polynomial continua, (B) fitting with a straight line close to the integration boundaries of the 1.5 μm region, and the 1.65 μm region, and (C) calculating the areas within the bounds.

Integrated band area ratio of the 1.65/1.5 μm regions was calculated for our laboratory-produced end members for pure crystalline and amorphous ice, along with mixtures of both phases in the temperature range of 10 – 170 K. Figure 4.11 shows the calculated band area ratios for ISL datasets which can be used for bulk crystallinity calculations of planetary surfaces as described later in this section. The integrated band area ratio (B) for the laboratory-acquired pure crystalline end member (defined as B_{cryst}) is calculated as 0.0529, while the laboratory-acquired pure amorphous end member (defined as B_{amorph}) is calculated as 0.0166 (see Table 4.1). Compared to recalculated Mastrapa *et al*. (2008) and ISL (2010), unpublished, the amorphous ice end members are in close agreement (0.0157 and 0.0144, respectively). However, our crystalline end member is lower than previous values (0.0669 and 0.0715, respectively) (Table 4.2). While it is possible that our lower value comes from contamination of amorphous ice in our 100% pure crystalline ice sample, the thermal history makes that unlikely. Our end member spectra were recorded after thermal annealing of ice to 150 K and cooling to 100 K, which should convert all amorphous ice to crystalline. Instead, a potential explanation might be:

1. Spectral differences may exist due to acquisition techniques (including illumination conditions) and thickness of samples. ISL samples are thicker (factor of 10 to 20) than samples from previous measurements of thin films. Increased scattering of our thicker sample can subdue the band strength for 1.65 μm absorption feature and lower the calculated value of B_{cryst}. Amorphous ice spectra are not similarly affected due to their characteristically low strength of the 1.65 μm band.

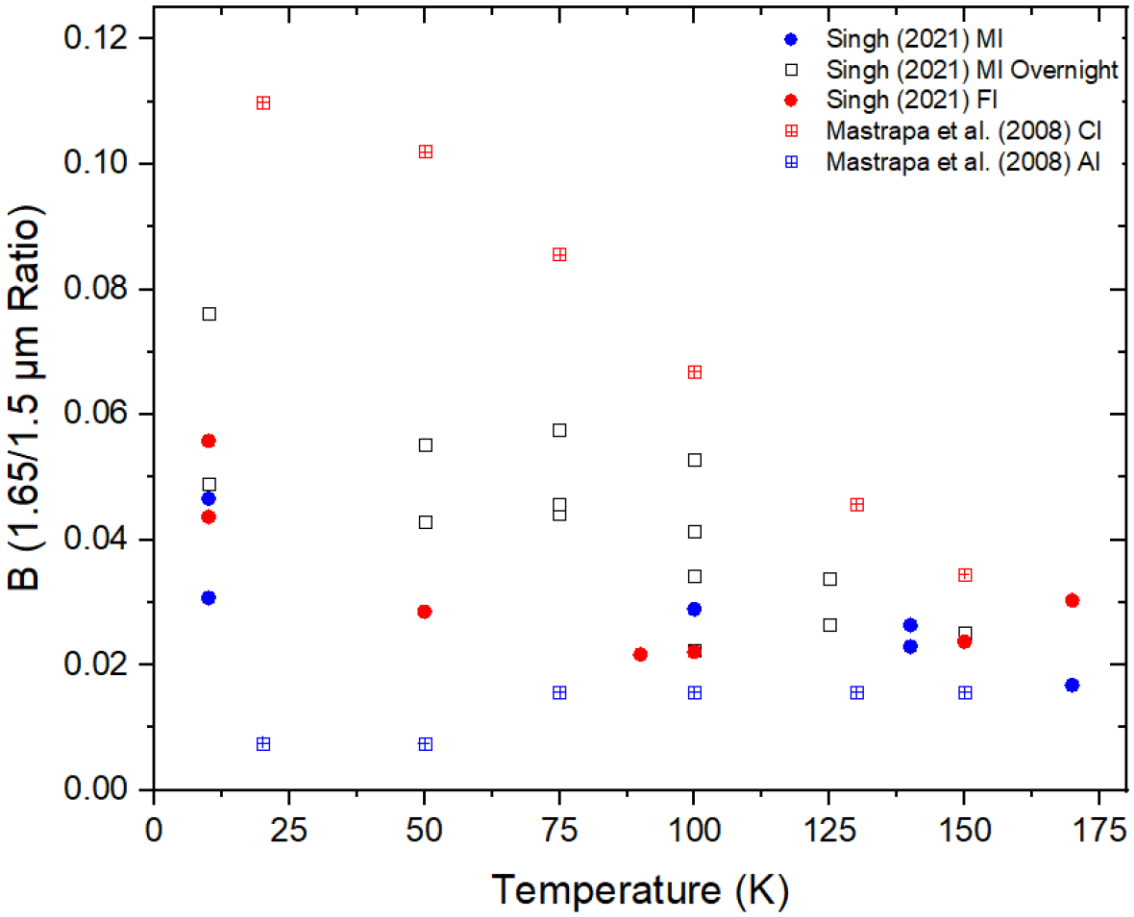

Figure 4.11: 1.65/1.5 µm integrated band area ratios at different temperatures for : (1) mist ice (blue circle), (2) mist ice with overnight equilibration (black square), (3) freezer ice (red circle) from this dissertation. Mastrapa *et al*. (2008) crystalline ice (red square) and amorphous ice (blue square) are also included for comparison.

Table 4.1: Calculation of laboratory end members for Crystalline (B_{cryst}) and Amorphous Ice (B_{amorph}) at different temperatures. If the water ice phase is uncertain, the value in *B* is used. Green represents end members at 100 K. All measurements were made at ultra-high vacuum conditions (Pressure < 10^{-8} mbar).

Formation Protocol	T [K]	1.5 µm Band Area	1.65 µm Band Area	B	B_{cryst}	B_{amorph}
Mist Ice	100	37.3283	1.0809	0.0289	-	-
Mist Ice	140	33.4078	0.8821	-	0.0264	-
Mist Ice	10	34.7334	1.6195	-	0.0466	-
Mist Ice overnight	100	31.7556	0.5285	-	-	0.0166
Mist Ice overnight	150	34.9628	0.8823	-	0.0252	-
Mist Ice overnight	125	34.2098	1.1578	-	0.0338	-
Mist Ice overnight	100	36.5099	1.9307	-	0.0529	-
Mist Ice overnight	75	38.8450	2.2359	-	0.0576	-
Mist Ice overnight	50	36.5899	2.6124	-	0.0714	-
Mist Ice overnight	10	39.6589	3.0213	-	0.0760	-
Freezer Ice	100	23.4881	0.5194	0.0221	-	
Freezer Ice	150	11.7199	0.3553	-	0.0303	-
Freezer Ice	10	12.5644	0.7017	-	0.0559	-

Table 4.2: Comparison of Band Areas between Mastrapa *et al*. (2008) data and this work.

Laboratory Dataset	**Temperature [K]**	**1.5 μm Band Area**	**1.65 μm Band Area**	**Phase**
Singh (2021) (MI)	10	34.1507	1.0502	-
	10 (Recool)	34.7334	1.6195	~ Crystalline
	100	37.3283	1.0809	~ Amorphous
	140 (Heat)	35.6854	0.8195	-
	140 (Recool)	33.4078	0.8821	~ Crystalline
	170	34.6942	0.5836	~ Crystalline
Mastrapa *et al*. (2008)	20	10.4358	0.0786	Amorphous
	20	29.9218	3.2872	Crystalline
	50	10.4358	0.0786	Amorphous
	50	28.2242	2.8799	Crystalline
	75	117.0461	1.8365	Amorphous
	75	28.8641	2.4710	Crystalline
	100	117.0461	1.8365	Amorphous
	100	27.7531	1.8590	Crystalline
	130	24.1746	1.1062	Crystalline
	150	25.5941	0.8834	Crystalline
Singh (2021) (FI)	10	12.2372	0.5349	-
	10 (Re-cooled)	12.5644	0.7017	~ Crystalline
	50 (Cool)	23.3414	0.6666	-
	90	23.5460	0.5107	-
	100	23.4881	0.5194	~Amorphous
	150	13.0173	0.3089	~ Crystalline
	150	11.7199	0.3553	~ Crystalline

4.2.3 Calculation of Crystallinity (C)

The 1.65/1.5 μm band area ratios of ground-based (or spacecraft) observations are considered a linear combination of the calculated end member ratios (B) for amorphous and crystalline water ice (Hansen and McCord, 2004; Mastrapa *et al*., 2008). Bulk surface crystallinity of planetary surfaces can thus be calculated from spectroscopic observations and laboratory measurements (as references) at similar temperatures, using the equation:

$$C = (B_{GBO} - B_{amorph}) / (B_{cryst} - B_{amorph}) \quad (4.2)$$

where C is the crystallinity of the ground-based observations for which we are solving, and B_{GBO} is the 1.65 ⁄ 1.5 μm integrated band area ratio using the ground-based observations (GBO). The calculated crystallinity provides an approximation of the bulk surface crystallinity and can be applied to future space-borne observations for surface characterization.

4.2.3.1 Limitations of this Technique:

1. To assess the bulk crystallinity of a planetary surface, contributions from non-water ice species to the 1.5 μm region are overlooked in the ratio, which could result in a derived crystallinity that differs from true surface crystallinity.
2. Spectral differences may exist between ground-based and laboratory observations due to their acquisition techniques (e.g., reflection vs transmission, spectral resolution,

illumination conditions, etc.), causing crystallinity values to occasionally exist outside of the ideal 0 – 1 range (Berdis, 2021).

3. The equation requires lab end members for crystalline and amorphous ice at different temperatures to capture phase transitions and/or variations in band strength during data collection. As shown in section 4.3.1.2, changes in B, such as due to rise in 1.65 μm band strength with low temperature, can lead to an increase in calculated crystallinity for ice samples, despite no theoretical basis for phase transitions.

In the next section, I will evaluate the temperature-dependence of the 1.5 μm and 1.65 μm bands, and calculate integrated band area ratio (B), and crystallinity (C) of water ice samples during various experiment sets using equation 4.2 mentioned above.

4.3 Temperature Dependent Evolution of Water Ice Spectral Feature:

To evaluate the role of temperature on the 1.5 μm and 1.65 μm absorption features, independent of water ice phase, two types of samples were deposited: (1) Mist Ice (or MI) sprayed at 77 K in LN , and (2) Freezer ice (or FI) frozen overnight at ~253 K. In an ideal scenario, deposition at 77 K is expected to form amorphous ice (in MI), while deposition at 253 K is expected to form hexagonal crystalline ice (in FI), thus providing two end members. Two sets of experiments are performed, and the 1.65/1.5 μm integrated band area ratio is calculated for comparison across varying thermal histories of samples. In the first set of experiments described below, both sample types were thermally cycled. For the second set, the samples were placed overnight at 100 K post deposition to allow equilibration prior to thermal cycling.

4.3.1 First Set: Direct Thermal Cycling *(relevant to all icy bodies)*

4.3.1.1. Mist Ice (MI)

Ice samples were prepared at 77 K using previously described methodology and placed inside the vacuum chamber at 100 K. Pressure of 7.8×10^{-6} mbar is achieved after placement. Thermal cycling is performed, and reflectance spectra is collected.

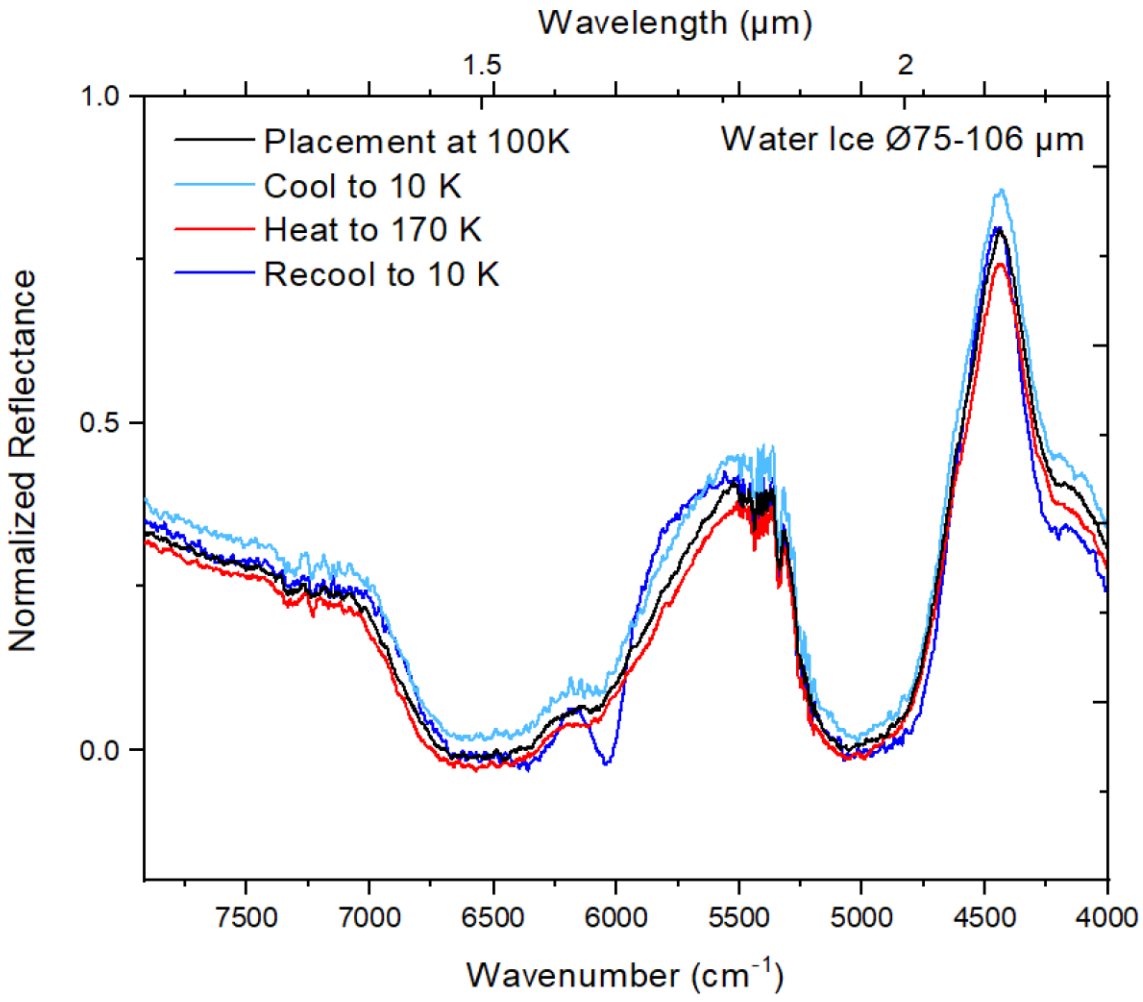

Figure 4.12: Reflection spectra are collected for mist ice (MI) samples: on placement inside chamber at 100 K (black), after cooling to 10 K to improve S/N ratio (light blue), on heating to 170 K (red), and on cooling back to 10 K (blue).

Normalized reflectance spectra of water ice samples for different grain sizes show a consistent transition behavior in the 1.65 μm band (increase in band depth on cooling, and on annealing) over the course of the experiment, while the 1.5 μm band remains consistent, as illustrated in Figure 4.12. Figure 4.13 quantitatively highlights the change in temperature during the experiment, along with changes in B and C.

After placement at 100 K, and cooling to 10 K, the collected spectra of MI samples for both temperatures show a subdued integrated band strength (and area) for the temperature sensitive 1.65 μm band (with a slight increase on cooling), which is more consistent with amorphous ice. Crystallinity calculation from equation (4.2), using Mastrapa *et al*. (2008) end members as reference, support this assertion with a large, calculated fraction of amorphous water ice (~80%) mixed with some crystalline ice (~20%). Note that these calculated values are an approximation of sample crystallinity, as mentioned in section 4.2.2.1. On heating to 170 K, the 1.65 μm band strength decreases further, as captured by the integrated band area ratio (B) plot in red (see Figure 4.13). On cooling back to 100 K, and subsequently to 10 K, the band depth and crystallinity increase significantly (factor of 2.5), with the spectra showing similarities to crystalline water ice with strong 1.65 μm features.

Theoretically, this would indicate a potential transition in crystal structure from amorphous ice (formed during deposition at 77 K) to cubic or hexagonal crystalline ice on heating beyond 130 K (plot in aqua blue). This is not captured by the crystallinity equation (4.2) (plot in green), but the band area ratio (B) accurately captures the reported temperature sensitivity of the 1.65 μm band (and to an extent, the 1.5 μm band). The phase change may also contribute to this change in B.

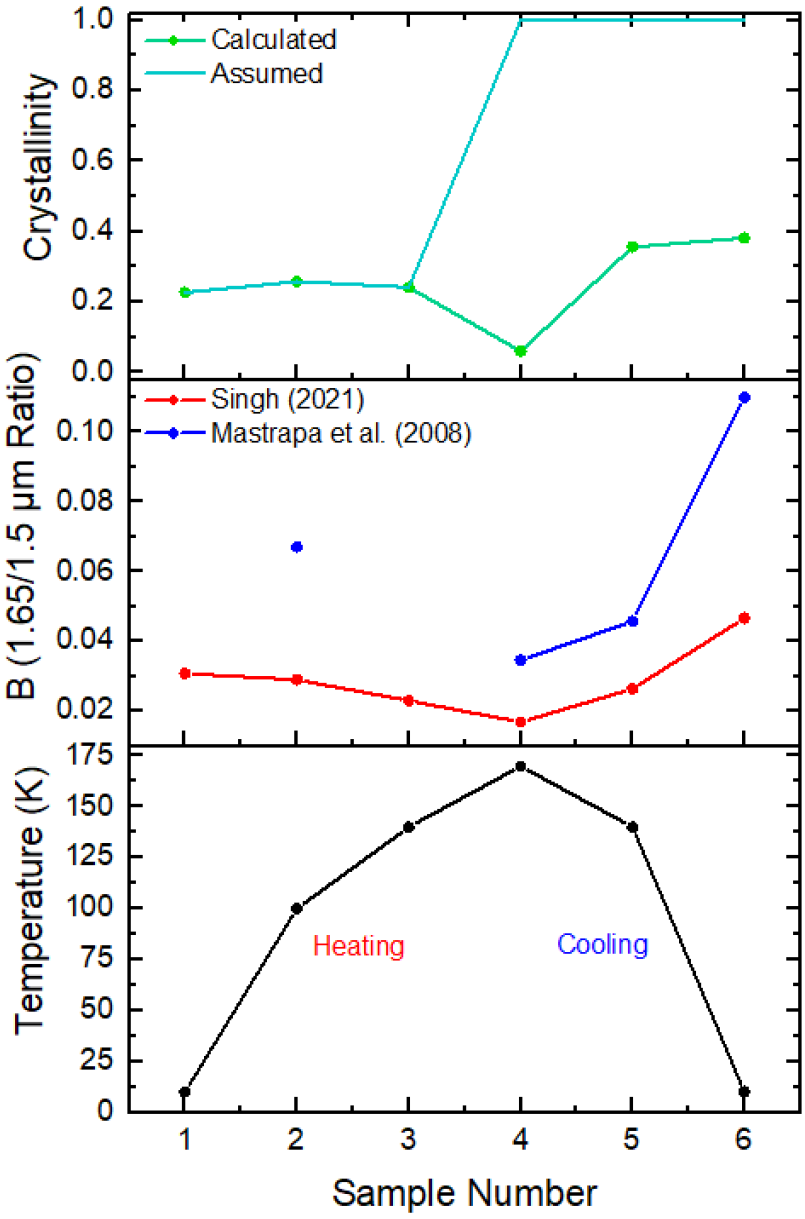

Figure 4.13: Crystallinity (C) and integrated band area ratio (B) are calculated for the SI sample over a broad range of temperatures (10-170 K) achieved during thermal cycling and compared to Mastrapa *et al*. (2008) B values, and theoretical crystallinity for ice.

The first set of experiments on SI samples demonstrate:

1. Temperature dependence of the 1.65 μm band for water ice, and consequently the 1.65/1.5 μm integrated band area ratio (B).
2. Calculated B ratios from this work (with thick ice samples) are lower than Mastrapa *et al*. (2008) B ratios (thin, ice films) at same temperatures.
3. Limitations of the crystallinity equation in capturing phase transitions at high temperatures, using current laboratory end members for amorphous and crystalline ice (including the lack of amorphous end members beyond 130K).
4. If phase transition on annealing is accurately interpreted, then the methodology for controlled ex-situ production of ice samples at 77 K in LN can potentially generate large quantities of thick, amorphous ice in the laboratory.

There is an additional possibility of formation of amorphous frost on top of the water ice sample during transfer to the chamber (Section 4.3.1.2), which may initially subdue the crystalline ice signal, and undergo the observed phase transition to during cycling.

4.3.1.2. Bulk Crystalline Ice or Freezer Ice (FI)

Figure 4.14: Freezer ice (FI) is ground, sieved and transferred to sample holder for the experiments in Section 4.3.1.2.

Water ice samples prepared by overnight freezing of ultrapure water at 253 K as a cylindrical column (Figure 4.14) are used to investigate the cause of the phase transition on annealing (amorphous ice during deposition versus amorphous frost during transfer), along with the temperature dependence of the 1.65 μm band. Relatively warm temperature of deposition should ensure the initial formation of hexagonal crystalline ice. This freezer ice is transferred to the ice deposition setup, submerged at 77 K in LN, and crushed with a mortar and pestle in LN to form small grains of crystalline ice. The ice grains are subsequently sieved to the desired grain size range (25-53 μm here) and placed inside the vacuum chamber at 100 K where they are thermally cycled following a similar procedure as in the previous section. One noticeable difference is that the ice sample was allowed to thermally equilibrate for ~ 30 minutes at 150 K: to ensure complete phase transition.

Collected reflectance spectra show the predicted increase in the 1.65 μm band depth with decrease in temperature to 10 K. On annealing, there is another slight increase in band

depth, which is unexpected for pure crystalline ice. An example of this trend is shown in Figure 4.15. To evaluate this, the integrated band area ratio (B) and crystallinity (C) are calculated; both increase by a factor of ~2 on initial cooling to 10 K (0.044 and 35% at 10 K) but are lower than Mastrapa *et al*. (2008) values. Compared to MI ice at this stage of the experiment, the band area ratio and crystallinity for the FI sample are again higher by a factor of ~ 1.5, implying a larger fraction of crystalline ice (~45%) in FI than in MI.

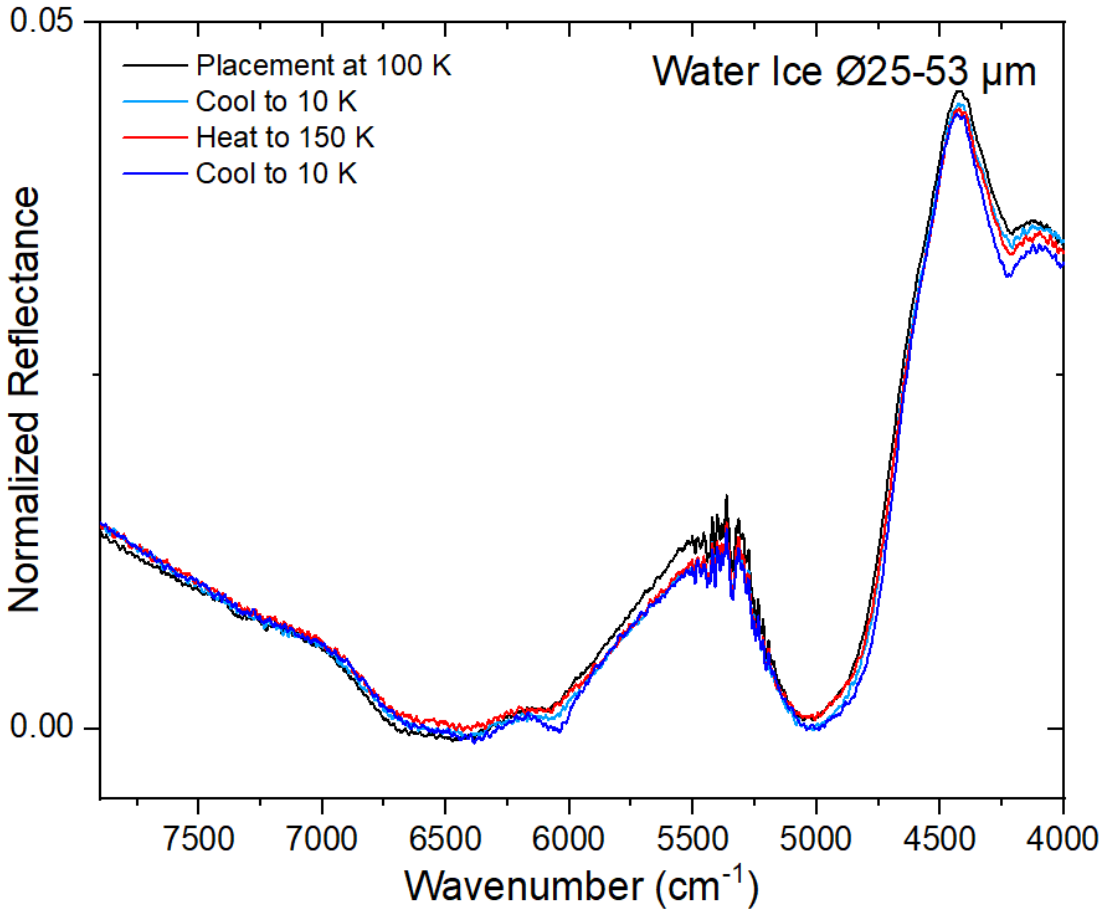

Figure 4.15: Reflection spectra are collected for freezer ice samples (FI) deposited at 250 K, crushed with mortar & pestle, sieved, placed inside chamber, and annealed.

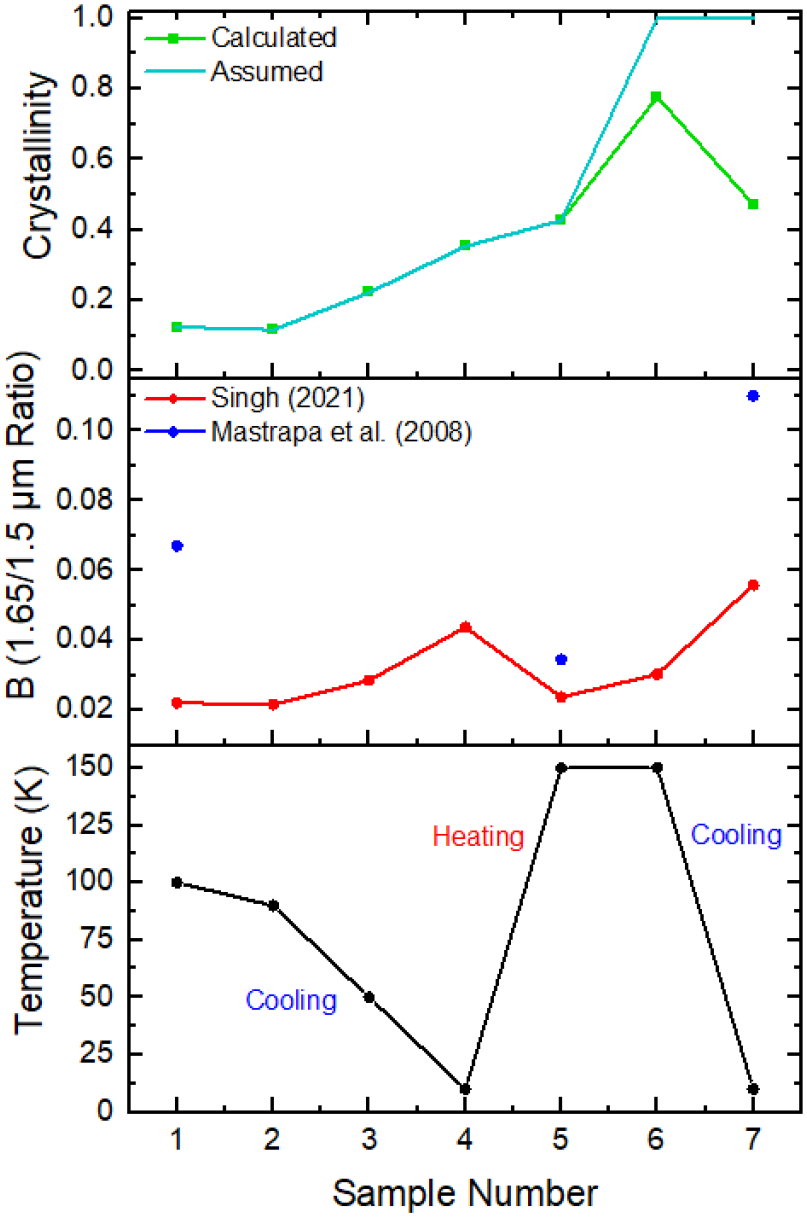

Figure 4.16: Crystallinity (C) and integrated band area ratio (B) are calculated for the FI sample over a broad range of temperatures (10-150 K) achieved during thermal cycling, and compared to Mastrapa *et al*. (2008) B ratios, and theoretical crystallinity for ice.

This result is intriguing as FI samples were expected to be crystalline rather than a mix of both phases. On annealing, the trend for B mirrors the temperature-dependence of

the 1.65 μm band: as the inverse of temperature trend. Curiously, both B and C rise during the 30-minute equilibration period at 150 K with the crystallinity nearly doubling. On cooling to 10 K, B reaches a final value of 0.056 (factor of 1.25 increase) with 78% calculated crystallinity. The inherent differences between the Mastrapa *et al*. (2008) dataset (used as reference) and this dataset indicate that even a fully crystalline sample from this work will not register as C = 1.0 (see section 4.1, 4.2.2.1 Limitations). Again, the crystallinity is assumed to be 100% pure after heating to 150 K (plot in aqua blue). All transitions are shown in Figure 4.16.

There are a few major takeaways from the freezer ice experiments:

1. Temperature dependence of the 1.65 μm band for water ice, and consequently the 1.65/1.5 μm integrated band area ratio (B) is reinforced.
2. Calculated B ratios from this work (for thick or bulk ice) are again lower than Mastrapa *et al*. (2008) B ratios (thin ice films) at same temperatures.
3. Initial change in B values on cooling can be attributed to increase in 1.65 μm band strength, but the low calculated crystallinity at 10 K and subsequent increase post annealing reintroduces the possibility of either:
    a. Formation of a thin layer of frost on the sample during transfer followed by a phase transition to crystalline ice on heating and equilibration at 150 K.
    b. Quenching of the crystalline ice in LN during sample preparation, which subdues the initial signal, which is restored post annealing. This scenario is detailed in section 4.3.2.

Both scenarios demonstrate the susceptibility of 1.65 μm band strength to the origin and (thermal) history of water ice samples and have broad application to ice crystallinity

calculations for the outer solar system. The formation of amorphous plume deposits on an equatorial, crystalline ice-rich surface for ocean worlds like Europa and Enceladus may change the spectral signals for spacecraft or GBO measurements, leading to interpretation as an amorphous-rich surface. Similarly, localized heating events may increase the calculated crystallinity of the surface, owing either to the temperature dependence or un-quenching of ice samples.

4.3.1.3 Sample Contamination and Other Limitations

Both SI and FI experiments have presented the possibility of sample contamination by frosting during transfer to the vacuum chamber. While the transfer is performed in a nitrogen environment, which should minimize any such contamination, it is important to investigate. Here, I present a calculation of skin depth or the maximum penetration depth. Skin depth (d) at a specific wavelength (λ) is the thickness of a layer within which the electromagnetic wave is attenuated by a factor of e (e being the base of the natural logarithm) (Jackson, 1975). For a transparent medium, ignoring the effects of scattering, it can be approximated as:

$$\text{Max Penetration Depth} = 1 / \text{Absorption co-efficient} \quad (4.2)$$

This is calculated to be ~360 μm for NIR light at the 1.65 μm band, using 27.79 cm^{-1} as the absorption co-efficient of water ice at 100 K (Grundy and Schmitt, 1998). Amorphous ice frost on top of sieved ice grains is not expected to form more than a few microns. If frosting exists, then the optical microscope (resolution of 6 μm) should capture

it on top of sieved grains of 25-150 μm with the progression of time. This is not observed, as seen in example images in Figure 4.17. If frost is present and undetected by the microscope, the sieve size of 25-53 μm (grain size) represents the higher limit of frost thickness.

Considering the penetration depth of the order of a few hundred microns, the beam should penetrate past the presence of any overlying frost layer. The lower, pristine ice grains (crystalline in case of FI) would contribute more to the collected reflectance signal, and the spectra should be representative of the underlying ice sample. Hence, the 1.65 μm band feature is present in the collected spectra, but the band strength and area might be subdued. This supports our interpretation of the phase transition occurring due to annealing of overlying frost (sublimation and redeposition as crystalline ice), though quenching of crystalline ice cannot be completely ruled out.

Another limitation yet to be considered is the role of grain size variation over the course of the experiments. Optical images reveal an increase in grain size on annealing. Potential sintering of grains is observed with formation of larger, angular grains and pore spaces among a matrix of ice grains, similar to observations by Molaro *et al*. (2019). While sintering analysis is beyond the scope of this dissertation, the increase in grain size and change in morphology on annealing could reduce the reflectance signal and increase band depths in a manner similar to the trend observed here. Grain size dependence of water ice spectral features is evaluated in section 4.5.

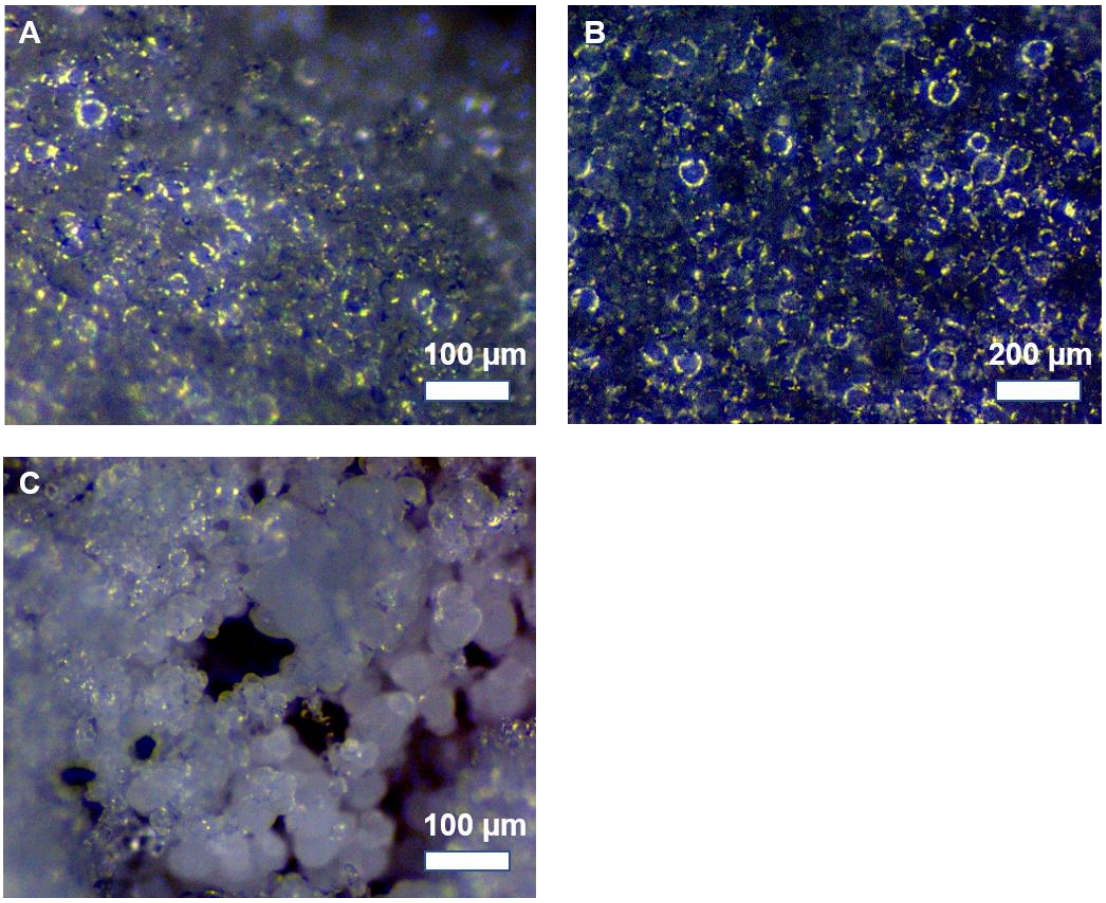

Figure 4.17: Images of (A) 25-53 µm and (b) 53-75 µm water ice grains post deposition, do not capture frosting. (C) 25-53 µm after annealing. Images acquired using a long-distance microscope.

4.3.2 Second Set: Overnight Placement of samples prior to thermal cycling

4.3.2.1 Mist Ice (MI Overnight)

The origins of the 1.65 μm band strength transitions are difficult to unravel, as demonstrated by the previous set of experiments. While the temperature dependence of the water ice spectra has been established, an additional set of experiments are performed here to investigate the role of thermal history. *How does ice behave after ~ one day on Europa's surface?* Ice samples of grain size 25-53 μm were placed inside the chamber at 100 K, left overnight (over periods of 5-72 hours), and monitored with both reflectance spectra and optical image collection. This change in procedure allowed the samples to thermally equilibrate, prior to thermal cycling. 100 K was chosen as the equilibration temperature as it was cold enough to avoid a phase transition from amorphous to crystalline ice, expected between 110 – 150 K (in an ideal case), and warm enough to avoid deposition of an overlying amorphous frost layer on the sample inside the vacuum chamber. 100 K is also the average surface temperature for Europa, and equilibration at 100 K provides us an inkling of the expected behavior of ice on the surface.

Figure 4.18 shows the change in sample thickness with time, while Figures 4.19 and 4.20 show the variations in reflectance spectra of a SI overnight sample over 72 hours of placement and annealing, respectively.

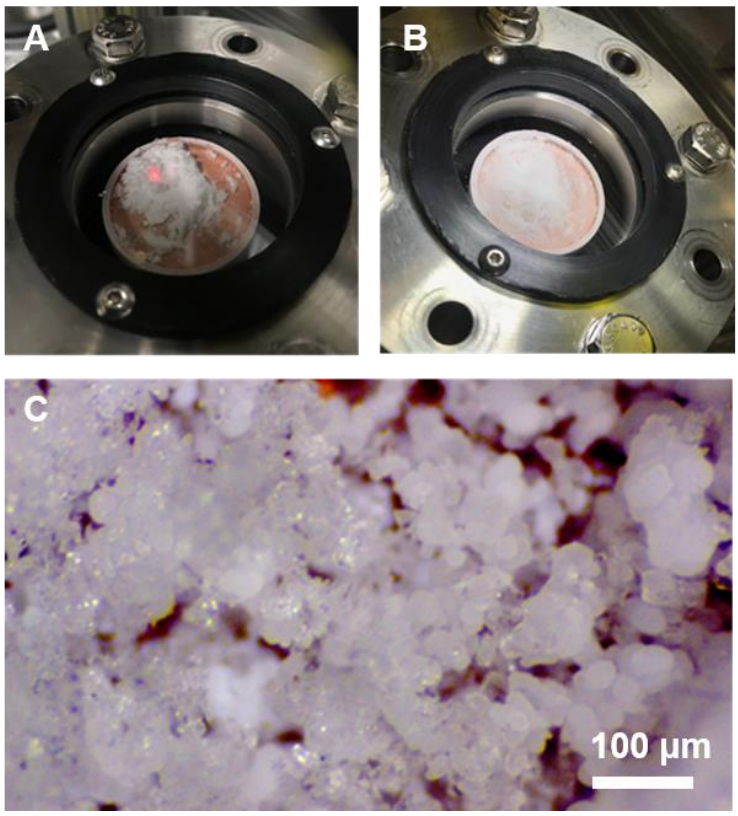

Figure 4.18: Images of ice left overnight at 100 K to allow equilibration at: (A) initial placement, and (B) after 72 hours. (C) A microscope image of the sample after 72 hours shows the formation of clusters (or a lattice) with variation in grain size.

The 1.65 µm band shows an increase in band depth when left to equilibrate after placement at 100 K, with an initial increase over the first 30 minutes to 1 hour (see figure 4.18) before stabilizing. The 1.5 µm band strength remains constant. Quantitative calculation of integrated band area ratio (B) and the crystallinity (C). Figure 4.21 supports this observation, with an increase in B (greater than a factor of 2) and a rise in crystallinity to ~40 – 45% after initial placement of mostly amorphous ice. The observed changes in B and C, and the time-period of sample equilibration is consistent with the results of the FI experiments (equilibration for 30 minutes at 150 K resulted in a 2x increase in

crystallinity). However, the temperature of 100 K should be too low to allow thermal annealing of amorphous to crystalline water ice.

Over the next 70 hours, both the band area ratio and crystallinity are generally consistent with a slight increase recorded between 6 and 72 hours. This behavior implies no significant changes in crystallinity via phase transitions, sublimation of ice, or deposition of vapor on top of the sample, after the initial change. Optical images reveal an evolution of the sample from a thick 2 mm layer to a fine, thin film (of ice) on the sample holder. Microscope images reveal an evolution in grain size and morphology due to potential sintering. Either of these changes could contribute to the variation in calculated crystallinity, as investigated in later sections.

Thermal cycling is performed, with another series of changes in band area and crystallinity observed. On heating to 150 K, band area predictably decreases with no significant change in crystallinity (consistent with other experiments), highlighting once again the temperature-dependence of the 1.65 μm band. Based on expected annealing of amorphous ice at temperatures greater than 130 K, and the similarities in spectral features for amorphous and crystalline ice at 150 K, the entire sample is assumed to be 100% crystalline (plot in aqua blue). On cooling to 10K, band area progressively increases to reach a maximum value at 10 K (0.0761). Figure 4.20 highlights the change in 1.65 μm band depth for sets of measurements at the same temperatures before and after annealing. As illustrated, the change is prominent at lower temperatures between 10 and 75 K.

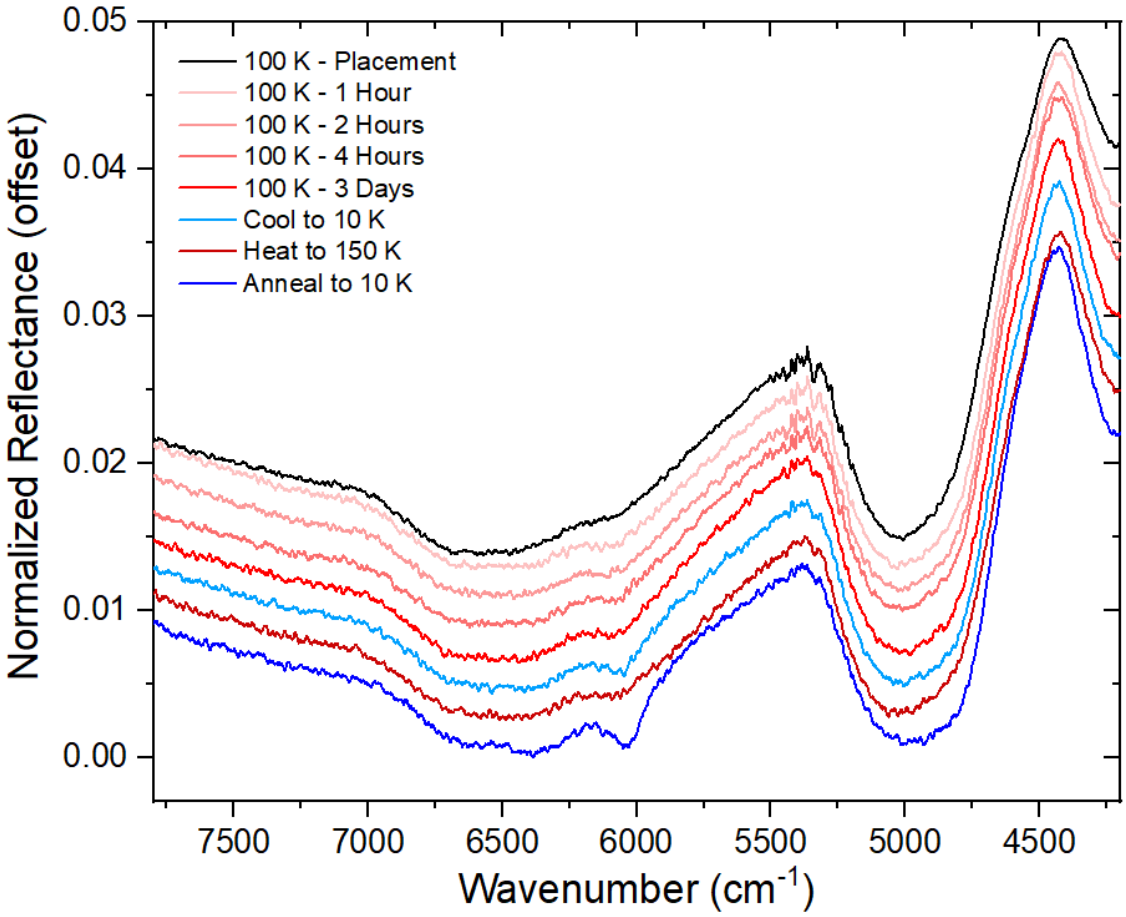

Figure 4.19: Normalized reflectance spectra of a water ice sample (MI overnight) at 100 K, collected over three days, and compared to spectra collected during thermal cycling.

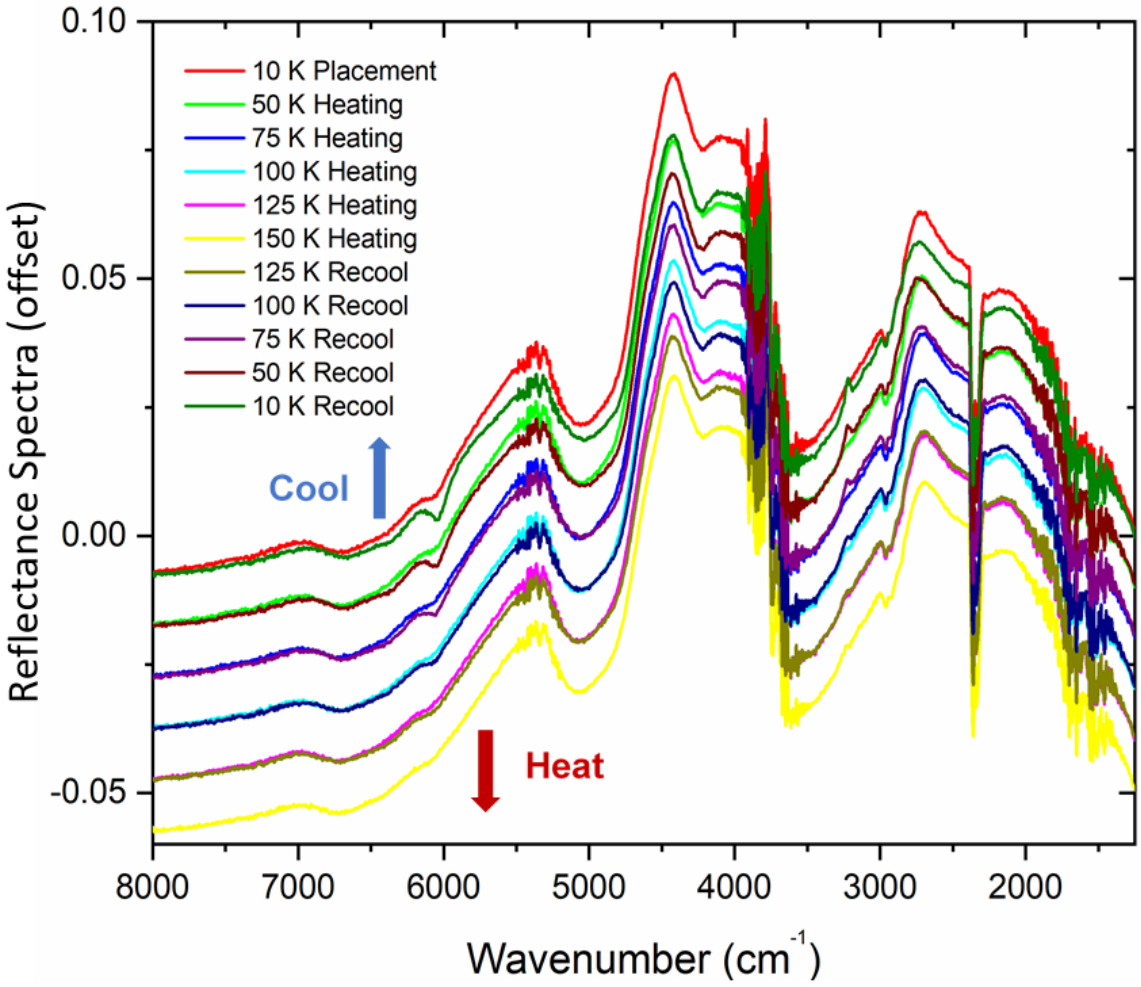

Figure 4.20: NIR Reflectance Spectroscopy of water ice sample (SI overnight) during thermal cycling. Spectra are coupled together for measurements at same temperatures, and offset to increase visibility.

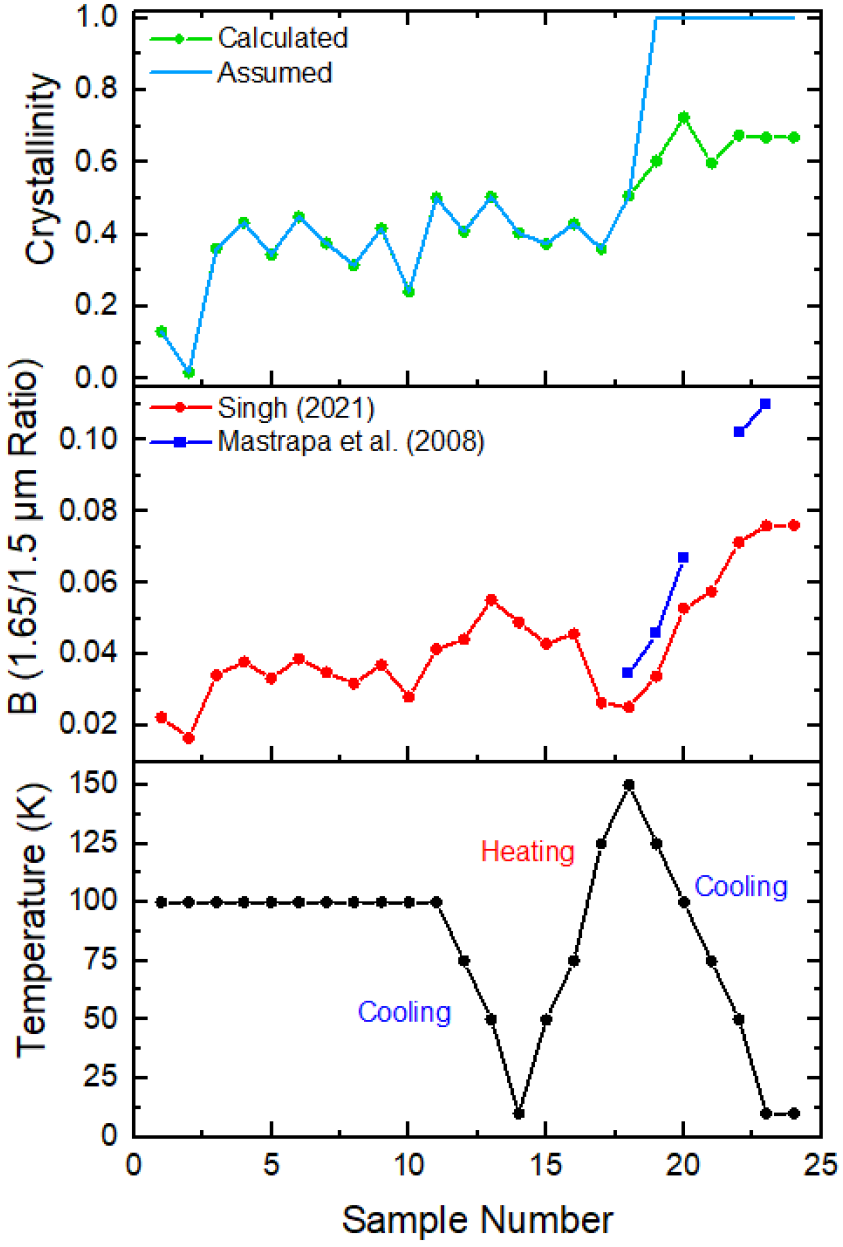

Figure 4.21: Crystallinity (C) and integrated band area ratio (B) are calculated for the MI overnight sample over a period of equilibration at 100 K and thermal cycling (10-150 K). Mastrapa *et al*. (2008) B values and theoretical crystallinity for ice are included.

Major takeaways of the SI overnight experiments include two crystallinity transition events potentially occurring over the course of the experiment, during initial placement and equilibration (~30 minutes) at 100 K, and during thermal cycling:

1. First transition event cannot be assigned to phase transition due to the temperature (100 K), and is proposed to be due to either:
    a) Contamination with amorphous frost prior to placement. During equilibration, the frost sublimes and redeposits as a thin film (possibly observed in images). Sample ends up as an amorphous-crystalline ice mixture (with 40-50% crystallinity).
    b) Quenching of ice during formation at 77 K, leading to the H atoms in the covalent bonds freezing in their disordered position and lowering the band strength. Strazzulla *et al*. (1991) and Mastrapa (2008) speculate that a free hydrogen atom can be trapped in the water ice lattice up to 70 K but may stay near their appropriate lattice site. On placement at 100 K, the increased temperature leads to the hydrogen atoms being free to overcome the temperature dependent energy barrier to reform the broken O-H bond, resulting in re-establishing a crystal lattice and increasing the band feature. Alternatively, unquenching and re-excitation of H atoms in the covalent bonds results in restored vibrational motion which increases band strength.
    c) With an increase in thickness of an amorphous water ice layer (due to vapor deposition inside the chamber), crystallization of the topmost layer of the sample could occur due to a warming effect of the subsurface layer ice.
2. Second transition event observed on cooling (after the heating phase) implies a clearer case of phase transition from ~50% amorphous to 100% crystalline ice, accompanied by an increase in integrated band area ratio (B).

3. Change in initial grain size range due to sintering could also contribute to differences in band strength. However, such a change should result in variation of absorption band depths across the entire NIR spectrum of water ice, which is not observed.
4. Protocols for cryogenic laboratory spectroscopy of ices should include a suitable time-period for thermal equilibration of samples inside the chamber, determined to be at least 30 minutes in this work. Allowing the ice to evolve and reach a steady state condition, similar to expected changes on Europa's surface post deposition, before collecting data could provide a more representative spectrum.

To summarize, previously described temperature dependence of the 1.65 μm band is demonstrated here, which further illustrates the need for collection of laboratory data at all relevant temperatures to better interpret icy bodies. However, considerations also need to be made for changes in grain size or change in sample thickness. The 1.65/1.5 μm integrated band area ratio (B) approach is proven here to capture both the temperature dependence and offers a reasonable approximation of crystallinity. However, the 1.65 μm band strength cannot be independently assigned to either ice crystallinity or temperature sensitivity, independent of the thermal history of the ice, which is not readily available for planetary bodies. To better interpret surface spectra, we must independently determine whether the following conditions are likely. *Are there any recent deposits of amorphous ice on the surface? Are there any active mechanisms for quenching of the ice?*

4.3.3 Unraveling the Role of Thermal History

To investigate previous reports that the heating history of a sample has no effect on the spectral features, barring a phase change, I use the ISL reflectance spectra measurements for water ice reported in section 4.3. Integrated band area ratios (B) of amorphous and crystalline water ice films from Mastrapa *et al*. (2008) are available for comparison during the cooling phase of the thermal cycle, after recalculation over the integration boundaries defined in section 4.2.

On cooling from 130 K to 10 K, all ISL samples and the Mastrapa crystalline ice samples show an increase in integrated band area ratios. However, the Mastrapa calculated B_{cryst} ratios are consistently higher than ISL measurements (Figure 4.22), while reported B_{amorph} ratios are comparable to ISL (MI and FI) measurements prior to thermal cycling and after heating to temperatures of 150 – 170 K. The spread in calculated B ratios can be attributed to:

1. **Detection techniques**: Mastrapa *et al*. (2008) transmission spectra were collected to derive optical constants of H_2O ice, with thin films and no grain size controls. ISL reflectance spectroscopy measurements (this work) were collected for direct comparison to spectra of Solar System objects, with following controls:
    a. Sample thickness: thick layers of water ice (up to 2 mm) were selected to be of suitable thickness to simulate reflection off a planetary surface (display infrared bands; thicker than penetration depth of light). Consequent increase in surface scattering off the ice contributes to the spread with variations in continuum levels and slope of spectra.

b. Grain sizes were selected to represent the range of Europa's modeled surface grain size, and they are larger than in previous measurements. Increase in size contributes to lower reflectance off the sample (and B ratios).

2. **Formation temperatures of samples and thermal history**: It has been previously reported that crystalline ice samples deposited at low temperatures and heated to the point of crystallization produce a spectrum that is different from crystalline samples made by directly depositing gas at temperatures above 140 K (Mastrapa *et al*., 2008).

Here, I extend this hypothesis to include thermal history in combination with formation temperature. In other words, amorphous ice samples deposited at 77 K (MI), heated to point of crystallization, and/or allowed to thermally equilibrate (undergoing complete phase transition) may produce a spectrum that is different from crystalline ice samples made by directly depositing at temperatures above 140 K. This holds true for the limited calculations of laboratory B ratios, presented in Figure 4.22, and is investigated further by determining B_{TH} (the change in B ratios with thermal history) in the next sub-section.

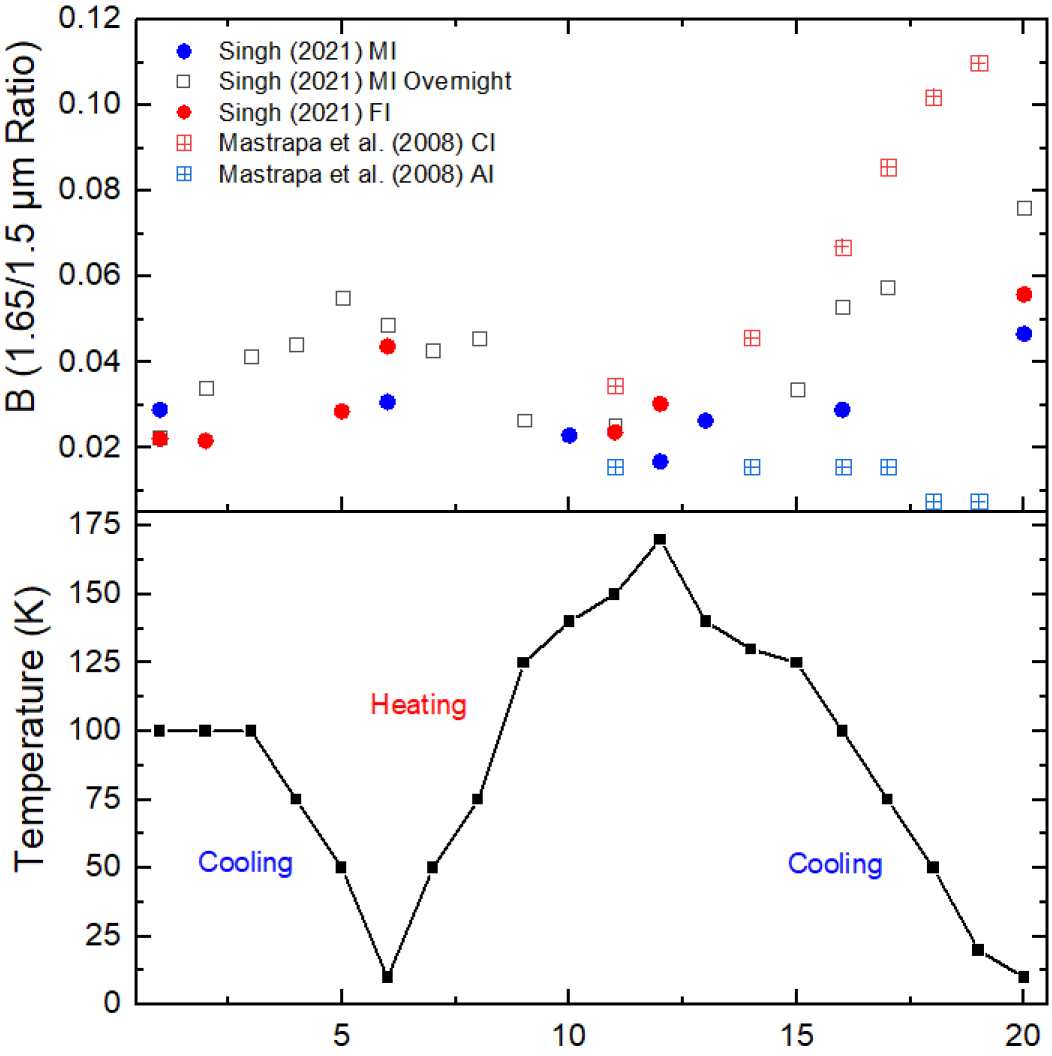

Figure 4.22: Variation in the 1.65/1.5 µm integrated band area ratio (B) with thermal history of the water ice samples, using ISL measurements of MI (blue circle), MI Overnight (black square), and FI (red circle). Mastrapa *et al.*, 2008 measurements are used for comparison.

Berdis (2021) also reports that the perceived spectroscopically derived crystallinity (which depends on B ratios) changes with the temperature of formation of samples (e.g., crystalline ice at 150 K vs 120 K) (see Figure 4.23). A detailed analysis of the laboratory spectra used in their work is pursued in section 4.3.4 for thickness analysis, and further supports this hypothesis: thermal history (including phase transitions) alters *B* ratios.

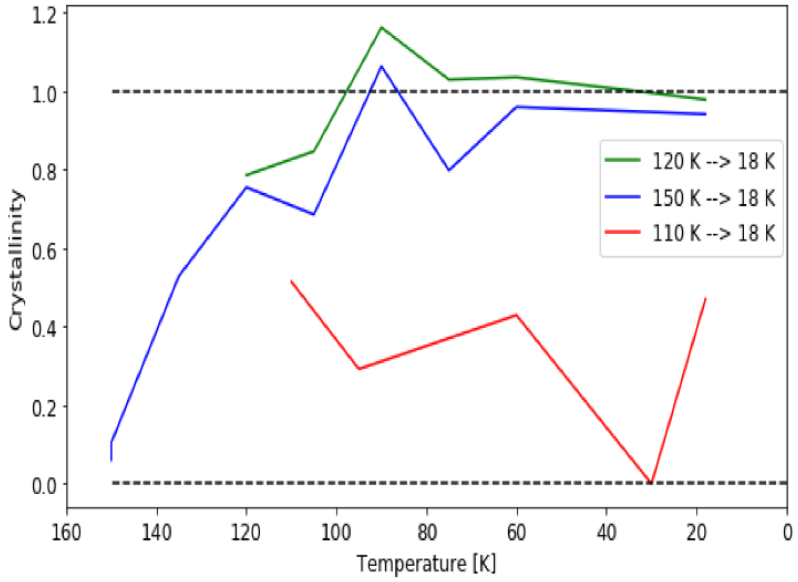

Figure 4.23: The calculated crystallinity for water ice samples depends on the formation temperature and thermal history, as highlighted by three cooling curves, starting at 150 K, 120 K and 110 K. Figure 2.12 from Berdis (2021).

4.3.3.1 Calculation of B_{TH}

The ratio of the 1.65/1.5 μm integrated band area ratio (B) is calculated for MI overnight and MI ice samples at three temperatures of (1) 100 K with initial placement vs after 72 hours, en route heating, and on cooling back down, (2) 150 K with heating during

annealing, and (3) 10 K prior to and after annealing. Equation 4.3 is used to calculate B_{TH}, to determine if both samples produce the same spectrum or band area ratios after placement at 100 K and to monitor their evolution with thermal history. If B_{TH} is equal to 1, then band area ratios are independent of thermal history.

$$B_{TH} = B_{MI\ Overnight} / B_{MI} \tag{4.3}$$

After initial placement at 100 K, both sets of spectra show a subdued 1.65 μm band strength, but the calculated B_{TH} is not equal to 1 (i.e. different initial band areas for two samples, with MI showing a greater value). Equilibration at 100 K reverses this trend with MI Overnight B ratio becoming greater due to the first crystallinity transition event. This behavior showcases the need to understand potential transition events even at 100 K. Subsequent thermal cycling reveals a disparity in calculated B ratios (via increasing B_{TH} trend). In other words, the spectra of water ice deposited at 77 K, placed at 100 K and immediately cooled to 10 K does not look the same as a sample deposited at 77 K, allowed to equilibrate at 100 K after placement, and then cooled to 10 K. Similarly, after heating both samples to 150 K with predicted formation of 100% crystalline ice, cooling back to 10 K, does not showcase the same change in band strength / area, as evidenced by changing B_{TH} ratios (Figure 4.24).

It is thus reasonable to conclude that the calculated B_{TH} varies with the thermal history of a sample. Additional measurements are needed to evaluate this relationship in detail and characterize the influence of thermal history on spectra.

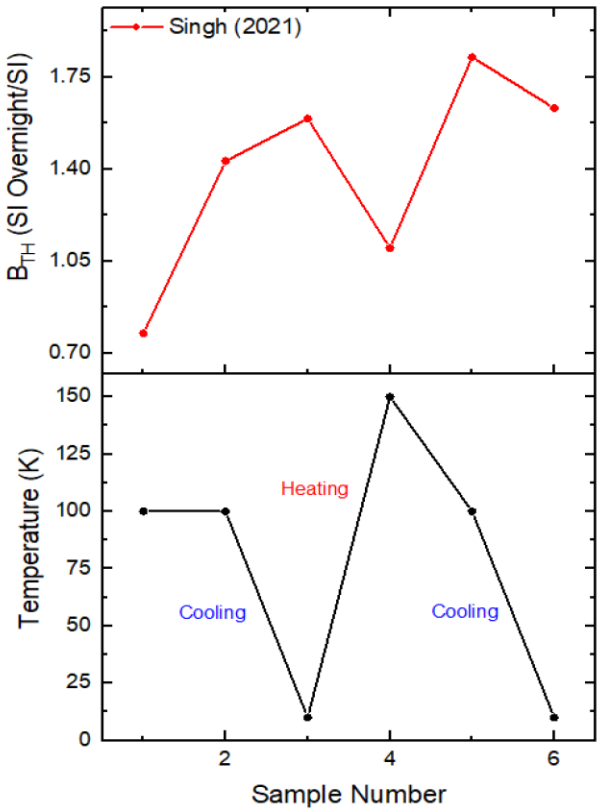

Figure 4.24: B_{TH} ratio for two water ice samples prepared identically, with varying thermal history: MI Overnight sample was allowed to equilibrate at 100 K for 3 days.

New sets of 100% amorphous and crystalline end member spectrums (e.g., B_{cryst} = 0.0529 and B_{amorph} = 0.0166 at 100 K) have been provided for thick, water ice in the ISL laboratory dataset. While additional constraints on planetary surface temperature (and thermal history) are required to ensure accurate comparison of end members to icy bodies, they can be used to approximate the behavior of H_2O–ice over a range of cryogenic temperatures. In Chapter 5, I provide a proof of concept for this approach, using these new end members to re-evaluate the surface crystallinity of Europa's leading hemisphere.

4.4 Thickness-Dependence of Water Ice Spectral Features

In this section, I explore the relationship between thickness of ice samples, and their 1.65/1.5 μm integrated band area ratio (B) and crystallinity (C). Our collected ISL reflection spectra (described in previous section) and ISL transmission spectra of crystalline and amorphous water ice, collected in 2010 by Dr. Murthy Gudipati (JPL) and Dr. Eleonora Ammannito (Italian Space Agency) are used for analysis. The transmission experiments were conducted using the Acquabella setup at ISL (Figure 4.5, described in Section 4.1.4.), and previously used to quantify the effects of temperature and ice thickness on the thermal conductivity of crystalline and amorphous water ice. Here, I have reevaluated ISL transmission datasets for two experiment sets (Table 4.3 provides a summary), to determine laboratory end members for amorphous and crystalline water ice and investigate the role of sample thickness in band strength variations.

1. Constant deposition at 100 K, followed by thermal annealing (February 12, 2010).
2. Constant deposition at 120 K, followed by thermal annealing (February 11, 2010).

Table 4.3: Water ice transmission experiments conducted in 2010, which are evaluated here for investigating the role of thickness.

Deposition at Constant T			Changing T (no deposition)
Date [MMDDYY]	T [K]	Thickness [μm]	T [K]
021210	100	0 – 2.9	100, 85, 70, 55, 18, 150, 30
021110	120	0 – 2.8	120, 150, 135, 120, 105, 90, 75, 60, 45, 30

Ice was vapor deposited at a constant temperature (100 K or 120 K, here) on a sapphire window inside the vacuum chamber, with a constant flow rate of ~ 8.5 nm per minute (Barnett *et al*., 2012). Both the deposition temperature and flow rate dictate the water ice phase. For the timescales in our two experiments, water vapor that was initially deposited at 100 K or 120 K is amorphous ice. The orientation of the sapphire window at 45º between FTIR spectrometer and spray nozzle allows the continuous acquisition of transmission spectra during vapor deposition (Figure 4.5). A background spectrum (T_0) is collected prior to vapor deposition, to capture the inherent spectrum of the sapphire sample holder, which is then removed from all measurements. Single beam transmission spectra (T) were subsequently collected every 15 minutes to capture spectral changes with the increasing thickness of the water ice layer. Post deposition, the samples were thermally cycled in ~ 15 K steps (ramp rate of 1 K per minute), with a spectrum acquired at each new stepped temperature.

All transmission spectra were converted to absorption spectra and baseline corrected, using the methodology established in Berdis (2021). Absorbance is calculated using the following form of the Beer-Lambert Law:

$$A_\lambda = - log_{10}(T / T_0) \quad (4.4)$$

where T is the sample transmission and T_0 is the background transmission. Figures 4.25 and 4.26 provide examples of this process with normalized absorbance spectra identified as crystalline and amorphous water ice after deposition at 100 K.

4.4.1 Deposition at 100 K

Ice was deposited at 100 K (at pressure of 10^{-7} mbar) for 5:45 hours (or 345 minutes) to achieve a maximum sample thickness of ~2.9 μm. Sample was subsequently (1) cooled to 18 K (ramp rate of 1 K per minute), (2) heated to 150 K, and (3) cooled back to 18 K. Transmission spectra collected at each stage have been evaluated here with a focus on the 1.65 μm band and 3.1 μm Fresnel peak, as shown in Figure 4.25. The 1.5 μm and 1.65 μm region reveal the formation of amorphous ice on deposition at 100 K, with band features remaining consistent throughout deposition and on cooling to 18 K (see Figure 4.26). This observation follows theoretical predictions for formation temperatures of amorphous ice and lack of any phase transitions at 100 K or on cooling. Owing to vapor deposition in a controlled environment, no frost is expected to form on the sample (as seen in Section 4.3.3) or undergo transition. After thermal annealing to 30 K, the 1.65 μm band strength increases significantly, with a change in shape of the 1.5 μm band. The spectra resemble crystalline water ice with the predicted phase transition on heating to 150 K.

The calculated integrated band areas increase roughly linearly with an increase in thickness on continued vapor deposition at 100 K (Figure 4.27). However, their ratio *B* decreases with increase in thickness to values more consistent with end members from reflection spectroscopy in Section 4.3.1. This trend is consistent for the 1.65/1.5 μm ratios (B), the 2.0/1.5 μm ratios, and the 3.1/1.5 μm band area ratios, and explains the higher values of B from Mastrapa *et al*. (2008)'s transmission spectra of thin films, as compared to our results in Section 4.3.1. On cooling to 18 K, another slight increase is initially observed, before annealing changes B ratios from 0.043 to 0.186. This is consistent with a

phase transition to crystalline ice. Laboratory end members for thin film, pure amorphous ice at 100 K, 85 K, and 75 K are obtained with B_{amorph} = 0.022, 0.0281, and 0.0348 respectively (with sample thickness of 2.9 μm). Table 4.4 lists the calculated end members from both experiments.

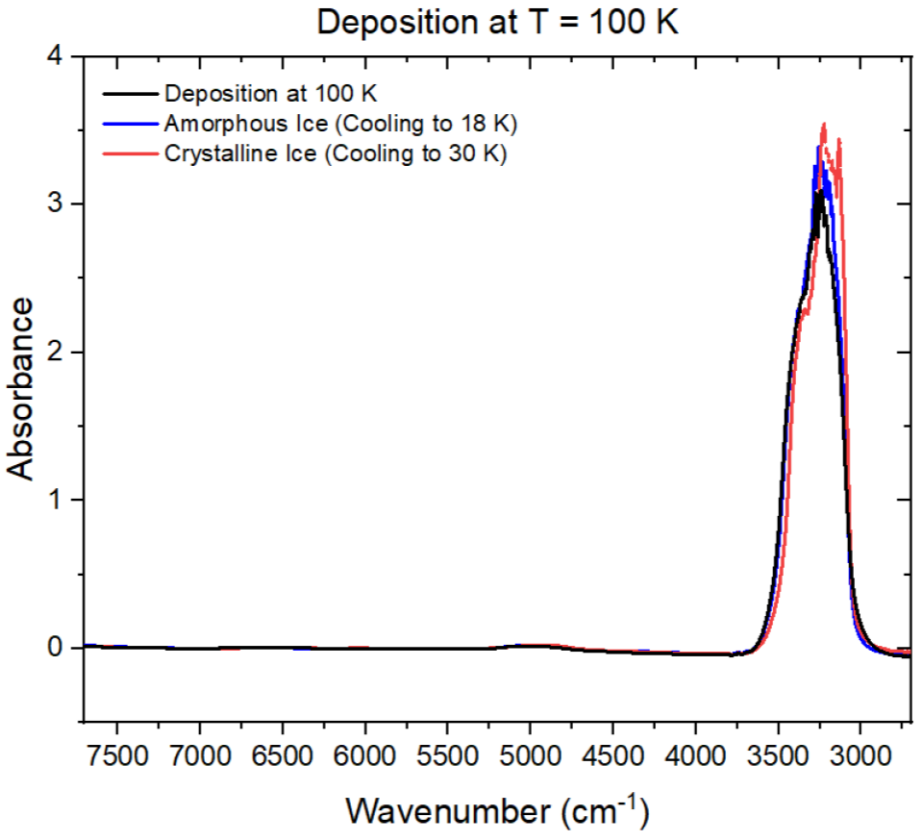

Figure 4.25: ISL Acquabella absorbance spectra of water ice samples after deposition has ceased at 100 K (black), on cooling to 30 K (blue) preserving amorphous ice, and after thermal cycling (heating to 150 K and cooling to 30 K) (red), creating crystalline ice. Background substrate spectrum was removed and baseline correction performed. These spectra were acquired on 12 February 2010.

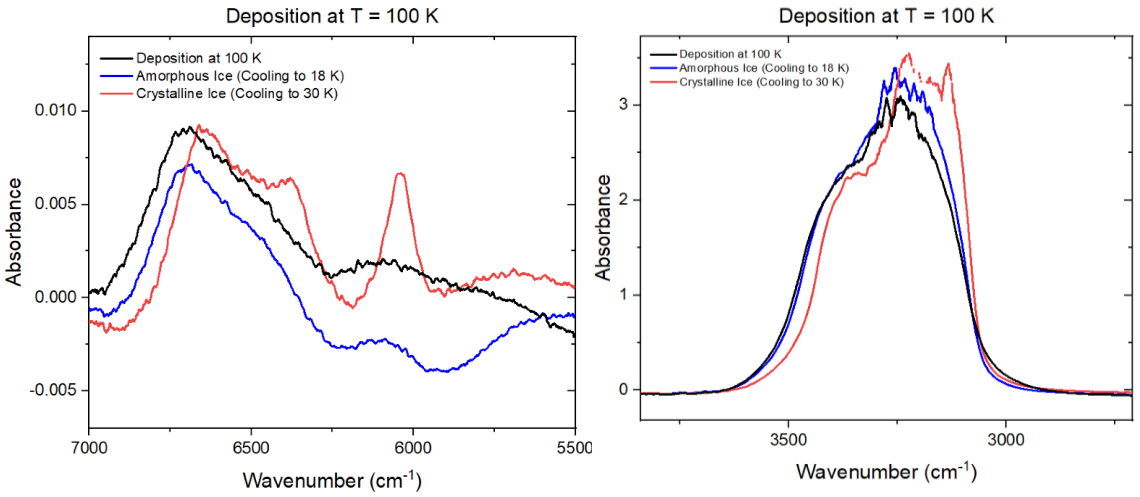

Figure 4.26: 1.65 μm (left) and 3.1 μm band variation (right) in spectra collected at different stages of the 100 K deposition experiment.

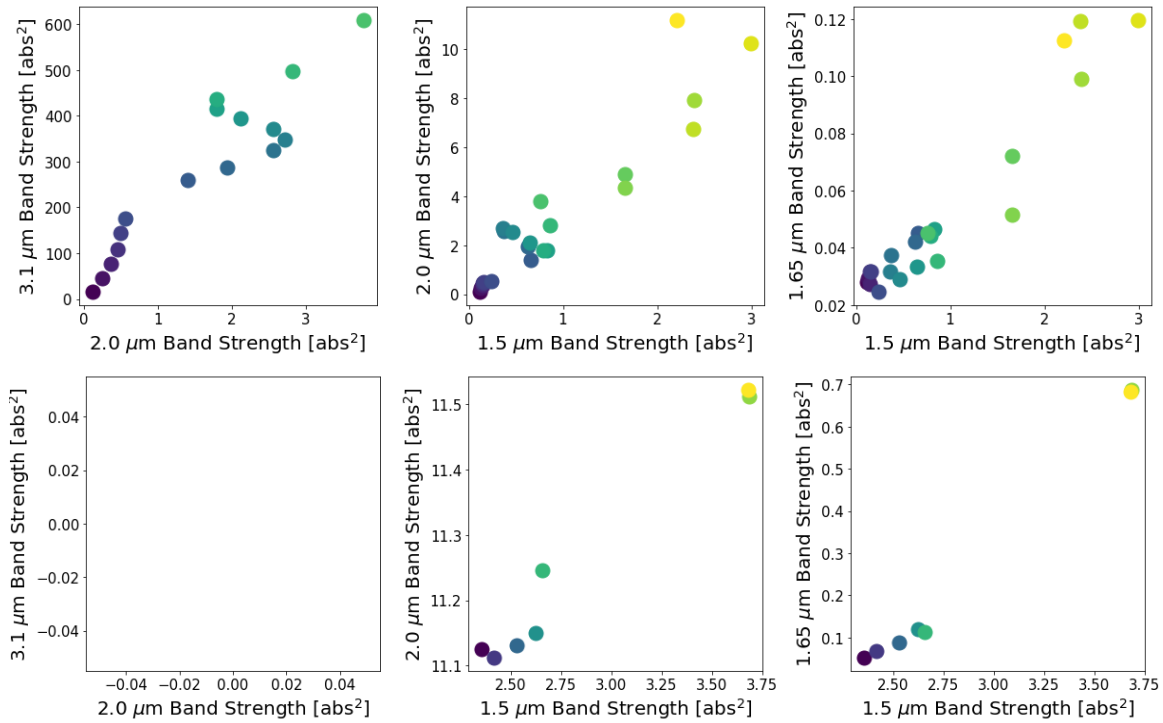

Figure 4.27: Linear relationship between integrated band areas and ice thickness (top) (lighter color with increasing thickness) with deposition at 100 K; (bottom) thermal annealing (cool to 18 K, heat to 150 K, cool to 30 K). As sample numbers increase/time progresses forward, colors change from purple to yellow. Images courtesy of Jodi Berdis.

4.4.2 Deposition at 120 K

Ice was deposited at 120 K (pressure of 10^{-6} to 10^{-7} mbar) for 5:30 hours (or 330 minutes) to achieve a sample thickness of ~2.8 µm. The experimental procedure differs here from the previous experiment in that the sample was deposited at a higher temperature (120 K versus 100 K), and there is no initial cooling stage (to 18 K) in the thermal cycle post deposition. Instead, the sample was directly heated to 150 K, at a ramp rate of 5 K per minute, and then cooled to 18 K. Additionally, a high flow rate of vapor was used in the latter 1:45 hours of deposition (or ~ 0.9 µm thick layer).

Transmission spectra were collected at each stage of the experiment, including in the 90 – 105 K temperature range after annealing, which are useful as laboratory end members of crystalline water ice for Europa (B_{cryst} = 0.0715 and 0.0843, respectively) (Table 4.4). Focusing on the 1.65 µm and 3.1 µm regions, the signal to noise ratio is low for the spectra collected during deposition (Figure 4.28). Figures 4.29 and 4.30 highlight spectral features of mostly amorphous ice at the end of deposition, but with a prominent 1.65 µm band, which is stronger than the strength observed at 100 K deposition in section 4.3.4.1. This indicates that while deposition at 120 K should theoretically lead to the formation of amorphous ice, the high flow rate may have introduced a component of overlying crystalline ice (~0.9 µm) on top of the sample. Laboratory end members for 100% pure amorphous ice cannot be obtained as a result.

After heating to 150 K, the signal to noise ratio improves on cooling. Post annealing, all deposited ice should undergo a phase transition to crystalline ice, which is captured in the spectra with the 1.65 µm band feature prominently visible at 100 K and at

30 K (with greater band strength). A roughly linear relationship is observed between increasing ice thickness and the calculated integrated band area ratios for 1.65/1.5 μm ratios, the 2.0/1.5 μm ratios, and the 3.1/1.5 μm band area. This is consistent with our previous results for the 100 K deposition experiment.

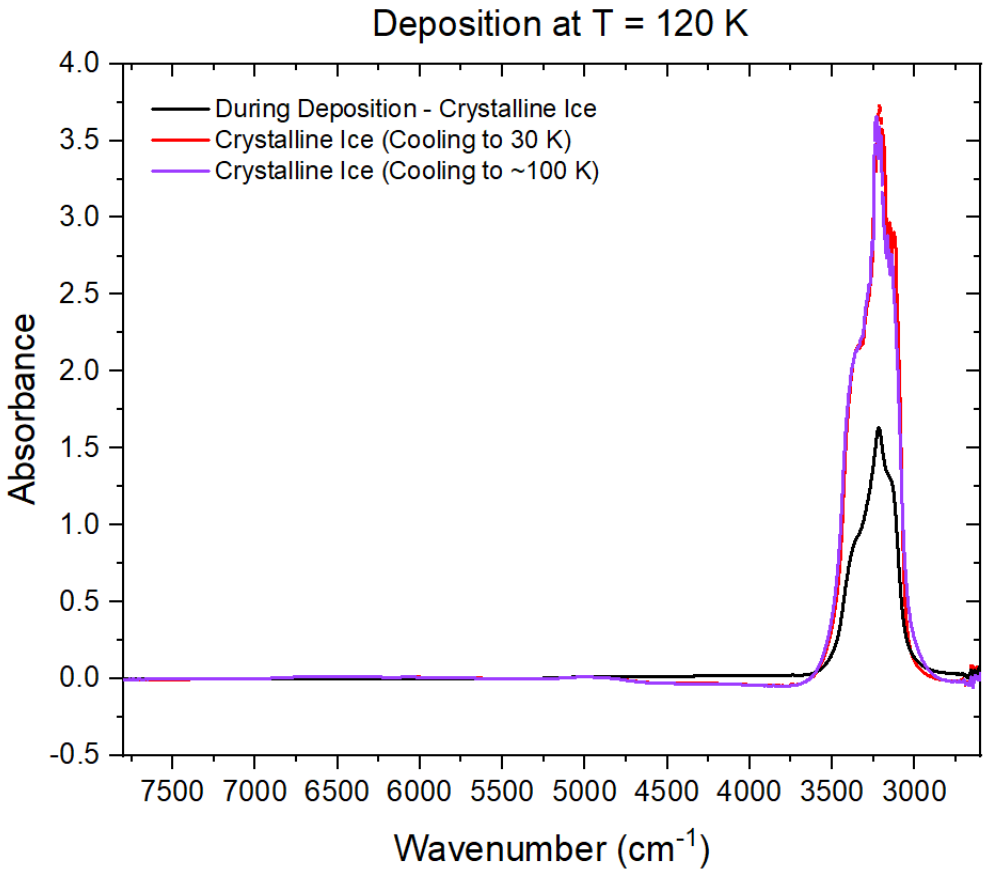

Figure 4.28: ISL Acquabella absorbance spectra of water ice samples after deposition has ceased at 120 K (black), and after thermal cycling (heating to 150 K and cooling) to 100 K (purple) and to 30 K (red). Background substrate spectrum was removed and baseline correction performed. These spectra were acquired on 11 February 2010.

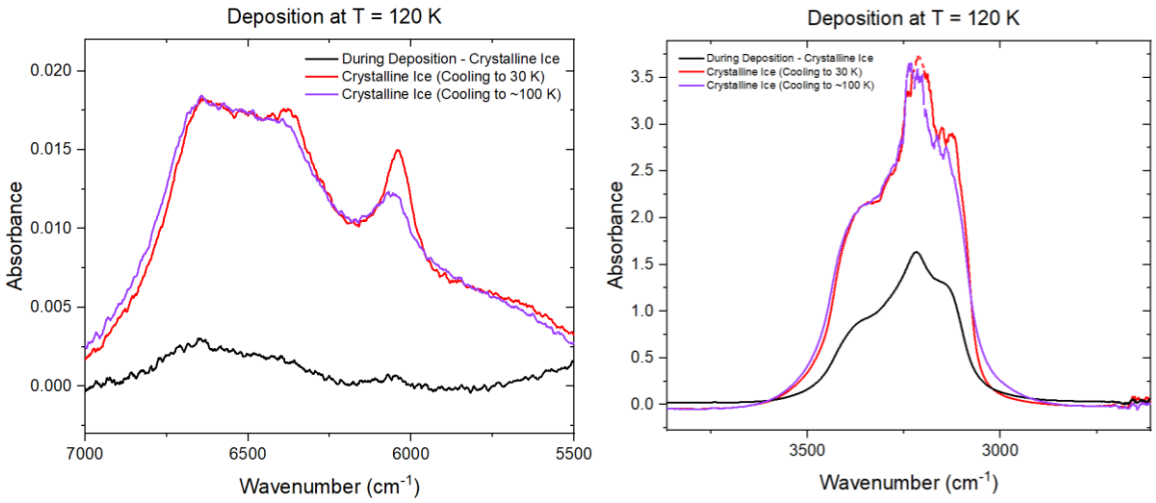

Figure 4.29: 1.65 µm (left) and 3.1 µm band variation (right) in spectra collected at different stages of the 120 K deposition experiment.

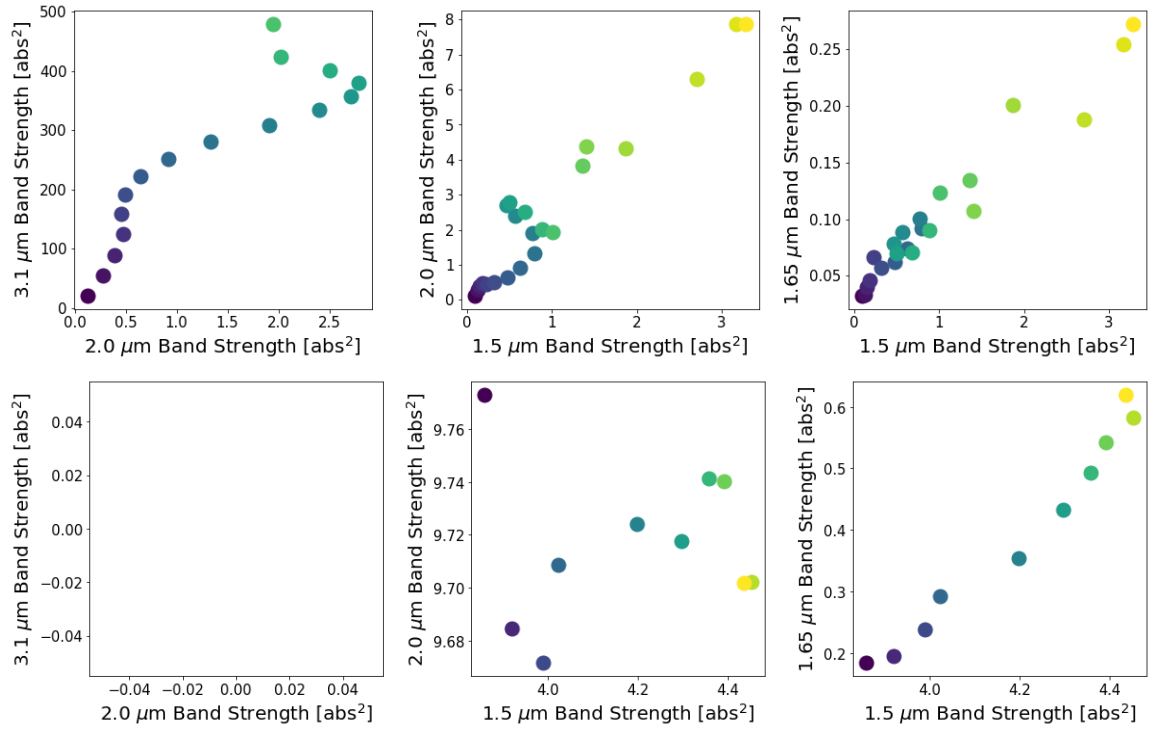

Figure 4.30: Linear relationship between integrated band areas and ice thickness (top) (lighter color with increasing thickness) with deposition at 120 K; (bottom) thermal annealing [heat to 150 K, then cool to 30 K]. As the sample numbers increase and time progresses forward, colors change from purple to yellow. Images courtesy of Jodi Berdis.

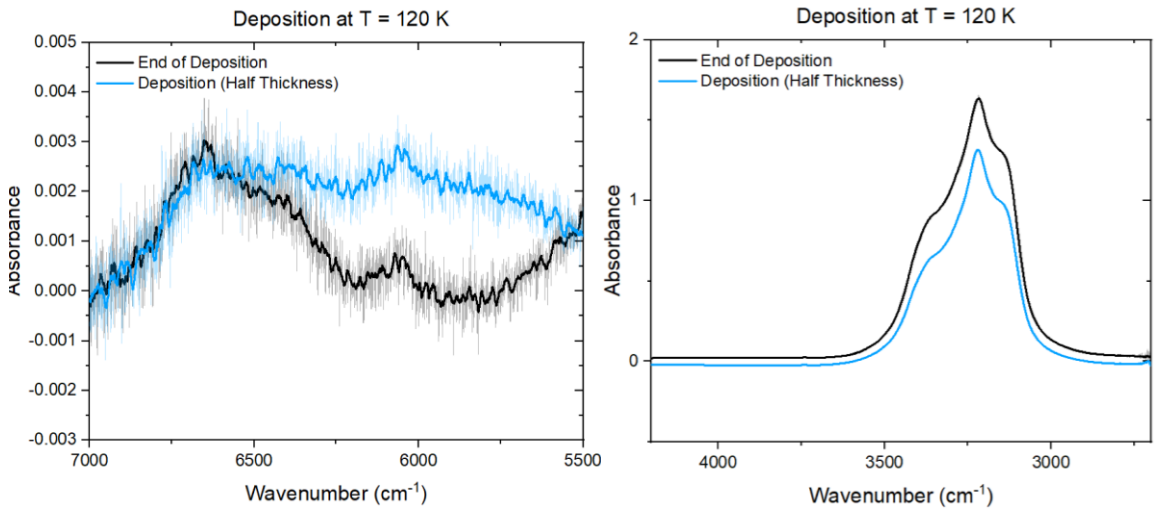

Figure 4.31: 1.65 µm (left) and 3.1 µm band variation (right) in spectra collected at different stages of deposition (thickness) at 120 K.

4.4.3 Unraveling the Role of Thickness

To investigate the dependence of the 1.65 µm band on sample thickness, i.e., the linear trend observed in thin films, I perform a quantitative investigation of the 1.65/1.5 µm integrated band area ratio (B) at 100 K for:

1. Transmission spectra collected at various thicknesses (Figure 4.31), including spectra collected in the first hour, from the two experiments described in this section.
2. Reflection spectra collected for thick samples (> 25 µm), as described in section 4.2.

Table 4.4: Integrated band area ratio (B) for amorphous and crystalline ice are compared for samples with various thicknesses and detection techniques at the same temperatures.

Spectroscopy Technique	**Formation Temperature [K]**	**Sample Thickness [μm]**	**Temperature [K]**	B_{cryst}	B_{amorph}
Uncertainty: ± 0.08 [v. thin] to ± 0.01 [thick]					
Transmission	100	<< 1 μm	100	-	0.1054
Transmission	100	~ 0.9 μm	100	-	0.0635
Transmission	100	~ 2.2 μm	100	-	0.0311
Transmission	100	~ 2.9 μm	100	-	0.0220
Transmission	100	~ 2.9 μm	85	-	0.0281
Transmission	100	~ 2.9 μm	70	-	0.0348
Uncertainty: ± 0.15 [v. thin] to ± 0.02 [thick]					
Transmission	120	<< 1.0 μm	120	B = 0.1753	
Transmission	120	~ 1.0 μm	120	B = 0.1297	
Transmission	120	~ 1.4 μm	120	B = 0.1031	
Transmission	120	~ 2.8 μm	120	B = 0.0694	
Transmission	120	~ 2.8 μm	105	0.0715	-
Transmission	120	~ 2.8 μm	90	0.0843	-
Reflection	77	25 μm (min.) to ~2 mm (max.)	100	0.0529	0.0166
Reflection	250	Frost to ~2 mm (max.)	100	B = 0.0221	
Reflection	77	75 μm (min.) to ~2 mm (max.)	100	B = 0.0289	

Table 4.4 displays the results of this investigation. Derived B ratios range between 2.20×10^{-2} and 1.75×10^{-1} for transmission spectra. Larger B ratios are associated with spectra collected for very fine films in the first hour (thickness << 1 μm), which are theorized to contain (constructive and destructive) interference patterns due to reflection off the lower and upper boundaries of the thin film, thus subduing the ice signal. These ratios should be discarded. With an increase in thickness, the band area ratio decreases to values more consistent with those derived using reflection spectroscopy (and previous work). Using the spread in B for samples, the uncertainty in calculations is estimated as ~10–25% for samples at maximum ice thickness. End members of amorphous and crystalline ice calculated using transmission spectra are $B_{amorph} = 0.022$ and $B_{cryst} = 0.0715$.

These results clearly indicate the dependence of the 1.65 μm band and integrated band area ratios on both thickness and temperature (along with thermal history). With an increase in thickness, the 1.65 μm band strength increases while the integrated band area ratio decreases. Additionally, band area ratios derived for reflectance spectra are generally lower than those derived for transmission spectra.

4.5 Variations with Grain Size

In the absence of optical constants, as is generally the case for ices in the outer solar system, laboratory reference spectra acquired at relevant environmental conditions are suggested for use in spectral unmixing analysis. As discussed in Chapter 3, grain size variations can impact the 1.65 μm and 1.5 μm band areas, and their integrated band area ratio (or B) for water ice. Here, I determine whether theoretical predictions for grain size behavior follow the results of our laboratory measurements and identify any discrepancies in the position and strength of NIR band features (1.5 μm, 1.65 μm, 2.0 μm and 3.1 μm) that have not yet been captured in the models. For example: *do the models fully explain single scattering albedo?* This will allow us to determine whether existing synthetic spectra are appropriate for interpretation of Solar System objects.

I have approached this comparison from two directions: laboratory reflection spectroscopy and Hapke spectroscopic modeling; the results are detailed below.

1. On the laboratory end, reflectance spectra of samples of "thick" pristine water-ice grains have been collected, with grain size ranging from 25-153 μm, in the near infrared (NIR) wavelength range, at temperatures of 10-170K.
2. On the Hapke modeling end, new synthetic spectra of water ice samples of comparable grain sizes (10-200 μm) have been generated at temperature of 100 K, updating previously modeled spectra (Dalton *et al*., 2012) with new optical constants (n and k values from Mastrapa *et al*., 2008).

4.5.1 Laboratory Reflection Spectroscopy for Grain Size Variation

Water ice samples were prepared using the protocols established in Section 4.1.2. Reflectance spectra of both ~ amorphous (mist ice) and crystalline (freezer ice) H_2O-ice samples with grain-size from 25 μm to > 212 μm (divided into 25 or 50 μm sets) were collected over a broad range of temperature conditions (10-170 K) and thermal history (including annealing). Building off previous research on grain size dependency for water ice and frost by Clark *et al*. (1980) and Taffin *et al*. (2012), this ISL dataset includes additional spectroscopic measurements of thick, optical quality samples over a broader wavelength range (1.25 – 8 μm), which is more applicable to future space-borne observations.

To illustrate observed trends in laboratory spectra, I have selected three sets of measurements which are evaluated in the range of 1.25 – 3.3 μm, as shown in Figure 4.32:

1. Mist Ice collected at 100 K after deposition (relevant to Europa).
2. Mist Ice collected at 10 K, after thermal annealing (heating to 150 K, then cooling to 10 K). 10 K is selected to maximize the signal to noise ratio of the spectrum.
3. Freezer Ice collected at 10 K.

Background was removed for all measurements, spectra were baseline corrected, and 1.65 μm band center positions were calculated (Table 4.5). An offset is introduced in all figures shown in this section to improve visibility of band features. All three sets of spectra display the theorized dependence on grain size, with an increase in grain size resulting in (a) a decrease in overall reflectance, and (b) the 1.5, 1.65 and 2 μm bands grow deeper (increased band depth) along with an observed broadening of the 1.5 μm band. This

trend is consistent with synthetic spectra from previous theoretical models and can be used to estimate planetary surface particle size distribution. (c) Table 4.5 indicates an increasing blue slope with increase in grain size due to a gradual shift in the position of 1.65 μm band center to shorter wavelengths. Taffin *et al*. (2012) reported this behavior for Gaussian centers of 1.5 and 1.55 μm bands, but an opposite trend for the 1.65 μm band. Center positions for our ISL dataset vary between 1.642 – 1.656 μm, which is also broader than the spread observed by Taffin *et al*. (2012) (~1.645 – 1.650 μm) for comparable grain sizes.

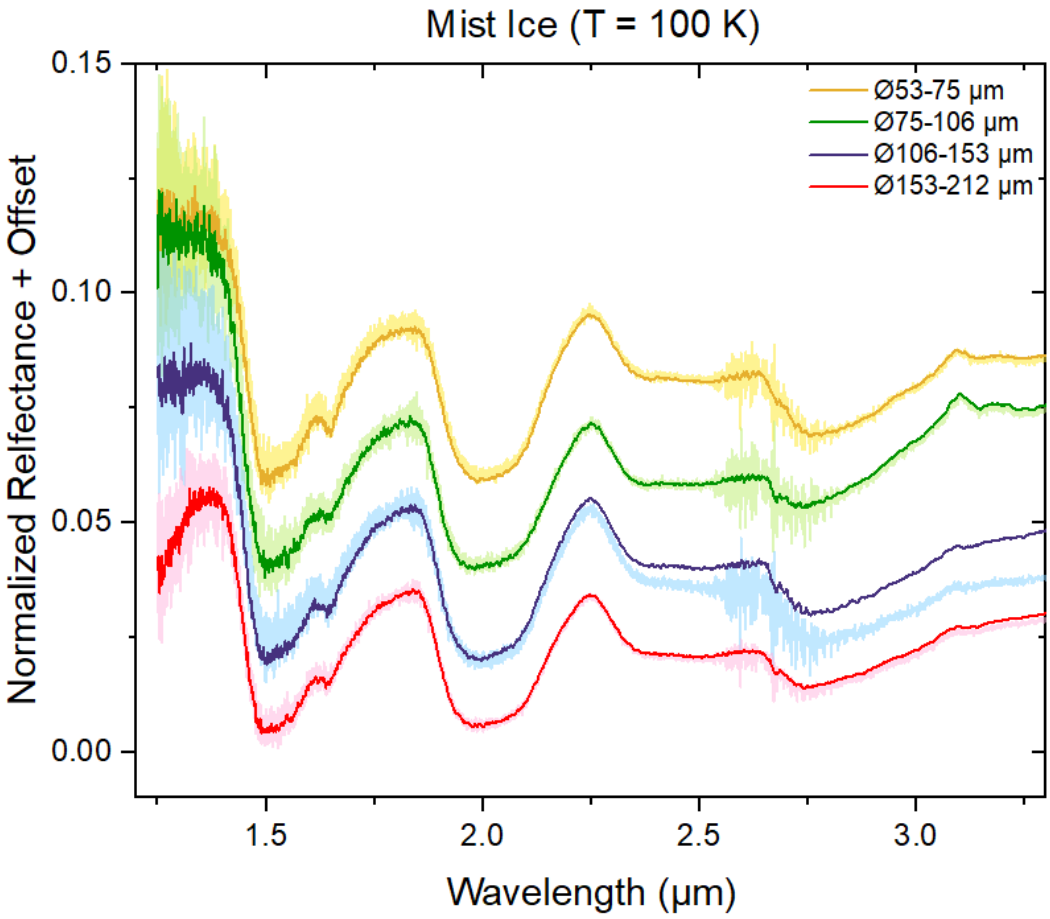

Figure 4.32: NIR reflection spectroscopy of mist ice with grain size of: [1] 53-75 μm (yellow), [2] 75-106 μm (green), [3] 106-153 μm (blue) and [4] 153-212 μm (pink). All spectra are offset, and unsmoothed spectra are shown underneath in the same colors.

Table 4.5: Shift in position of the 1.65 μm Band Center with change in grain size.

Sample Type	**Grain Size [μm]**	**1.65 μm Band Center [cm^{-1}]**
FI (Crystalline)	25-53	6038 ± 3
FI	53-106	6059 ± 3
FI	106-153	6058 ± 12
MI (Mist Ice)	53-75	6068 ± 4
MI	75-106	6079 ±12
MI	106-153	6082 ± 13
MI	153-212	6087 ± 17
MI Anneal	25-53	6049 ± 1
MI Anneal	53-75	6052 ± 4
MI Anneal	75-106	6040 ± 10
MI Anneal	106-153	6063 ±7
MI Anneal	153-212	6058 ± 16
MI Anneal	greater than 212	6072 ± 3

Spectra collected for mist ice at 100 K display a subdued 1.65 μm band strength, which becomes prominent on annealing due to a predicted phase transition to crystalline ice, and a better signal to noise ratio (Figure 4.33). However, annealed spectra do not fully replicate the spectral signatures of freezer (crystalline) ice. In particular, crystalline ice spectra show a lower overall reflectance, with a greater 2 μm band depth and a broader 1.5 μm band region (i.e., smaller band area ratio and calculated crystallinity) than annealed ice. This may indicate that either the phase transition of amorphous to crystalline ice was incomplete, or changes in grain size and shape on annealing may affect the signal. To put this in a broader context, a mixture of amorphous and crystalline ice on a planetary surface may 'appear' crystalline, but in the absence of an understanding of its formation mechanisms, surface temperature and thermal history, it is difficult to decipher the precise crystallinity (or age) of the ice.

There are two main takeaways from the analysis of laboratory datasets:

1. Theorized grain size dependence of water ice spectral features was successfully demonstrated and is generally consistent with previous laboratory results.
2. Formation temperature and thermal history continue to play a role in band evolution. Additional experiments with a focus on ice sintering are recommended to understand the morphological changes in the ice.

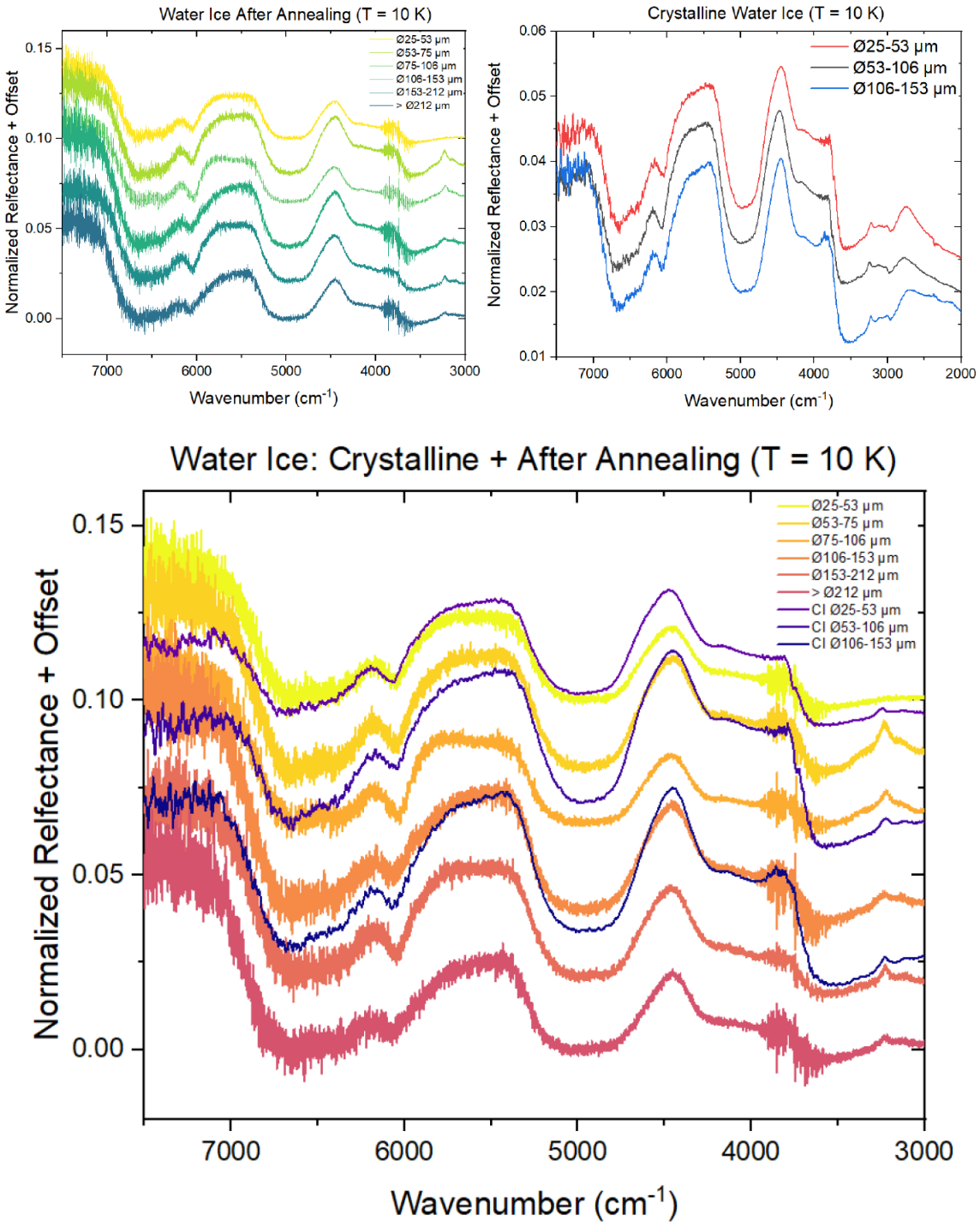

Figure 4.33: NIR spectroscopic measurements of water ice samples: mist ice (yellow to red) after annealing and freezer ice (shades of violet) are compared at similar grain sizes.

4.5.2 Hapke Bidirectional Reflectance Modeling for Grain Size Variation

Hapke Bidirectional Reflectance Theory provides an analytic solution for describing the scattering of light from surface particles and includes corrections for comparing laboratory transmission and reflection spectra with observational planetary spectra (Hapke 1981, 1984, 1986). The Hapke model has been widely used on airless planetary surfaces across the Solar System, from our Moon and Europa to Pluto and KBOs. It provides estimates of surface regolith properties (like porosity, albedo, roughness) and is used for synthesizing endmember reflection spectrum (using optical constants, illumination conditions, temperature, etc.) for spectral mixture analysis (Lucey, 1998; Li and Mustard 2003; Shirley *et al*., 2010; Dalton *et al*., 2012).

For Europa, Dalton *et al*. (2012) produced synthetic spectra of crystalline water ice for compositional interpretation of Galileo NIMS measurements. Here, the Hapke model outlined in Grundy (1995) thesis (based on the scattering theory) was used by collaborator Jodi Berdis to produce synthetic spectra of crystalline and amorphous water ice for grain sizes of 10, 20, 50, 100, 150, and 200 μm, using more recently published sets of optical constants (n and k) for amorphous and crystalline water ice from Mastrapa *et al*. (2008). These optical constants were collected at T = 100 K, which is the average equatorial surface temperature of Europa, and mirrors the conditions simulated during laboratory reflection spectroscopy in section 4.3.2. The incidence, emission, and phase angles for each spectrum are selected as 35º, 35º, and 70º, respectively, to replicate laboratory illumination conditions. Grain porosity of 0.1 is assumed (Johnson *et al*. 2017) to compute the compaction parameter (Hapke 1963; Eqn 7 Buratti 1985). An asymmetry factor of -0.15

(Buratti 1983, 1985), and a mean macroscopic roughness parameter of 10º (Domingue *et al*. 1991) are used. The generated spectra are shown in Figure 4.34.

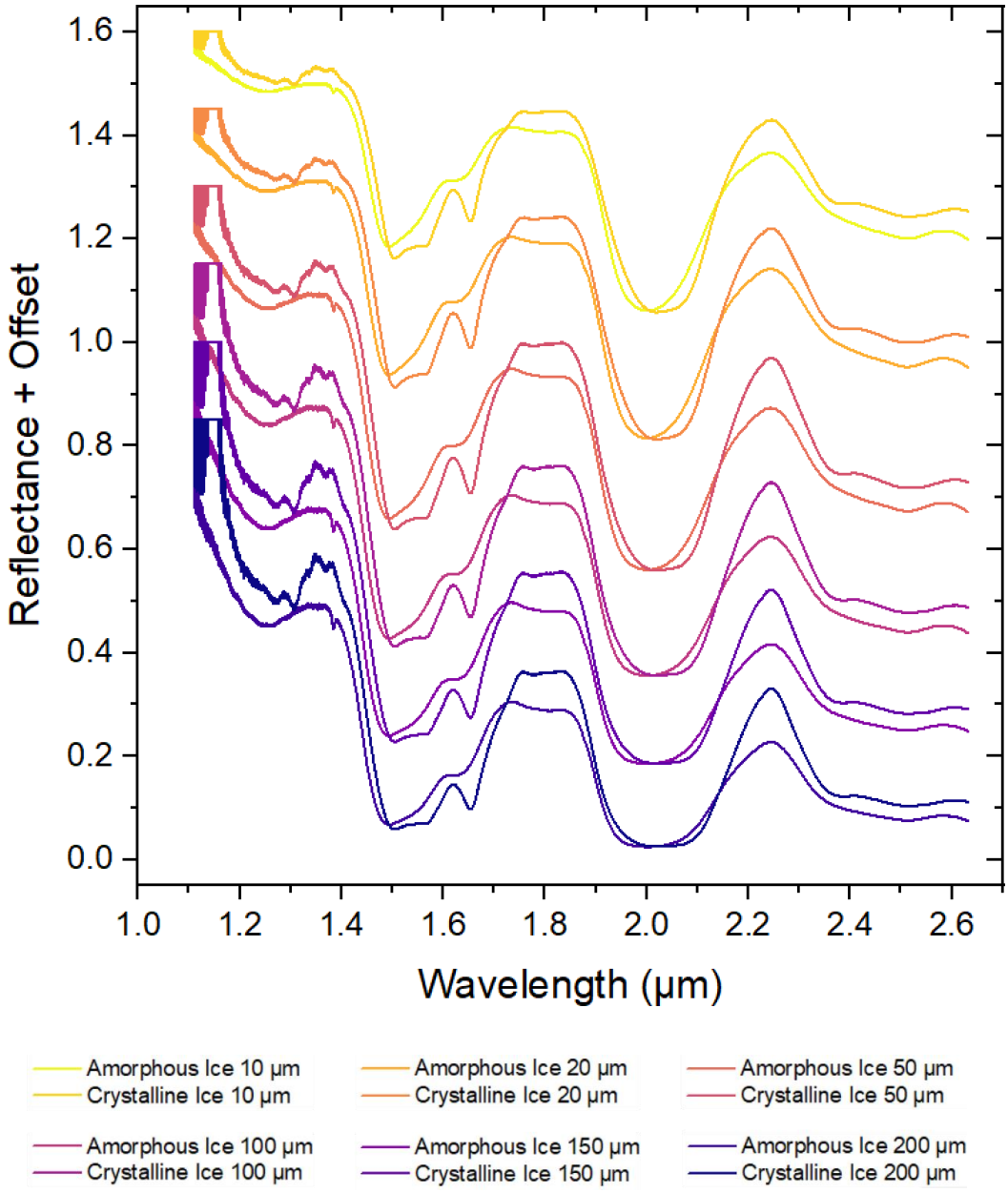

Figure 4.34: Hapke synthetic spectra of Amorphous and Crystalline Water Ice with grain size variation for comparison to lab results (illumination conditions = 35º, 35º, 70º).

The synthetic spectra generated for this study demonstrate the differences in the shapes and the strength of amorphous and crystalline water ice absorption features. Using the 1.65 μm band as an example, the absorption feature is sharp with a greater band depth and a red shift in position of the band center for crystalline water ice compared to amorphous ice. Both sets of spectra however highlight that the overall spectral reflectance and depths of absorption features are dependent on grain size, with a trend consistent with laboratory results presented in the previous section.

4.5.2.1 Relationship between Integrated Band Area Ratio (B) and Grain Size

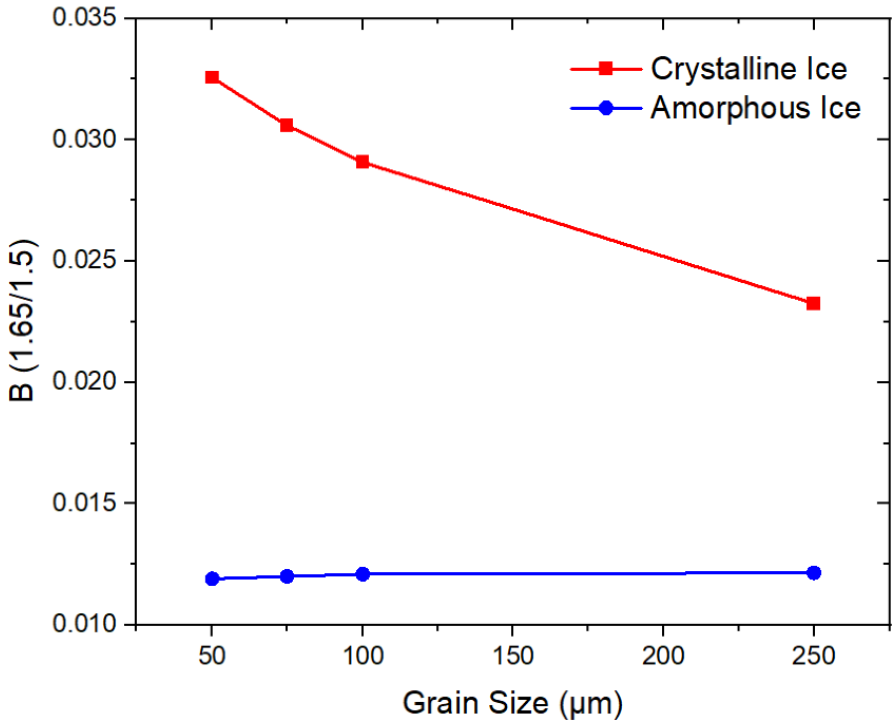

Figure 4.35: The integrated band area ratio (B) was calculated at various grain sizes for Hapke Modeled synthetic spectra of amorphous (blue) and crystalline (red) water ice.

Using the generated synthetic spectra of amorphous and crystalline water ice, I evaluated the relationship between spectral features and grain size by calculating the 1.65/1.5 μm integrated band area ratio (B) (Figure 4.35). Four grain sizes are selected in the range of 50-250 μm, which is consistent with predictions of Europa's surface grain size.

The overall magnitude of B is smaller for amorphous ice (which is consistent with literature, as the 1.65 μm band should be very small) and remains largely unaffected by the increase in grain size. Crystalline ice shows a negative trend between B and increasing grain size. This finding needs to be considered with caution owing to lack of data points. A detailed analysis will be pursued in future to evaluate this behavior, with independent characterization of grain size dependent changes in the band strengths and area for the 1.5 μm and 1.65 μm features. At this preliminary stage, laboratory spectra indicate that an increase in grain size can increase the absorption for both the 1.5 μm and 1.65 μm bands. However, the change is more prominent for the 1.5 μm band, which increases in depth and broadens thus lowering the ratio (see Figure 4.34).

4.5.3 Comparison of Laboratory Results to Synthetic Spectra

Grain size dependency has been established with both approaches. In this section, our results are combined to evaluate whether modeled spectra capture the shape and strength of absorption features observed in laboratory reflectance spectra of water ice at different grain sizes. Synthetic spectra of both amorphous and crystalline ice at 100 K are compared to Mist Ice (at 100 K and after annealing at 10 K). A constant offset is added to all spectra to increase visibility. Figure 4.36 highlights the observed differences.

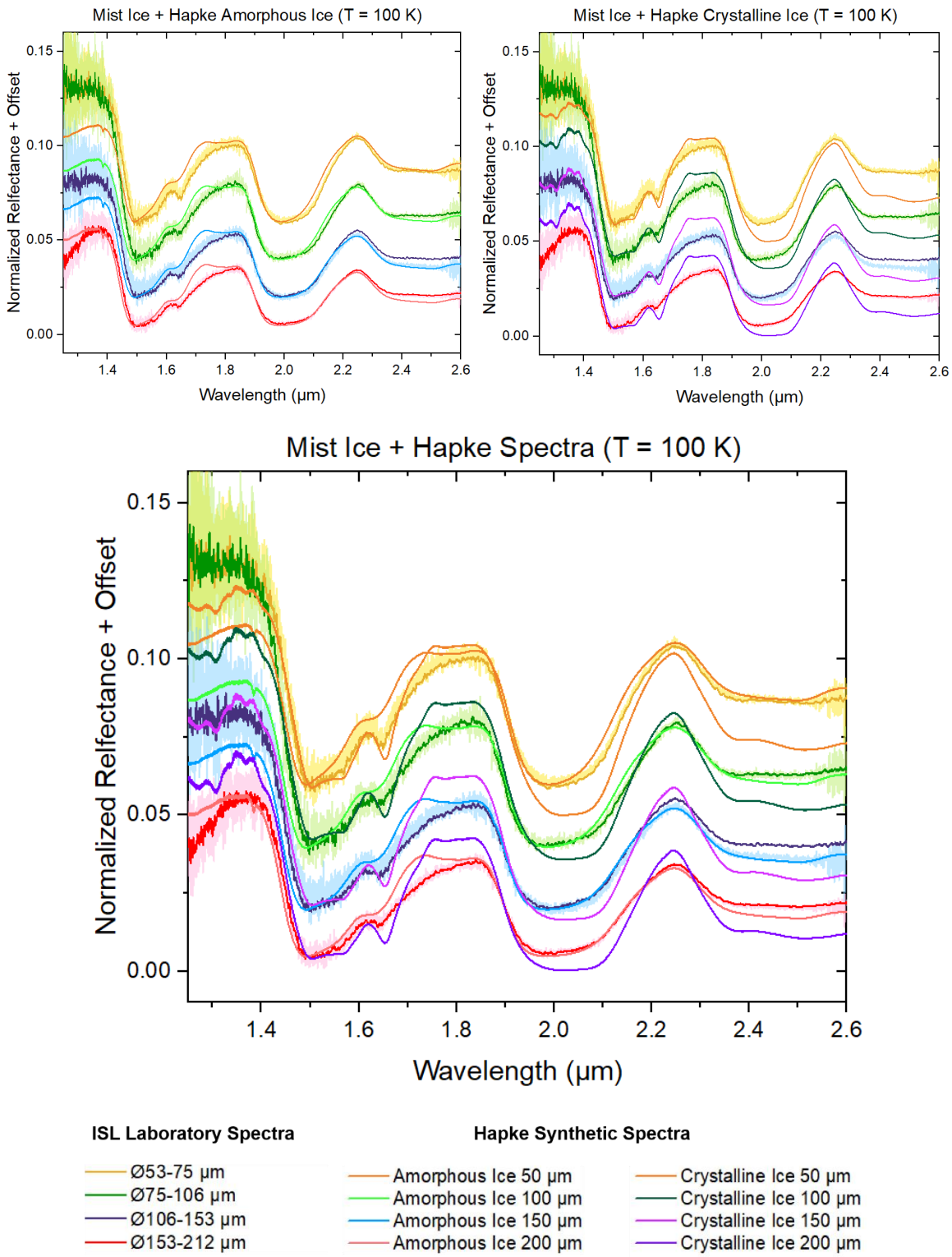

Figure 4.36: NIR spectroscopic measurements of mist ice at 100 K and synthetic spectra of amorphous and crystalline ice are compared to highlight variations in band shapes.

At 100 K (Figure 4.36), synthetic spectra capture the notable absorption band features with comparable band depths but do not directly overlap with collected lab spectra (of mostly amorphous ice) under identical reflectance parameters of incidence, emission, and phase angles. Notable changes observed include:

1. **Red shift** in overall spectral reflectance from amorphous ice– mist ice– crystalline ice.
2. **1.5 μm region:** Absorption band strength is captured consistently across all three spectra, but the band shape differs at the 1.65 μm band (described below) and at the right boundary. Boundary is sharp and well defined for synthetic spectra, extending to ~1.72 μm and ~1.75 μm for amorphous and crystalline ice respectively, versus a gradual change for laboratory spectra, extending to ~1.84 μm.
3. **1.65 μm region:** Laboratory spectra lie between amorphous and crystalline end members. Band depth is stronger than amorphous ice with lower overall reflectance, but significantly weaker than for crystalline ice. Red shift in band center position is prominently visible here (from amorphous to mist ice to crystalline), indicating a dependence on ice phase.
4. **2.0 μm region:** Crystalline ice has a greater band depth than both mist ice and amorphous ice

The shape and strength of the 1.65 μm features at 100 K indicate that laboratory mist ice is primarily composed of amorphous ice with a small component of crystalline ice. This is consistent with our predictions in section 4.3. On annealing (heating to 150 K, and cool to 10 K), the mist sample is expected to undergo a phase transition to crystalline ice. Collected spectra of mist ice at 10 K offer an imperfect comparison for a crystalline end member due to varying temperatures (and signal to noise ratio) but are still valuable. It

shows an increase in the 1.5 μm and 1.65 μm band depths along with a red shift in 1.65 μm band center position: it now resembles synthetic crystalline ice (Figure 4.37).

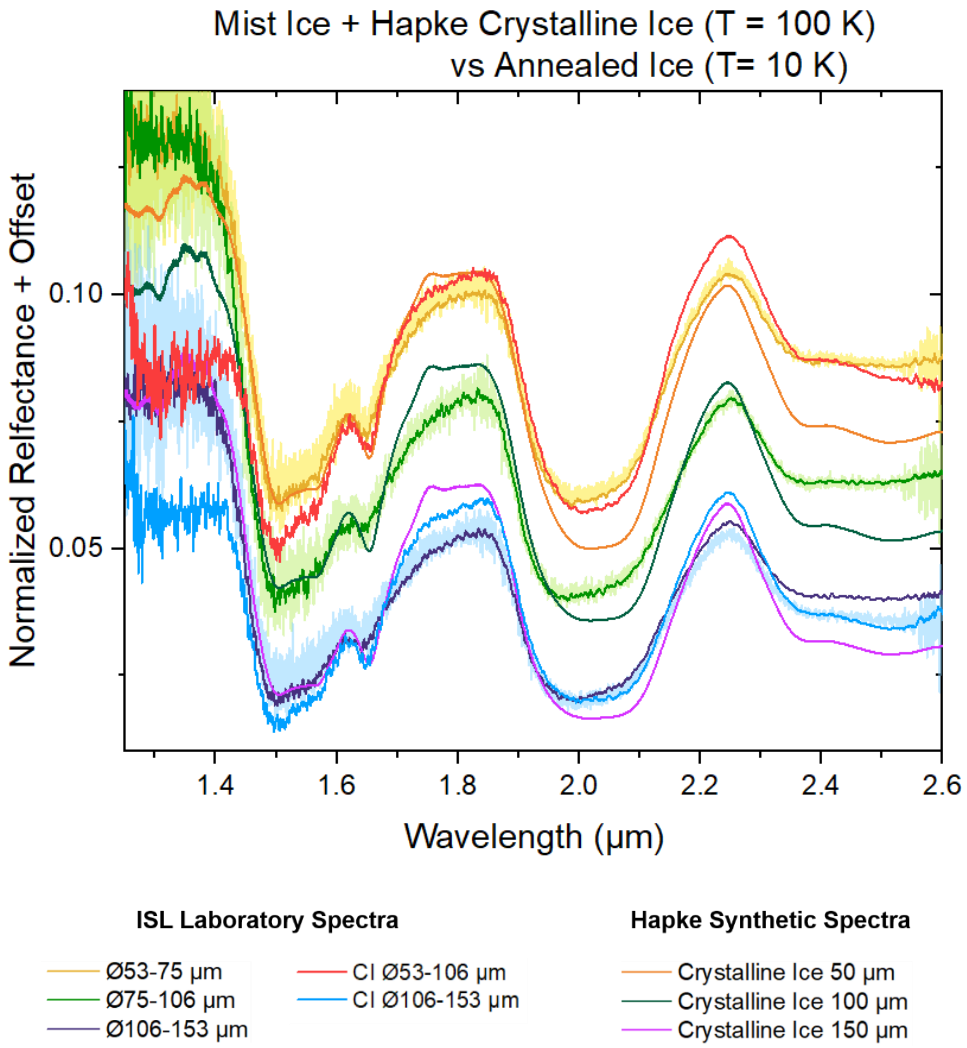

Figure 4.37: NIR spectroscopic measurements of mist ice and mist ice after annealing are compared to synthetic spectra of crystalline water ice.

Key questions remain: are the differences in band shapes due to the compositional variations of the laboratory sample (less than 100% pure) or a manifestation of the model's treatment of scattering behavior? Synthetic spectra assume a continuous, uniform surface of water ice with consistent grain size and shape. Our laboratory samples are closer to real surfaces, as non-uniform surfaces with a range of grain sizes and shapes. Integrated band area ratios (and crystallinity) are currently being calculated to offer a direct comparison between Hapke synthetic spectra and laboratory reflectance spectra. A quantitative spectral unmixing approach is also being pursued with collaborator Jodi Berdis, based on the technique of Hansen and McCord (2004), using the ISL grain size dependent spectral dataset to reevaluate the surface composition of two regions on Europa's leading hemisphere. Any observed changes will provide an inkling into the role of grain size inputs in spectral models.

4.6 Discussion, Comments and Recommendations

The interdependency of changes in temperature, thickness, and grain size on integrated band area ratios and crystallinity complicates interpretation of planetary surfaces. At the Ice Spectroscopy Lab, I have developed a new cryogenic reflection spectroscopy setup to enable collection of spectra at various temperatures (10-250 K) suitable for application to outer solar system bodies. Recommended protocols for the formation of thick (~ 2 mm), grain-size controlled amorphous and crystalline ice samples (+ salts, organics, bacteria, etc.) are detailed in the chapter, along with major takeaways of experiments. To briefly summarize, the ISL laboratory spectral dataset has demonstrated

the theorized (and rarely measured) evolution of absorption band features in the near infrared region due to variations in temperature, sample thickness, and grain size. These spectra and results will be publicly available, and future work on the spectroscopy of ices of various chemistries and under the effects of radiation is being proposed.

Formation temperature and thermal history of ice samples have been identified as key constraints on calculations of band area ratios and bulk crystallinity. In other words, characterization of a planetary surface requires some insight into the processes for formation of icy material on the surface (e.g., plumes, cryovolcanism), and its evolution through time via active surface processes. I have also (inadvertently) characterized the impact of an overlying layer of frost or amorphous ice on the surface, as reported for Europa. The spectral reflectance signal is subdued and can alter the calculated composition of a planetary surface, including misclassification as amorphous-rich ice.

Based on available results, Hapke synthetic spectra for amorphous and crystalline water ice, generated using Mastrapa *et al*. (2008) optical constants, offer a reasonable approximation of the grain size dependence of absorption features in ~ 1.25-2.7 μm. They are recommended for interpretation of remote sensing observations of icy bodies, in the absence of laboratory spectra. The ISL group is attempting to provide this laboratory dataset over a broad wavelength range (1.25-8 μm) for thick, grain-size controlled samples with different formation temperatures and thermal histories. New laboratory end members for amorphous and crystalline ice have been calculated using both transmission and reflection spectroscopy. In Chapter 5, I will use these end members to reevaluate the surface crystallinity of Europa's leading hemisphere and estimate the surface age and environmental conditions required to reach its present state.

CHAPTER 5

A HISTORY OF EUROPA'S SURFACE ICE EVOLUTION: CONSTRAINING CRYSTALLINITY AND AGE

The results presented in the previous chapter provide a useful means of determining the crystallinity of a planetary surface, while also highlighting the complexity of assigning spectral feature variations to phase transitions and temperature or thickness or grain size effects. With these limitations in mind, I make extensive use of the 1.65/1.5 μm band area ratio technique to determine the surface crystallinity of Europa's leading hemisphere. This is key to understanding the role of physical processes such as thermal annealing and cryovolcanism in surface evolution, which is discussed here, and on the chemistry of the ocean. This calculated crystallinity is used to estimate a range of surface ages (and conditions) for Europa and reevaluate previous age estimates. Finally, the spatial crystallinity and timescales of evolution for the surface are coupled with our current understanding of the environmental conditions to propose a criterion for the selection of regions on interest on Europa.

5.1 Introduction

The ocean-bearing world, Europa, is one of NASA's key targets for exploration of habitable worlds (NASA 2014 SMD Science Plan; Pappalardo *et al*. 2017; Hand *et al*. 2017). One of the four Galilean moons of Jupiter discovered ~410 year ago, Europa likely

is a differentiated body with an iron (± sulfur) core, a silicate mantle, and an overlying H_2O subsurface ocean up to 100 km thick, with an icy crust (Carr *et al*., 1998; Pappalardo *et al*., 1999). The surface is predicted to be relatively young (40–90 Ma) (Zahnle *et al*. 2008; Pappalardo *et al*., 1999; Bierhaus *et al*., 2009), indicating recent geological activity with potential resurfacing within the last 200 Ma, and is characterized by a complex series of cracks and ridges that may link the surface to the ocean, a potential habitat (Chyba *et al*., 2001; Figueredo *et al*., 2003; Prockter *et al*., 2017; Howell and Papalardo, 2018). However, orbiting at a distance of 6.71 x 10^5 km (~ 9.38 R_J) from Jupiter, Europa's surface is subjected to Jupiter's magnetospheric radiation, bombarded with solar wind electrons, ions, and photons, and micrometeorite impacts and sputtering by energetic ions (O^{+n}, S^{+n}) from Io (Garrett *et al*., 2005, 2011; Moore and Hussmann, 2009; Cooper *et al*., 2001; Paranicas *et al*., 2009; Patterson *et al*., 2012; Nordheim *et al*., 2018), all of which can modify the extruded materials and affect the physical and chemical properties of the surface (Hudson and Moore 2001; Prockter *et al*. 2017). Table 5.1 lists some physical characteristics and predictions for Europa.

Relatively fine-grained water ice combined with hydrated materials is found on Europa's surface, with the subsurface liquid water ocean thought to influence the surface directly due to upwelling diapirs, plumes, other forms of cryovolcanic activity (Pappalardo *et al*., 1998; Collins and Nimmo, 2009; Roth *et al*., 2014), and tectonic resurfacing (Pappalardo *et al*., 1999; Greenberg *et al*., 2000; Figueredo and Greeley, 2004). The deposition of ice on the surface could occur due to a variety of surface-subsurface exchange processes, and once emplaced on the surface, it can undergo phase transitions, changes in

grain size and other physical properties, etc. Active processes affecting these changes are reviewed in Chapter 2.

Current crystallinity estimates of the surface range from ~27% to 95% (as detailed in Section 5.3), while grain size estimates vary from 5 μm to a few mm for the remotely sensed layer (Dalton *et al*., 2012, Shirley *et al*., 2010; Hansen and McCord, 2004; Prockter *et al*., 2017). Combined, these surface physical properties can be used as a tool to determine relative exposure age of observed materials.

Table 5.1: Characteristics of Europa

Parameter [Unit]	**Europa**
Mass [kg]	4.80×10^{22}
Equatorial Radius [km]	1560.8
Density [g/cm^3]	3.013
Surface Gravity [m/s^2]	1.315
Escape Velocity [km/h]	7.293×10^3
Semimajor Axis – Sun [AU]	5.2
Semimajor Axis – Parent Body [km]	6.711×10^5
Orbit Eccentricity	0.0101
Solar Orbital Period [y]	11.86
Rotational Period [Earth days]	3.55
Bond Albedo	0.68
Average Surface Temperature [K]	100
Predicted Age [Ga]	~ 4.5
Average Surface Age [Ma]	~ 60 Ma
Predominant Surface Material	H_2O
Predominant Surface Terrains	Ridged Plains (60%), Chaos (~ 40%)

Note. – Most values acquired from JPL Solar System Dynamics). Other references: Peale (1999); Bierhaus *et al*., 2009; Fanale *et al*., 2001

5.2 Europa's Surface Age – Previous Estimates

Europa has a heterogeneous ice shell with the presence of several distinct surface features, including ridged plains, young chaos terrain, impact craters, etc. (Doggett *et al*., 2009). Ridged plains are predicted to dominate ~60% of the surface, with the remaining 40% assigned to chaotic terrains (with ~18 to 22% fresh chaos) and non-icy materials (Greenberg *et al*., 1999; Fanale *et al*., 2000). Compared to its neighboring Galilean satellites, Europa is characterized by the relative scarcity of craters. There are approximately ~150 craters with diameter > 1 km, 16 complex craters with diameter between 3-27 km, and 6 craters with diameters > 30 km (Bierhaus *et al*., 2009). Unlike the Moon or Mars which are impacted by small asteroid populations, Jupiter-family comets are the chief source of these impact craters on Europa, with an impact rate lower than asteroid impact rates on the Moon (Bierhaus *et al.,* 2009 and references therein). This variation in impactor source and flux means that we cannot use the established lunar cratering record (or size-frequency distribution) to accurately estimate age in the outer solar system. The lack of a global survey at a high resolution and uniform illumination conditions (~11%) coupled with the limited detection of preserved impact craters on Europa, further complicates the estimation of surface age.

Over the past three decades, there have been several estimates of Europa's surface age. More recently, there is a consensus at ~60 Ma, with Zahnle *et al*. (2003) estimating a best-fit average age of ~30-70 Ma and Bierhaus *et al*. (2009) estimating ~40-90 Ma using crater size-frequency distributions, areal densities, and their spatial variation in context of (cometary) projectile infall rates. The difference in age arises due to a change in crater

counts after Beirhaus *et al*. (2009) further removed potential secondaries. As the crater count goes down, so does the age. The lack of constrains on the rate of comet impacts, which is best known to a factor of 3 on Europa, also increases the uncertainty in global average surface age to 20 to 200 Ma. As the flux goes down, the age goes up.

However, long-standing questions remain: (1) *Are the collected set of craters representative of the entire surface or only for the primary population captured in the Galileo swaths? (2) Why is the cratering density of the younger chaos regions higher than on ridged terrains?* In this section, I proceed with an attempt to address these questions by evaluating the role of chaos terrain and the spatial distribution of mapped impact craters. I also hope to provide a context within which our interpretations of surface age using derived crystallinity can be placed, including the uncertainties in current estimates of age and on surface conditions.

5.2.1 Limitations of Image Resolution and Chaos Crater Density

Chaos terrain on Europa is defined as a distinct region characterized by the presence of polygonal blocks of ridged plains within a matrix of hummocky material (Doggett *et al*., 2009 and references therein). They are assumed to be younger than ridged terrain owing to cross-cutting relationships (Pappalardo *et al*., 1999; Figueredo and Greeley 2004), with a cyclic transition between the two terrains. However, chaos terrain "*has a systematically higher density, and in two diameter bins this difference is factors of several greater than the error bars*" (Bierhaus *et al*., 2009), which implies older age. This is an unexplained discrepancy.

To unravel this, I present Europa's global crater maps (Figures 5.1 through 5.3), modified from Schenk and Turtle (2009) to include approximate spatial bounds for chaos terrain from Leonard *et al*. (2018) and imaging data resolution from Galileo and Voyager spacecrafts from Bierhaus *et al*. (2009). There are some minor issues in digitization of the cratering map, notably around the location of unidentified crater NN2, but the distribution is broadly representative of the location of craters on Europa.

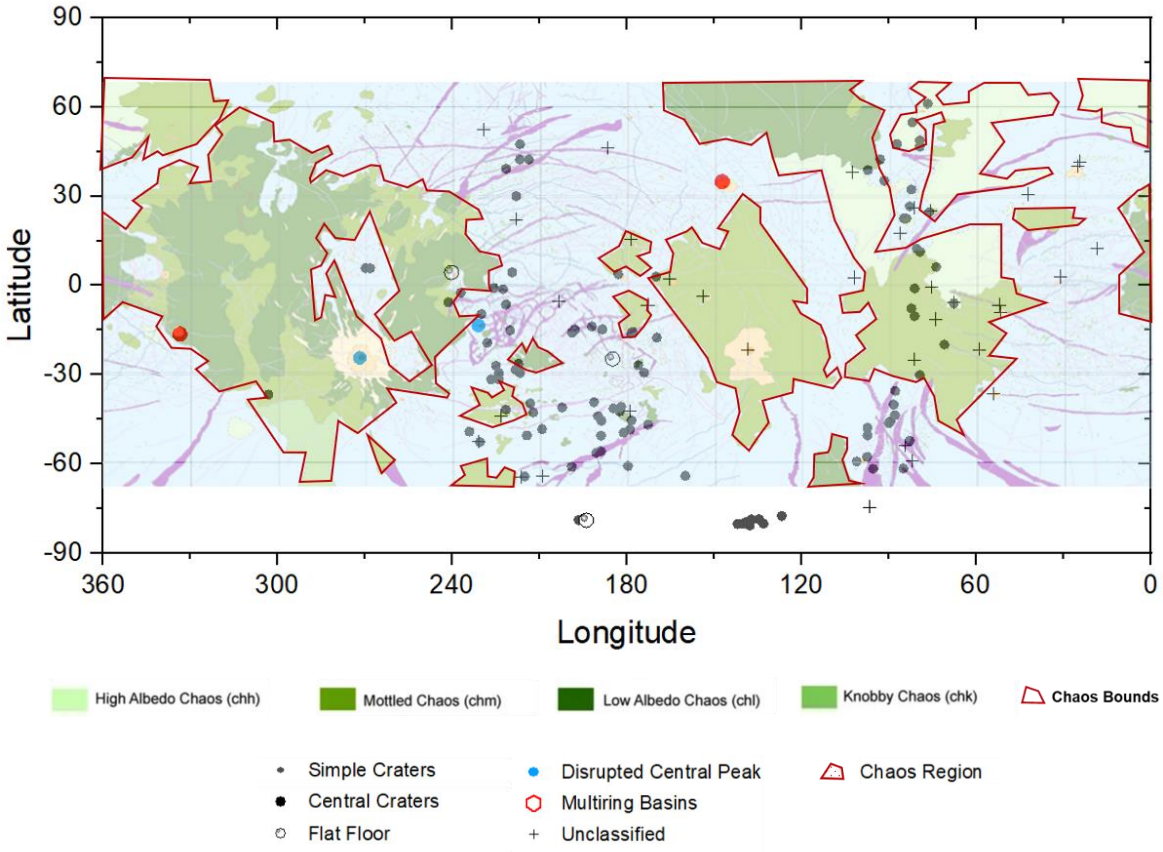

Figure 5.1: Global geologic map of Europa superimposed with approximate spatial bounds (in red) for chaos terrain distribution (in green), and craters greater than 1 km diameter. Map modified from Leonard *et al*. (2018).

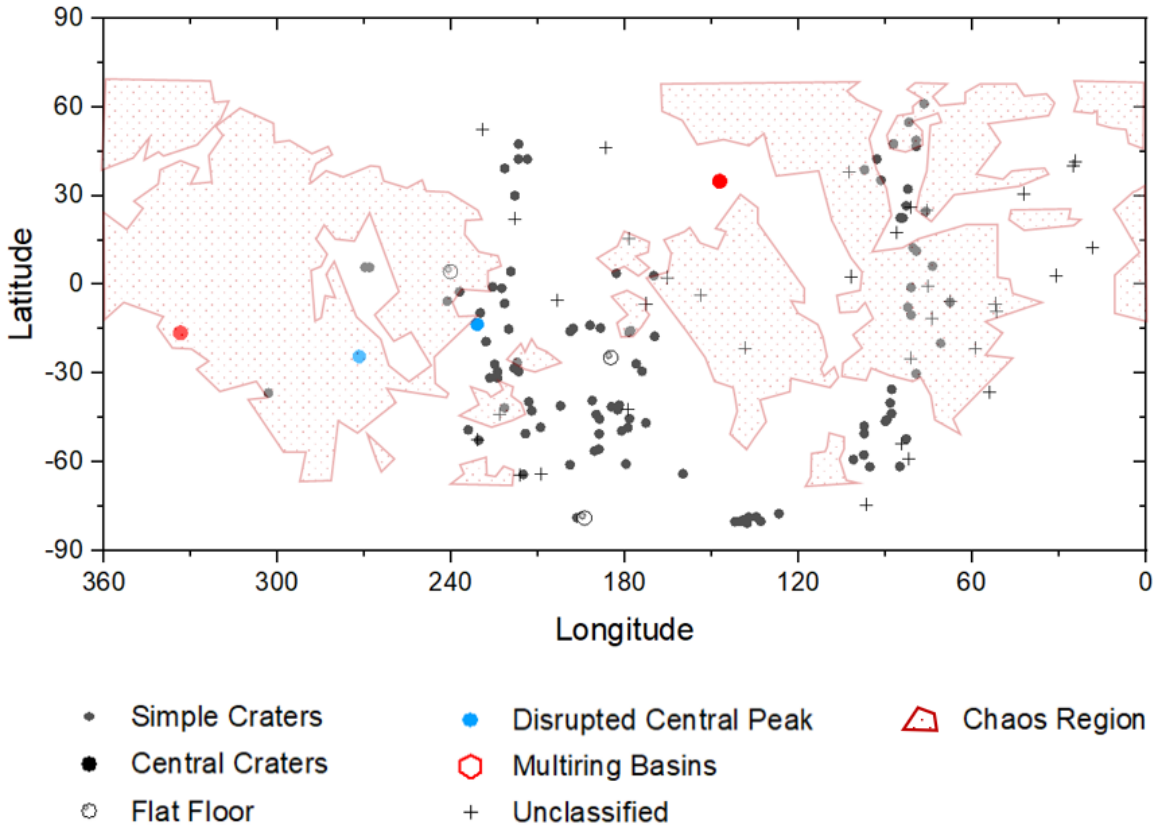

Figure 5.2: Global map of craters on Europa greater than 1 km diameter, overlaid with the approximate distribution of chaos terrain on Europa. Craters digitized from Schenk and Turtle (2009); approximate chaos terrain distribution from Leonard *et al*. (2018).

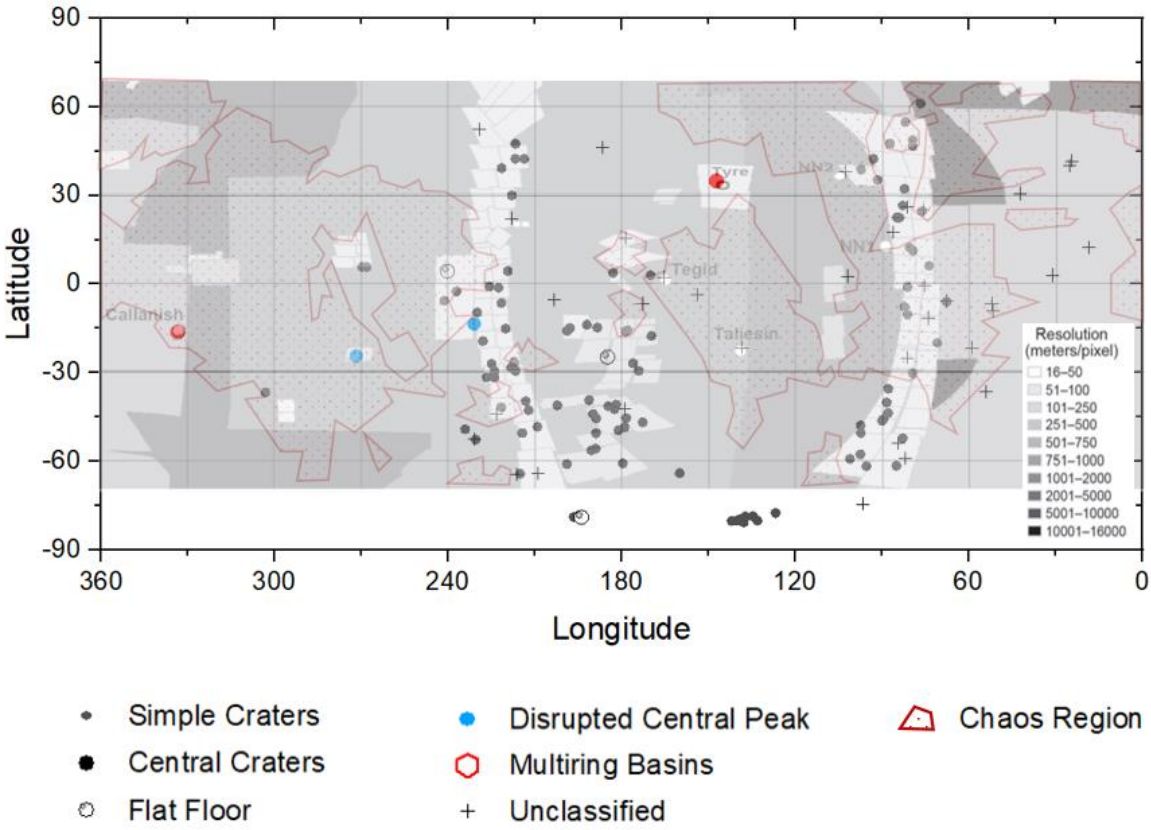

Figure 5.3: Global image resolution map of Europa with measurements from Galileo and Voyager, overlaid with craters greater than 1 km diameter and approximate bounds of chaos terrain. Map modified from Bierhaus *et al*. (2009).

An asymmetric hemispheric distribution of craters is observed, with most detections located within two zones covering the entire range of latitudes: between longitudes 60º to 120º on the leading hemisphere, and longitudes ~150º to 240º on the trailing hemisphere. A closer look at our image resolution map (see figure 5.3) reveals that most primary craters (D < 30 km; including single, flat floor, central peak, disrupted central peak or unclassified) lie within the two Galileo near pole-to-pole swaths of high-resolution regional coverage images (~230–450 meter/pixel) of Europa's leading and trailing hemispheres, acquired during orbits 15 and 17. Other primary craters detected near the

antijovian point are also correlated to the availability of high image resolution coverage. However, the location of craters with a larger diameter (D >30 km; including multiring basins) is not coincident with image resolution – they are primarily located between longitudes 100º and 170º, as noted by Bierhaus *et al*. (2009). This dichotomy suggests that the global detection of craters is a product of both image resolution coverage and crater diameter. The natural conclusion is that smaller diameter craters are easier to detect and classify with higher image resolution coverage, while larger diameter craters can still be detected at lower resolutions (due to multiple pixels spread).

Extending this analysis to chaos terrain, our global crater maps highlight the relatively negligible detection of craters on the trailing hemisphere, which is characterized by an abundance of mottled, low albedo or knobby chaos (Leonard *et al*., 2018). Most detections of primary craters (single, central peak and unclassified) in chaos terrain lie on the leading hemisphere between latitudes -30º to 15º and 50º to 60º, longitudes 45º to 75º. These detections again correspond to the Galileo higher image resolution swaths of <250 meters/pixel, increasing our confidence in the proposed conclusion. The two larger diameter craters in chaos terrain (Taliesin, NN2) lie in lower resolution coverage. Coupling the spatial distribution of chaos terrain and the expected projectile infall rates (more abundant in leading hemisphere), it is worth considering whether the limited areal coverage of high-resolution images in chaos terrain (more abundant in leading hemisphere) leads to a biased sample set of craters in ridged plains versus chaos features. This could explain the origin of higher crater density in chaos terrain as compared to ridged plains. It also offers an alternate explanation to the one proposed by Pappalardo *et al*. (1999), who suggest that the high density is an indicator of cyclic transitions between the two terrains, leading to

periodic global resurfacing. Detailed regional investigations of chaos terrain on Europa (including size distributions) are currently underway (Leonard *et al*., 2020; Mills, Leonard and Pappalardo *et al*., 2020), and future work will include extending the analysis presented in this section with a sensitivity test. I intend to constrain the relationship between spatial distribution of chaos and ridged terrain, their localized crater density, and available image resolution.

As I proceed with calculations of bulk crystallinity for Europa's leading hemisphere and its application to surface age estimates below, this section will serve to contextualize those estimates (Section 5.4, 5.5). Our results here support the need for a comprehensive global survey of Europa's surface at a uniformly high resolution to confidently detect all potential craters on the surface, irrespective of crater diameter (or crater degradation). It would be reasonable to extend our conclusions regarding image resolution coverage to a global scale, and expect the number of small, primary craters on Europa's surface to increase with the availability of higher resolution images. The Europa Imaging System (EIS) onboard the NASA Europa Clipper mission will globally map the surface at a resolution of ~50 meter/pixel (Turtle *et al*., 2016; Patterson *et al*., 2019), which should be sufficient to unravel the cratering record for Europa, including spatial distribution in chaos terrains versus ridged plains, and estimate the surface age.

Also, it is worth remembering that the average surface age does not represent the age (or crater surface density) everywhere. It is feasible that large sections of Europa's surface are older (or younger) than 60 Ma, and a spatial variation in the surface crater density may be observed for newly identified craters. This principle also holds for age estimates using crystallinity, as will be discussed in Section 5.5.

5.3 Observed versus Modeled Crystallinity of Europa

There have been several attempts to constrain approximate fractions of crystalline and amorphous water ice on Europa's surface. Hansen and McCord (2004) used the 1.65 μm band to determine the depth of transition from amorphous to crystalline ice on Europa. They suggested that at a depth of ~ 1 mm (i.e., depth probed by NIR observations) and deeper, water ice on Europa is predominantly crystalline, however nearly all the water ice above a depth of ~ 1 mm is amorphous. Ligier *et al*. (2016) produced crystalline and amorphous water ice maps from near-infrared (NIR) ground-based observations of Europa, using the Very Large Telescope, and suggested that the relative fraction of crystalline and amorphous water ice on the surface can elucidate the balance between crystallization due to thermal relaxation and amorphization due to particle bombardment. They found that crystalline water ice makes up ~ 40 − 55% of all material on the leading hemisphere, and the amorphous-to-crystalline water ice ratio is 0.57 globally (C = 64%).

Berdis *et al*. (2020) used ground based full-disk spectroscopic observations of Europa's leading hemisphere to determine surface crystallinity using two methodologies: (1) computation of amorphous ice fraction for a given radiation dose, surface temperature, and age of Europa's surface, and (2) the crystallinity calculation equation using one ground-based, full-disk, spectroscopic observation (B_{GBO}) at surface temperature of ~100 K, and two laboratory end member transmission spectra (integrated band area ratios of 100% pure crystalline and amorphous ice: B_{cryst} & B_{amorph}):

$$C = (B_{GBO} - B_{amorph}) \ / \ (B_{cryst} - B_{amorph}) \tag{5.1}$$

where C is the bulk crystallinity of Europa's leading hemisphere.

They found that their modeled crystallinity of 80-95% for Europa's leading hemisphere, incorporating only effects from thermal relaxation and ion particle bombardment, is significantly higher than their crystallinity ranges of 27-36% derived from ground-based observations and transmission spectra. This discrepancy may be a result of the processes mentioned in Chapter 2, Table 2.2**,** or it may arise from uncertainties in the crystallinity calculations. Using our results from Chapter 4, I reevaluate the crystallinity calculation for Europa using new laboratory end member spectra of crystalline and amorphous water ice samples with grain size of 25-53 μm, with a focus on identifying improvements enabled by our reflection spectra and explaining the discrepancies with modeled crystallinity.

5.4 New Crystallinity Calculation for Europa's Leading Hemisphere

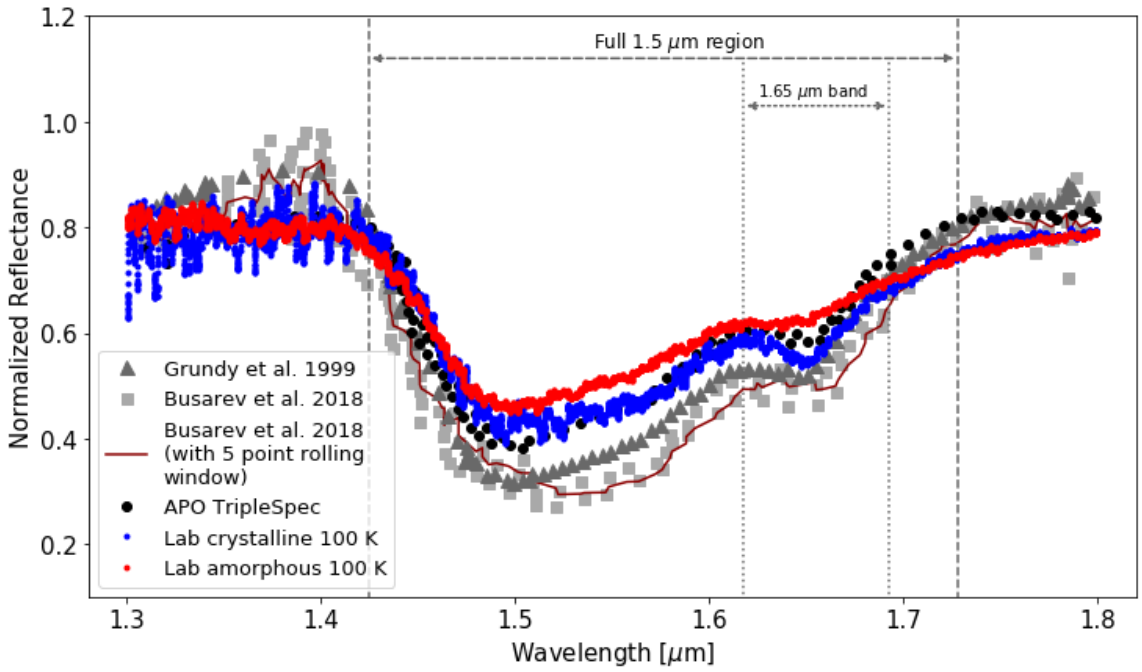

Figure 5.4: New ISL reflection spectra of amorphous (red) and crystalline water ice (blue) at 100 K (25-53 μm grain size from this work) are plotted over full-disk, ground-based reflection spectra in the full 1.5 μm region of Europa's leading hemisphere.

Determining the crystallinity of a planetary surface using existing laboratory end members of amorphous and crystalline ice films as "ground truth" can be problematic, in both spectral models and the crystallinity equation. As our Chapter 4 experiments indicate, the integrated band area (B) and calculated crystallinity depend on:

1. Detection Technique.
2. Formation temperature of the sample, temperature at which the data was collected, and its thermal history.
3. Sample Thickness.
4. Grain size of samples along with changes due to potential sintering.

All these factors have been shown to alter the shape and strength of the 1.65 μm and 1.5 μm absorption features of water ice and have been captured to a limited extent in previous datasets. Using the new ISL lab reflection spectra and end members of water ice, which capture the effects of these factors, allows us to re-interpret the crystallinity of Europa's leading hemisphere. ISL laboratory reflection spectra end members for 100% crystalline (B_{cryst} = 0.0529) and amorphous ice (B_{amorph} = 0.0166) are plugged into equation (5.1) concurrently with three ground-based, full-disk, spectroscopic observations of Europa's leading hemisphere from Grundy *et al*. (1999), Busarev *et al*. (2018) 5-point moving window, and Berdis *et al*. (2020). Figure 5.4 highlights the ISL laboratory spectra of amorphous and crystalline water ice along with the three ground-based observations in the 1.3 – 1.8 μm region. Acquisition details of the ground-based observations and calculation of integrated band area ratios (B) are included in Berdis *et al*. (2020), and briefly summarized here.

Grundy *et al*. (1999) observations were obtained using the OSIRIS spectrometer on the Lowell Observatory 1.8 m Perkins telescope. The ASTRONIRCAM spectrograph on the Caucasian Mountain Observatory 2.5 m telescope was used for the Busarev *et al*. (2018) observations; for this analysis, they are smoothed with a 5-point moving window average to overcome the lower signal-to-noise ratio. Berdis *et al*., 2020 collected NIR observations with the TripleSpec instrument on the Astrophysical Research Consortium (ARC) 3.5 m telescope at Apache Point Observatory (APO).

Table 5.2 highlights the results of the bulk crystallinity calculation. Calculated crystallinity for Europa's leading hemisphere increases from the previously estimated 27-36% (using transmission spectra) to values of 46-52% with the new end members

(reflection spectra). Our calculated range of 46-52% lies within the crystallinity range of 40-60% derived from Ligier *et al*. (2016)'s NIR spectral maps of Europa's leading hemisphere. The recalculated Mastrapa *et al*. (2008) end members (B_{cryst} = 0.0669 and B_{amorph} = 0.0157) for the integration boundaries of 1.5 and 1.65 μm regions identified in Chapter 4, Section 4.2.2, are used to determine a crystallinity range of 35-38%. This range is more consistent with the 34-36% crystallinity derived by Berdis *et al*. (2020) for 2010 ISL transmission data. There is thus a discrepancy between the crystallinity calculated with transmission spectra (range of 34-38%) and reflection spectra (range of 46-52%). It implies a dependence of the integrated band area (B) and crystallinity calculations on detection technique. The reflection spectroscopy technique employed in this work should offer a more accurate comparison to planetary surface observations, and the consistency with spectral mixing results increases our confidence. There are however uncertainties associated with these calculations, which are addressed in the next section.

Table 5.2: Observed vs Modeled Global Crystallinity of Europa' s Leading Hemisphere

Crystallinity / Lab Dataset	Grundy *et al*., 1999 B_{GBO} = 0.0336	Busarev *et al*., 2018 (5-point window) B_{GBO} = 0.0353	TripleSpec Berdis *et al*., 2020 B_{GBO} = 0.035	Ligier *et al*., 2016 Spectral Modeling	Berdis *et al*., 2020 Thermophysical Modeling
Mastrapa *et al*. 2008 (Recalibrated in blue) B_{cryst} 0.0741, 0.0669 B_{amorph} 0.0182, 0.0157	27.5% 34.9%	30.5% 38.3%	30.1% 37.7%	40-60%	80-95%
Berdis *et al*., 2020 B_{cryst} = 0.0715 B_{amorph} = 0.0144	33.6%	36.6%	36.1%		
Ice Spectroscopy Lab (This work) B_{cryst} = 0.0529 B_{amorph} = 0.0166	**46.8%**	**51.5%**	**50.7%**		

5.4.1 Uncertainties in Crystallinity Estimates:

There are three primary sources of uncertainties in the crystallinity estimates:

1. ISL laboratory end members for 100% amorphous and crystalline ice used in the crystallinity equation (5.1) are assumed to be pure phases. These assumptions are based on the formation temperature and expected phase transitions over the thermal history of the sample. For example, an ice sample heated to 150 K is assumed to undergo a phase change to pure crystalline ice, and the crystalline end member is chosen after cooling back to 100 K. If there is any mixing of phases, then the band area inputs into the equation will change, resulting in different estimates of crystallinity.
2. Difference in acquisition methods and grain size: the error bars calculated for laboratory transmission spectra are ~10% in Mastrapa *et al*. (2008) due to sample thickness, and 10–20% in the 2010 ISL work due to interference wave patterns in the spectra. Both are addressed in the ISL reflection spectra (this work). An ISL sample with grain size of 25-53 μm (representative of small sized grains on Europa) was selected in this work for crystallinity calculation. Other grain size measurements are available and will be used in a future study to provide a comprehensive understanding of the role of grain size in crystallinity.
3. Ground Based Observations have an uncertainty smaller than the size of data points in the spectra, on the order of 10^{-6} to 10^{-7}% of the measured reflectance. However, a good SNR is needed as unsmoothed Busarev *et al*. (2018) observations (with low

SNR) are calculated to have a crystallinity of ~65-71% which is twice the crystallinity calculated with the 5-point moving average.

4. Additional Processes: contributions of micrometeorite annealing, and geophysical processes are not included in the crystallinity calculation with Equation 5.2 or in thermophysical modeling. Berdis *et al*. (2020) modeled the contribution of plumes to be less than 1% to crystallinity, but other processes such as cryovolcanism or upwelling diapirs causing localized heating are yet to be studied, and their contribution cannot be quantified as of now. The high modeled crystallinity of 80-95% is difficult to reconcile with our calculations (or even with spectral unmixing results), and points towards the need to include additional resurfacing processes which are yet to be characterized.

5.5 New Estimates for Age of Europa's Leading Hemisphere and Predictions for Surface Conditions

Europa's surface age can be calculated with the alternate approach of using the calculated bulk crystallinity of the surface. The crystallinity percentage has been used in the past to determine the approximate age of surfaces in the outer solar system, to first approximation, using the equation established by Fama *et al*. (2010). This age estimate is based on the measured rate of ice phase transformation under various environmental conditions:

$$1\text{-}C = \Phi_{Amax} (1 - \exp [-kFt / N]) \quad (5.2)$$

Dalle Ore *et al*. (2015) used this equation to determine the approximate ages of two craters on Saturn's moon Rhea (between 320 and 560 Ma). I have similarly computed the approximate age of Europa's leading hemisphere (with its higher crater density) by applying Equation 5.2 with a range of crystallinity percentages (C) calculated in the previous section. Other equation inputs were derived either from the methodology of Berdis *et al*. (2020) and Dalle Ore *et al*. (2015) (adapted from Fama *et al*., 2010 and Baragiola *et al*., 2013), or from recent literature. Table 5.3 lists the parameter values used and their references.

Any determination of age requires tight constraints on surface conditions, which are captured in the equation parameters. There are, of course, uncertainties in these parameters for Europa but reasonable estimates can be derived for all of them. I have also

attempted to include a broad range of parameter values to capture different regions on the surface (equatorial versus polar), and determined the conditions required to meet the current ~ 60 Ma age estimate.

A maximum amorphous fraction, Φ_{Amax}, of 0.9 to 1.0 was used (Dalle Ore *et al*., 2015). The fitting parameter, k, based on water ice irradiation temperatures at 70 to 100 K was initially selected in the range of ~ 0.07 to 0.12 (Fama *et al*., 2010, Fig. 1; Baragiola *et al*., 2013, Fig. 16.3), following the methodology of Berdis *et al*. (2020). Here, I included additional k values for Europa's surface temperatures (60-110 K, including equatorial and polar regions) to extend the range to 0.01 – 0.20. Details are provided in Table 5.4.

Particle flux, F, of 2.55 x 10^7 cm^{-2} s^{-1} (from Table 2 of Cooper *et al*., 2001) was calculated by adding the total number of protons (1.5 x 10^7 cm^{-2} s^{-1}), oxygen ions (1.5 x 10^6 cm^{-2} s^{-1}), and sulfur ions (9.0 x 10^6 cm^{-2} s^{-1}) that impact on the surface and potentially induce amorphization (Mastrapa, 2008). While the energetic electron radiation dose constitutes >75% of the incident irradiation energy on Europa (Nordheim *et al*., 2018), proton and ion impacts on Europa are expected to sputter the icy surface more efficiently than electrons (at the few μm – mm depths), and they can significantly alter surface ice morphology and grain size. Hence, they are the only particles considered in this calculation. Nordheim *et al*. (2018)'s calculated flux of protons at Europa is also considered for this work, by integrating the area under the curve: 3.15 x 10^6 cm^{-2} s^{-1} sr^{-1} or 3.96 x 10^7 cm^{-2} s^{-1} (Figure 5.6). Both the Cooper *et al*. (2001) and Nordheim *et al*. (2018) fluxes were calculated at Europa's approximate distance from Jupiter, and all protons are assumed to reach Europa's surface. Johnson *et al*. (1988) demonstrated that the trailing hemisphere receives 5 - 15 times more ion flux (calculated here as 1.05 x 10^7 cm^{-2} s^{-1}) than the leading

hemisphere (i.e., in the range of 7 x 10^5 cm^{-2} s^{-1} to 2.1 x 10^6 cm^{-2} s^{-1}). The F values selected here thus represent upper limits for the leading hemisphere.

The number of H_2O molecules, N, of 1.60 x 10^{19} to 9.4 x 10^{19} housed within 1 cm^2 cross-section, and 5 to 30 μm vertical penetration depth was used. These depths are chosen based on the approximate penetration of 1 MeV oxygen and sulfur ions, and 1 MeV protons respectively (Cheng *et al*., 1986).

Table 5.3: Time Equation (Eqn. 5.2) Variables.

Parameter	Description	Value	Reference
t	Age of the Surface (Exposure time)	Seeking	
C	Crystalline fraction	0.3, 0.468, 0.515	This work
Φ_{Amax}	Maximum amorphous fraction	0.9 – 1	1
F	Irradiation flux	2.55 x 10^7 cm^{-2} s^{-1} 3.96 x 10^7 cm^{-2} s^{-1}	2
N	Number of H_2O molecules in volume V; for V = 5 – 30 μm x 1 cm x 1 cm	1.6 – 9.4 x 10^{19} # molecules	3
k	Fitting parameter dependent on temperature	~ 0.01 – 0.02	2

[1]Dalle Ore *et al*., 2015

[2]Cooper *et al*., 2001; Nordheim *et al*., 2018

[3]Cheng *et al*., 1986

[4]Fama *et al*., 2010; Baragiola *et al*., 2013; Fig. 16.3

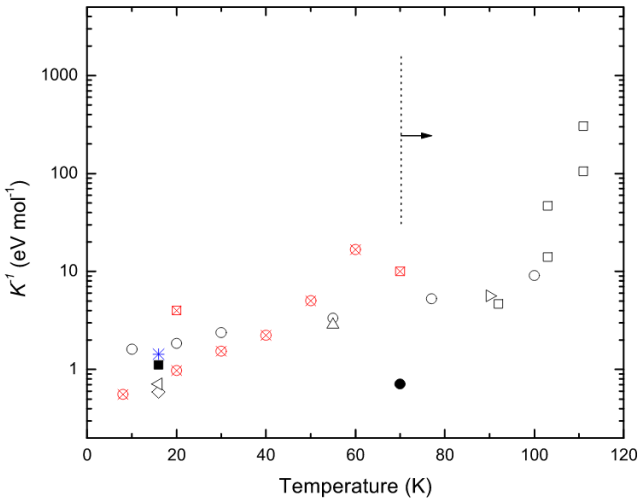

k	Temperature (K)
0.01	110
0.022	100
0.07	100
0.12	100
0.20	90
0.20	80
0.09 (e^-)	60

Figure 5.5, Table 5.4: Fitting parameter (k) vs temperature plot for 100 keV protons from Fama *et al*., 2010, used to populate table for relevant temperature conditions on Europa.

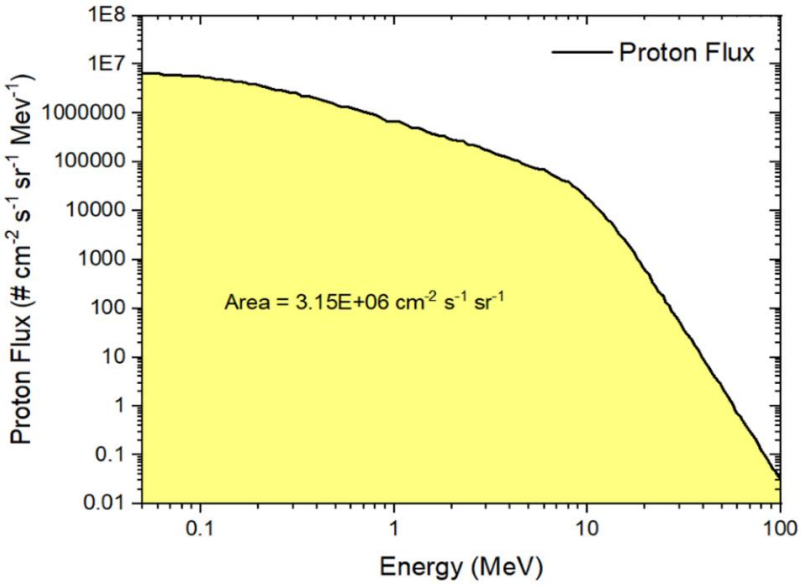

Figure 5.6: Representative proton flux distribution and calculated area (or dose) at Europa for the leading hemisphere, modified from Nordheim *et al*. 2018 Figure 2.

Assuming a surface temperature of 100 K, I initially obtained an age of ~1.5 Ma, which is significantly younger than previous estimates of ~ 60 Ma (Bierhaus *et al*., 2009), and hard to reconcile with the geologic record. Repeating our calculating after adjusting the fraction of maximum amorphous ice to 1.0, I obtain an age of ~1.27 Ma. Assuming slightly different values of k (0.12 to 0.01), an estimated age range of 0.5 to 10.5 Ma is obtained; this change indicates that surface temperature (or k value) has a strong contribution to the age estimate, with 110 K providing a better fit with the cratering age. With that in mind, I used k-values for 110 K for the next set of calculations. When the depth of penetration was changed to 5 μm (N = 1.60 x 10^{19} molecules) instead of 30 μm, the resulting age estimate drops to 1.78 Ma. Using Nordheim *et al*. (2019) flux values, I obtain an age estimate of ~6.7 Ma. When the Cooper *et al*. (2001) particle flux was changed by a factor of ±5 and ±10, the surface age range extended significantly from ~1 Ma to 104 Ma, with maximum age obtained at lowest particle flux. Using crystallinity values from transmission spectra of Mastrapa *et al*. (2008) (~ 0.3), an age range of 8.7 to 17.5 Ma is obtained, while decreasing the particle flux by a factor of 10, increases the range to 87 – 175 Ma. Inputs corresponding to all determined surface ages are highlighted in Table 5.5.

Surface temperature and particle flux are thus identified as two equation parameters significantly affecting the age estimate, which is theoretically supported by our understanding of thermal annealing and charged particle bombardment. This finding increases our confidence in the applicability of the Fama *et al*. (2010) equation to age calculations, but the conditions required to match cratering age estimates is concerning.

Table 5.5: Estimates of Surface Age for Europa based on different surface conditions captured in equation parameters. Green represents the cratering age estimates; red represents youngest calculated age.

C	k	Φ_{Amax}	F	N	Time (Ma)
Crystallinity = 0.468 & 0.515					
0.468	0.07	0.9	2.55×10^{7}	9.40×10^{19}	**1.49**
0.515	0.12	1	2.55×10^{7}	1.60×10^{19}	**0.11**
Fraction of Max. Amorphous Ice = 1					
0.468	0.07	1	2.55×10^{7}	9.40×10^{19}	**1.27**
k = 0.01 & 0.022 (T = 110 K), 0.12 (T = 100 K), 0.20 (T = 90 K)					
0.468	0.01	0.9	2.55×10^{7}	9.40×10^{19}	**10.45**
0.468	0.022	0.9	2.55×10^{7}	9.40×10^{19}	**4.75**
0.468	0.12	0.9	2.55×10^{7}	9.40×10^{19}	**0.87**
0.468	0.20	0.9	2.55×10^{7}	9.40×10^{19}	**0.52**
Subsequent calculations use a surface temperature of 110 K *(k = 0.01 or 0.022)*					
Penetration Depth = 5 μm (N = 1.60×10^{19})					
0.468	0.01	0.9	2.55×10^{7}	1.60×10^{19}	**1.78**
Particle Flux = 2.55×10^{6}, 2.55×10^{8}, 5.10×10^{6} (± factor of 10, - factor of 5) 3.96×10^{7} [Nordheim et al. 2018]					
0.468	0.01	0.9	2.55×10^{6}	9.40×10^{19}	**104.54**
0.468	0.01	0.9	2.55×10^{8}	9.40×10^{19}	**1.05**
0.468	0.01	0.9	5.10×10^{8}	9.40×10^{19}	**52.27**
0.468	0.01	0.9	3.96×10^{7}	9.40×10^{19}	**6.73**
Age Estimate of 40-90 Ma					
0.468	0.022	0.9	2.55×10^{6}	9.40×10^{19}	**47.52**
0.515	0.01	0.9	5.10×10^{6}	9.40×10^{19}	**45.24**
0.468	0.01	0.9	7.92×10^{6}	9.40×10^{19}	**33.66**
Using Mastrapa et al. 2008 Crystallinity					
0.3	0.01	0.9	5.10×10^{6}	9.40×10^{19}	**87.91**

The age range of **~ 40 Ma to 90 Ma** can be obtained for our range of surface crystallinity values (46.8 to 51.5%) under the environmental conditions described below. I have also included scenarios where such conditions may be feasible on the surface:

1. Surface temperature of 110 K (with k values of 0.01 to 0.22) – *lower k value from higher temperature leads to higher age.*
    - There are multiple locations on Europa, especially in the equatorial region which are predicted to reach a surface temperature in the range of 110-130 K during a Europan day (See Figure 5.7) (Spencer *et al*., 1999; Rathbun *et al*., 2010; Ashkenazy 2019).
    - The minimum detectable temperature of a 100 km^2 hotspot in Galileo Photopolarimeter-Radiometer datasets range from 116 K to 1200 K, depending on location (Rathbun *et al*., 2010). It is likely that undetected hotspots may be present on Europa's surface which contribute to spatial changes in crystallinity (and changes in fitting parameter for the age equation). The Europa Clipper Europa Thermal Emission Imaging System (E-THEMIS; Richey *et al*., 2018) should enable the detection of these hotspots and provide tight constraints on surface temperature.
2. Particle flux is lowered by a factor of 5 or 10, which is feasible for Europa's leading hemisphere (Johnson *et al*., 1988) – *lower the flux, higher the age.*
    - Cooper *et al*. (2001) flux lowered by a factor of 5 or 10
      ($F = 2.55 \times 10^6$ to 5.10×10^6 cm^{-2} s^{-1})
    - Nordheim *et al*. (2018) flux lowered by at least a factor of 5
      ($F = 7.92 \times 10^6$ cm^{-2} s^{-1})

3. Amorphous ice fraction of 0.9 to 1.0 – *higher the fraction, lower the age.*
4. Penetration depth of 30 μm (assuming a large fraction of high energy protons impact the surface) – *higher the depth, higher the age.*
5. Crystallinity (0.3 to 0.6) is naturally an important parameter for age estimates – *higher the crystallinity, lower the age* (C of 0.9 has an age < 0.6 Ma, while C of 0.11 has an age of ~260 Ma).

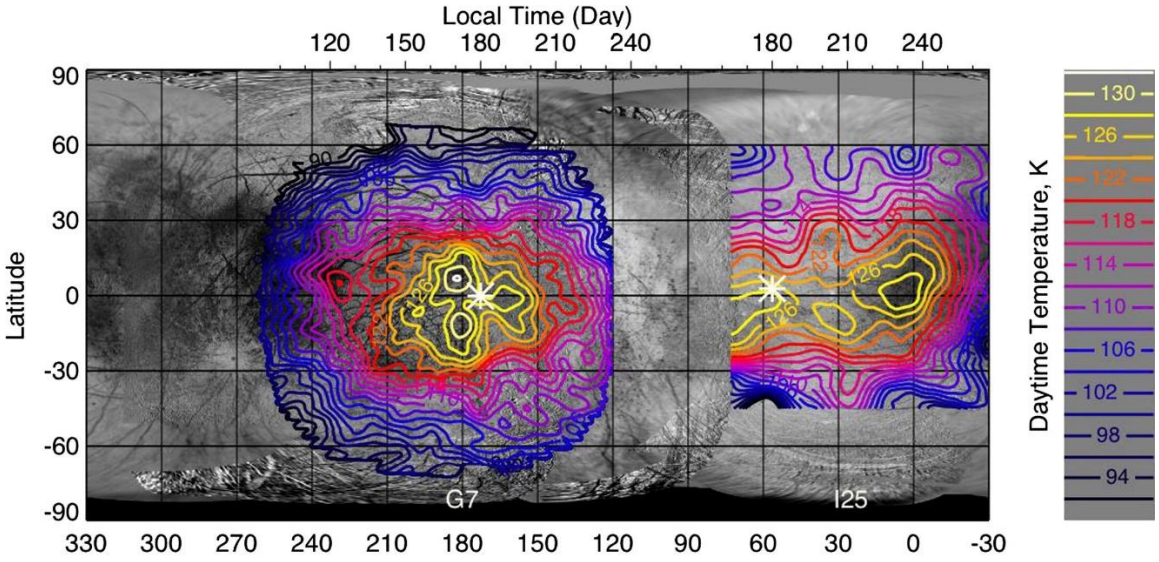

Figure 5.7: Daytime temperatures on Europa from composites of Galileo PPR datasets. Image modified from Rathbun *et al*. (2010).

As mentioned above, our determined age range is younger than predictions for Europa's surface, unless the surface parameters are modified with reasonable estimates. Here, alternate explanations are considered for this discrepancy:

1. Our laboratory reflectance dataset does not take into consideration the role of charged particle bombardment in evolution of integrated band area ratios (B). Hence, while these new measurements have accounted for some of the discrepancy between calculated crystallinity of 46-52%, spectral modeled crystallinity of 40-60%, and thermophysical modeled crystallinity of 80-95% (~10% closer than transmission data), irradiated laboratory spectra may further address this discrepancy. This in turn will alter the surface age further.
2. Recalibration of Mastrapa *et al*. (2008) laboratory end members to fit our reflectance data boundaries can lower confidence in the calculated B values, and subsequent crystallinity and age values. However, existing calculations of crystallinity (~27.5 to 37%) from transmission data put the surface age using this equation in the range of ~2.01 to 2.7 Ma (using the original set of surface parameters)**.** Clearly, there is a significant disconnect between the age estimates from the cratering density and the crystallinity calculation, which cannot be addressed without tighter constraints on the environmental conditions captured in the parameters.
3. Phase angle of the measurements can also have an impact on the band shape and integrated band area of the spectra. The laboratory reflection spectra were collected at 70º phase angle while the full disk observations are at 0º phase angle.
4. The leading hemisphere is mostly sheltered from high flux of charged particle bombardment, particularly at high latitude, and we expect the particle flux to be lower

than the trailing hemisphere. I have made estimates of a lower flux in our calculations, but there is a need for spacecraft measurements of particle flux on each hemisphere and estimates of the spatial evolution of flux over time.

5. The penetration depth of protons and ions (or electrons) is not well constrained at the expected energies on Europa. While reasonable estimates can be made, a more comprehensive understanding of their behavior is needed through cryogenic laboratory experiments on thick ice samples at relevant energies (up to 100 MeV).
6. As mentioned in the previous section, Europa's calculated surface age of ~ 60 Ma (Zahnle *et al*., 2003; Schenk *et al*., 2015) is encumbered by the lack of a global survey at a uniform image resolution. We expect the cratering record and estimated age to change with new measurements from Europa Clipper.
7. Potential localized resurfacing of Europa's surface coupled with spatial crystallinity variations could explain a younger age for the surface. It is unfeasible for us to use the full disk data to evaluate this claim – there is a need for a future study focused on unraveling the crystallinity and age of specific regions of interest on Europa. This will be one of the major goals of future study.

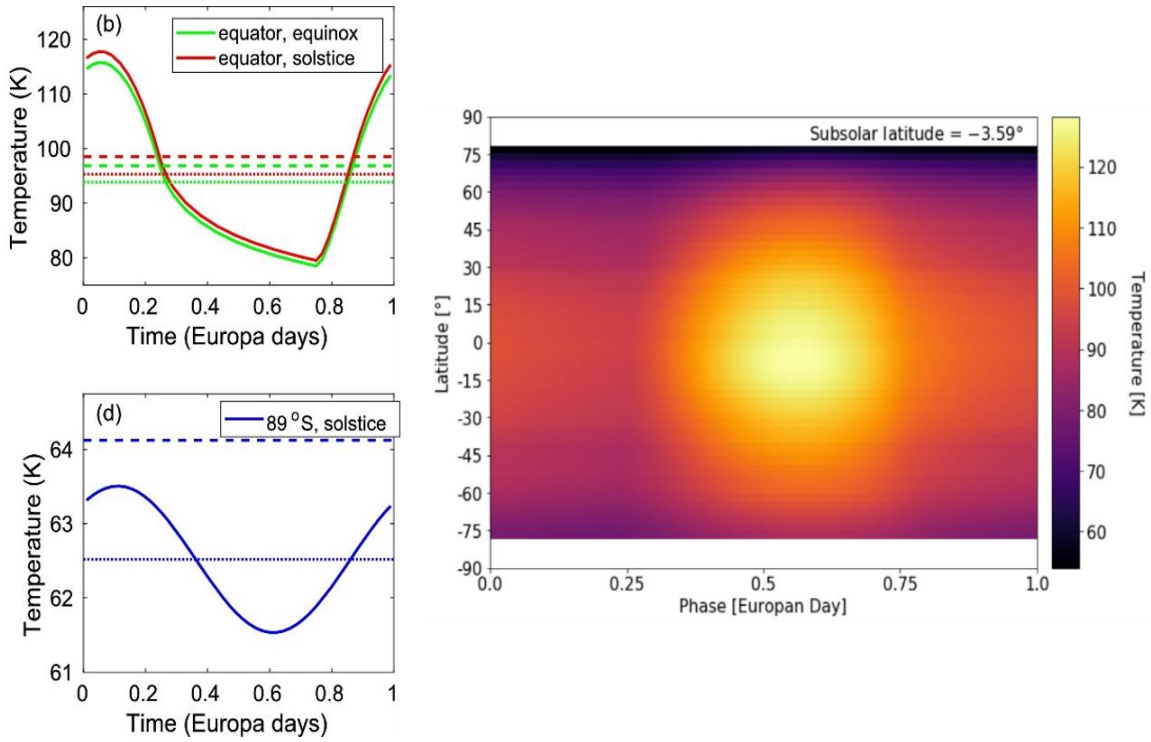

Figure 5.8: Simulated surface temperature variation for equatorial and polar regions on Europa during a phase day (modified from Ashkenay 2019 and Berdis *et al*. 2020).

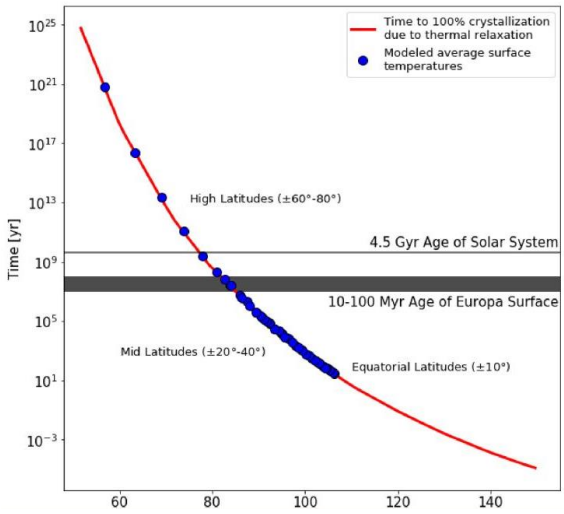

Temperature	Time to 100% C
60 K	> 4.5 Ga
80 K	10-100 Ma
110 K	10 years
120 K	0.1 years
130 K	~8 hours
150 K	~few minutes

Figure 5.9, Table 5.6: Temperature dependent annealing timescales of amorphous ice to 100% crystalline water ice are captured for various temperatures on Europa's surface. Image from Berdis *et al*. (2020).

5.6 Proposed Surface Evolution of Europa and Spatial Crystallinity

Europa's leading hemisphere has been predicted to have more amorphous than crystalline water ice in the top 1 mm layer (Hansen and McCord, 2004). Our work suggests equal proportions as a full-disk average (46-52%, Table 5.2), similar to global estimates of Ganymede. Spatial variations in the abundance of crystalline and amorphous water ice are, however, expected due to changes in particle flux and thermal history with location, and due to contributions from other temporal resurfacing processes. A broad global pattern of more amorphous ice in the high-latitudes to polar regions, and more crystalline ice in equatorial to mid-latitude regions is predicted for Europa, as detailed below.

Thermal Annealing: The surface temperature of Europa is estimated to lie in the range of ~ 60 K in polar regions to 132 K in equatorial regions (Spencer *et al*., 1999; Rathbun *et al*., 2010; Ashkenazy 2019). However, with diurnal shifts in temperature as much as 40 K at the equator (Figure 5.8), water ice lying in Europa's equatorial to mid-latitude regions is expected to undergo the thermal annealing and equilibration processes performed in our laboratory experiments (Chapter 4). Kouchi *et al*. (1994) estimated the time needed for amorphous ice to fully crystallize due to thermal relaxation, which combined with one-dimensional thermophysical modeling of spatially dependent average surface temperatures on Europa (Berdis *et al*., 2020) provides us with transition timescales of the order of a few minutes at 150 K to a few hours at 130 K to ~1000 years at 100K (Figure 5.9, Table 5.6). Therefore, most of the water ice deposited within these temperature zones on Europa is expected to undergo a phase transition to 100% crystalline ice. Further, sublimation loss of H_2O in these regions is estimated to be at a rate of 1 μm yr^{-1} to 1 mm

yr^{-1} (the top amorphous ice layer) (Fagents *et al*., 2000), which could expose any underlying crystalline ice (Hansen and McCord, 2004). As a side note, the timescale of a few minutes at 150 K (replicated in the lab procedure) increases our confidence in phase transition predictions and selection of pure end members for FI, MI, and MI Overnight samples on heating (Chapter 4). For polar regions, the time required for 100% crystallization is of the order of the age of the solar system (> 4.5 Ga), and most of the amorphous ice is expected to survive with minimal spatial variation in crystallinity. This is consistent with recent spectral unmixing results which find that the mean crystallinity of Europa's south pole 17e009 Galileo NIMS cube was 15% (Berdis, 2021).

Crystallinity estimates based on temperature are thus latitude dependent. At steady state conditions, the calculated crystallinity range of 46-52% for Europa's leading hemisphere should include contributions from mostly crystalline ice at equatorial regions (close to 100%), and mostly amorphous ice at polar regions. Any temporal variations in crystallinity would arise due to present day geophysical processes such as cryovolcanism or depositions of plume materials on the surface.

Radiation Effects: Estimates based off thermal annealing are complicated by spatial considerations of the role of magnetospheric particle bombardment on Europa. Operating at competing timescales of ~0.6-600 years (Table 5.7), crystalline water ice is expected to convert to amorphous ice (or at least, the formation of ice with spectra similar to amorphous ice post irradiation) (Mastrapa 2008). Nordheim *et al*. (2018) calculated that the leading hemisphere receives high-energy electrons (20 – 100 MeV, rising to 40 – 100 MeV at latitudes >35°) and protons, but far less flux than the trailing hemisphere. For the equatorial leading hemisphere, the low flux-high energy bombardment would result in a

higher crystallinity than the trailing hemisphere. As captured in amorphization timescales calculation (Equation 5.3), crystallinity decreases with time due to magnetospheric particle interactions, taking 0.6 to 600 years for 100% transition to amorphous ice on Europa.

Figure 5.10, Table 5.7: Radiation dependent amorphization timescales of crystalline ice to 100% amorphous water ice are captured for various ion fluxes on Europa's surface (Nordheim *et al*., 2018), using equation 5.3 (from Fama *et al*., 2010). Image). Image of Europa's leading hemisphere electron cutoff energies from Nordheim *et al*. (2018).

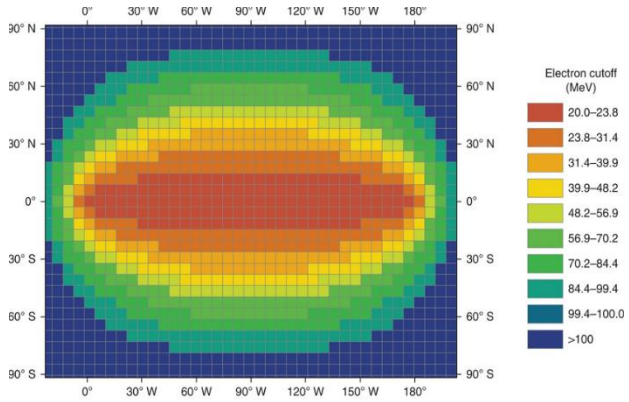

Ion Flux [$cm^{-2}\ s^{-1}$]	**Time to 100% A** [years]
10^4	634
7×10^5	9.06
2.1×10^6	3.02
1.05×10^7	0.61

$$T_{amorph} = \frac{1}{\Phi\ \sigma_A} \qquad (5.3)$$

where, Φ is the ion flux, σ_A is the amorphization cross-section, and $\Phi\sigma_A$ represents an average, over the ion type and energy distribution. Values selected here are $\sigma_A = 5 \times 10^{-15}\ cm^2$, and range of Φ cover ion fluxes at Europa's leading ($10^4\ cm^{-2}\ s^{-1}$, $7 \times 10^5\ cm^{-2}\ s^{-1}$ to $2.1 \times 10^6\ cm^{-2}\ s^{-1}$) and trailing hemispheres ($1.05 \times 10^7\ cm^{-2}\ s^{-1}$), from Fama *et al*. (2010) and estimates from Johnson *et al*. (1988).

For the leading hemisphere, these timescales are closer to 3-9 years (Table 5.7), which is comparable to thermal annealing timescales (0.1-10 years) at temperatures between 110-120 K, and lower than annealing timescales at temperatures below 110 K

(e.g., ~ 500 years to 10 Ma). Thermal annealing would try to convert amorphized ice back to crystalline ice in the equatorial regions, however radiation induced amorphization is expected to be the more dominant process based on current estimates of temperature, particle flux, and timescales. Beyond 120 K – which equatorial surface regions are predicted to reach during the diurnal cycle – thermal annealing should occur within ~0.1 years, so any % amorphized ice due to radiation is expected to convert back to 100% crystalline water ice. Combining thermal annealing and charged particle bombardment, equatorial to mid-latitude regions should maintain an abundance of crystalline ice on the surface for regions with temperature greater than 120 K, while a mixture of ices dominated by amorphous water ice would exist at lower temperatures.

The high-latitude (>65°) leading hemisphere region with mostly amorphous ice is dominated by high-energy protons resulting in the most benign radiation environment. If a source of crystalline ice is identified (via cryovolcanism, localized hotspots, micrometeorite annealing, etc.), a gradual decrease in crystallinity would be expected with time, further increasing the amorphous ice content. Overall, polar regions with the higher amorphous ice content, colder surface temperatures (high k values), are estimated to be comparable in age (using Equation 5.2) to equatorial regions with high crystalline ice content and warmer temperatures. The equation, however, cannot differentiate between new deposits of amorphous or crystalline ice which are yet to undergo phase transitions (via annealing or irradiation) and old deposits which remain the same due to environmental conditions. This is problematic, and age equation estimates thus need to be supplemented with estimates of physical and chemical properties, as discussed in Section 5.7.

Combining the contributions of both thermal annealing and radiation-induced amorphization, we expect a global pattern of mostly amorphous water ice in the polar regions, and a mixture of amorphous and crystalline ice phases at equatorial to mid-latitude regions, which result in a bulk crystallinity of ~47-52% on Europa's leading hemisphere. Spatial variations in crystallinity are expected due to changes in temperature and thermal history of the ice, particle flux, and the role of localized resurfacing.

Resurfacing Processes: Additional processes such as plume deposition and quenching of the ice need to be considered for a comprehensive understanding of the evolution on ice on Europa, despite poor constraints on their behavior. First, the migration of amorphous plume materials has been evaluated (Kouchi *et al*., 1994; Hansen and McCord 2004, Berdis *et al*., 2020). Formation of an overlying layer of frost, as observed in our laboratory results, would subdue the signal of crystalline water ice; the surface would look more amorphous than crystalline, which is consistent with the predictions of Hansen and McCord 2004. The equilibration timeline of 30 minutes to 1 hour observed at 100 K in the lab has implications for mid-latitude regions on Europa. Post deposition, the amorphous frost would be expected to gradually transition to crystalline ice, increasing the crystallinity. Subsequent thermal cycling due to day-night cycles on Europa would result in pure crystalline ice. On the contrary, at higher latitudes, all water ice will be deposited as (and remain) amorphous. Future spectroscopic observation by Europa Clipper, if conducted in the wake of plume detections, might provide better constraints on the abundance and the role of plumes in surface crystallinity variations: by comparison with previous ground-based observations.

Quenching of crystalline ice is potentially observed in the laboratory but not well constrained on Europa. It is hypothesized here to occur post radiolytic bombardment (sputtering), a constant phenomenon on Europa which gardens the surface, ejecting neutral atoms and grains of water ice at velocities of ~ 1 km s^{-1} (Johnson *et al*., 1998, Allen *et al*., 2008). The H_2O particles can reach up to 300 km in altitude, undergo changes in temperature (heating due to bombardment, cooling while falling through the thin atmosphere) before reaching the ~100 K surface where they are deposited. Newly deposited crystalline ice can resemble amorphous ice spectra due to this hypothesized quenching, explaining some of the discrepancy in crystallinity between observations and models. After undergoing multiple cycles of annealing, their spectra are restored to crystalline ice. Future work will focus on understanding this process in the laboratory with irradiation experiments.

5.7 Identifying Parameters for Target Site Selection

Selection of regions of interest for future exploration, and the search for life, requires a rigorous understanding of the geological and chemical context of the environment. While a comprehensive framework for biosignature investigation, such as the NASA Ladder of Life Detection (Neveu *et al*., 2018) is beyond the scope of this dissertation, I will focus here on the contextual search for biosignatures. On Europa's surface, this translates to the search for remotely detectable, recent deposits of unaltered subsurface oceanic materials. The cratering record and stratigraphic (cross-cutting) relationships have been used to estimate the relative age of various terrains or features on

Europa (Leonard *et al*., 2018). The age equation presented in this work provides another tool for spatial characterization of age, given constraints on environmental conditions.

Hand *et al*. (2009) previously noted that chemical differences between surface features, coupled with estimates of radiolytic processing and age, can help determine endogenous vs exogenous origin. They identified smooth plains, low albedo smooth terrain (e.g., Castalia Macula), etc. as endogenic terrain, based on the criteria of Figueredo *et al*. (2003). More recently, Nordheim *et al*. (2018) identified locations on Europa where magnetospheric radiation has processed surface material down to a depth of at least 10 cm (received a dose of 100 eV per 16 amu in less than 10 Myr), rendering them unsuitable to host life (Figure 5.10). Combined with our understanding of (1) ice crystal structure (Section 5.6), (2) grain size distributions, (3) surface composition, (4) expected environmental conditions and (5) geomorphology of locations, I propose a criterion to evaluate regions of interest for future exploration of Europa. Table 5.7 lists the surface attributes and rationale identified here for classification, along with references.

The criteria split the locations into recent deposits of oceanic material versus old, altered deposits, based on the parameters listed below. In the absence of available parameters (e.g., physical properties such as grain size or ice crystallinity), spectral unmixing approaches can be pursued to estimate them for various locations on Europa using Galileo NIMS measurements or future Europa Clipper measurements:

1. **Ice Crystallinity:** The interdependence of ice crystal phase, temperature, and radiation effects complicates identification of a specific phase as a recent deposit (as indicated by results from Chapter 5). Therefore, crystallinity is useful if the formation mechanism

(plumes vs local hotspots) and/or thermal history of a region is known. Predictions which support the survival of amorphous or crystalline ice are made accordingly.

2. **Grain Size and Degree of Sintering:** Relatively larger grains (75-100 μm) are expected in older, higher albedo regions, and smaller grains more abundant in younger, lower albedo regions (Prockter *et al*., 2017). With sintering, the ice grains are expected to change their shape and size, while radiolytic disruption will further alter grain size.
3. **Composition / Concentration of Non-icy Materials and Role of Radiation:** The presence of salts is considered an important indicator of oceanic composition (as detailed in Chapter 6). Post emplacement on the surface, the water ice and salts (or organics) are expected to be radiolytically altered creating byproducts, thus providing a short timescale over which these materials remain unaltered. Spatial constraints on particle flux can further help with the classification. For example, the leading hemisphere materials experience less radiolytic processing and should be more indicative of endogenous material.
4. **Optical Albedo:** A host of processes ranging from radiation damage to compositional variations over time have been suggested for the different albedos observed on Europa's surface. In general, the albedo is expected to be brighter for older deposits, and darker for young materials (which is contrary to what we see on our Moon)

To classify a study area as a region of interest, we need to (a) determine whether the data supports recent exposures of oceanic materials (Table 5.7 attributes) and (b) identify influential attributes. For (a), if we observe locations with favorable surface attributes in our study area, then we are likely observing "fresh" regions. Such a region needs to be geomorphologically contextualized with a "ground-truth", i.e., analysis of the

cratering record, evidence of recent activity (e.g., mobility) such as low albedo bands, chaos terrain or smooth plains (Figueredo *et al*., 2003). Based on our results, we can classify such a site for targeting by Europa Clipper or a future Lander/Cryobot. However, if the region displays only some of the predicted attributes (e.g., it has large, sintered grains but salts that look unaltered by irradiation), that probably suggests oceanic material, but it cannot confidently be classified as a "fresh" location. In such a case, constraints on influential attributes are required (b), in this example case: resistance of salts to irradiation and implications for biosignature preservation. *Are biosignatures likely to survive at higher irradiation doses and shallower depths due to the presence of salts (acting as shields)?*

The proposed criteria provide a rough framework within which the search for biosignatures can be contextualized on the surface. Pursing this work is an important goal of future study.

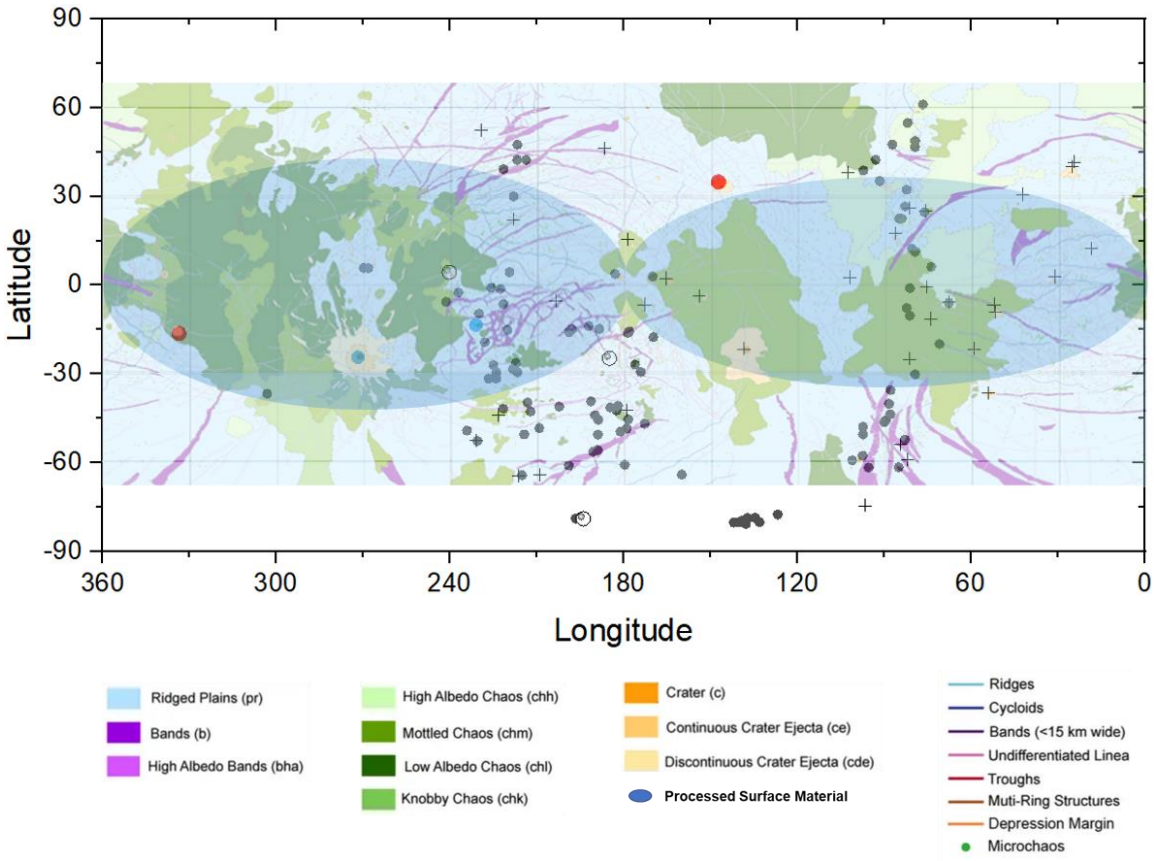

Figure 5.11: Regions of Interest for Europa are constrained to mid to high latitudinal regions (~ 40° to 70°), due to processing at equatorial regions and predominance of amorphous ice (old and new) at polar regions. Magnetospheric radiation lenses modified from Nordheim *et al*., 2018.

Table 5.8: Present understanding of Europa' s surface attributes form the basis of identification of regions of interest

Surface Attribute	Recent, Oceanic Deposits	Old, Altered Deposit	Rationale
Ice Crystal Structure	Crystalline ices at T <100 K Amorphous Ice at T >100-120 K	Amorphous ices at T <80 K	Exposure to radiation amorphizes the ice at T <80 K; H_2O vapor frosting at T <120 K results in fresh amorphous ice.
Grain Size and Degree of Sintering	Small, unsintered grains of spherical morphology	Larger grains with angular morphology	Grains sinter over time to become large and angular, fusing together; Old regions lack smaller ice grains due to disruption by radiation-induced sputtering
Composition / Concentration of non-icy materials	Unaltered salts ($MgSO_4$, NaCl, etc.) and H_2O	Alteration byproducts	Younger deposits exhibit limited to no radiation-induced chemical modification
Optical Albedo and Roughness	Darker (low albedo)	Brighter	Bands brighten with age: frost deposition, radiation damage, and/or compositional variations in source material over time
Present Understanding References: Figueredo *et al.*, 2003; Prockter *et al*., 2017; Fama *et al*., 2009; McCord *et al*., 1999; Carlson *et al*. 2002, 2009; Shirley *et al*. 2010; Johnson *et al*., 2019; Jaumann *et al*., 2008; Hand *et al*., 2009; Nordheim *et al*., 2018			

6.8 Discussion, Comments and Recommendations

The abundance of icy materials in the outer solar system dictates the need for new laboratory measurements of ice properties at relevant environmental conditions. In Part I of this dissertation, I have attempted to identify and address some of the limitations of existing spectroscopy techniques and datasets for application to remote sensing observations. Developing laboratory procedures and instrumentation for sample preparation and cryogenic reflection spectroscopy of planetary enabled me to obtain critical new measurements with appropriate thickness, grain size, and temperature and provides a pathway to future work on various chemistries and with the effects of radiation. I have applied these new measurements to Europa as a proof-of-concept. Bulk crystallinity and age calculation techniques presented here provide first order approximations and constraints on the surface conditions and evolution of ice. Spectral unmixing techniques to estimate surface compositions are also supported by our measurements and will be pursued in future to provide a rigorous interpretation of Europa's surface properties. Overall, these techniques are immediately applicable to other icy worlds and will enable new discoveries with increased science return of past space missions and support future missions like Europa Clipper and Dragonfly.

In Chapter 5, I have included several recommendations for future observations with the Europa Clipper mission, focusing on the EIS and MISE instruments to provide better constraints on the age (cratering record), surface composition, and identification of regions of interest. In the decade prior to that, my focus lies on improving our ability to interpret these measurements. Laboratory experiments remain a major component of that approach.

PART II ENABLING IN-SITU EXPLORATION

CHAPTER 6

OCEAN WORLD EXPLORATION WITH CRYOBOTS: HERITAGE ON EARTH AND ENVIRONMENTAL CHALLENGES TO CONSIDER

In Part II, our focus shifts to the interior of Icy Ocean Worlds like Europa and I try to unravel the behavior of the ice (e.g., viscosity, tectonics), identify the challenges arising due to environmental conditions (such as temperature, chemistry, etc.), and develop the technology required to enable exploration of ice shells and subsurface oceans.

6.1 Overview of Ocean Worlds Exploration

Exploration of ocean worlds such as Europa and Enceladus are particularly intriguing us as potential abodes of life beyond Earth. Ocean worlds may harbor conditions conducive to life, including containing liquid water, essential chemistry, sources of heat or energy, and time (Greenberg *et al*., 2000; Chyba and Phillips, 2001a, b, Cable *et al*., 2020). The heat is generated for Europa and Enceladus through tidal dissipation due to their eccentric orbits about their parent planets, Jupiter and Saturn, respectively (Ojakangas and Stevenson, 1989; Soderlund *et al*., 2014). The orbit eccentricity means the distance to Jupiter/Saturn varies, leading the moon to change its shape in response, which generates internal friction within the moon's interior that provides heat to maintain the ocean (Greenberg *et al*., 1998). Predicted contact of the (salty) ocean with a rocky silicate core

can potentially create a geochemically rich environment, like conditions existing on the terrestrial seafloor around hydrothermal vents (Hussmann *et al*., 2006).

However, accessing the subsurface ocean or melt pockets trapped within an ice shell on Europa (or other ocean worlds) poses significant challenges. From a technological perspective, a successful exploration mission will require starting in vacuum at cryogenic temperatures, penetrating 10's of km through an ice shell and diving 100's of kms through the ocean to explore the seafloor (Anderson *et al*., 1998), while maintaining communication. This journey entails navigating through an ice shell with unknown thermophysical and mechanical properties (*how hard is the ice?*; Henderson *et al*., 2019), surviving tidal stressing, potential faulting with cm's of displacement, and other resurfacing events, and/or exposure to salts, sulfuric acid and other potentially caustic chemistries. Coupled with potential plume activity, these are significant challenges to overcome. A robust communication strategy and hardware that can provide data transmission rates adequate to achieve science and exploration objectives are critical for any future missions to access the subsurface of an ocean world.

Following a systematic pathway to exploration (and life detection) (Figure 6.1), after an orbiter/fly-by mission (Europa Clipper, JUICE) and a Lander to Europa (Hand *et al*., 2017) or Enceladus (MacKenzie *et al*., 2020), a robust technology concept has emerged for effectively exploring the interior of the ice shell: the ice penetrating robot, or "cryobot" (Howell *et al*., 2020).

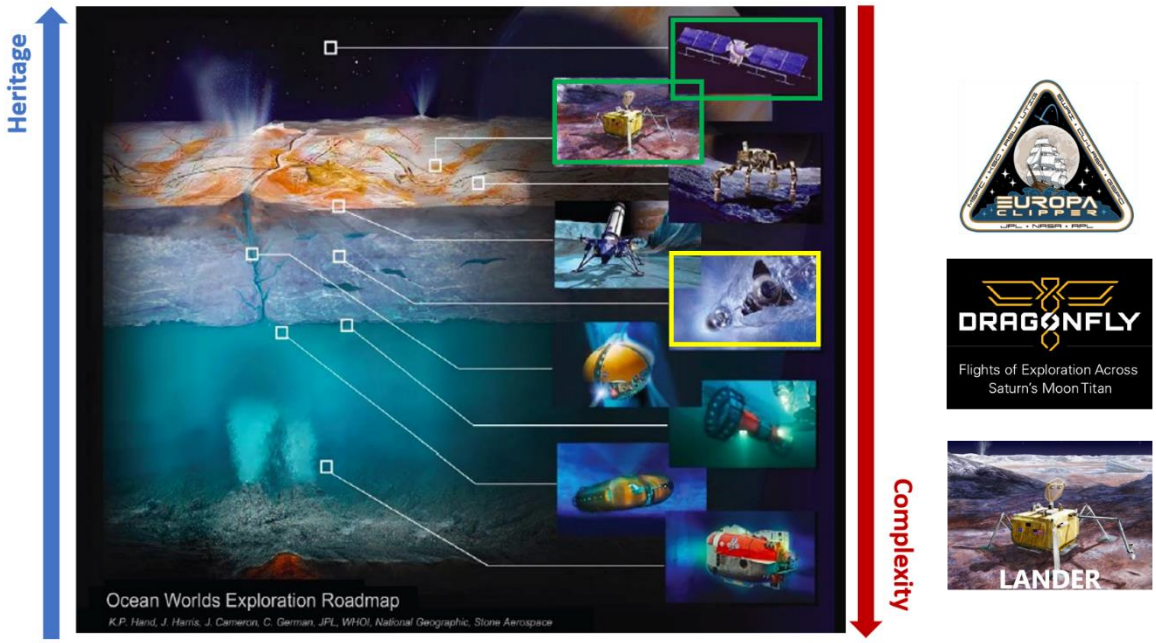

Figure 6.1: The Ocean World Exploration Roadmap identifies Cryobots as one of the next stages of exploration, after Europa Clipper, Dragonfly, and a potential Lander.

6.2 Current State of Research and Technology for Cryobots

A cryobot penetrates through the ice by melting or excavating icy material (and non-icy contaminants), using melting, cutting or a hybrid method. Terrestrial ice-probes have been proposed and/or developed for decades (e.g., Cryobot, Zimmerman *et al*., 2001; Ice Diver, Winebrenner *et al*., 2013; VALKYRIE, Stone *et al*., 2014), with recent field work in Antarctica and Greenland exploring the viability of the concept for future planetary missions (Bar-Cohen and Zacny, 2009; Zacny *et al*., 2016, SLUSH, 2018). However, these technologies require sustained development and integration to mature the cryobot system. One key research priority is communication (Howell *et al*. 2020).

Previous studies have discussed the issue of through-ice and in-ocean communications. Signal losses in cable, high mass/volume for spaceflight, and a significant risk of tearing of the tether due to shearing or refreezing of the ice-channel, during the descent phase of the mission have been identified as concerns (Dachwald *et al*., 2020). The use of communication tethers has been proposed, with coupled radio frequency (RF) relay 'pucks' to enable communication between a descending probe and a surface lander (Bryant *et al*., 2002; Cwik *et al*., 2018; Oleson *et al*., 2019). In the next section, I will explore the heritage of tethers in ice-ocean environments and detail the challenges which it will face on ocean worlds, and in our laboratory.

6.3 Communication Technology

Maintaining robust communication over the duration of an exploration campaign is a central component of mission design. For ocean worlds exploration, this entails extended communication with a melt probe as it descends through what may be 10's of km of a tectonically (and/or chemically) hostile environment. To ascertain the feasibility of employing various forms of optical communication on Europa and other ocean worlds, our multi-disciplinary team is testing the mechanical and data transfer performance of commercial optical tethers that are currently used for polar submersible exploration. The goal is to ascertain whether these commercial tethers might perform across a pre-existing active fault in the brittle portion of an ice shell—identified as a mission risk scenario—and if not, can we use the information learned to develop improved tethers and/or develop a multi-component communication strategy.

6.3.1 Present-day Application of Tethers

Fiber optic micro-tethers currently exist that have lengths sufficient to traverse Europa's ice shell and have sufficiently low mass to allow delivery as part of a planetary mission; both wire-guided munitions and oceanographic robotics represent established applications. Such expendable tethers payout from a spool on a vehicle as it moves and allow high bandwidth communications over large distances, sufficient to transmit multiple channels of high-definition video and support direct operator control.

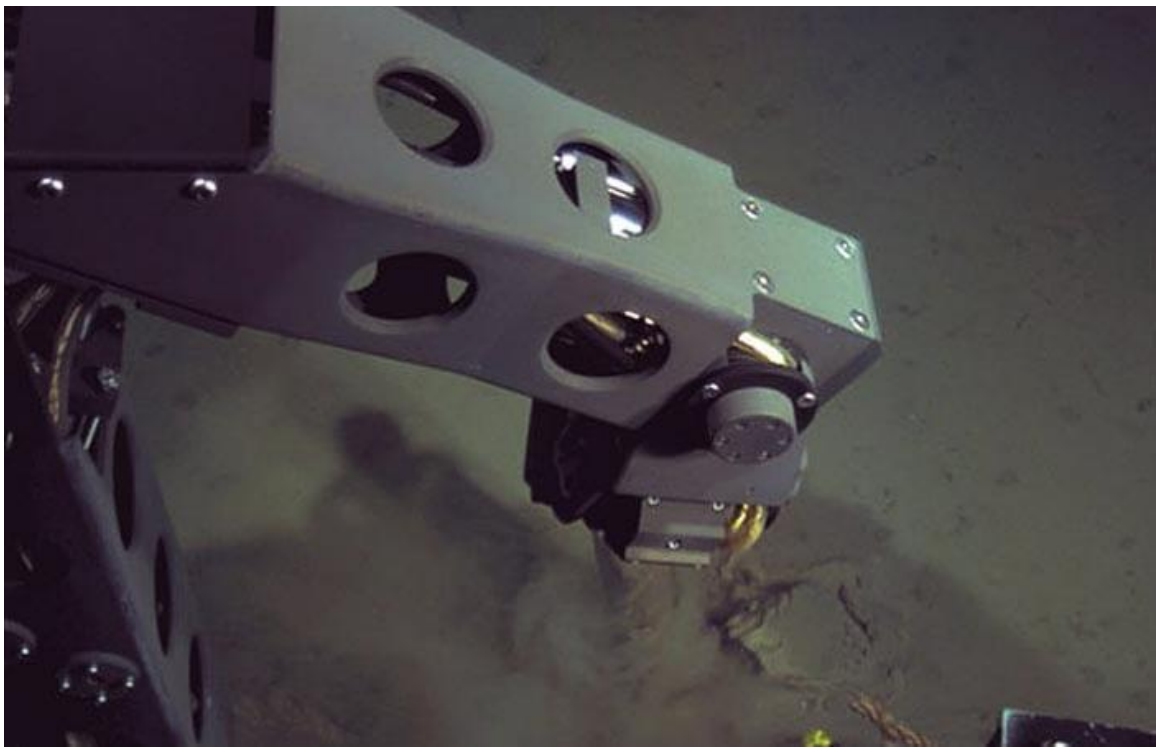

Figure 6.2: The vehicle Nereus exploring the bottom of the sea floor, using a (bare fiber) tethering system for real time video and data transmission (image courtesy of WHOI).

6.3.1.1 Polar Exploration: NUI and Nereus as exemplars

In terrestrial applications of tethers, the Nereus (Bowen *et al*., 2009) and NUI (Jakuba *et al*., 2018) vehicles have used 20 km spools of bare fiber, 250 μm in diameter, to reach the deepest parts of Earth's ocean (~ 11 km), and to reach from the ice-water interface to the seafloor beneath the ice-covered Arctic Ocean (Figure 6.2). Both applications have required decoupling the motion of the vehicle from its host vessel. Micro Tethers are "precision wound" into a spool with wraps arranged such that, though the spool remains fixed, the tether pays out without residual torsion to avoid line kinking and a combination of a canister and binder retains the tether within the spool to prevent the formation of loose wraps that foul payout. On Nereus and NUI, an aluminum canister, silicone oil binder, and rubber wiper arrangement used with bare fiber achieves a nearly velocity-independent payout tension of less than 1 N, a critical feature since the fiber cannot withstand more than a 1.7 N tensile load indefinitely (Grosenbaugh *et al*., 2007)

6.3.1.2 Borehole Research: Distributed Sensing (Strain, Location & Temperature)

Optical fibers have been successfully installed in km deep boreholes in Greenland and Antarctica for glaciological applications of distributed strain sensing (Liehr *et al*., 2009), acoustic sensing (DAS) and temperature sensing (DTS) (Booth *et al*., 2020), with sub-meter spatial resolution and accuracy greater than 0.15°C. The fibers survived in a temperatures range of ~250 to 273 K, and surface ice velocity of 550 m a^{-1}, demonstrating the feasibility of using fiber optic tethers to explore (and study thermal processes) in a high

deformation environment (see Table 6.1 for material properties). However, the long-term durability of these tethers is yet to be established, with failure observed in a field campaign as early as ~ 6 weeks (e.g., due to onset of temperature gradient vacillations) (Law *et al*. 2020).

These studies can serve as proof of concepts for subsurface deployment and science capabilities of tethers for Ocean Worlds exploration, if we can address the environmental challenges associated with ocean worlds, as detailed in the next section.

Table 6.1: Optical fiber used for distributed temperature sensing (DTS) and distributed acoustic sensing (DAS) in Greenland.

Solifos BRUsens	Fibers enclosed in a gel-filled stainless steel capillary tube, further protected by stainless steel wires and a polyamide outer sheath. OD 4.8 mm, Hydrostatic pressure resistance = 30 Ma, Tensile Strength = 3 kN

6.4 Predicted Conditions on Ocean Worlds like Europa and Enceladus

The conditions on the icy moon Europa are considerably different from terrestrial conditions. Communication tethers could face challenges of chemical degradation, shearing in the ice shell, and potential embrittling of components due to long term exposure to extreme cold. Characterizing these ice shell environments at the surface and in the interior will provide key engineering and design constraints for ice and ocean access technologies under development and help retire the technological risks (Howell *et al*., 2020). In this section, we will explore the environmental conditions expected in Europa's ice shell, which we will simulate in laboratory experiments in Chapter 7.

6.4.1. Presence of Ocean and Surface Chemistry

Europa is thought to possess a global interior ocean of water underneath its ice shell (Carr *et al*., 1998), which is predicted by geochemical models to be enriched in Mg^{2+}, Na^{+}, Cl^{-}, and SO_4^{2-} ions (Kargel *et al*., 2000; Zolotov and Shock, 2001; Marion, 2002; Zolotov and Kargel 2009; Vu *et al*., 2016). Galileo Near-Infrared Mapping Spectrometer (NIMS) revealed predominant non-ice components on the heavily radiation-bombarded trailing hemisphere, including spectra interpreted as $MgSO_4$ hydrates, sulfuric acid hydrates, and sulfate salts (Carlson *et al*., 2002, 2009; McCord *et al*., 1998), NaCl (Trumbo *et al*., 2019; Hand *et al*., 2015), Mg-bearing chlorinated species (Ligier *et al*., 2016; Johnson *et al*., 2019), and Na and Mg sulfates (Fischer *et al*., 2015; Vu *et al*., 2016, Johnson *et al*., 2019), some of which are correlated with large-scale geologic units such as chaos and dark regions. Other ocean worlds are suggested to have ammonia in the ice shell, like Enceladus (Squyres *et al.*, 1983; Kargel, 1992; Kargel and Pozio, 1996; Waite *et al*., 2009), Titan (Fortes *et al*., 2007), and Triton (Hogenboom, 1997). Optical tethers have never been tested for survival under these chemistries, which can potentially damage the outer jacket or lead to optical propagation loss due to reaction with the strength members in the tether.

6.4.2 Temperature Conditions and Predicted Behavior of Ice Shell

Based on the predicted temperature conditions of Europa's ice shell and the presence of a ~100 km thick subsurface ocean underneath, we expect the temperature range to lie between the average surface temperature (-173ºC or 100 K) and the melting point of

ice (0ºC or 273 K, or slightly lower depending on the composition of the ocean). For this work, we breakdown this range of temperatures into three sections of the ice shell:

1. Near-surface of the ice shell (95-120K): The surface temperature for Europa's ice shell is predicted to lie in the range of 70-90 K (polar latitudes) to 100-125 K (equatorial latitudes) over an Europan day, with an average surface temperature of ~100K (Spencer *et al*., 1999, Rathbun *et al*., 2010 Berdis *et al.*, 2020, see Figure 5.8 in Chapter 5).
2. Interior of the shell (120-220K): The most active section of the shell, with potential tectonics (pre-existing faults), melt pockets, transitions in ice behavior from brittle/semi-brittle to ductile, will also pose the most hazard to a tether. The temperature range is chosen here to lie between 120 and 220 K, though this work and future modeling efforts will better constrain this zone.
3. Near ice-ocean interface (230-270K): At the ice-ocean interface, we expect the solid and liquid phase of water to co-exist, with temperatures close to the melting point of ice at ~273 K. The presence of salts like NaCl, etc. will decrease the melting point to as much as ~250 K.

These sets of conditions cumulatively represent the homologous temperature range:

$$T/T_m = 0.34- 0.99 \quad (6.1)$$

Therefore, like rock on the earth, the ice in the icy shell will transition between brittle rheology at the surface to ductile rheology at depth. The transition from brittle to ductile behavior has mostly been studied by extrapolating behavior in either regime and determining the depth at which the strengths likely intersect. The thermal gradient of Europa is unknown and depends on whether the ice shell is purely conductive or if the

lower regions is convecting. In the simplest case, one could take the temperature difference and an estimate of the thickness and assume a linear relationship with depth. Dombard and McKinnon (2006) estimated a thermal gradient of 18K/km and strain rate of 10.0E-15 for a pure water ice shell. Using laboratory values for the frictional strength of ice (i.e., Byerlee's law; Beeman *et al*., 1988) in the shallow region and the viscous flow law (Goldsby and Kohlstedt, 2001) for the ductile region, they determined a lithospheric strength envelope for ice on Europa, based on its dependence on depth: increasing strength due to increasing lithostatic pressure vs decrease in strength due to temperature increase promoting ductile flow. They predicted the brittle-ductile transition (BDT) to occur at ~2.7 km depth from the surface in the ice shell (with surface temperature of 80 K, grain size of 200 microns).

It is this variation with stress and temperature with depth that we need to test against the tether. The range of mechanical behavior that is controlled by the extreme temperature profile provides a design challenge. Hardware and communications need to survive the full range of tectonic behavior in the shell. Specifically, it is the faulting and sliding behavior in the upper brittle portion that provides the biggest potential obstacle, as well as largest unknown.

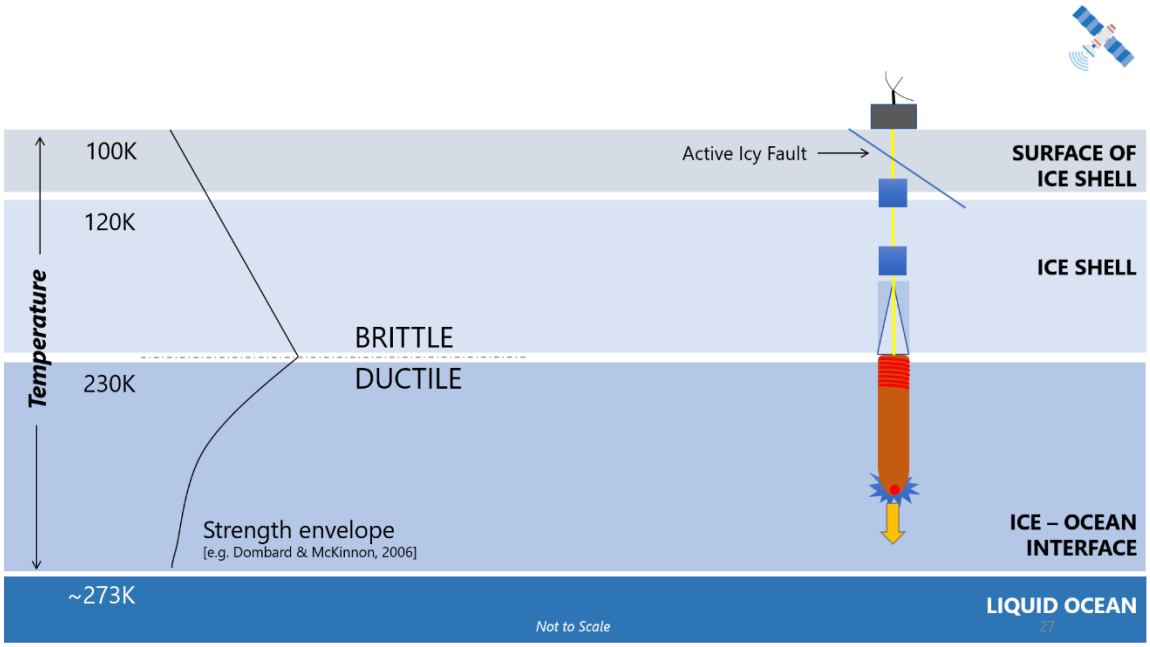

Figure 6.3: Ice Shell conditions are simulated in the laboratory in three temperature ranges.

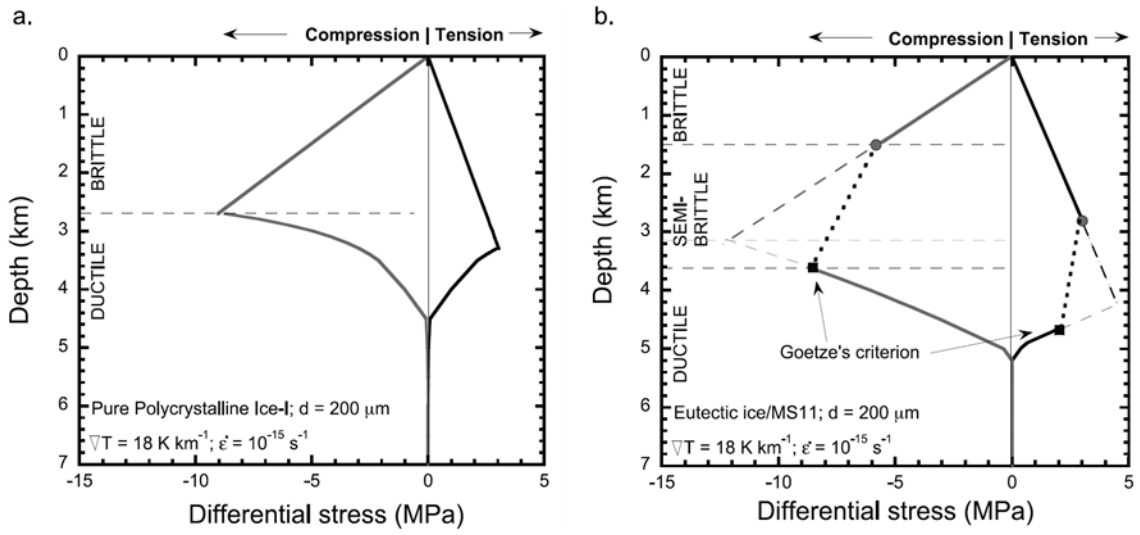

Figure 6.4: Strength envelopes for pure polycrystalline ice and ice-MS11 eutectic (McCarthy *et al.*, 2011, using assumptions from Dombard and McKinnon (2006), Spaun and Head 2001).

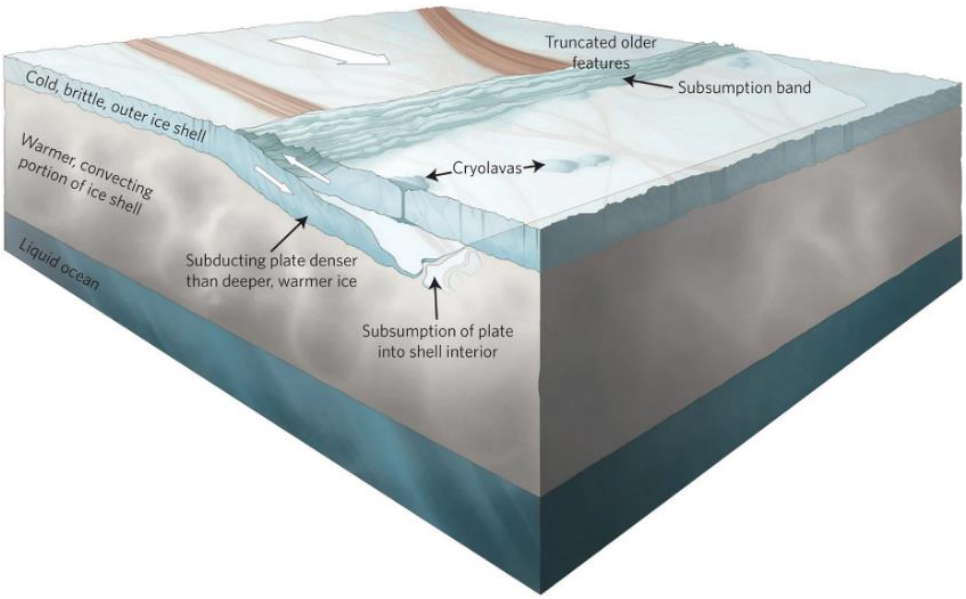

Figure 6.5: Conceptual Model of Europa's ice shell from Katterhorn and Prockter 2014, highlighting a cold, brittle, outer portion of the ice shell into its warmer interior.

6.4.3 Faulting on Ocean Worlds: Stress, Strain and Shear Velocities

The mechanics of several classes of tidally stressed faults on Europa are poorly understood. For instance, cycloids are a class of features that are inferred to slip at rates of a few m/s (Hoppa *et al*., 1999; 2000). A qualitative concept called tidal "walking" was introduced to describe how the fault normal and fault shear stresses drive open/close and strike-slip motions (e.g., Tufts *et al*., 2000). Improved models of strike-slip motion on icy faults include friction and the Coulomb criterion to determine whether and when (in the tidal cycle) sliding occurs (e.g., Smith-Konter and Pappalardo, 2008; Olgin *et al*., 2011). Additionally, a reconstruction of the northern Falga Regio provided strong evidence for a subduction-like process, which implies plate-scale thrust faulting (Kattenhorn and Prockter, 2014). Subsequent studies are identifying additional evidence for plate-like

motions (e.g., Collins *et al*., 2016). Although evidence is mounting that Europa's ice shell is a regionally active mobile lid, the proposed models cannot predict whether earthquake-like stick-slip motion can occur, nor the location with depth that this would be expected.

6.4.3.1 Predicted Stress, Strain, and Shear Velocity

Although there is no way to know fault sliding rates from existing surface imagery, we can consider end-member scenarios. One scenario would be slow rates associated with creeping of a fault. Creeping strike-slip faults on Earth, which are driven by plate tectonics, slide at rates on order of 10^{-9} m/s. Europan faults, driven instead by tidal forcing, probably creep at higher rates, on order of 10^{-7} m/s (Nimmo and Gaidos, 2002). On the other end of the spectrum would be a fault that is otherwise stuck but then lurches forward during a seismic event. In lieu of observational evidence to provide event slip rates on Europa, we use basic relations from elasticity that state that the ratio of propagation speed to slip speed nearly equals the ratio of the elastic shear modulus to peak-to-residual stress drop at the front (Rubin, 2011). The average stress drop $\Delta\tau$ can be estimated from elastic properties (effective shear modulus μ') and an assumption about the downdip extent of slip W (Pollard and Segall, 1987):

$$\Delta\tau/\mu' = \delta/W \tag{6.2}$$

From kinematics, the maximum slip speed, V_{max}, equals the propagation speed, V_{prop}, multiplied by the maximum slip gradient. Combining these two relationships provides:

$$V_{prop} / V_{max} = \alpha \, (\mu' / \Delta\tau_{p\text{-}r}) \quad (6.3)$$

where α is a scaling factor that depends on the spatial distribution of strength reduction behind the peak stress, but is close to 1 for quasi-static elasticity and subscript p-r stands for peak-to-residual (e.g., Ampuero and Rubin, 2008). As an estimate for propagation speed, we take the shear wave speed velocity through ice (~2000 km/s). Based on Rubin (2011) slip relationships and the parameter values for ice, slip rates during an event may be as fast as 10^{-3} m/s. Consequently, in Chapter 7, I explored velocities in the range 10^{-7} to 10^{-3} m/s, to simulate these end members, and determined their survivability in ice.

6.5 Classic Examples of Frictional Behavior of Ice: Shear Stress Dependence on Velocity

Laboratory friction experiments have long been used to determine rock and ice frictional strength and stability as a way of understanding the mechanics of earthquakes and faulting (e.g., Dieterich, 1972; 1978; 1979; Scholz 1998; 2019) and more recently, glacier sliding (e.g., Zoet *et al*., 2013; McCarthy *et al*., 2017). It is beyond the scope of this chapter to go into a detailed exploration of friction and faulting. However, since the experiments performed are an adaptation of a double-direct-shear friction experiment, it is worth describing some of the classic and representative features of experimental friction data. Figure 6.6 shows a typical experimental program consisting of velocity steps and slide-hold-slides. The data is from a system of ice sliding on rock (McCarthy *et al*., 2017), but nearly identical responses are seen for rock samples (e.g., Dieterich, 1972; Beeler *et al*., 1994; Marone, 1998).

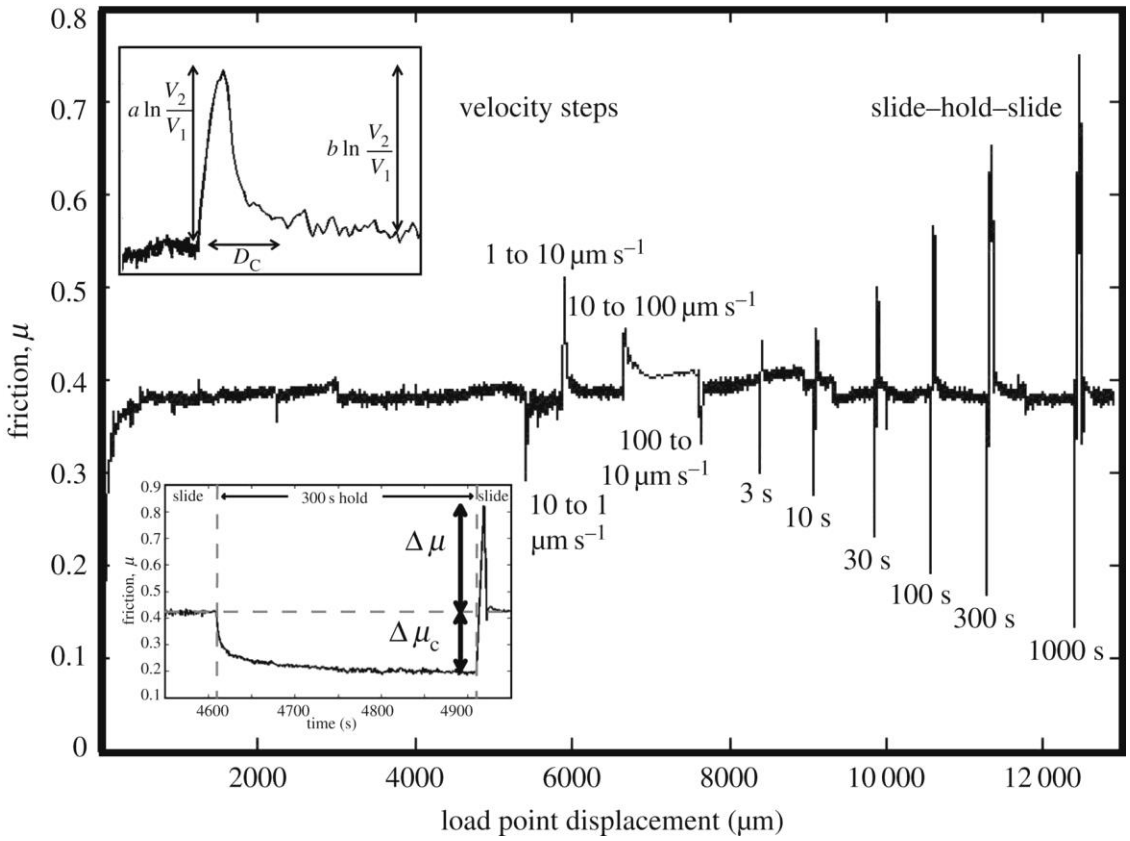

Figure 6.6: Example of a velocity step and slide-hold-slide driving program, and frictional behavior for polycrystalline ice sliding on two granite blocks. Instantaneous stress jumps are highlighted in the main figure, while insets show: (top) a single velocity step used to determine rate-state friction parameters; (bottom) relaxation of friction on the onset of hold, and friction peak when sliding is resumed. Image from McCarthy *et al*., 2017, Figure 2.

6.5.1 Instantaneous Stress Jumps (with step change in velocity)

Upon initial loading, friction slowly increases until the system comes to steady state. Then instantaneous changes in the load point velocity are imposed. In the example, an order of magnitude steps (up and down) were employed. In response to an up-step, the frictional response immediately jumps up (the "direct effect") and then evolves back down to a new steady state friction value. The upper left inset shows how these velocity steps are analyzed to determine the so-called rate- and state-dependent friction parameters (e.g., Dieterich, 1978; Ruina, 1983). Not shown here, but in systems of granular interfaces like till or gouge, the direct effect is not so dynamic and peak-like. Instead, friction in granular systems demonstrates a gradual hill shape with a velocity increase (e.g., Chester, 1994).

6.5.2 Relaxation Curves (during velocity holds)

During slide-hold-slides, the driving piston moves forward at a constant rate and then is held constant for increasing durations (in Figure 6.6 from 3 to 1000 s). The piston does not move backward, so the friction does not fall to zero. Rather, the held piston causes the friction to slowly relax, which can be seen in the lower left inset that is plotted against time. The relaxation is due to a combination of the apparatus itself and the sliding interface. Upon sliding again, the friction jumps up due to time-dependent healing at the sliding interface. That change in friction after a hold typically increases according to the log of time (e.g., Beeler *et al*., 1994). Healing is generally attributed to increase of real contact area, which consists of the asperities that are in contact at the microscopic level. In ice,

healing has been known to be quite large compared to that of rock due to the high homologous temperature and more easily deformable asperities (e.g., McCarthy *et al*., 2017; Zoet and Iverson, 2018).

6.5.3 Stable, Smooth Sliding versus Unstable (Stick-Slip) Sliding

In Figure 6.6 shown here, the new steady state friction after an increase in velocity is greater than the previous value. This type of response is known as velocity-strengthening, whereas if the new friction after a velocity increase is lower, it is termed velocity-weakening. Whether a system is velocity-strengthening or velocity-weakening is very important in rock mechanics because it determines the stability of the fault. When a system is velocity strengthening, it means that the fault strength increases when the fault is pushed at faster velocities and earthquakes cannot nucleate. On the other hand, if the system is velocity-weakening, it is considered unstable and stick-slip like motions (earthquakes) can nucleate. Although the relatively warm ice-on-rock system shown in Figure 6.6 is demonstrating stable, velocity-strengthening behavior, ice-on-ice friction studies at very cold temperatures that have shown a variety of velocity-strengthening and velocity-weakening behavior are possible, controlled by both temperature and sliding velocity (Schulson and Fortt, 2012).

CHAPTER 7

SURVIVING IN OCEAN WORLDS: AN EXPERIMENTAL CHARACTERIZATION OF MECHANICAL AND OPTICAL PERFORMANCE OF FIBER OPTIC TETHERS ACROSS ICE FAULTS

In Chapter 6, I have established the heritage of optical tethers in ice and identified the (environmental) challenges associated with their application to the outer solar system. Here, the ability of these tethers to survive in hostile environments is evaluated, using cryogenic laboratory shear testing.

7.1 Materials and Methods

7.1.1 Description of Tethers Selected

Tethered communication techniques have great heritage from state-of-the-art terrestrial ocean exploration. While fiber optic micro-tethers with length and mass (Table 7.1) sufficient to support proposed Europa cryobot architectures (e.g., Wilcox, 2017; the NASA Compass study) have already been deployed for terrestrial applications, their ability to withstand in-ice conditions on Europa has not been demonstrated. In particular, tether failure modes in the presence of shear stresses at low temperature (i.e., faulting in Europa's ice shell) is not well understood. Further, while fiber-optic tethers offer unparalleled data

transfer rates for minimal size, mass, and power, their spooling mechanisms remain untested at Europa-like conditions.

To assess the robustness to shear of optical fiber tethers, I selected two particularly robust types of tether from Linden Photonics Inc. that are commercially available. These were the (i) Linden Photonics Inc. Strong Tether Fiber Optic Cable (STFOC) and (ii) Linden High Strength STFOC (a jacketed, kevlar-reinforced STFOC referred to here as HS STFOC). Similar designs have been qualified for space flight (O'Riorden and Mahapatra, 2012), and have previously proven effective for use under hydrostatic pressures in the deep-sea under-ice ocean submersibles (Jakuba *et al*., 2018; German *et al*., 2019). Linden is also able to supply its cables as self-supporting spools (normally for deployment from undersea vehicles, but likely adaptable to a cryobot because payout will occur in liquid water melt behind the vehicle).

In addition, a two-conductor copper ribbon was also selected for testing, owing to copper's low temperature ductility that may prolong survival, and its potential to actively heat the tether, in situ, while embedded in Europa's icy crust. Such ribbons are deployed routinely in oceanographic surveys worldwide, from eXpendable Bathy Thermographs (XBTs, Sippican Inc.) and payout from a similarly wound spool.

7.1.1.1 Known Material Properties

Linden's tethers are relatively lightweight and flexible, with minimal optical propagation loss over kilometers of cable (STFOC attenuation @1310 nm is < 0.45 dB/km & @1550 nm is <0.35 dB/km). The STFOC included a bare fiber with a hermetic primary

strength coating (jacket) of Liquid Crystal Polymer (LCP), which protects the inner fiber from moisture (e.g., reaction with hydrogen leads to transmission loss over time). The LCP is surrounded by an abrasion / crush resistant outer layer. The HS STFOC is representative of an armored cable that approaches maximum tenable mass for space flight. The HS STFOC tether includes an additional layer of Kevlar strength members braided over the top, with a final outer jacket of polyurethane. These tethers range in diameter from XBT Cu ribbon (0.26 mm) to lightly armored cable (1.9 mm), with a mass of 0.2 to 3.6 kg per kilometer. They are capable of supporting tensile loads of 50 lbs (STFOC), up to 250 lbs (HS STFOC, Linden Photonics).

7.1.1.2 Unknown Material Properties

To date, there has been limited deployment of optical communication tethers in icy environments (with active shear faulting), as highlighted in the previous chapter (Section 6.3). As a consequence, there is a gap in the literature about the material properties of these tethers related to their behavior in ice. In particular, Linden Photonics Inc. have performed measurements of the tensile strength of tethers, but these tests were not performed at cryogenic conditions, or while frozen in ice. Shear Strength of tethers has not been reported at any conditions. The cryogenic adhesive behavior of tether jacket materials, and their tolerance of various chemistries (such as salts or sulfuric acid) is yet to be determined. The optical communication performance and any potential decays arising due to long soaks in ice for depths of 30+ km over the suggested 3-year period of a cryobot mission are not known. This is problematic considering the reported failures of optical tethers in ice after

just ~6 weeks after deployment down a 1 km depth borehole in Greenland (Law *et al.* 2020). In this work, I attempt to determine some of these unknown material properties with cryogenic laboratory testing.

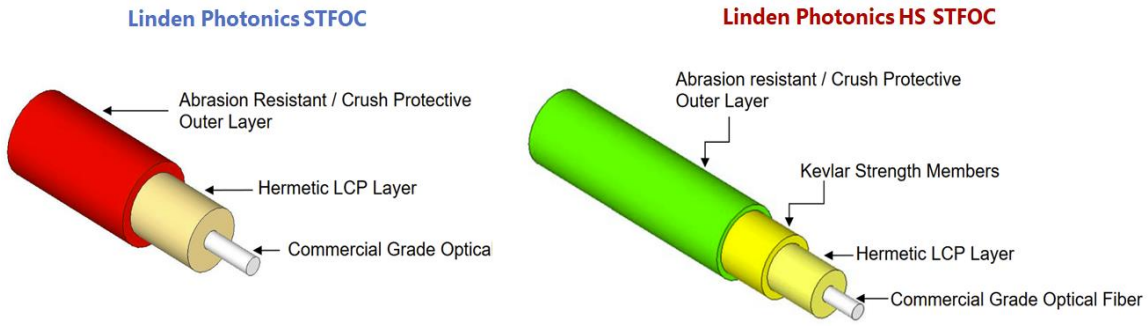

Figure 7.1: Layers of a Linden Photonics Inc. High Strength Strong Tether Fiber Optic Cable, and Strong Tether Fiber Optical Cable.

Table 7.1: Known Material Properties of Tethers selected for this work.

HS-STFOC	Tight buffered. Thermoplastic Polyurethane (TPU) jacket, Kevlar braid, Liquid crystal polymer (LCP) primary strength/sealing layer. 1.9 mm OD, 3.6 kg/km, 250 lbf tensile strength.
STFOC	Tight buffered. Liquid crystal polymer (LCP) primary strength/sealing layer. 0.76 mm OD, 0.6 kg/km, 50 lbs tensile strength.
XBT Copper Ribbon	0.133 x 2 mm OD, 0.2 kg/km

7.1.2. Sample Preparation

7.1.2.1 Ice Fabrication Mold

To test the strength of tethers fully embedded in ice, a custom, stainless steel three-section die is used (Figure 7.2) that applied pretension to the tether, around which I froze a polycrystalline ice sample with two pre-existing faults in a vertical orientation (theta = 0º). Our design takes advantage of relevant double shear testing methods developed previously to test cables embedded in concrete (e.g., Mirzaghorbanali *et al*., 2017; Rasekh, *et al*., 2017). For example, the die has a central to side ice block length ratio of 3:2 (4.95 to 3.3 cm), with a height and width of ~4.95 cm, and a total sample length of 29 cm. There are two 3.8 cm diameter mandrels at the outer ends, around which the tether was wrapped. The diameter was chosen based on the manufacturer's recommended turn radius of the tether. A combination of a plug, fairlead and retainer components at both ends of the ice blocks allowed the tether to run out of the mold, while maintaining vacuum inside. A strap held the tether down without crimping and the mandrels were rotated and locked into place with set screws to pre-tension the tether within the mold. During sample fabrication, the mold was connected to a vacuum at the top via suction cups and is connected to a volume of deionized water at the bottom via tubing and two valves. One valve chooses between the center section and the outer sections and the second valve controls flood water flow.

Figure 7.2: 3D model of Ice Fabrication Mold Components for freezing tethers in ice (model courtesy of collaborator Matt Silvia).

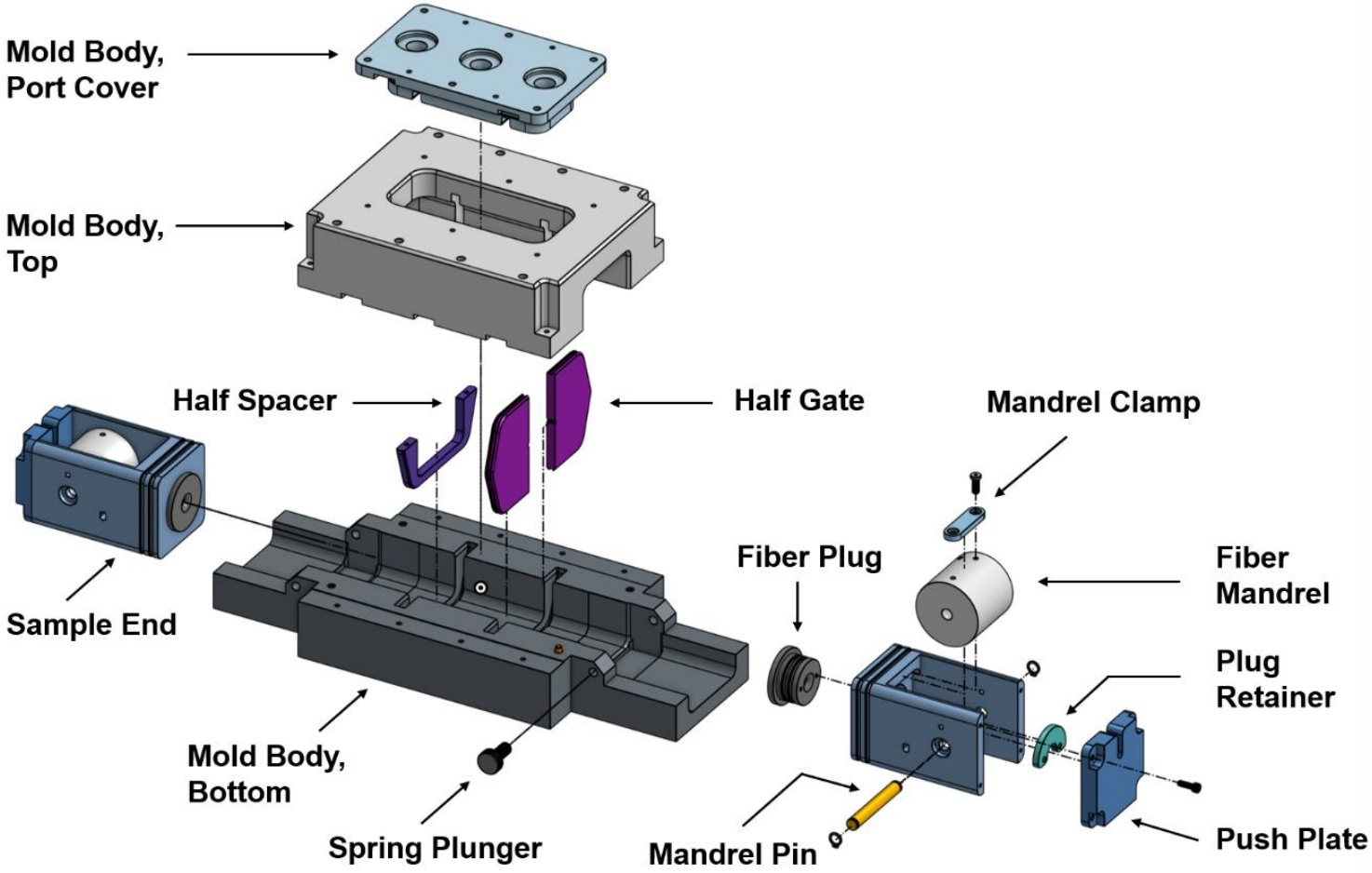

7.1.2.2 Ice Manufacturing and Freeze-in Protocol

To ensure uniform ice with controlled properties, the “standard ice” method of ice fabrication (Cole, 1979) is followed that utilized ground seed ice that was sieved between 250 - 500 micron mesh sieves and lightly packed into the die. A vacuum was pulled from the top of the die and deionized water was introduced from the bottom through small holes in the floor of the die. The die and floodwater were first equilibrated at 0ºC for ~30 minutes prior to flooding. After flooding was complete, the die was placed on a cold plate within a freezer, with insulation around the sides to promote directional freezing. The sections were frozen in steps (first the central block, then the outer blocks) with interfaces lubricated with a (Sprayon) release agent and oil. This die and protocol proved to be a reliable method for making an intact sample assembly (Figure 7.3, 7.4) with tethers pre-tensioned and fully frozen within the ice (Singh *et al.*, 2019, 2021).

By following this procedure, the grain size of the surrounding ice was uniform and reproducible, confirmed by analysis of images made by a Leica light microscope housed within a cold room (T= ~260 K). The ice produced by this method had an average grain size of 2.08 mm ± 0.22 as determined by the linear intercept method with a correction factor of 1.5 (Gifkins, 1970). Additionally, two “control” samples were created by following the same protocols and die as above, but not including the tether.

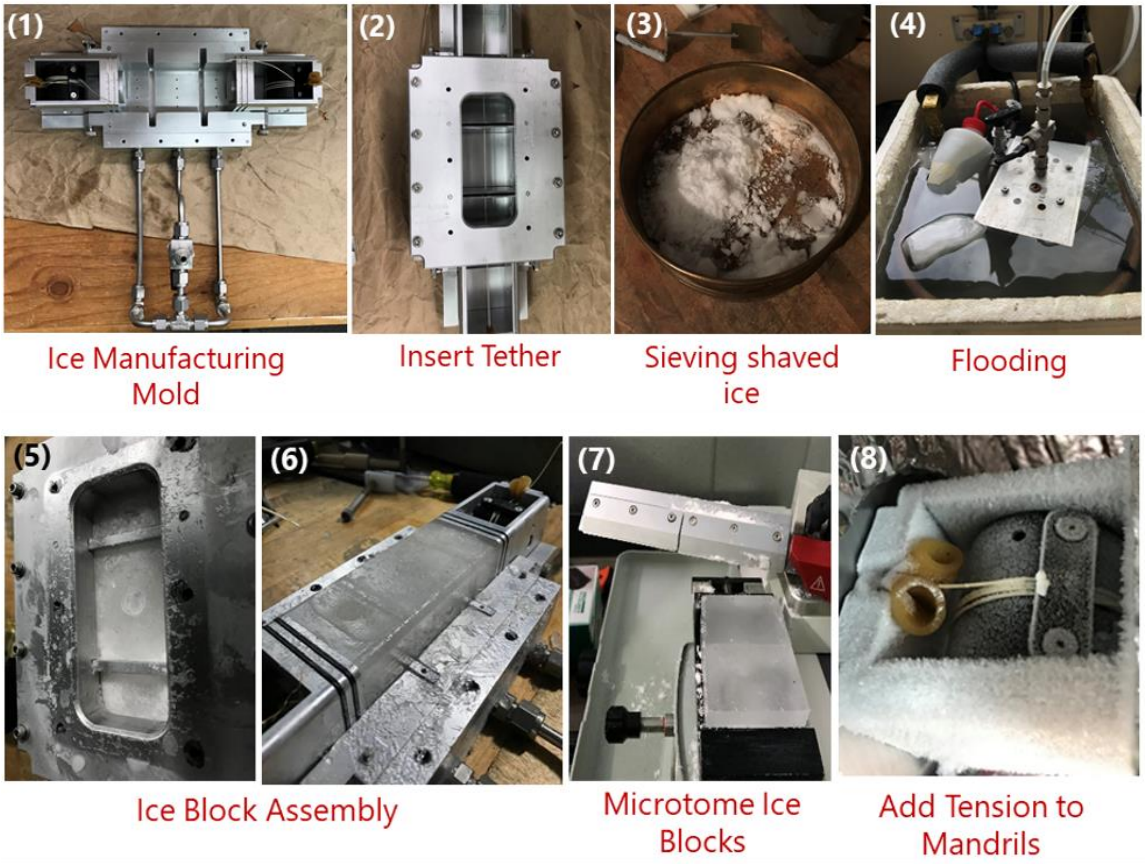

Figure 7.3: Ice sample fabrication protocol. Polycrystalline ice blocks of controlled grain size, porosity and impurity content are fabricated using a modified "standard ice" protocol (Cole, 1979) (1-5). Linden STFOC and HS STFOC tethers are embedded in ice (6-8).

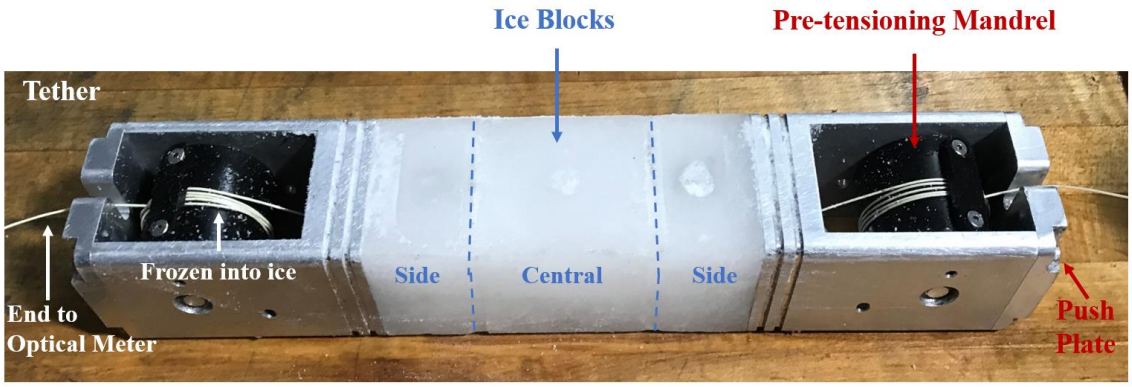

Figure 7.4: Custom sample assembly that allows pre-tensioned tethers to be frozen into ice. A small layer of lubrication between side and central blocks, along with the geometry of forcing, causes the ice to break along the dash lines and shear the tether during loading.

7.1.3 Instrumentation and Test Conditions

7.1.3.1 Servo-Hydraulic Biaxial Deformation Apparatus

Shear tests were conducted using a cryogenic biaxial deformation apparatus located at Lamont Doherty Earth Observatory (LDEO), described in McCarthy *et al*., (2016) (Figure 7.5). We employed a modified double-direct-shear configuration, with the tether embedded through the middle of all three ice blocks. Servo-controlled hydraulic pistons applied a normal stress in the horizontal direction while a velocity program controls the downward vertical velocity, pushing the central sliding block past the outer stationary blocks. Load cells and direct current differential transformers (DCDTs) located outside the cryostat measured normal/shear load and displacement over time. The resolutions of load and displacement are 39 Pa and 0.7 micron, respectively. The frame can hold a maximum force of 123.7 kN in the vertical direction and 35.6 in the horizontal direction.

Our experimental temperature range (100 – 260 K) was chosen to represent the full range of thermal conditions in the icy shell, excluding those conditions already tested in terrestrial applications. Temperature was maintained by a Liquid Nitrogen (LN)-cooled circulating chiller that pumps low temperature fluid (ethanol-water mixture) through copper channels next to the sample in a cryostat. For the lowest temperatures, the cryostat was directly cooled by LN flowing through the channels. Vacuum is used for thermal insulation, and temperature was monitored to ±0.1K by Resistive Temperature Detectors (RTDs; Omega P-ULTRA) embedded in the walls of the cryostat adjacent to the sample. Low thermal conductivity ceramic pistons (Macor™) were used to translate stress from the

hydraulic pistons to the sample ends, passing through teflon seals in steel plates on the side panels of the cryostat. Data was logged versus displacement for a selection of displacement speeds and temperatures.

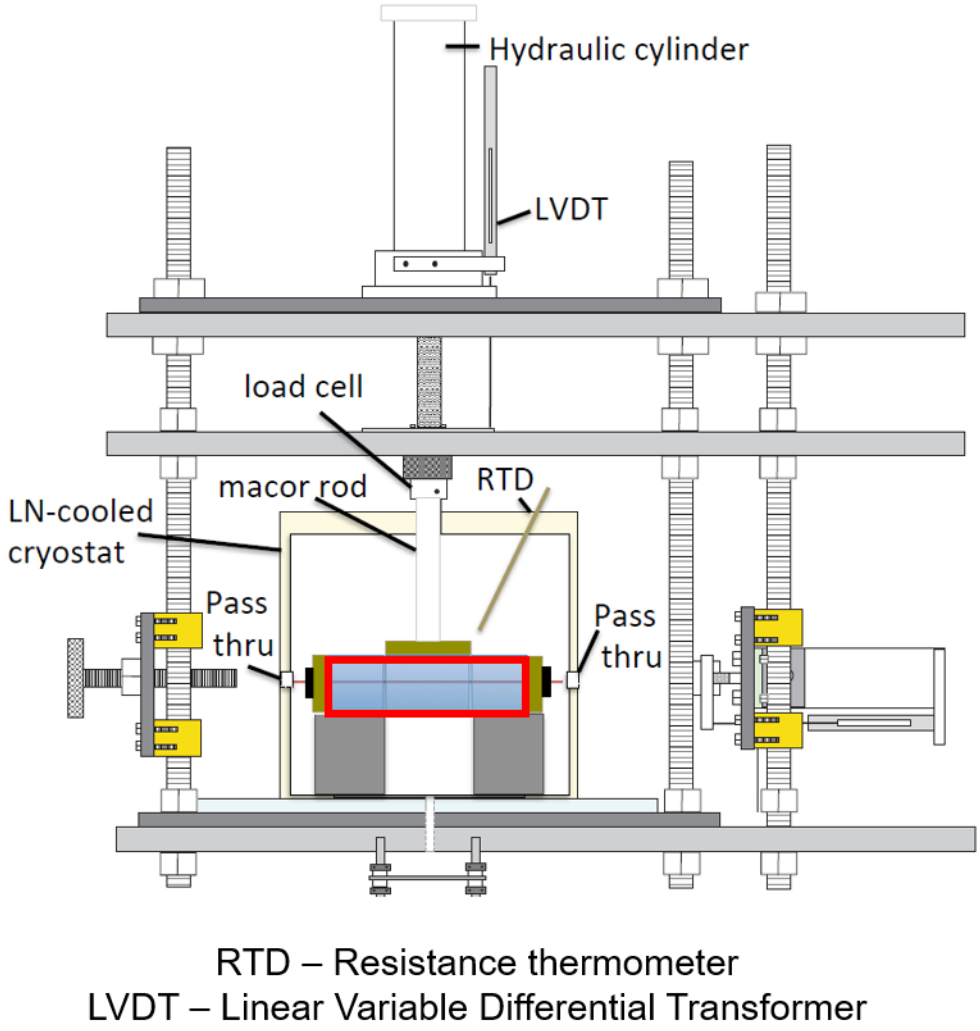

Figure 7.5: LN-cooled biaxial apparatus at LDEO. Tethers were frozen into ice and loads applied as indicated by arrows. Ends of tethers were wrapped around mandrels and passed through the cryostat for monitoring for optical performance.

7.1.3.2 Optical Source and Meter

The communications performance and viability of each tether was continuously monitored while inside the test apparatus. Pass-through ports on the side of the cryostat allow the two ends of the tether to pass and connect to an Optical Power meter (OptoTest OP250). Optical transmission loss was continuously measured during testing using a Stabilized Light Source at 1310 nm with OP735 Benchtop Optical Power Meter. Additionally, some samples were measured using a Luna OBR 4600 Optical Backscatter Reflectometer unit, which had greater precision in tracking optical transmission loss over long ranges (greater than 2kms) at a spatial resolution of 10 microns, with a single connection-single scan. In both cases, ends of each side of the tether were stripped to the fiber, cleaned and fusion spliced to optical cables connected to the source and the detector. For the final set of tests at 230 K, pigtail connectors were pre-attached to remove the need for fusion splicing. We also monitored optical loss prior to and during freezing of the tethers inside the solid blocks of ice, as controls, and compared to performance at the end of testing to characterize any degradation.

7.1.3.3 Microscopic Characterization

Characterization of representative ice samples before and after testing were conducted using a Leica DM2700 light microscope housed within a cold room (260 K). Prior to imaging, a mirror finish was obtained on the imaged surface using a microtome. Images were taken in refracted light and in most cases since the grain size was so large,

were taken in only 2.5x magnification. Sublimation after microtoming accentuates grain boundaries. From these images, we used linear intercept method to determine grain size.

7.1.3.4 Shear Velocities and Driving Program

The ability of the tethers to withstand shear force is likely dependent on the rate of shearing. Here, we will consider end member scenarios, as there are no known fault sliding rates. One scenario would be slow rates associated with creeping of a fault. On the other end of the spectrum would be a fault that is otherwise stuck but then lurches forward during a seismic event. For these tests, the sample assembly was pushed together under feedback-controlled normal stress (~100 kPa) and the central sliding block were forced down under controlled velocities that represent a potential range of fault sliding behavior on Europa and Enceladus (Nimmo *et al*., 2007; Sleep, 2019), from creeping (ramps of 0.5, 1, and 10 micron/s) to seismic, stick-slip events (100, 200, and 300 micron/s; complete range of 3.0E-04 to 5.0E-07 m/s), each following a zero-velocity hold. Even without knowing Europa's slip rates exactly, these tests provide a measure of the robustness of tethers to shear. We use a MATLAB routine that creates a simple LabView driving program. When running, the program overrides manual control and provides a voltage to the vertical servo-valve that drives the vertical piston cylinder forward at a designated speed for a designated time. The driving program consists of a series of velocity steps and holds (see Table 7.2 for details) to simulate the expected behavior of a pre-existing ice fault frozen along the path of the cryobot, during the stages of (1) reactivation (loading); (2) long periods of creeping

motion along the fault planes followed by periods of inactivity (creeping to holds); and (3) sudden slips or ice quake events.

The total displacement length is limited by the 20 mm (or, 2 cm) stroke of the vertical DCDT's high resolution linear range. Hence the total vertical displacement during testing was either 1.5 cm or 2.4 cm, depending on the total number of driving velocity programs which were run. For the 1.5 cm displacement case, I ran one program (ICE #1, a sample of which is provided in Figure 7.6). For 2.4 cm displacement, at the end of the first program, the DCDT was re-zeroed to its lowest position and a new program was run consisting only of high velocity shear events (or ice-quakes) with zero-velocity holds in between (combined program referred to as ICE #2). The period of re-zeroing, and associated changes in recorded stress and displacement are eliminated during data processing. Samples of driving programs are provided in Figure 7.6

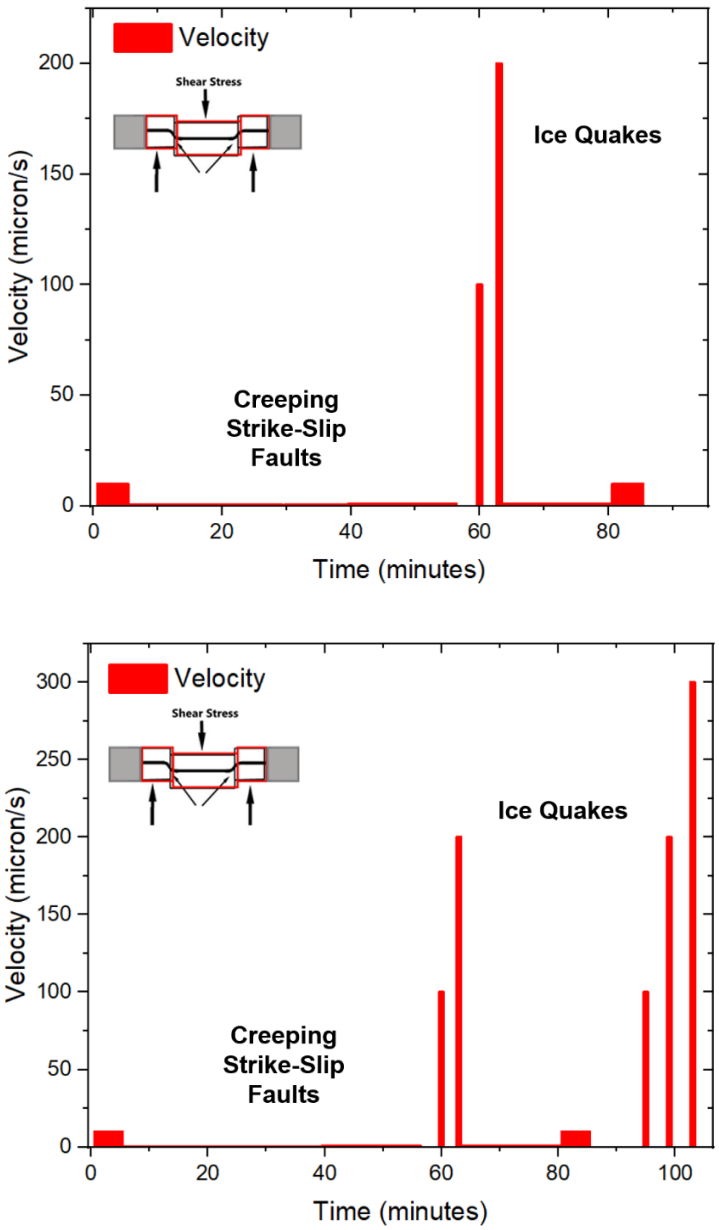

Figure 7.6: ICE#1 (top) and ICE#2 (bottom) velocity driving programs used during double direct shear tests.

Table 7.2: The velocity-control driving programs (ICE#1 & ICE#2) used for shear testing.

Velocity (micron/sec)	Time (sec)	Shear Event	Displacement (mm)
0	60	Hold	0.0
10	300	Loading / Creeping	3.0
0.5	2000	Creeping Strike-Slip	4.0
1	1000	Creeping Strike-Slip	5.0
0	200	Hold (/ Relaxation)	5.0
100	30	Ice-Quake (Sudden Slip)	8.0
0	200	Hold	8.0
200	15	Ice-Quake (Sudden Slip)	11.0
1	1000	Creeping Strike-Slip	12.0
10	300	Creeping Strike-Slip	15.0
0	200	(Long) Hold	15.0
Additional ramps of Ice-Quakes added to ICE#1 program: full set referred as **ICE#2**			
100	30	Ice-Quake	18.0
0	200	Hold	18.0
200	15	Ice-Quake	21.0
0	200	Hold	21.0
300	10	Ice-Quake	24.0
0	200	Hold	24.0

Table 7.3: List of Samples and Driving Program used for their tests.

Tether Type	Temperature (K)	Driving Program	File ID
STFOC	260	ICE#1	C0060
HS STFOC	260	ICE#1	C0061
HS STFOC	~ 250	ICE#2	C00144
STFOC	230	ICE#1	C00133
HS STFOC	230	ICE#2	C00150
Control	230	ICE#2	C00158
HS STFOC	220	ICE#1	C00147
STFOC	198 – 227	ICE#1	C00137
HS STFOC	199	ICE#1	C00139
STFOC	195	ICE#1	C00142
HS STFOC	120	ICE#2	C00149
STFOC	95 – 100	ICE#2	C00148

7.2 Results of Shear Testing

An extensive set of double-direct shear experiments were successfully conducted for pure water ice samples with embedded Linden STFOC and HS STFOC tethers using a cryogenic biaxial friction apparatus (Figure 7.7). The XBT Cu Ribbon broke during sample preparation and was discarded for testing. Mechanical properties of the tether-ice assemblage, such as peak shear stress achieved to activate faulting, shear stress vs velocity relationship, etc., and optical transmission loss of tethers were measured. The experimental temperature range of 95 – 260 K is comparable to Europa's ice shell temperatures (from the near-surface to melting near the ice-ocean interface), with the velocity range of $5x10^{-7}$ to $3x10^{-4}$ m/s representing creeping faults and ice-quakes on Europa. A control sample of pure water ice without tethers was also tested at 230 K for comparison.

✓ *Ductile-ish behavior*
✓ *Brittle-ish behavior*

TETHER TYPE	TEMPERATURE RANGE									
	260K	248K	237K	230K	220K	198-233K	199K	195K	120K	95-103K
STFOC	✓			✓		✓		✓		✓
HS STFOC	✓	✓	✓		✓		✓		✓	
ICE (Control)				✓						

Figure 7.7: Ice Shell conditions tested for both Linden tethers.

7.2.1 Initial Peak Stress for Ice Fault Activation: Implications for Ice Strength

The initial strength of the ice block-tether assemblage until cracking at interfaces, depends primarily on the strength of ice and as such depends on temperature. Hence, while it is valuable to report the peak stresses survived by the samples at the start of shear testing, this section elucidates more of an understanding of the ice behavior at a range of ice shell temperatures, rather than the limitations of tethers.

The ice interface breaks at a peak stress of ~70–300 kPa at 260 K, with measured friction (shear/normal stress) exceeding that of the known friction of ice at these conditions (0.2 to 0.6 depending on velocity; Schulson and Fortt, 2012). The STFOC-ice sample 'faults' are activated at the lower peak stress of 67 kPa, while the HS STFOC sample requires a higher peak stress of 296 kPa for activation. This trend is consistent throughout testing down to 95 K, with the HS STFOC samples offering more resistance to breaking. A loud audible pop is heard at the instant of cracking, with a significant drop in shear stress and the interfaces becoming visible through the cryostat windows. With cooling, the initial peak stress required increases to ~550 kPa (HS STFOC) at 237 K to – 1061* kPa (HS STFOC) at 230 K which is the temperature at which we observe the ice in our experiments to display a transition from ductile to brittle behavior. At temperatures colder still, the peak stress required jumps to 1201 kPa (HS STFOC) at 220 K. For a few experiment runs (HS STFOC at 199 K and STFOC at 195 K, 200 – 230 K), the data was clipped at 1061 kPa due to the calibration of the vertical load cell (working range was initially limited to ensure greater accuracy at low stress). The vertical load cell was subsequently recalibrated to broaden the recording range for these high stress tests. At the lowest temperatures of testing

(95 K to 120 K), the peak stresses increased further, up to ~ 1.3 MPa (for STFOC) at 100 K to ~1.5 MPa (HS STFOC) at 120 K, demonstrating a roughly linear temperature dependence of ~ 8kPa/K.

For the control sample, the recorded peak stress is ~1.55 MPa at 230 K, which is ~0.3 to 0.5* MPa (*data was clipped) higher than the recorded peak stress for the ice-tether samples at similar temperatures, and comparable to recorded stress at the coldest temperatures tested (~120 K). The only difference between both samples is the lack of a tether in the control sample. A preliminary conclusion can be made that the presence of a tether might add resistance (or stress) to the surrounding ice, and potentially lowers the strength of the ice leading to cracking at a lower peak strength.

The peak stresses documented here (Figure 7.8, Table 7.4) represent the initial breaking of the interfaces. In all cases, the optical readings confirm that neither of the two tethers display any damage during this ice fracture process. Thus, we can confidently state that both tethers can survive reactivation of faults at cryogenic temperatures on Ocean Worlds, while the ice experiences peak stresses of the order of ~1.3 to 1.5 MPa. Subsequent high velocity events did contribute damage to the outer jacket, as will be described below.

Table 7.4: Peak Stress vs Temperature behavior for ice-tether samples during shear testing

Temperature (K)	Peak Stress (kPa)	Tether Type
100	1288*	STFOC
120	1467	HS STFOC
195	1061*	STFOC
199	1061*	HS STFOC
200 – 230	1061*	STFOC
220	1201	HS STFOC
230	1061*	STFOC
230	1548	Control Ice
237	550	HS STFOC
260	296	HS STFOC
260	67	STFOC

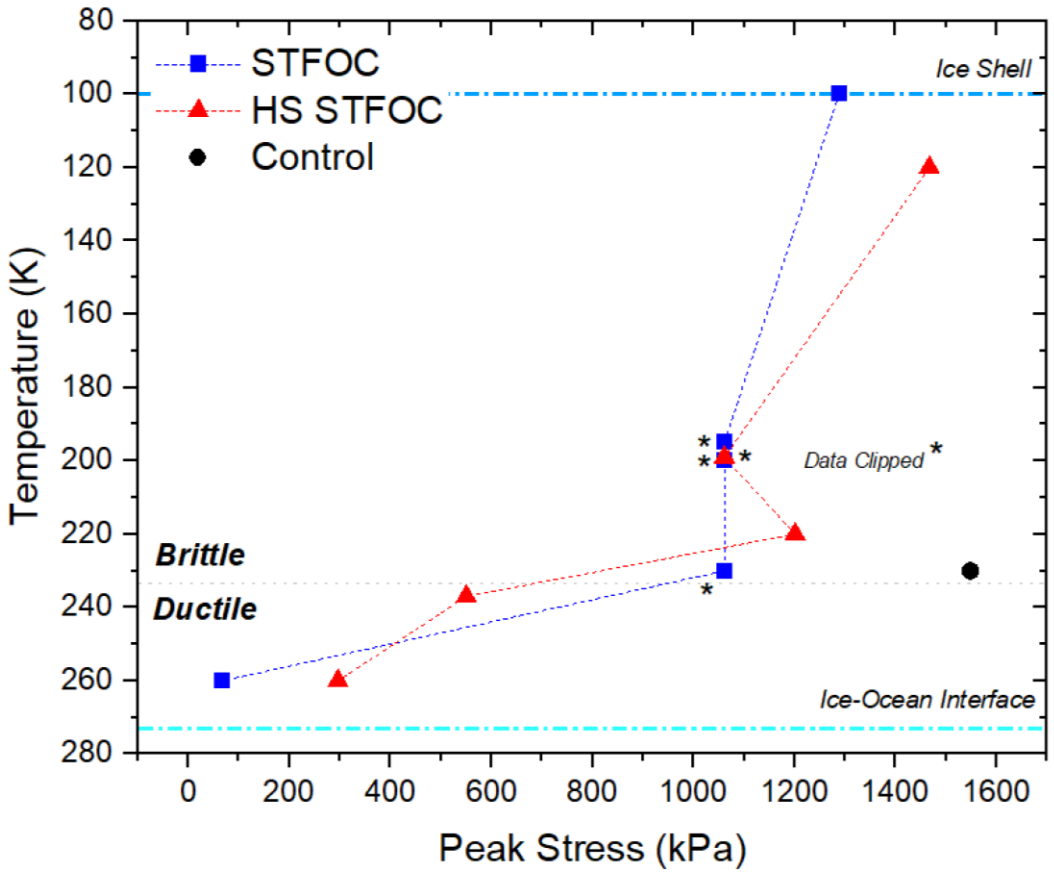

Figure 7.8: Peak stress survived by Linden tethers and control ice sample over the range of ice shell temperatures.

7.2.2. Shear Stress: Velocity versus Temperature Relationship

Figure 7.9 is a plot of shear stress (black) and velocity (red) vs. time for the STFOC tether tested at 230 K demonstrating a representative response to the applied velocity program(s). The initial increase in shear stress from zero occurs prior to the sample sliding and represents the stiffness of the apparatus and sample assembly. In a typical friction test, this value increases only to the steady-state friction value and then levels off. However, in these experiments the sliding interfaces have been welded intact by the two-step freezing protocol. The peak stress after the initial ramp is due to the interfaces breaking, described in section 7.2.1. In this case the two interfaces broke separately, thus the double peak (the first of which has clipped data), with a very large stress drop in between. The spike in the red velocity data at ~75 minutes was not part of the programmed routine; it represents the piston lurching forward in response to the first interface breaking. The downstep in velocity at about 77 minutes is superimposed on the relaxation and not evident in this dataset, but the small step up in velocity (from 0.5 to 1 micron/s) is seen in the response at 110 minutes. That the shear stress response is gradual and hill-like suggests that the sliding interface contains some ice gouge from the initial break. The relatively smooth data at these two velocities are clear examples of stable sliding at these conditions.

At approximately 128 minutes, the piston was stopped, and classic relaxation of the apparatus and interfaces was observed. Following this, a 100 micron/s event was imposed by the routine. The response of the system was to break into a series of stress drops (~300 kPa), with the piston lurching forward at each drop, as shown in the red velocity data. That the stress returned to similar values after each drop indicates that the interfaces were still

somewhat intact. This contrasts with the response to the 200 micron/s event at ~135 minutes. Here the stress drops were smaller (~100 kPa) spaced closer in time, and did not return to previous values, causing an overall decline in the shear stress. This indicates a breaking up and damaging of the ice interfaces. The gradual increase of shear stress in response to the velocity step at ~138 minutes further implies this. During both high velocity periods, the jagged response is representative of unstable, stick-slip behavior in the system at these conditions. Audible pops were heard at each stress drop. Similar behavior was observed in the tether-less control sample at a similar temperature, so the stress drops are due to the ice and central plastic forcing block sliding and/or ice cracking, and not due to the tether.

All other tests demonstrate some variation on the above description due to the temperature and sliding behavior of the ice, and the inferred character of the interface (i.e., intact versus full of gouge). In the following section, I will describe the variations in sliding with temperature and velocity, demonstrating the striking range of conditions that the tether experienced during testing (Figure 7.10 and 7.11).

Figure 7.9: (A) Representative shear stress and velocity versus time curve for the STFOC tether at 230 K, highlighting (B) peak stress achieved; (C), (D) are ice quake events.

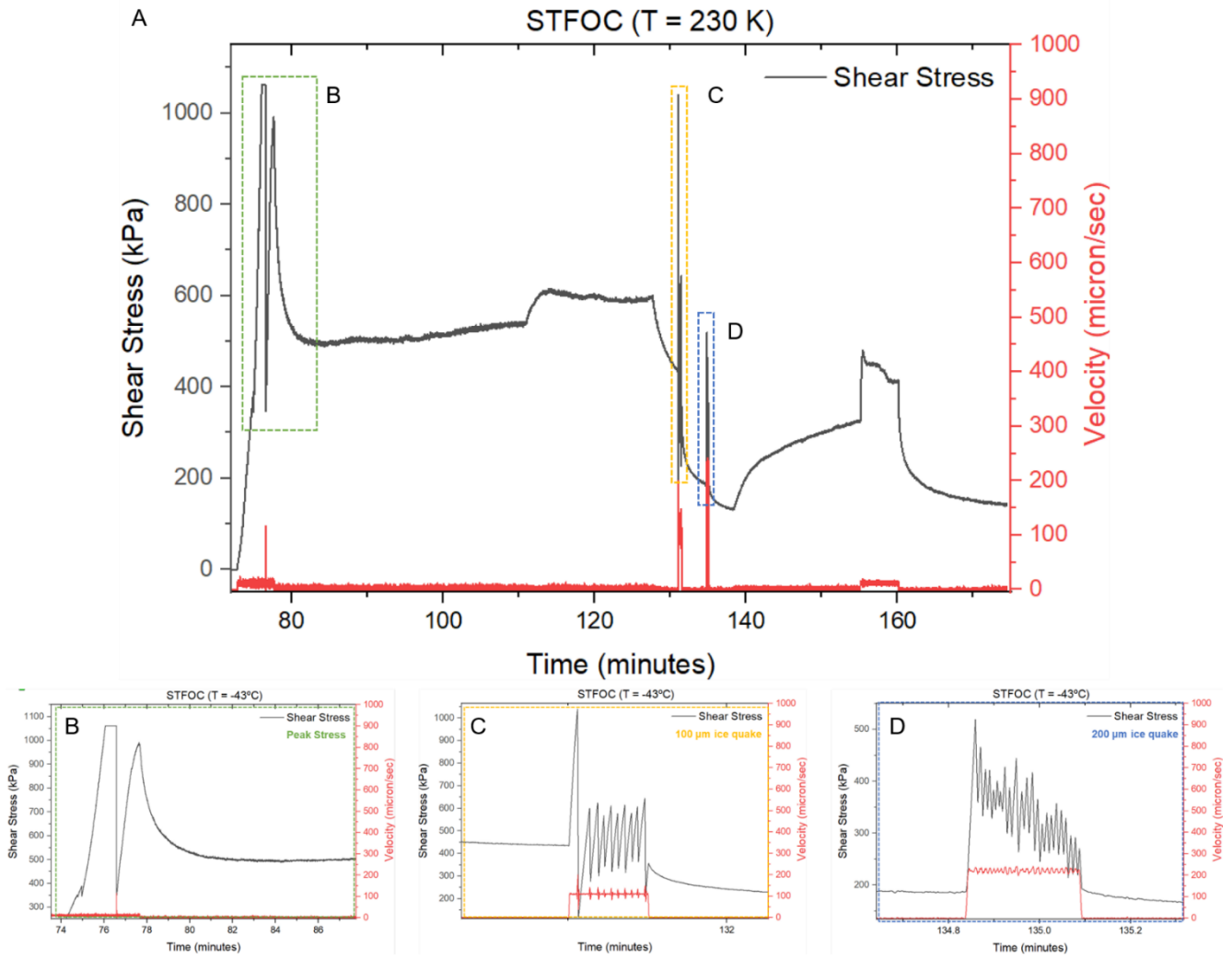

7.2.2.1 Shear Stress versus Displacement Curves: Implications for Europa

Figure 7.10 and 7.11 show shear curves for each of the temperature-velocity combinations tested for the Linden tethers. The curves indicate that for both tether assemblies at low velocity ($5x10^{-7}$ to $1x10^{-5}$ m/s) and high temperature (> 200 to 250 K), the frictional response is generally smooth and steady. At 250 K, the warmest temperatures studied, stable sliding is observed at any velocity. This sliding would be associated with velocity-strengthening behavior, as described in section 6.5.3. At intermediate temperatures (195 – 199 K), large stress drops are observed at low velocities, while high velocities have multiple stick-slip events, demonstrating clear velocity-weakening behavior. Both the STFOC and HS STFOC samples show multiple repeatable drops of 40-80 kPa in shear stress during the loading phase of the driving program. During follow up velocity ramps of 0.5 to 1 micron/sec, the shear stress stabilized around an average of ~900 kPa, with consistent stress drops 90 to 140 kPa (see Figure 7.13). At the coldest (100 – 120 K), fastest conditions, the system is transitioning back to stable sliding. These results are nearly identical to those seen in a pure ice-on-ice (tetherless) friction study at comparable conditions (Schulson and Fortt, 2012; Figure 3) and to our control sample (Figure 7.12). This demonstrates two key points:

1. In these shear experiments, the tether is not radically affecting the ice response; instead, the tether appears to be along for the ride.
2. Our study with the crudely broken and imperfectly planar sliding interfaces, similar to reactivated faults on Europa, confirms the previously well-constrained results of Schulson and Fortt (2012). It provides robust confirmation of the distinct temperature

and velocity dependence of frictional sliding in ice, which is significant for its potential application on Europa.

If the stability of friction is so closely tied to temperature, as demonstrated here, it suggests that a "seismogenic zone" may be present at depth on Europa, as has been identified on Earth (thought instead to be due to creation of rock gouge with depth, Marone and Scholz, 1988). Although it is beyond the scope of this dissertation to map a zone of instability with depth on Europa, continued work in that area is being conducted by collaborators (McCarthy *et al*., 2018). The results presented here (consistent with Schulson and Fortt, 2012) suggest that there may be a variation of sliding behavior with depth such that the uppermost and lowest portions of the ice shell would be sliding smoothly (and slowly), whereas at a mid-range in temperature and depth, icy faults could initiate stick-slip, rapid Europa-quake events. Thus, Europa may naturally be providing a wide range in temperature and sliding velocity conditions that are fairly consistent with those conditions I have tested our tethers against here.

Figure 7.10: Shear stress curves (scale bar: 100 kPa) vs displacement (scale bar: 1 mm for 5 x 10^{-7} m s^{-2} to 1 x 10^{-5} m s^{-2}; 3 mm for 1 x 10^{-4} m s^{-2} and 2 x 10^{-2} m s^{-2}) of STFOC tethers for temperature-velocity combinations tested under an applied normal stress of 100 kPa.

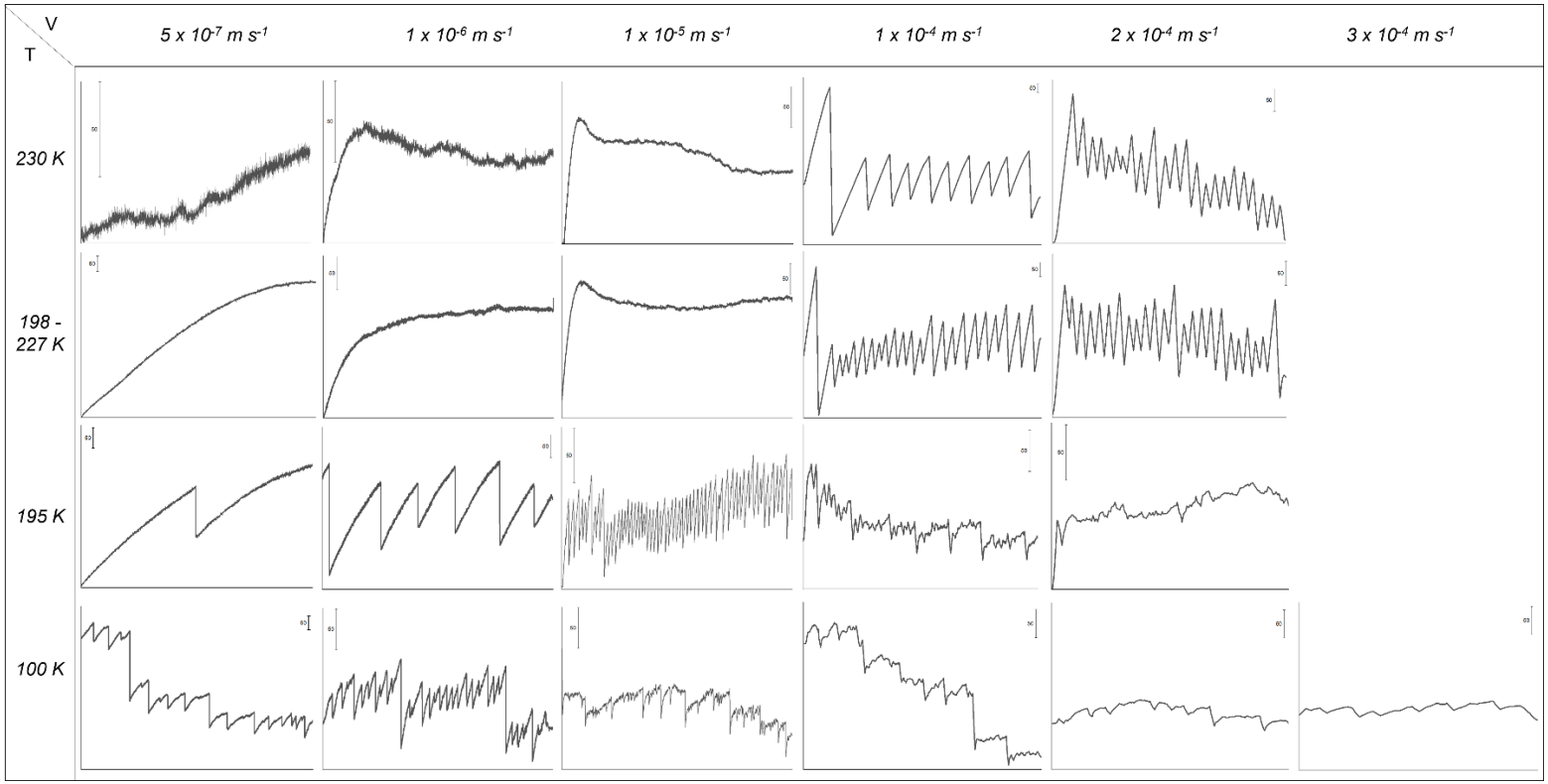

Figure 7.11: Shear stress curves (scale bar: 50 kPa) vs displacement (scale: 1 mm for 5 x 10^{-7} m s^{-2} to 1 x 10^{-5} m s^{-2}; 3 mm for 1 x 10^{-4} m s^{-2} and 2 x 10^{-2} m s^{-2}) of HS STFOC tethers for temperature-velocity combinations tested under an applied normal stress of 100 kPa.

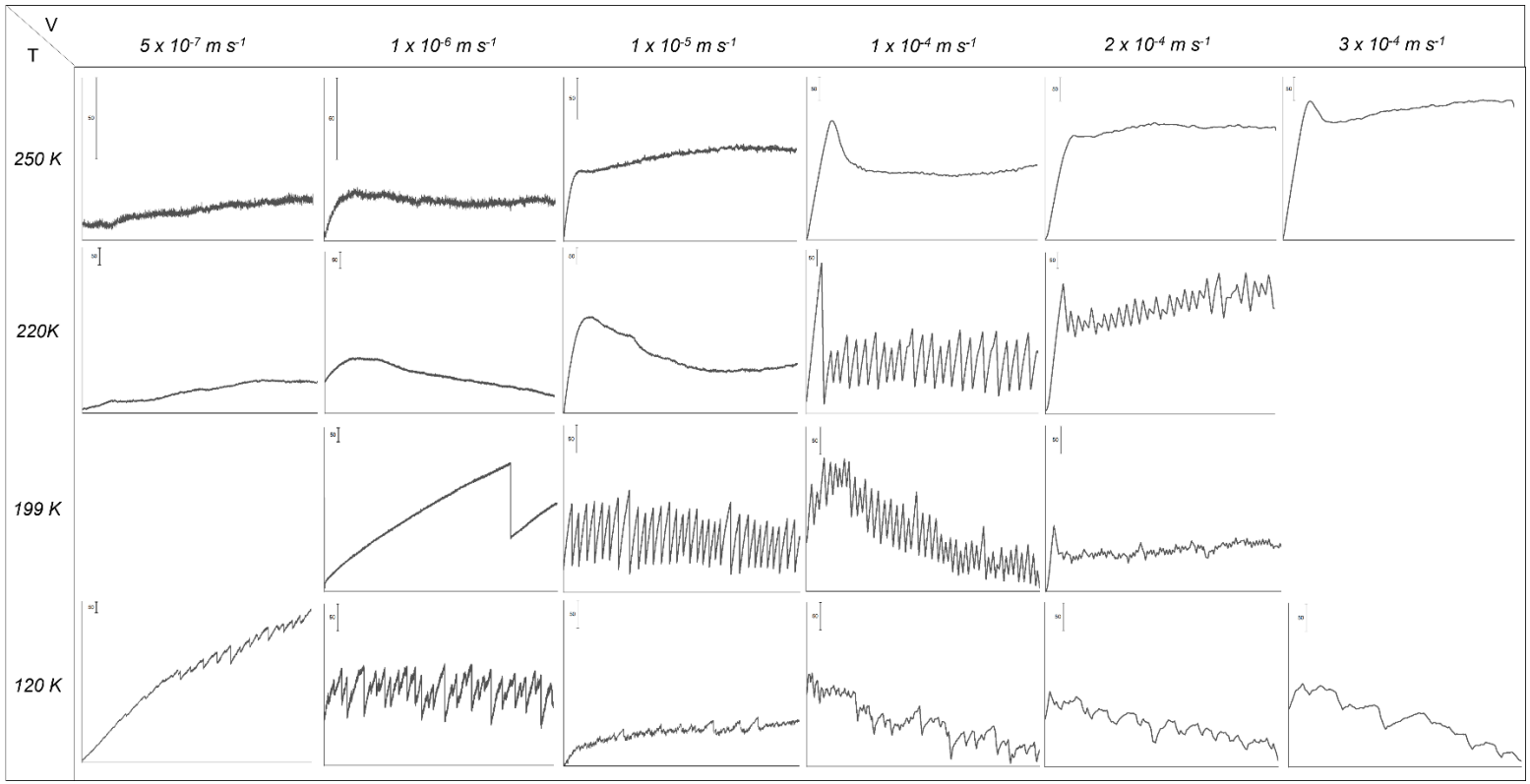

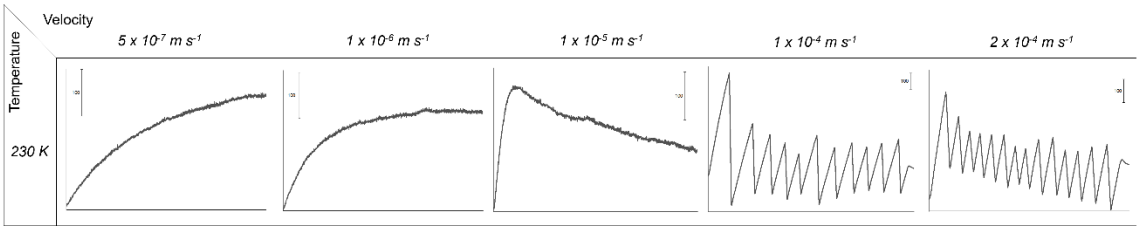

Figure 7.12: Shear stress curves (scale bar: 100 kPa) vs displacement (scale: 1 mm for 5 x 10^{-7} m s^{-2} to 1 x 10^{-5} m s^{-2}; 3 mm for 1 x 10^{-4} m s^{-2} and 2 x 10^{-2} m s^{-2}) of control sample of ice for temperature-velocity combinations tested under an applied normal stress of 100 kPa.

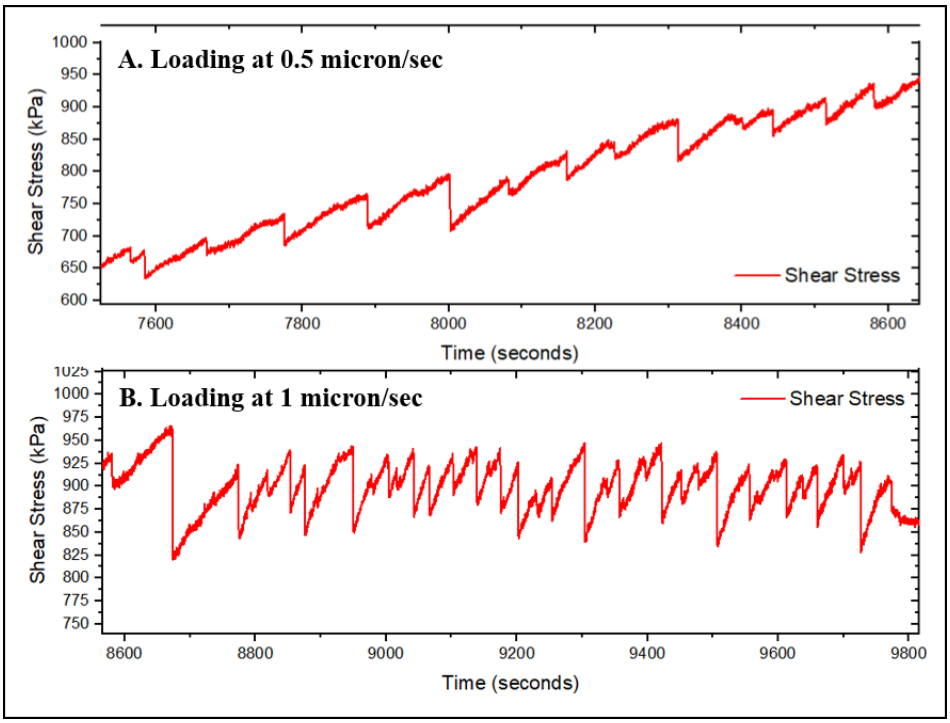

Figure 7.13: Examples of stress drops observed during loading at 0.5 and 1 micron/sec velocity for HS STFOC tether at 199 K.

7.2.3 Behavior of Ice: BDT Temperature

The ice behavior relative to the embedded tether during shearing greatly depended on temperature. At warm temperatures, the ice behaves viscously allowing the tether to cut a groove through the ice (Figure 7.14 B). This behavior is consistent in tests performed for ice at ~ 250 K using two different protocols for making ice samples (freezing with and without tethers in ice). In contrast, cracking and ultimately pulverizing of the ice was observed at the coldest temperatures, with cracking predominantly observed at the high shearing rates of 100, 200 and 300 micron/s (Figure 7.14 C, 7.15). This phenomenological brittle to ductile transition occurred at around 230 K.

Our laboratory results and BDT temperature cannot be directly scaled to Europa because BDT is not only temperature dependent, but it also depends on confining pressure and on strain rate (a broad range of which is captured in laboratory testing). On Europa, calculations of BDT temperature and depth require constraints on thermal gradient and ice chemistry. For example, with the addition of salts to the ice shell (e.g., two phase ice-$MgSO_4$ eutectic composition), the strength envelope (and BDT transition) would include a zone of semi-brittle behavior. Future tests will evaluate the role of chemistry in the observed phenomenological BDT transition.

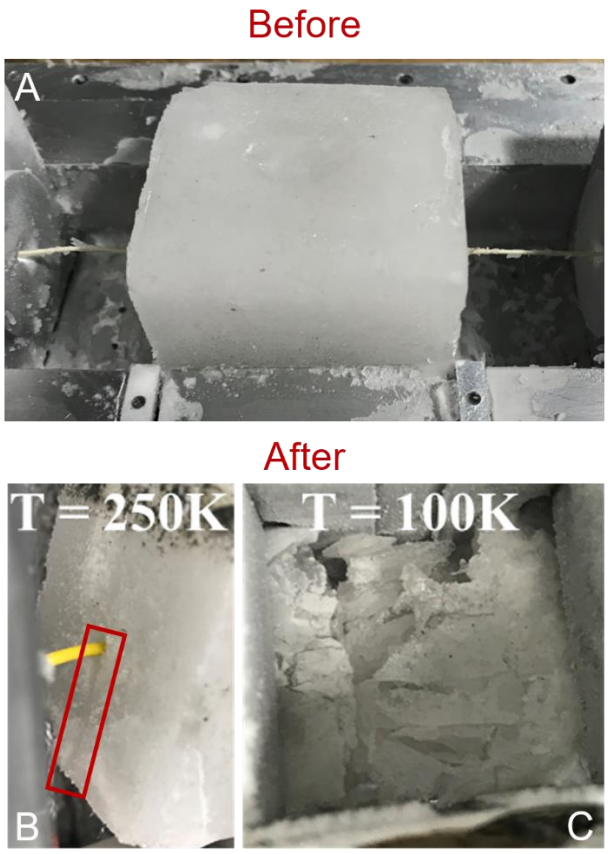

Figure 7.14: The behavior of the (A) central ice sample after shear testing depends on the temperature of the ice: (B) It behaves viscously at warmer conditions (image on left) and the tether cuts a groove; (C) at colder temperatures, the ice is pulverized (image on right).

Figure 7.15: Ice Sample with STFOC tether after shear testing at ~ 230 K (brittle portion of ice shell): the central ice block is completely pulverized.

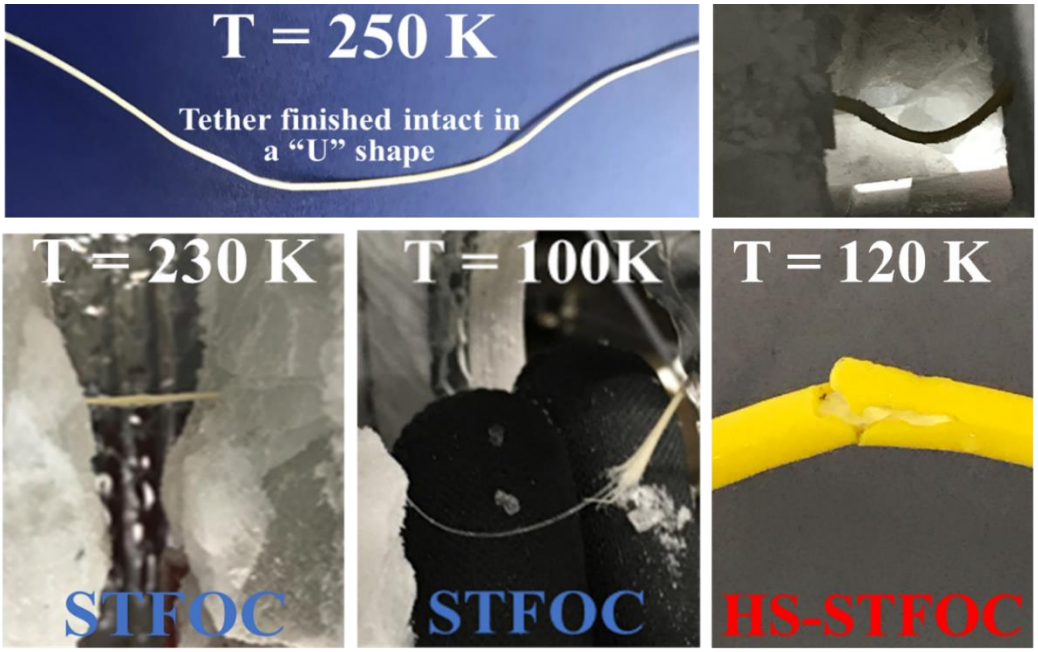

Figure 7.16: Damage to the outer layer of STFOC and HS STFOC at 100 K, to accommodate shearing, with kinks observed at lower temperatures.

7.2.4 Macroscopic Damage to Tether

Both the Linden Photonics Inc. Strong Tether Fiber Optic Cable (STFOC) and a High Strength STFOC survived shearing across pre-existing 'ice-faults' in a pure water ice shell (Figure 7.16). At intermediate to warm temperature conditions (195-260 K), the tethers remain largely undeformed, finishing in a u-shape after testing. Only at the coldest temperatures (~ 100 K) and highest velocities tested (3 x 10-4 m/s), did I observe that the LCP strength jacket of the STFOC tether broke, revealing the intact optical fiber inside. The HS STFOC tether also survived at the coldest temperatures, with a minor cut to the outer polyurethane jacket and a kink at the shear interface. No damage was observed to the Kevlar braid, LCP strength member or the optical fiber inside. At these temperatures, the

ice is cold (and hard) enough to partially prevent any movement of the tether through the ice to accommodate the vertical stress. However, the tethers proved robust to these conditions, with increased confidence in the HS STFOC tethers.

7.2.5 Microscopic Characterization of Ice Samples After Testing

Exemplars of both warm (260 K) and cold (195 – 199 K) ice samples were evaluated to constrain the grain size of the ice (Figure 7.17 D), as described in Section 7.1.2.2, and identify deformation patterns. Consistent with the macroscopic observations of ductile behavior of ice at warm temperatures (250 – 260 K) described in Section 7.2.1, microscopic grooves cut by tethers are visible at the interfaces and around the center of the sample housing the tether, with a surrounding flow-like pattern due to potential melting and refreezing of the ice (Figure 7.17 A, B). At colder temperatures, with progressing cracking of the central blocks of ice and macroscopic observations of brittle behavior (from 230 K to 100 K), microscopic fractures are visible in both the central and side blocks (Figure 7.15). Microscopic characterization of post-tested samples revealed a large network of fractures pervading the ice samples (Figure 7.18), which likely lowered the strength of the ice and allowed movement of the tether through the surrounding ice, resulting in survival at colder temperatures.

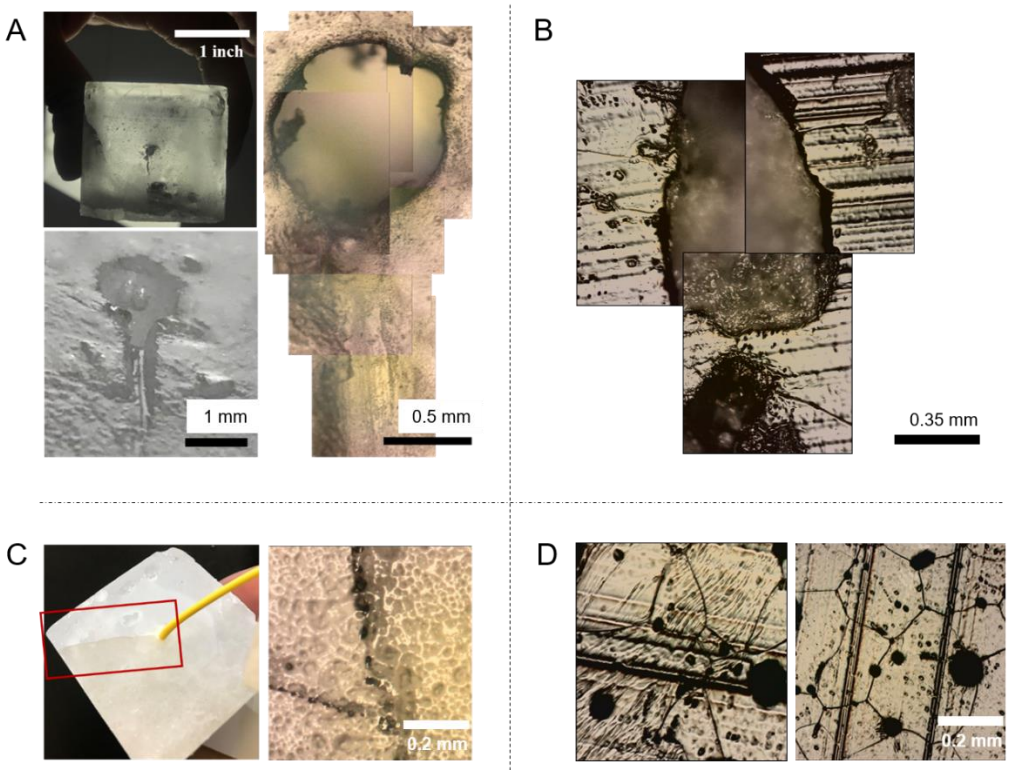

Figure 7.17: Visual and microscopic characterization of ice samples after testing reveal: (A, B) at 260 K, grooves cut in the ice by a tether; (C) at 230 K, fractures in the ice. (D) images of ice away from the tether were used to characterize the grain size of the ice, which was found to be uniform over the specimens tested.

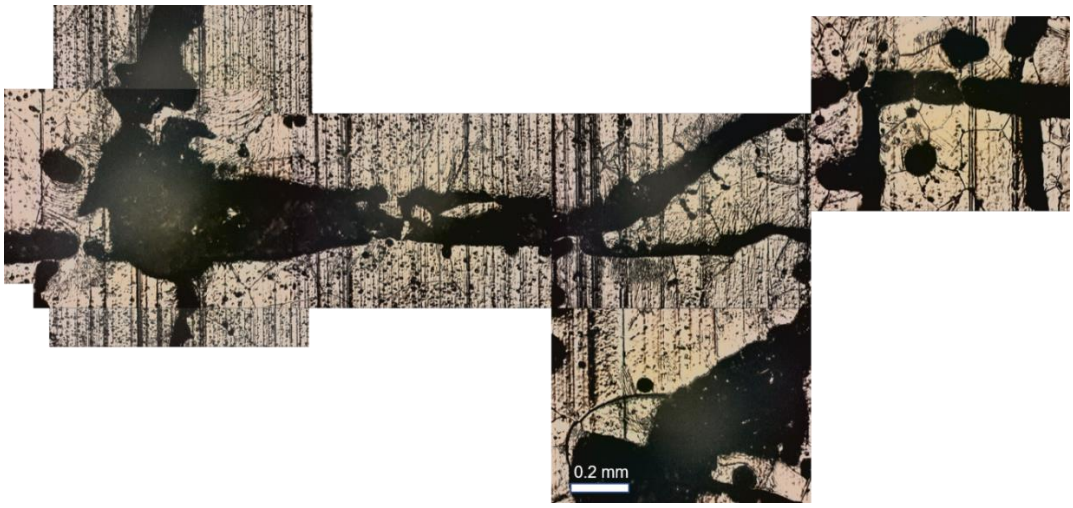

Figure 7.18: Fracture network formed inside ice sample post shear testing at 199 K.

7.2.6 Optical Signal Loss Characterization

I attempted to record the optical signal and any subsequent transmission loss for both Linden tethers, using the procedure mentioned in the section 7.1.3.2. The optical meter reports -90 dB if no signal is detected, with higher reported values (e.g., 1-2 dB to -70 dB) indicating data transmission. Transmission loss is determined by the relative change in signal during testing.

7.2.6.1 Linden Photonics Inc. STFOC

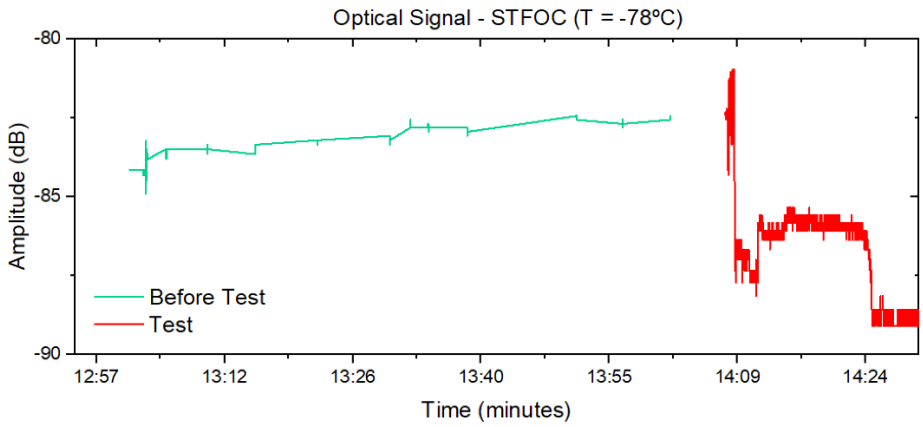

Figure 7.19: Optical Signal recorded for Linden Photonics Inc. STFOC tether at 195 K.

The optical signal was collected for STFOC tethers at 195 K, with a very low signal (approximately -83 dB) post freezing in ice and after fusion splicing (see Figure 7.19). The source of low transmission signal at the start of testing can either be issues in (i) fusion splicing, or (ii) due to crimps/breaks in the fiber during loading inside the ice fabrication

mold or during testing. During the velocity driving program runs, I observe another drop to -90 dB implying complete loss of signal.

The recorded signal for STFOC tethers is currently insufficient for successful data transmission and could potentially rule them out for application in any future mission. However, before such a classification is made, a new set of spatial measurements are required with a high-resolution optical backscatter reflectometer (future work detailed in Section 7.2.7) to investigate the source of initial signal loss.

7.2.6.2 Linden Photonics Inc. HS STFOC

The optical signal was successfully collected for HS STFOC tethers for the temperature range of 120 K to 250 K, with individual measurements at 250 K, 237 K, 220 K, 199 K and 120 K, as shown in Figure 7.20. There is an observed transmission loss of approximately -30 dB or -65 dB prior to the freezing of tether in ice or the start of shear testing. We can assign the 35 dB difference (i.e., between -30 dB and -65 dB loss) to an issue with fusion splicing in initial testing, as the final two tests with the observed -30 dB loss were:

1. At 237 K, where a pigtail connector was pre-attached to the tether.
2. At 120 K, the fibers were perfectly aligned during splicing.

While this initial loss is concerning, the signal is better than the STFOC tether. Further investigation (with spatial distribution of signal) is again required to identify the cause of signal loss prior to testing: crimps or breaking of the tether during sample handling versus an issue with signal detection in the low-resolution optical power meter used.

During shear testing, the relative drop in signal is negligible at ~ 250 K, 237 K and 120 K, with variations in the range of ±0.05 (min) to ±1.0 dB (max) observed during velocity ramps (creeping faults to ice quakes, respectively). The low signal to noise ratio at 199 K adds a ±5 dB error to the signal, which remains consistent throughout testing, and is difficult to correlate to velocity drops. At ~ 250 K, an additional event with -6 dB drop is observed at 10:40, which is assigned to human intervention (the tether was accidentally displaced by the author). At ~11:05, a small amount (1.4 dB) of permanent damage is recorded, while at ~11:10, the meter again notes the strain but recovers quickly. For the 220 K test, a similar drop and recovery of -1.5 dB is recorded at ~13:05. Correlation between these signal drops and strain due to velocity ramps reveals the capabilities of tethers as strain gauges (Figure 7.20).

At the end of testing, the HS STFOC tether is manually cut which coincides with a drop in signal to -90 dB (purple curve), implying total loss. I can thus conclude that the tether was transmitting signal (at -30 dB or -65 dB) throughout testing, up to the time of failure due to cutting of the tether. Coupled with the consistency in optical signals recorded during shear testing at cryogenic temperatures, it increases our confidence in the data transmission abilities of HS STFOC tethers for future missions.

Figure 7.20: Optical signal recorded for Linden Photonics Inc. HS STFOC tether at: (A) ~ 250 K, (B) 237 K, (C) 220 K, (D) 199 K, and (E) 120 K, highlighting variations in signal (±0.5 to ±5.0 dB) during velocity ramps.

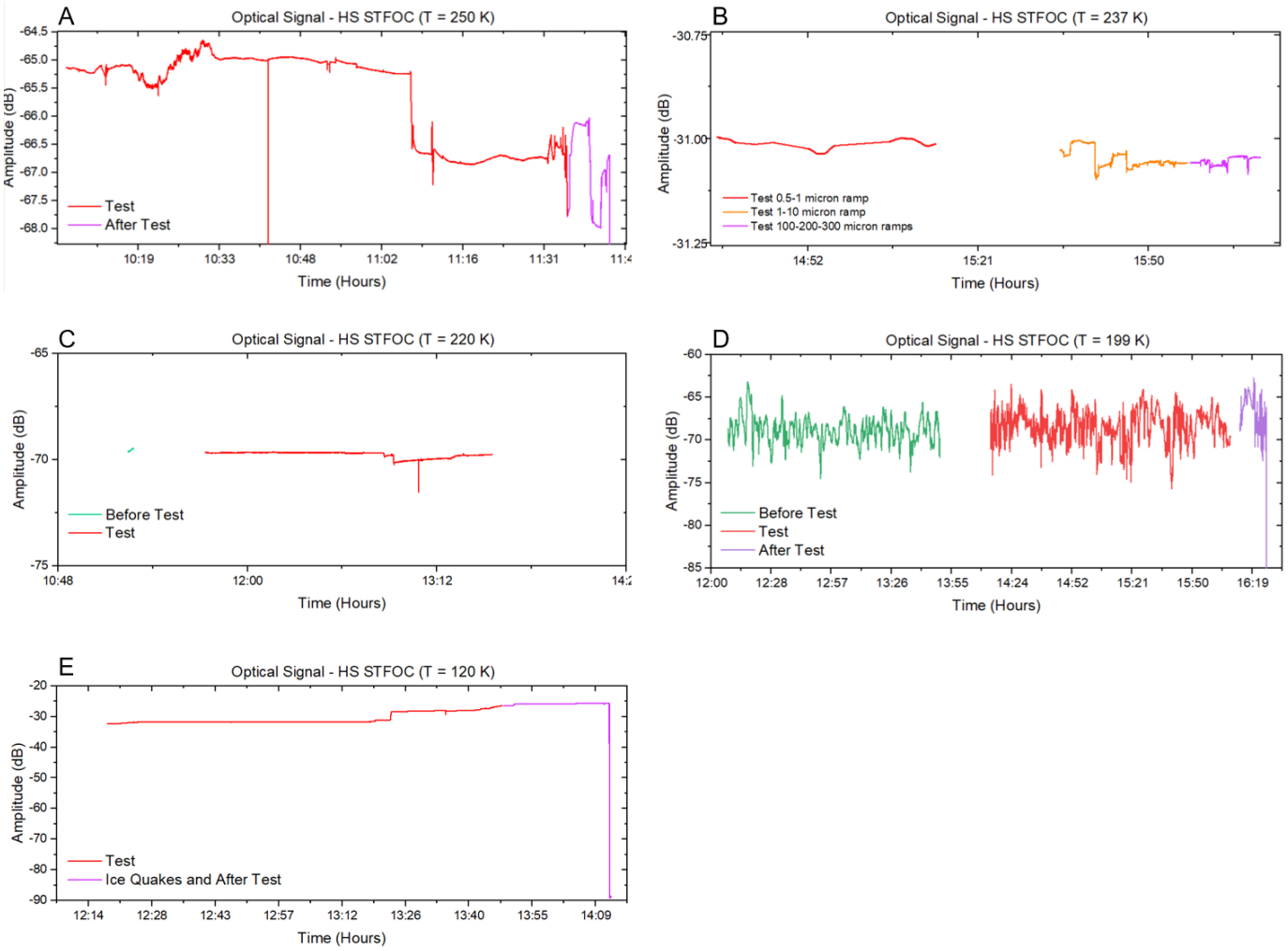

7.2.7 Strain and Sub-mm Optical Measurements: Proof of Concept to Demonstrate Tether Science Capabilities

Using a high-resolution Luna OBR 4600 Optical Backscatter Reflectometer (OBR) as a proof-of-concept, I was able to perform distributed sensing during shear testing: to monitor changes in strain along the 3-meter-long fiber, at a spatial resolution of 10 microns. Our results demonstrate that this unit was capable of identifying the location of the two shear planes (or faults) between the central and side blocks (see Figure 7.22). It was also able to locate two strain events due to shearing at the mandrels on each side, with minor variations in strain at the catenaries.

In additional optical measurements (with sub-mm resolution along the length of the tether), a similar trend in optical signal is observed (to section 7.2.5), with initial optical transmission loss (prior to testing), consistent behavior in signal during testing, and complete failure after manually cutting the wire. Using the additional capabilities of the Luna instrument, I was also able to locate the signal loss along the length of the tether (with sub-mm resolution) frozen inside the sample and identify the location of the ice faults. Figure 7.21 broadly shows two signal peaks corresponding to the two fault planes where the tether is under strain.

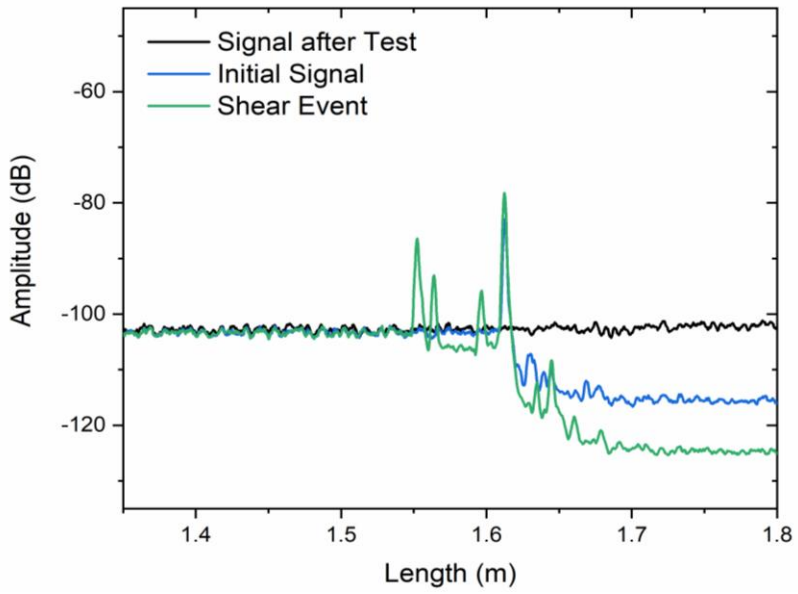

Figure 7.21: Optical signals recorded by Luna OBR instrument show sub-mm resolution variations in signal strength.

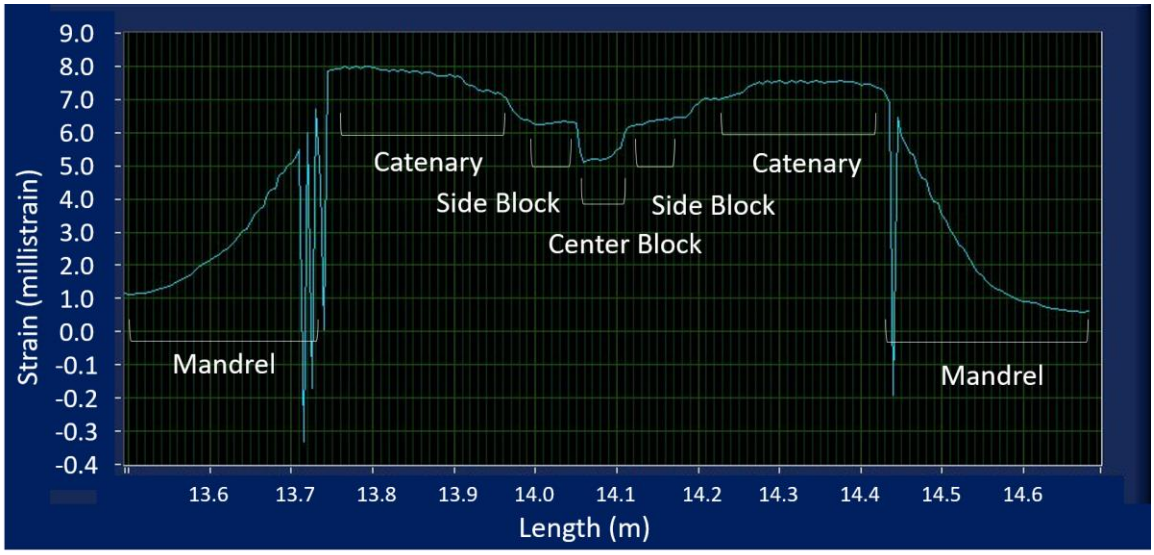

Figure 7.22: Strain measurements of STFOC tether as a proof of concept.

7.3 Discussion

7.3.1 Do Tethers have a viable application to exploration of ice shells on ocean worlds? – An interdisciplinary approach

7.3.1.1 Modeling and Laboratory Testing

Our cryogenic laboratory tests indicate that both the Linden STFOC and HS STFOC tethers can survive displacements of 1.5 – 2.4 cm for a total tether length of 13.2 cm embedded in the ice, with minor damage to the outer jackets at 100 K. In this section, we compare these laboratory displacement results to predicted tidally induced slip displacements at icy faults - to determine survivability of technology to faulting motions observed on icy satellites. This allows us to contextualize hardware tolerance and performance of the tethers and identify where in the ice shell they are viable for exploration.

Initial models of stress and fracture formation in Europa's ice shell have been pursued (Figure 7.23; Lien *et al*., 2020, 2021) to quantitatively characterize the stress and strain imposed by surface faults, at 5º, 20º and 45º orientations from vertical, on a melting cryobot (5.2-m-long with a 0.5-m diameter following Oleson *et al*. 2019) and its communication tether. Each fault was modeled to a depth of 900 m within the brittle portion of a homogenous ice shell (density = 920 kg/m^3), with the minimum and maximum expected coefficients of friction of ice, μ = 0.1 and 0.55 (Beeman *et al*., 1988). Tidal stress data from models by Walker *et al*. 2020 were applied to these fault models at Europa's sub-

Jovian point (latitude 0º, longitude 0º) as an end member scenario for maximum tidal stress. Displacements resulting from a fault slip event were calculated at the order of ~ a few cm.

Of the faults modeled, the Lien *et al*. 2021 initial results predict only the 45º fault (with coefficient of friction = 0.1) would exceed our lab maxima displacement with displacements up to ~ 3 cm. A coefficient of friction = 0.1 is low compared to experimentally derived friction (0.26 – 0.65) at these velocity and temperature conditions by Schulson *et al*., 2012 (Table 2), and represents a more extreme scenario. These results increase our confidence in the robustness of both Linden tether types we tested to survive at the environmental conditions expected in a pure, seismically active water ice shell, for most faults of orientation 0º through 20º irrespective of peak stresses, shear velocities, expected displacement, or ice behavior. Therefore, tethers may offer a viable pathway for exploration of Europa's interior with further tether design development possible to increase the robustness to the more extreme fault conditions.

Furthermore, the distributed sensing capabilities of tethers demonstrated here (section 7.2.6) is extremely exciting for ocean world exploration. The ability to use tethers as strain gauges to record the strain profile of the ice shell, estimate the temperature profile, and constrain fault orientations and motions at depth provides additional mission capabilities for characterizing the interior of the ice shell.

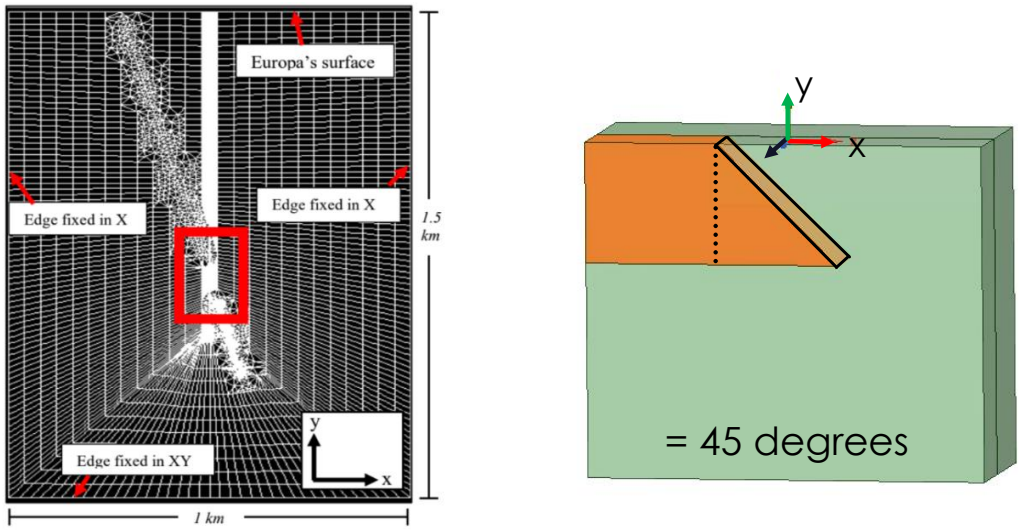

Figure 7.23: Modeled fault within Europa's ice shell (in 2D and 3D) at specified angle of 45º from vertical, disconnected by cryobot melting. Communication tether is subjected to fault displacement, which was modeled for two coefficients of friction (Lien *et al*. 2021).

7.3.2 Limitations

Although the tethers survived the shear tests, at the coldest temperatures (~100 K) the outer jackets were damaged, and inner fibers stretched showing a need for further tether development. Further, the shear tests performed do not represent the full range of potential damage that may be inflicted on a tether, both in terms of geometry of stressing and chemistry of surrounding ice. Optical transmission results indicate a need to eliminate signal loss prior to testing, with improved fusion splicing, handling, and/or loading of tethers in the sample.

Ongoing modeling efforts from the previous section have identified the need for further shear testing at greater displacements, which can be achieved by modifying the driving velocity program in future work.

7.3.3 Future Work

From a laboratory perspective, future tests have been proposed by our team to explore additional material properties (e.g., adhesive strength) and performance of the Linden Photonics Inc. HS STFOC and additional tethers with different jacketing material and strength layers, focusing on ideal performance at specific temperature/chemical conditions and considerations for reducing overall mass. Results from these tests can be used to develop a custom prototype tether with enhanced strain tolerance that incorporates a "loose tube" construction, which in turn will be performance tested. In future testing, we will also focus on strain and temperature measurements using the OBR 4600 to create strain and thermal profiles of ice samples during laboratory testing and in field campaigns.

From a modeling perspective, the cycle of tidal bulging on Europa is expected to result in a back-and-forth motion along the fault, but fault displacements are poorly constrained. There is a need to globally explore faults on Europa's surface and over the entire tidal cycle to simulate when fault "events" would be likely to occur, and at what depth, and to determine overall total deformation.

The next phase of research beyond that outlined here would be to implement a program of representative testing in the field, coupled to a model cryobot, using a combination of cryogenic chambers to reproduce the extremely cold, hard and brittle conditions expected at the outer shell of Europa or Enceladus and field deployments drilling into Earth's cryosphere to approach the warmer and more ductile conditions to be encountered deeper, closer to and at their ice-water interfaces, where conditions particularly conducive to life are anticipated. As more data, and better constraints, become

available (e.g., from the Europa Clipper mission), we will be well-positioned to assess the efficacy of available tethers and identify any required improvements to make them viable within Europa's ice shell.

7.4 Comments and Recommendations

Our work represents the first stage to enabling the search for extraterrestrial life and exploration of an ocean world, through evaluation of tethered techniques as a means of communication with a cryobot, tunneling its way through an ice shell to access an underlying ocean. I have attempted to raise the Technology Readiness Level (or TRL) of tethered communication technology to 4, through a robust set of laboratory tests, and eliminated some of the technical risk to the overall penetration system. Ongoing and proposed laboratory tests coupled with field deployment will further enhance our capabilities for exploration of ocean world interiors, with a target mission to the outer solar system in the 2030s.

On a subsystem scale, I have identified the limitations of commercially available tethers, and identified the Linden Photonics Inc. High Strength STFOC tether (HS STFOC) as a viable selection for future testing. Subsequent development of custom tether concepts based on the HS STFOC design (with lighter jacket materials, enhanced strain tolerance, etc.) are recommended for application to various ocean world chemistries.

Finally, there is a need for continued financial support to improve our current understanding of ice shell and ocean properties (to identify environmental hazards), and to develop sub-systems to a maturity ready for preliminary design within the next decade.

CHAPTER 8

CONCLUSIONS AND FUTURE WORK

8.1 How Far Have We Come? Advancements to Support Future Exploration

In support of the exploration of potentially habitable Ocean Worlds, this dissertation provides two major advances, as detailed in the previous chapters. First, improvements in spectroscopic diagnostic capabilities for interpretation of icy surfaces have been achieved (Chapter 4), with inclusion of environmental parameters like thermal history, controls on sample properties like thickness and grain size, and sufficient spectral coverage for robust comparison to spacecraft observations (Chapter 3). New protocols for laboratory spectroscopy are provided, and the integrated band area ratio technique is used to estimate Europa's leading hemisphere bulk crystallinity as 47-52% and age (Chapter 5). The cratering record of Europa is also evaluated along with the limitations of image resolution to contextualize age estimates from crystallinity. Based on these findings, the role of complex processes which govern the evolution of icy worlds can now be approximately quantified, the lack of constraints on surface conditions revealed, which now need to be addressed, and a framework has been developed to select target sites of interest for future in-situ exploration (Chapters 4 and 5). Recommendations are also included for Europa Clipper measurements.

Second, some of the technical risk to a cryobot mission to Ocean Worlds has been retired by improving the TRL of tethered communication technology to 4 (Chapter 7). This

advance has been achieved by identifying the limitations and optical performance of tethers for exploration of seismically active icy interiors. Expected range of temperature and velocity conditions in Europa's ice shell are simulated in a laboratory and the mechanical properties of the ice shell, which a melt probe and its tether would encounter, are characterized. Surprisingly, some of the tethers (e.g., Linden Photonics Inc. High Strength STFOC) are identified to be robust to testing and are recommended for further analysis and field deployment.

Combined, these findings enable new discoveries of ocean worlds and provide yet another foothold towards answering key questions about Europa's spatially varying surface properties, its ocean chemistry, and ultimately its habitability.

8.2 Future Steps

The techniques presented in this dissertation are broadly applicable to icy ocean worlds and can help unravel their diversity, characterize their ice shells at the surface and the interior, and guide ongoing and future technology development for assessing their habitability. New questions and avenues of research have also been identified, and to conclude this work, I propose select research topics to be pursued in the short term to augment our findings and discuss my long-term goals as an experimental geologist.

8.2.1 Short-Term Projects

Experiments are generally limited in scope by the availability of equipment. With the development of new capabilities at ISL, I can study ices of various chemistries (e.g., with NaCl, $MgSO_4$, H_2SO_4, etc.), with grain size-controlled reflection spectroscopy at various temperatures and irradiation conditions (electrons, protons, and ions). Calculation of optical constants of these ices using reflection spectra, instead of the traditional transmission spectra, remains a priority. The robustness of the Chapter 4 and 5 results could also be tested by spectroscopy of D_2O ice and/or diffraction experiments on MI, FI ice samples to unambiguously determine the amorphous to crystalline ice fraction and end member ratios.

Calculation of laboratory end members of 100% amorphous and crystalline water ice at other grain sizes is currently being pursued, for application to crystallinity and age calculations of Europa, Callisto, and Ganymede in the Jovian system, and Enceladus in the Saturnian system (using Equations 5.1 and 5.2). Other icy worlds in the Uranian and Neptunian systems such as Ariel, Umbriel, Titania, Oberon, and Triton will be investigated in future, using available spectral observations, to provide a comprehensive overview of the distribution of water ice (and age) in the outer solar system, and to prepare for a future ice giants mission and the potential Trident mission. This approach of comparative planetology for crystallinity and age estimates in the outer solar system, with consideration for changing radiation flux and thermal crystallization rates, will improve our understanding of active surface processes, surface composition, and evolution on native

ice-giant satellites, Kuiper Belt Objects (KBO), and Ocean Worlds. It also provides an alternate method of age classification.

However, to increase confidence in age estimates using crystallinity, we first need to investigate the source of discrepancies with cratering age on Europa, and overcome the lack of constraints on surface conditions in the outer solar system. (1) We need to further account for the role of geophysical processes and provide better constrains on the surface temperature and particle flux. I envision a two-fold modeling and geomorphological plus mapping analysis for localized characterization of present-day surface properties on Europa, and generation of spatial density maps of endogenic versus exogenic geological features. (2) Ground Truth: Ganymede is our solar system's only known moon with an intrinsic, global magnetic field, and a target for the upcoming ESA JUICE mission: it offers an end member case for improving age calculations with crystallinity, using well constrained equation parameters for surface conditions (of temperature, ion flux). Understanding the age and evolution of ice on Europa and Ganymede, and its correlation to surface geology will be essential to enhancing the science return of future missions.

In Part II of this dissertation, I investigated a tethered architecture that could survive on Jupiter’s moon, Europa, owing to its high potential for a near term subsurface exploration missions. The environmental conditions simulated in our laboratory tests mirror those predicted for Europa’s ice shell, however, these conditions and test results are also relevant to other icy worlds in the outer solar system. I propose a detailed future study, to identify the range of (interior) conditions expected on the suite of possible ocean worlds and determine whether a cryobot would work on all icy worlds, or if there is a need to develop independent concepts tailored to the requirements of each ocean world.

Building off the results presented in Chapter 7 with support from the NASA COLDTech program, our team will design, build, and test a robust optical communication tether prototype for ocean world conditions. We will explore the performance of HS STFOC and additional tethers with different jacketing material and strength layers, develop a custom "loose tube" prototype with enhanced strain tolerance, and extend the shear testing to account for tethers being pulled along length within ice, measuring its adhesion to ice. Our focus is on achieving ideal performance at relevant temperatures and chemical conditions, with considerations for reducing overall mass and improving TRL to 5, followed by field deployment (as detailed in Chapter 7, Section 7.3.3).

8.2.2 Long-Term Goals

The proposed criterion for selection of target sites of young, oceanic material on icy ocean worlds (Chapter 5) represents another step towards reconnaissance assistance for a future lander or a melt probe, building on the results of this dissertation and research over the past two decades. In the longer term, there is a need to develop this criterion further, combining investigations using remote sensing data, laboratory studies, and modeling to improve our understanding of the surface physics and chemistry of (icy) ocean worlds, asteroids, comets, and now, interstellar objects. Specifically, we need to address the questions of: *What is the composition of the surface, and how does it vary from the equator to the poles, and at sites of suspected recent activity like chaos terrain? How is ice (thermally and mechanically) processed at locations of faulting on icy worlds or during impact events?* Future work will address these questions with spectral unmixing of existing

Galileo NIMS datasets and future Europa Clipper and JUICE measurements of icy worlds. Coupled with laboratory datasets, acquired with the unique testing capabilities for ice spectroscopy and mechanics which I have developed in this dissertation, we will get closer to unraveling the history of ice in the outer solar system.

Future exploration of Ice Giants and their satellites, which include potential ocean worlds and a captured KBO with active plumes, offer another tantalizing opportunity to learn about the environmental conditions and formation (or evolution) mechanisms at work in the outer solar system – currently unknown parameters in the age equation (5.2). A future orbiter mission to the Uranian and/or Neptunian systems with: (1) a magnetometer and a plasma/energetic particle detector (to determine magnetic field strength, orientation, and composition of ions), (2) a UV-VIS-NIR spectral imager (~0.2 to 5 μm wavelength coverage to determine surface composition), and (3) a narrow-angle imager (resolution of ~50 m per pixel for global mapping) can address existing knowledge gaps. With up to ~65% of their masses made of water ice and other ices like methane and ammonia (Guilot *et al.* 2005), the techniques presented in this dissertation can also be applied to determine the diverse surface geology and age of their satellites. It will provide key information about how resurfacing processes such as cratering, tectonics, plume deposition and cryovolcanism operate at cryogenic temperatures. It may also help find young terrains on their surfaces with potential biosignatures. Therefore, they will be a focus of my research.

Circling back to the question I posed earlier: *How do we access the interior of an ice shell?* Development of laboratory instrumentation coupled with analog field research can help develop new pathways for exploration, and I will continue to pursue this work, with the goal of becoming an instrument scientist for missions to the outer solar system.

REFERENCES

Allen, M., P. Beauchamp, R. Carlson, K. Cooper, B. Drouin, J. Pearson, H. Pickett, D. Rodgers, P. Siegel, A. Skalare, S. Gulkis, S. Chattopadhyay (2008), "Astrobiology from europan orbit", Astrobiology Science Conference 2008, San Jose, California, Astrobiology 8:2, 296.

Ampuero, J.P. and A. M. Rubin (2008), "Earthquake nucleation on rate and state faults: Aging and slip laws", Journal of Geophysical Research 113.

Anderson J. D., G. Schubert, R. A. Jacobson, E. L. Lau, W. B. Moore, W. L. Sjogren (1998), "Europa's differentiated internal structure: inferences from four Galileo encounters", Science 25; 281(5385): 2019-22. PMID: 9748159.

Ashkenazy, Y. (2016), "The surface temperature of Europa", Heliyon **5**(6): e01908.

Baragiola, R.A., M. A. Fama, M. J. Loeffler, M. E. Palumbo, U. Raut, J. Shi, G. Strazzulla (2013), "Radiation Effects in Water Ice in the Outer Solar System", in: The Science of Solar System Ices, Gudipati, M.S., Castillo-Rogez, J. (Eds.), Astrophysics and Space Science Library: 527.

Bar-Cohen, Y. and K. Zacny (2009), "Drilling in extreme environments: penetration and sampling on Earth and other planets", Hoboken, NJ: Wiley press, 825 pp.

Barnett, I. L., A. Lignell, M. S. Gudipati (2012), "Survival depth of organics in ices under low-energy electron radiation (<= 2 keV)", The Astrophysical Journal **747**(1): 13.

Beeman, M., W. B. Durham, S. H. Kirby (1988), "Friction of ice", Journal of Geophysical Research **93**: 7625–763.

Beeler, N. M., T. E. Tullis, and J. D. Weeks (1994), "The roles of time and displacement in the evolution effect in rock friction", Geophysical Research Letters **21**: 1987-1990.

Bekaert, D. V., G. Avice, B. Marty, B. Henderson, M. S. Gudipati (2017), "Stepwise heating of lunar anorthosites 60025, 60215, 65315 possibly reveals an indigenous noble gas component on the Moon", Geochimica et Cosmochimica Acta **218**: 114–131

Berdis, J. R., M. S. Gudipati, J. R. Murphy, N. J. Chanover (2020), "Europa's surface water ice crystallinity: Discrepancy between observations and thermophysical and particle flux modeling", Icarus 341, 113660.

Berdis, J. R. (2021), "Implications for Surface Processes through the Investigation of Crystalline and Amorphous Water Ice on Europa". Ph.D. thesis. New Mexico State University.

Bertie, J. E. and E. Whalley (1964), "Infrared spectra of ice i_h and i_c in the range 4000 to 350 cm^{-1}", Journal of Chemical Physics **40**(6): 1637–1645.

Bierhaus, E.B., K. Zahnle, C. R. Chapman (2009), "Europa's Crater Distributions and Surface Ages", in: Europa, Pappalardo, R.T., McKinnon, W.B., Khurana, K.K. (Eds.), p. 161.

Blaney, D.L., C. Hibbitts, R. O. Green, R. N. Clark, J. B. Dalton, A. G. Davies, Y. Langevin, J. I. Lunine, M. Hedman, T. B. McCord, S. L. Murchie, C. Paranicas, F. P. Seelos, J. M. Soderblom, S. Diniega, M. Cable, D. Thompson, C. Bruce, A. Santo, R. Redick, D. Hahn, H. Bender, B. Van Gorp, J. Rodriguez, P. Sullivan, T. Neville, S. Lundeen, M. Bowers, B. Bryce, J. Hayes, R. Hourani, K. Ryan, E. Zarate, L. B. Moore, K. Maynard, I. M. McKinley, D. Johnson, P. Aubuchon, J. Fedosi, R. Wehbe, R. Calvet, P. Mouroulis, V. White, D. Wilson (2019), "The Europa Clipper Mapping Imaging Spectrometer for Europa (MISE): Using Compositional Mapping to Understand Europa", in: Lunar and Planetary Science Conference, p. 2218.

Booth, A. D., P. Christoffersen, C. Schoonman, A. Clarke, B. Hubbard, R. Law, S. H. Doyle, T. R. Chudley, A. Chalari (2020), "Distributed Acoustic Sensing of Seismic Properties in a Borehole Drilled on a Fast-Flowing Greenlandic Outlet Glacier", Geophysical Research Letters 47(13): e2020GL088148.

Bowen, A.D., Yoerger, D.R., Taylor, C., Mccabe, R., Howland, J., Gomez-Ibanez, D., Kinsey, J.C., Heintz, M., McDonald, G., Peters, D. and Young, C. (2009), "The Nereus hybrid underwater robotic vehicle", Underwater Technology, **28**(3), pp.79-89.

Bryant, S. (2002), "Ice-embedded transceivers for Europa cryobot communications. In Proceedings", IEEE Aerospace Conference 1. pp. 1-356.

Buratti, B. (1983), "Photometric Properties of Europa and the Icy Satellites of Saturn", Ph.D. thesis. Cornell University, New York, NY.

Buratti, B., M. Golombek (1988), "Geologic implications of spectrophotometric measurements of Europa", Icarus **75**, 437-449.

Busarev, V.V., A. M. Tatarnikov, M. A. Burlak (2018), "Comparison and Interpretation of Spectral Characteristics of the Leading and Trailing Hemispheres of Europa and Callisto", Solar System Research **52**: 301-311.

Cable, M.L., M. Neveu, H.W. Hsu, and T.M. Hoehler (2020), "Enceladus", In: Planetary Astrobiology (Eds: V.S. Meadows, G.N. Arney, B.E. Schmidt and D.J. Des Marais). University of Arizona Press, 217-246.

Carr, M. H., M. J. S. Belton, C. R. Chapman, M. E. Davies, P. Geissler, R. Greenberg, A. S. McEwen, B. R. Tufts, R. Greeley, R. Sullivan, J. W. Head, R. T. Pappalardo, K. P.

Klaasen, T. V. Johnson, J. Kaufman, D. Senske, J. Moore, G. Neukum, G. Schubert, J. A. Burns, P. Thomas, and J. Veverka (1998), "Evidence for a subsurface ocean on Europa", Nature **391**: 363–365.

Carlson, R.W., M.S. Anderson, R.E. Johnson, M.B. Schulman, and A.H. Yavrouian (2002), "Sulfuric acid production on Europa: the radiolysis of sulfur in water ice", Icarus, 157, 456–463.

Carlson, R. W., W. M. Calvin, J. B Dalton, G. B. Hansen (2009), "Europa's Surface Composition", In Europa. R. T. Pappalardo, W. B. McKinnon and K. Khurana. Tucson, Arizona, USA, The University of Arizona Press: 283-328.

Chen, J., and C. Yoo (2011), "High density amorphous ice at room temperature", Proceedings of the National Academy of Sciences, **108**, 7685 - 7688.

Cheng, A.F., P. K. Haff, R. E. Johnson, L. J. Lanzerotti (1986), "Interactions of planetary magnetospheres with icy satellite surfaces", in: Burns, J.A., Matthews, M.S. (Eds.), IAU Colloq. 77: Some Background about Satellites: 403-436.

Chester, F. M. (1994), "Effects of temperature on friction: Constitutive equations and experiments with quartz gouge", Journal of Geophysical Research **99**(B4), 7247-7261.

Chyba, C.F. and C.B. Phillips (2001), "Europa as an Abode of Life. Origins of Life and Evolution of Biospheres", Origins of Life and Evolution of Biospheres **32**(1), 47-68.

Chyba, C. F. and C. B. Phillips (2001), "Special Feature: Possible ecosystems and the search for life on Europa", Proceedings of the National Academy of Sciences **98**: 801–804.

Clark, R. N. (1980a). "Water frost and ice: The near-infrared spectral reflectance 0.65–2.5 μm." Journal of Geophysical Research Solid Earth **86**(B4): 3087-3096.

Clark, R.N., F. P. Fanale, A. P. Zent (1983), "Frost grain size metamorphism: Implications for remote sensing of planetary surfaces", Icarus **56**: 233-245.

Clark, R. N. and T. L. Roush (1984). "Reflectance spectroscopy: Quantitative analysis techniques for remote sensing applications", Journal of Geophysical Research Solid Earth **89**(B7): 6329-6340.

Clark, R. N., R. Carlson, W. Grundy, K. Noll (2013), "Observed ices in the Solar System", in: The Science of Solar System Ices, Gudipati, M.S., Castillo-Rogez, J. (Eds.), Astrophysics and Space Science Library: 3-46.

Collins, G., and F. Nimmo (2009), "Chaotic Terrain on Europa", in: Europa, Pappalardo, R.T., McKinnon, W.B., Khurana, K.K. (Eds.): 259.

Collins, G. C., B. B. Cutler, J. P. Brenes Coto, L. M. Prockter, W. W. Patterson, S. A. Kattenhorn, A. R. Rhoden, and C. M. Cooper (2016), "Plate motions on Europa from Castalia Macula to Falga Regio", Lunar and Planetary Science Conference, #1903.

Cook, J.C., S. J. Desch, T. L. Roush, C. A. Trujillo, T. R. Geballe (2007), "Near-Infrared Spectroscopy of Charon: Possible Evidence for Cryovolcanism on Kuiper Belt Objects", The Astrophysical Journal **663**: 1406-1419.

Cooper, J.F., R. E. Johnson, B. H. Mauk, H. B. Garrett, N. Gehrels (2001), "Energetic Ion and Electron Irradiation of the Icy Galilean Satellites", Icarus **149**: 133-159.

Cole, D. M. (1979), "Preparation of polycrystalline ice specimens for laboratory experiments. Cold Regions Science and Technology", **1**: 153-159.

Cruikshank, D. P (1993), "Icy Bodies in the Solar System: Present and Future of Infrared Studies", Astronomical Society of the Pacific, Vol. **41**:21.

Cwik, T., W. Zimmerman, A. Gray, B. Nesmith, R.P. Casillas, J. Muller, D. Bell, S. Bryant, A. Karapetian, R. Otis, K. Hand, M. Brandt, K. Zacny, and A. Sengupta (2018), "A Technology Architecture for Accessing the Oceans of Icy Worlds", 69th International Astronautical Congress, Bremen, Germany, October 1-5, 2018.

Dalle Ore, C.M., D. P. Cruikshank, R. M. E. Mastrapa, E. Lewis, O. L. White (2015), "Impact craters: An ice study on Rhea", Icarus **261**: 80-90.

Dalton, J.B., (2007), "Linear mixture modeling of Europa's non-ice material based on cryogenic laboratory spectroscopy" Geophysical Research Letters **34**: L21205.

Dalton, J. B., C. S. Jamieson, J. H. Shirley, K. M. Pitman, M. Kariya, P. Crandall (2013), "Laboratory Reference Spectroscopy of Icy Satellite Candidate Surface Materials", AGU #P34B-01.

Dachwald, B., Mikucki, J., Tulaczyk, S., Digel, I., Espe, C., Feldmann, M., Francke, G., Kowalski, J. and Xu, C. (2014), "IceMole: a maneuverable probe for clean in situ analysis and sampling of subsurface ice and subglacial aquatic ecosystems", Annals of Glaciology, **55**(65), pp.14-22.

Dieterich, J.H. (1972), "Time-dependent friction in rocks", Journal of Geophysical Research 77, 3690-3697.

Dieterich, J.H. (1978), "Time-dependent friction and the mechanics of stick-slip", Pure Applied Geophysics 116, 790-805.

Dieterich, J.H. (1979), "Modeling of rock friction, 1, Experimental results and constitutive equations", Journal of Geophysical Research 84, 2161-2168.

Doggett, T., R. Greeley, P. Figueredo, K. Tanaka (2009), “Geologic Stratigraphy and Evolution of Europa's Surface”, In Europa, Tucson, Arizona, USA, The University of Arizona Press: 137-160.

Dombard, A.J. and W.B. McKinnon (2006), “Folding of Europa’s icy lithosphere: An analysis of viscous-plastic buckling and subsequent topographic relaxation”, Journal of Structural Geology.

Domingue, D.L., B. W. Hapke, G. W. Lockwood, D.T. Thompson (1991), “Europa's phase curve: Implications for surface structure”, Icarus **90**: 30-42.

Dubois, D. (2018), “Study of Titan's Upper and Lower Atmosphere: An Experimental Approach”. Ph.D. thesis. Universite Paris-Saclay.

Fagents, S.A., R. Greeley, R. J. Sullivan, R. T. Pappalardo, L. M. Prockter, Galileo SSI Team (2000), “Cryomagmatic Mechanisms for the Formation of Rhadamanthys Linea, Triple Band Margins, and Other Low-Albedo Features on Europa”, Icarus **144**: 54-88.

Fama, M., M. J. Loeffler, U. Raut, R. A. Baragiola (2010), “Radiation-induced amorphization of crystalline ice”, Icarus **207**(1), 314-319.

Fanale, F.P., Y. H. Li, E. De Carlo, C. Farley, S. K. Sharma, K. Horton, J. C. Granahan (2001), “An experimental estimate of Europa's "ocean" composition independent of Galileo orbital remote sensing”, Journal of Geophysical Research **106**: 14595–4600.

Figueredo, P., R. Greeley, S. Neuer, L. Irwin, and D. Schulze-Makuch (2003), “Locating Potential Biosignatures on Europa from Surface Geology Observations”, Astrobiology **3**(4): 851–861.

Figueredo P., and R. Greeley (2004), “Resurfacing history of Europa from pole-to-pole geological mapping”, Icarus **167**(2): 287-312.

Fischer, P. D., M. E. Brown, and K. P. Hand (2015), “Spatially resolved spectroscopy of Europa: the distinct spectrum of large-scale chaos”, The Astronomical Journal **150**:164.

Fortes, A.D., P.M. Grindrod, S.K. Trickett, and L. Vocadlo (2007), “Ammonium sulfate on Titan: Possible origin and role in cryovolcanism”, Icarus **188**: 139–153.

Garrett, H. B., S. M. Levin, S. J. Bolton, R. W. Evans, B. Bhattacharya (2005), “A revised model of Jupiter’s inner electron belts: Updating the divine radiation model”, Geophysical Research Letters **32**(4): L04104(1-4).

Garrett, H. B., I. Katz, I. Jun, W. Kim, A. C. Whittlesey, R. W. Evans (2011), “The Jovian Charging Environment and Its Effects—A Review”, IEEE Transactions on Plasma Science **40**(2): 144-154.

German, C.R., A. D. Bowen, M. V. Jakuba, A. Boetius, V. S. N. Schlindwein, S. Bünz, E. Ramirez Llodra and the PS86 (2014), PS101 (2016) and KPH708 (2019) cruise teams (2019), "Exploring ice-covered oceans, top to bottom experiences in the Arctic with NUI(5k)". AGU Fall Meeting, Abstract # P51B-03.

German et al. Exploring Ocean Worlds: Ocean System Science to Support the Search for Life. Planet. Sci. Journal, submitted.

Gifkins, R. C. (1970), "Optical Microscopy of Metals", Elsevier, New York.

Goldsby, D. L. and D. L. Kohlstedt (2001), "Superplastic deformation of ice: Experimental observations," Journal of Geophysical Research **106**(B6): 11017-11030.

Greenberg, R., P. Geissler, B.R. Tufts, and G.V. Hoppa (2000), "Habitability of Europa's crust: The role of tidal-tectonic processes", Journal of Geophysical Research—Planets, 105(E7), 17551-17562.

Grosenbaugh, M.A., Whitcomb, L.L., Bingham, B., Gobat, J.I. and Young, C. (2007), "Numerical simulation of the deployment of a hybrid ROV optical fiber tether", In: ASME 2007 26th International Conference on Offshore Mechanics and Arctic Engineering (pp. 633-639), American Society of Mechanical Engineers.

Grundy, W.M. (1995), "Methane and Nitrogen Ices on Pluto and Triton: a Combined Laboratory and Telescope Investigation" Ph.D. thesis. The University of Arizona.

Grundy, W. M. and Schmitt, B. (1998), "The temperature-dependent near-infrared absorption spectrum of hexagonal H_2O ice", Journal of Geophysical Research **103**(Ell): 25,809-25,822.

Grundy, W. M., M. W. Buie, J. A. Stansberry, J. R. Spencer, and B. Schmitt (1999), "Near-infrared spectra of icy outer solar system surfaces: Determination of H_2O ice temperatures", Icarus **142**: 536–549.

Gudipati, M. S., and L. J. Allamandola (2004), "Polycyclic Aromatic Hydrocarbon Ionization Energy Lowering in Water Ices", The Astrophysics Journal, **615**, L177.

Gudipati, M. S. and L. J. Allamandola (2006), "Unusual Stability of Polycyclic Aromatic Hydrocarbon Radical Cations in Amorphous Water Ices up to 120 K: Astronomical Implications", The Astrophysics Journal, **638**:286-292.

Guillot, T. (2005), "The Interiors of Giant Planets: Models and Outstanding Questions", Annual Review of Earth and Planetary Sciences, **33**: 493-500.

Gundlach, B., S. Kilias, E. Beitz, J. Blum (2011), "Micrometer-sized ice particles for planetary-science experiments - I. Preparation, critical rolling friction force, and specific surface energy", Icarus **214**(2):717-723.

Gundlach, B., J. Ratte, J. Blum, J. Oesert, S. N. Gorb (2018), “Sintering and sublimation of micrometre-sized water-ice particles: the formation of surface crusts on icy Solar System bodies”, Monthly Notices of the Royal Astronomical Society **479**(4): 5272-5287.

Hagen, W., A. G. G. M. Tielens, and J. M. Greenberg (1981), “The infrared spectra of amorphous solid water ice and ice i_c between 10 k and 140 k”, Chemical Physics **56**: 367–379.

Hand, K. P., C. F. Chyba, J. C. Priscu, R. W. Carlson, and K. H. Nealson (2009), “Astrobiology and the Potential for Life on Europa”, In Europa, Tucson, Arizona, USA, The University of Arizona Press: 641-682.

Hand, K. P. and Carlson, R. W. (2015), "Europa's surface color suggests an ocean rich with sodium chloride", Geophysical Research Letters **42**(9): 3174-3178.

Hand K.P., A.E. Murray, J.B. Garvin *et al*. (2017), *Report of the Europa Lander Science Definition Team*, NASA, 264pp, (link).

Hanley, J., J. B. Dalton, V. F. Chevrier, C. S. Jamieson, R. S. Barrows (2014), “Reflectance spectra of hydrated chlorine salts: The effect of temperature with implications for Europa”, Journal of Geophysical Research (Planets) **119**: 2370-2377.

Hansen, G. B. and T. B. McCord (2004), “Amorphous and crystalline ice on the Galilean satellites: A balance between thermal and radiolytic processes”, Journal of Geophysical Research: Planets **109**(E1).

Hapke, B.W. (1963), “A theoretical photometric function for the lunar surface”, Journal of Geophysical Research **68**, 4571-4586.

Hapke, B. (1981), “Bidirectional reflectance spectroscopy. I – Theory”, Journal of Geophysical Research **86**: 3039-3054.

Hapke, B. (1984) “Bidirectional reflectance spectroscopy 3. Correction for macroscopic roughness”, Icarus **59**: 41-59.

Hapke, B. (1986), “Bidirectional reflectance spectroscopy 4. The extinction coefficient and the opposition effect”, Icarus **67**: 264-280.

Hibbitts, C. A., K. Stockstill-Cahill, B. Wing, C. Paranicas (2019), “Color centers in salts - Evidence for the presence of sulfates on Europa”, Icarus **326**: 37-47.

Henderson, B.L., M. S. Gudipati, F. B. Bateman (2019), “Leeb hardness of salty Europa ice analogs exposed to high-energy electrons”, Icarus **322**: 114-120.

Hendrix A. R., T. A. Hurford, L. M. Barge, M. T. Bland, J. S. Bowman, W. Brinckerhoff, B. J. Buratti, M. L. Cable, J. Castillo-Rogez, G. C. Collins, S. Diniega, C. R. German,

A. G. Hayes, T. Hoehler, S. Hosseini, C. J. A. Howett, A. S. McEwen, C. D. Neish, M. Neveu, T. A. Nordheim, G. W. Patterson, D. A. Patthoff, C. Phillips, A. Rhoden, B. E. Schmidt, K. N. Singer, J. M. Soderblom, S. D. Vance, (2018), "The NASA Roadmap to Ocean Worlds", Astrobiology **19**(1): 1-27. Epub 2018 Oct 13. PMID: 30346215; PMCID: PMC6338575.

Hoppa, G., B.R. Tufts, R. Greenberg, and P.E. Geissler (1999), "Formation of cycloidal features on Europa", Science **285**: 1899-1902.

Hoppa, G., R. Greenberg, B. R. Tufts, P. Geissler, C. Phillips, and M. Milazzo (2000), "Distribution of strike-slip faults on Europa", Journal of Geophysical Research **105**: 22,617-22, 627.

Hogenboom, D.L., J.S. Kargel, G.J. Consolmagno, T.C. Holden, L. Lee, and M. Buyyounouski (1997), "The ammonia–water system and the chemical differentiation of Icy Satellites", Icarus **128**: 171–180.

Howell, S. M., and R. T. Pappalardo (2018), "Band Formation and Ocean-Surface Interaction on Europa and Ganymede", Geophysical Research Letters **45**(10): 4701-4709.

Howell, S. M., W. C. Stone, K. Craft (2020), "Ocean Worlds Exploration and the Search for Life", Planetary Science and Astrobiology Decadal Survey 2023–2032.

H. Rept. 114-130 (2015, May 27) Commerce, Justice, Science, and Related Agencies Appropriations Bill, 2016. 114th Congress, House of Representatives, Washington, DC. Available online at https://www.congress.gov/congressional-report/114th-congress/house-report/130/1.

Hudson, R.L. and Moore, M.H. (2001), "Radiation chemical alterations in solar system ices: An overview", Journal of Geophysical Research **106**: 33275-33284.

Hussmann, H., F. Sohl, T. Spohn (2006), "Subsurface oceans and deep interiors of medium-sized outer planet satellites and large trans-neptunian objects", Icarus 185(1): 258-273.

Irvine, W. M., and J. B. Pollack (1968), "Infrared optical properties of water and ice spheres", Icarus **8**(1–3).

Jackson, J. D. (1975), "Classical Electrodynamics", 2nd ed., Wiley, New York, p. 131.

Jakuba, M.V., Roman, C.N., Singh, H., Murphy, C., Kunz, C., Willis, C., Sato, T. and Sohn, R.A., (2008), "Long-baseline acoustic navigation for under-ice autonomous underwater vehicle operations", Journal of Field Robotics, 25(11-12), pp.861-879.

Jakuba, M.V., C.R. German, L.L. Whitcomb, A. Branch, K. Hand, T. McFarland, A.D. Bowen, J.C. Kinsey, and S. Chien (2018), "Teleoperation and robotics under ice: Implications for planetary exploration", IEEE Aerospace, Big Sky MT. pp. 1-14.

Jaumann, R., K. Stephan, G. B. Hansen, R. N. Clark, B. J. Buratti, R. H. Brown, K. H. Baines, S. F. Newman, G. Bellucci, G. Filacchione, A. Coradini, D. P. Cruikshank, C. A. Griffith, C. A. Hibbitts, T. B. McCord, R. M. Nelson, P. D. Nicholson, C. Sotin, R. Wagner (2008), "Distribution of icy particles across Enceladus' surface as derived from Cassini-VIMS measurements", Icarus **193**: 407-419.

Jenniskens, P. and D. F. Blake (1994), "Structural transitions in amorphous water ice and astrophysical implications", Science: **265**(5173): 753-756.

Jenniskens, P. and D. F. Blake (1996), "Crystallization of amorphous water ice in the solar system", Astrophysical Journal **473**, 1104–1113.

Jenniskens, P., D.F. Blake, A. Kouchi (1998), "Amorphous Water Ice. a Solar System Material", in: Solar System Ices, Schmitt, B., de Bergh, C., Festou, M. (Eds.), p. 139.

Jewitt, D.C. and J. Luu (2004), "Crystalline water ice on the Kuiper belt object (50000) Quaoar", Nature **432**: 731-733.

Johnson, R.E., M. L. Nelson, T. B. McCord, J. C. Gradie (1988), "Analysis of Voyager images of Europa - Plasma bombardment", Icarus **75**: 423-436.

Johnson, P. V., R. Hodyss, T. H. Vu, M. Choukroun (2019), "Insights into Europa's ocean composition derived from its surface expression", Icarus **321**: 857-865.

Kargel, J.S. (1992), "Ammonia-water volcanism on icy satellites: Phase relations at 1 atmosphere", Icarus **100**: 556–574.

Kargel, J.S. and S. Pozio (1996), "The Volcanic and tectonic history of Enceladus", Icarus **119**: 385–404.

Kargel, J. S., J. Z. Kaye, J. W. Head III, G. M. Marion, R. Sassen, J. K. Crowley, O. P. Ballesteros, S. A. Grant, and D. L. Hogenboom (2000), "Europa's crust and ocean: origin, composition, and the prospects for life", Icarus, **148**(1): 226-265.

Kattenhorn, S.A., and Prockter, L.M., (2014), "Evidence for subduction in the ice shell of Europa", Nature Geoscience **7**: 762-767.

Kempf, S., N. Altobelli, C. Briois, E. Grün, M. Horányi, *et al*. (2014), "SUDA: A Dust Mass Spectrometer for Compositional Surface Mapping for a Mission to Europa", European Planetary Science Congress, Sep 2014, Cascais, Portugal. EPSC2014-229 (2 p.). insu-029227999.

Kouchi, A., T. Yamamoto, T. Kozasa, T. Kuroda, and J. M. Greenberg (1994), “Conditions for condensation and preservation of amorphous ice and crystallinity of astrophysical ices”, Astronomy and Astrophysics **290**, 1009–1018.

Kou, L., D. Labrie, and P. Chylek (1993), "Refractive indices of water and ice in the 0.65- to 2.5-μm spectral range," Appl. Opt. **32**, 3531-3540.

Law, R., P. Christoffersen, B. Hubbard, S. Doyle, T. Chudley, M. Bougamont, and C. Schoonman (2020), “Distributed fibre-optic temperature sensing in a 1 km borehole drilled on a fast-flowing glacier in Greenland”, EGU General Assembly 2020, Online, 4–8 May 2020, EGU2020-2433.

Leonard, E. J., D. A. Patthoff, D. A. Senske, and G.C Collins (2018), “The Europa Global Geologic Map”, Planetary Geologic Mappers Meeting 2018, LPI Contrib. No. 2066.

Li, L., and Mustard, J.F. (2003), “Highland contamination in lunar mare soils: Improved mapping with multiple end-member spectral mixture analysis (MESMA)”, Journal of Geophysical Research: Planets **108**, 5053.

Lien, R. K. Craft, M. Walker, C. German, M. Jakuba, R. Lorenz, C. McCarthy, W. Patterson, A. Rhoden, M. Silvia, V. Singh. (2021), “Modeling Fracture Hazards at Europa for Cryobot Tunneling and Communication”, LPSC 52, Abstract #1005.

Lien, R. and K. Craft (2020), “Modeling Fracture Hazards at Europa for Cryobot Tunneling and Communication”, AGU Fall meeting, Abstract# P052-06

Liehr, S., P. Lenke, M. Wendt, K. Krebber, M. Seeger, E.Thiele, H. Metschies, B. Gebreselassie, J. C. Münich, “Polymer Optical Fiber Sensors for Distributed Strain Measurement and Application in Structural Health Monitoring”, IEEE.

Ligier, N., F. Poulet, J. Carter, R. Brunetto, F. Gourgeot (2016), “VLT/SINFONI Observations of Europa: New Insights into the Surface Composition”, The Astronomical Journal **151**(6):163.

Loeffler, M. J., P. D. Tribbett, J. F. Cooper, S. J. Sturner (2020), “A possible explanation for the presence of crystalline H2O-ice on Kuiper Belt objects”, Icarus **351**: 113943.

Lucey, P.G. (1998), “Model near-infrared optical constants of olivine and pyroxene as a function of iron content”, Journal of Geophysical Research **103**: 1703-1714.

Lunine, J. (2006), “Origin of Water Ice in the Solar System”, Meteorites and the Early Solar System II.

MacKenzie, S., M. Neveu, A. Davila, K. Craft, J. Lunine, M. Cable, J. Eigenbrode, R. Gold, C. Phillips-Lander, J. Hofgartner, H. Waite, C. Glein, C. McKay, and the Orbilander Team (2020), “Enceladus Orbilander”, Planetary Science Mission Concept

Studies program report for the *2023-2032 Planetary Science and Astrobiology Decadal Survey*.

Marone, C. (1998), "The effect of loading rate on static friction and the rate of fault healing during the earthquake cycle", Nature 391, 69-72.

Marone, C. and C. H. Scholz (1988), "The depth of seismic faulting and the upper transition from stable to unstable slip regimes", Geophysical Research Letters **15**(6): 621-624.

Marion, G. M. (2002), "A molal-based model for strong acid chemistry at low temperatures", Geochimica et Cosmochimica Acta, 66(14), 2499-2516.

Martin, R.G., M. Livio (2012), "On the evolution of the snow line in protoplanetary discs", MNRAS **425**, L6-L9.

Mastrapa, R.M.E. and R. H. Brown (2006), "Ion irradiation of crystalline H_2O-ice: Effect on the 1.65 μm band", Icarus **183**: 207-214.

Mastrapa, R. M. E. (2008), "Water Ice and Radiation in the Solar System". Ph.D. thesis. The University of Arizona.

Mastrapa, R. M., M. P. Bernstein, S. A. Sandford, T. L. Roush, D. P. Cruikshank, C. M. Dalle Ore (2008), "Optical constants of amorphous and crystalline H_2O–ice in the near infrared", Icarus **197**: 307–320.

Mastrapa, R. M., S. A. Sandford, T. L. Roush, D. P. Cruikshank, C. M. Dalle Ore (2009), "Optical constants of amorphous and crystalline H_2O–ice: 2.5-22 μm (4000-455 cm^{-1}) Optical Constants of H_2O–ice", The Astrophysical Journal **701**: 1347.

Mastrapa, R.M.E., W. M. Grundy, M.S. Gudipati, (2013). "Amorphous and Crystalline H_2O-Ice", in: The Science of Solar System Ices, Gudipati, M.S., Castillo-Rogez, J. (Eds.), Astrophysics and Space Science Library, p. 371.

McCarthy, C., R.F. Cooper, D.L. Goldsby, W.B. Durham, and S.H. Kirby (2011), "Transient and steady-state creep response of ice-I and magnesium sulfate hydrate eutectic aggregates", Journal of Geophysical Research—Planets, **116**(E4), E04007.

McCarthy, C., H.M. Savage, T. Koczynski, and M.A. Nielson (2016), "An apparatus to measure frictional, anelastic, and viscous behavior in ice at temperate and planetary conditions", Review of Scientific Instruments, 87, 055112.

McCarthy, C., H. Savage, and M. Nettles (2017), "Temperature dependence of ice-on-rock friction at realistic glacier conditions", Philosophical Transactions of the Royal Society A, 375(2086), 20150348.

McCarthy, C., T. Caswell, A. Domingos, A.O. Katz, D. C. Newtown, D. Zhang, and H. M. Savage (2018), "Friction of Ice partial melt systems: a possible source of seismicity on icy satellite faults", 49th Lunar and Planetary Science Conference, Abstract #2419.

McCord, T.B., G.B. Hansen, F.P. Fanale, R.W. Carlson, D.L. Matson, T.V. Johnson, W.D. Smythe, J.K. Crowley, P.D. Martin, A. Ocampo, C.A. Hibbitts, and J.C. Granahan (1998), "Salts on Europa's surface detected by Galileo's near infrared mapping spectrometer", Science, **280**(5367), 1242-1245.

Mills, A., E. J. Leonard, and R. T. Pappalardo (2020), "Chaos Blocks on Europa: An Analysis of Orientation and Size Distributions", American Geophysical Union 2020 Meeting #753884.

Mirzaghorbanali, A. H. Rasekh, N. Aziz, G. Yang, S. Khaleghparast, J. Nemcik (2017), "Shear strength properties of cable bolts using a new double shear instrument, experimental study, and numerical simulation", Tunnelling and Underground Space Technology, 240-253.

Molaro, J. L., M. Choukroun, C. B. Phillips, E. S. Phelps, R. Hodyss, K. L. Mitchell, J. M. Lora, G. Meirion-Griffith (2019), "The microstructural evolution of water ice in the solar system through sintering", Journal of Geophysical Research: Planets **124**(2): 243-277.

Moore, M. H. and R. L. Hudson (1992), "Far-Infrared Spectral Studies of Phase Changes in Water Ice induced by Proton Irradiation", The Astrophysical Journal, **401**: 353-360.

Moore, J. M. and H. Hussmann (2009), "Thermal Evolution of Europa's Silicate Interior", In Europa, R. T. Pappalardo, W. B. McKinnon and K. Khurana. Tucson, Arizona, USA, The University of Arizona Press: 329-349.

Narten, A. H., C. G. Venkatesh and S. A. Rice (1976), "Diffraction pattern and structure of amorphous solid water at 10 and 77 °K", The Journal of Chemical Physics, **64**, 1106.

NASA (2014), *Science Plan* (link).

NASA (2015), *Astrobiology Strategy* (link).

NASA (2020), *Science 2020-2024 A Vision for Science Excellence* (link).

National Research Council (2011), *Vision and Voyages for Planetary Science in the Decade 2013-2022* (NRC) (link).

Neveu, M., L. E. Hays, M. A. Voytek, M. H. New, and M. D. Schulte (2018), "The Ladder of Life Detection", Astrobiology. Nov 2018. 1375-1402.

Nimmo, F. and E. Gaidos (2002), "Strike-slip motion and double ridge formation on Europa", Journal of Geophysical Research **107**:E4.

Nimmo, F., J.R. Spencer, R.T. Pappalardo, and M.E. Mullen (2007), "Shear heating as the origin of the plumes and heat flux on Enceladus", Nature **447**: 289–291.

Nimmo, F. and R. T. Pappalardo (2016), "Ocean worlds in the outer solar system", Journal of Geophysical Research: Planets **121**(E8): 1378-1399.

Nolin, A. and J. Dozier (2000), "A Hyperspectral Method for Remotely Sensing the Grain Size of Snow", Remote Sensing of Environment **74**: 207-216.

Nordheim, T.A., K. P. Hand, C. Paranicas (2018), "Preservation of potential biosignatures in the shallow subsurface of Europa", Nature Astronomy **2**: 673-679.

Ockman, N. (1958), "The infra-red and raman spectra of ice", Advances in Physics **7**: 199–220.

O'Riorden, S, Mahapatra (2017), "Radhard optical patchcords and packaging for satellites using liquid crystal polymers", In: International Conference on Space Optics—ICSO 2012; 2017 Nov 20 (Vol. 10564, p. 105641I). International Society for Optics and Photonics.

Ojakangas, G. W., and D. J. Stevenson (1989), "Thermal state of an ice shell on Europa", Icarus, **81**: 220– 241.

Oleson, S., J.M. Newman, A. Dombard, D.A. Meyer-Dombard, K. Craft, J. Sterbentz, A. Colozza, B. Faller, J. Fittje, J. Gyekenyesi, and R. Jones (2019), "Compass Final Report: Europa Tunnelbot", NASA/TP—2019-220054.

Olgin, J. G., B. R. Smith-Konter, and R. T. Pappalardo (2011), "Limits of Enceladus's ice shell thickness from tidally driven tiger stripe shear failure", Geophysical Research Letters **38**: L02201.

Pappalardo, R. T., M. J. S. Belton, H. H. Breneman, M. H. Carr, C. R. Chapman, G. C. Collins, T. Denk, S. Fagents, P. E. Geissler, B. Giese, R. Greeley, R. Greenberg, J. W. Head, P. Helfenstein, G. Hoppa, S. D. Kadel, K. P. Klaasen, J. E. Klemaszewski, K. Magee, A. S. McEwen, J. M. Moore, W. B. Moore, G. Neukum, C. B. Phillips, L. M. Prockter, G. Schubert, D. A. Senske, R. J. Sullivan, B. R. Tufts, E. P. Turtle, R. Wagner and K. K. Williams (1999), "Does Europa have a subsurface ocean? Evaluation of the geological evidence", Journal of Geophysical Research **104**, E10, 24015–24055.

Pappalardo, R. T., D. A. Senske, H. Korth, D. Blankenship, D. Blaney, P. Christensen, S. Kempf, C. Raymond, K. Retherford, E. P. Turtle, J. H. Waite, J. Westlake, G. C. Collins, K. Hand, J. Lunine, M. McGrath, F. Nimmo, C. Paty, J. Soderblom, J. R. Spencer, C. Paranicas, S. Solomon, Europa Science Team (2017), "The Europa Multiple-Flyby Mission: Synergistic Science to Investigate Habitability", 48th Lunar and Planetary Science Conference: 1964.

Paranicas, C., R. W. Carlson, R. E. Johnson (2001), “Electron bombardment of Europa”, Geophysical Research Letters **28**: 673-676.

Patterson, G.W., A. S. McEwen, E. P. Turtle, C. M. Ernst, R. L. Kirk (2019), “Data Products from the Europa Imaging System (EIS) on Europa Clipper”, in: Teuben, P.J., Pound, M.W., Thomas, B.A., Warner, E.M. (Eds.), Astronomical Data Analysis Software and Systems XXVII, p. 605.

Patterson, G.W., C. Paranicas, L. M. Prockter (2012), “Characterizing electron bombardment of Europa's surface by location and depth”, Icarus **220**: 286-290.

Peale, S. J. (1999), “Origin and Evolution of the Natural Satellites”, Annual Review of Astronomy and Astrophysics **37**:533-602.

Petrenko, V. F. and R. W. Whitworth (1999), “Physics of Ice”, Oxford, England: Oxford University Press.

Pollard, D. D., and Segall, P. (1987), “Theoretical displacements and stresses near fractures in rock”, in: Fracture Mechanics of Rock, ed. BK Atkinson, pp. 277-349.

Pommerol, A. and Schmitt, B. (2008), “Strength of the H2O near-infrared absorption bands in hydrated minerals: Effects of measurement geometry”, Journal of Geophysical Research **113**(E12).

Porter, S. B., S. Desch, J. C. Cook (2010), “Micrometeorite impact annealing of ice in the outer Solar System”, Icarus **208**: 492-498.

Poston M. J., A. Mahjoub, B. L. Ehlmann, J. Blacksberg, M. E. Brown, R. W. Carlson, J. M. Eiler, K. P. Hand, R. Hodyss, and I. Wong (2018), “Visible near-infrared spectral evolution of irradiated mixed ices and application to Kuiper Belt Objects and Jupiter Trojans”, The Astrophysical Journal **856**:124.

Poston, M. J., R. W. Carlson, K. P. Hand (2017), “Spectral Behavior of Irradiated Sodium Chloride Crystals Under Europa-Like Conditions”, Journal of Geophysical Research - Planets **122**(12): 2644-2654.

Prockter, L. M., J. H. Shirley, J. B. Dalton, L. W. Kamp (2017), “Surface composition of pull-apart bands in Argadnel Regio, Europa: Evidence of localized cryovolcanic resurfacing during basin formation”, Icarus **285**: 27-42.

Rasekh H., N. Aziz, A. Mirza, J. Nemcik, X. Li, G. Yang, and S. Khaleghparast (2017), “ Double shear testing of cable bolts with no concrete face contacts”, Procedia Engineering **191**: 1169-1177.

Rathbun, J.A., N. J. Rodriguez, J. R. Spencer (2010), “Galileo PPR observations of Europa: Hotspot detection limits and surface thermal properties”, Icarus **210**: 763-769.

Richey, C., R. T. Pappalardo, D. Senske, H. Korth, K. Craft, R. L. Klima, C.B. Phillips (2018), "The Europa Clipper Mission: Science Objectives and Mission Status Update", in: AGU Fall Meeting Abstracts: P53F-3018.

Roth, L., K. D. Retherford, J. Saur, D. F. Strobel, P. D. Feldman, M. A. McGrath, F. Nimmo (2014), "Orbital apocenter is not a sufficient condition for HST/STIS detection of Europa's water vapor aurora", Proceedings of the National Academy of Science 111, E5123-E5132.

Rubin, A. M. (2011), "Designer friction laws for bimodal slow slip propagation speeds", Geochemistry, Geophysics, Geosystems, **12**(4).

Ruina, A.L. (1983), "Slip instability and state variable friction laws", Journal of Geophysical Research: **88**, 10,359-10,370.

Schenk, P. M., and E. P. Turtle (2009), "Europa's Impact Craters: Probes of the Icy Shell", In Europa, Tucson, Arizona, USA, The University of Arizona Press:181-198.

Schmitt, B., E. Quirico, F. Trotta, W. M. Grundy (1998), "Optical Properties of Ices from UV to Infrared", in: Solar System Ices, Schmitt, B., de Bergh, C., Festou, M. (Eds.), p. 199.

Scholz, C. H. (1998), "Earthquakes and friction laws", Nature 391(6662), 37-42.

Scholz, C. H. (2019), "The mechanics of earthquakes and faulting", Cambridge university press.

Schroeder, P.A. (2002), "Infrared spectroscopy in clay science", Teaching Clay Science 11, 181-206.

Shirley, J.H., J. B. Dalton, L. M. Prockter, L. W. Kamp (2010), "Europa's ridged plains and smooth low albedo plains: distinctive compositions and compositional gradients at the leading side–trailing side boundary," Icarus **210**: 358-384.

Singh, V., C. McCarthy, K.L. Craft, C. R. German, M. V. Jakuba, R. D. Lorenz, G. W. Patterson, A. Rhoden, and M. Walker (2019), "How (not) to lose communication with your submersible on Europa: An experimental study for characterizing the shear performance of tethers under confinement in ice", 2019 AGU, Abstract #491548.

Singh, V., C. McCarthy, M. Silvia, M. Jakuba, C. German, K. Craft, W. Patterson, R. Lorenz, A. Rhoden, M. Walker, and R. Lien (2021), "Communication Tethers May Survive Shearing Across Ice Faults on Europa", 52nd LPSC, Abstract #2403.

Schulson, E.M. and A. L. Fortt (2012), "Friction of ice on ice", Journal of Geophysical Research **117**: B12204.

Smith-Konter, B. and R. T. Pappalardo (2008), “Tidally driven stress accumulation and shear failure of Enceladus’s tiger stripes”, Icarus **198**: 435-451.

Soderlund, K.M., B.E. Schmidt, J. Wicht, and D.D. Blankenship (2014), “Ocean-driven heating of Europa’s icy shell at low latitudes”, Nature Geoscience **7**: 16-19.

Soffen, G. A., and C. W. Snyder (1976), “The First Viking mission to Mars”, Science, **193**, 759-766.

Sleep, N.H. (2019), “Friction in cold ice within outer Solar System Satellites with reference to thermal weakening at high sliding velocities”, Journal of Geophysical Research—Planets, **124**(9), 2397-2413.

Spaun, N. A., and Head, J. W., (2001), “A model of Europa's crustal structure: Recent Galileo results and implications for an ocean”, Journal of Geophysical Research: Planets **106**(E4): 7567-7576.

Spencer, J., L. K. Tamppari, T. Z. Martin and L. D. Travis (1999), “Temperatures on Europa from Galileo Photopolarimeter-Radiometer: Nighttime Thermal Anomalies”, Science **284**(5419): 1514-1516.

Squyres, S.W., R.T. Reynolds, P.M. Cassen, and S.J. Peale (1983), “The evolution of Enceladus”, Icarus **53**: 319–331

Strazzulla, G., G. Leto, G. A. Baratta, and F. Spinella (1991), “Ion irradiation experiments relevant to cometary physics”, Journal of Geophysical Research **96**(E2), 17547–17552.

Stone, W. B. Hogan, V. Siegel, S. Lelievre (2014), “Progress towards an optically powered cryobot”, Annals of Glaciology **55**(65):1-13

Sugisaki, M., H. Suga, and S. Seki (1969), “Calorimetric study of glass transition of the amorphous ice and of the phase transformation between the cubic and hexagonal ices”, In N. Riehl (Ed.), Physics of Ice, pp. 329–343. New York: Platinum Press.

Tachibana, S., A. Kouchi, T. Hama, Y. Oba, L. Piani, I. Sugawara, Y. Endo, H. Hidaka, Y. Kimura, K. Murata, H. Yurimoto, N. Watanabe (2017), “Liquid-like behavior of UV-irradiated interstellar ice analog at low temperatures”, Science Advances 3(9): eaao2538

Taffin, C., O. Grasset, E. Le Menn, O. Bollengier, M. Giraud, S. Le Mouélic (2012), “ Temperature and grain size dependence of near-IR spectral signature of crystalline water ice: From lab experiments to Enceladus' south pole”, Planetary and Space Science **61**(1): 124-134.

Thomas, E. C., R. Hodyss, T. H. Vu, P. V. Johnson, M. Choukroun (2017), "Composition and Evolution of Frozen Chloride Brines under the Surface Conditions of Europa", ACS Earth Space Chem **1**: 14−23.

Trumbo, S. K., M. E. Brown, and K. P. Hand (2019), "Sodium chloride on the surface of Europa", Science Advances 5, eaaw7123.

Tufts, B.R., R. Greenberg, G. Hoppa, and P. Geissler (2000), "Lithospheric Dilation on Europa", Icarus **146**: 75-97.

Tulk, C. A., J. J. Molaison, A. R. Makhluf, C. E. Manning, D. D. Klug (2019), "Absence of amorphous forms when ice is compressed at low temperature", Nature **569**: 542–545.

Turtle, E. P., N. Thomas, L. Fletcher, A. Hayes, C. Ernst, G. Collins, H. Geoffrey, C. Hansen, R. L. Kirk, F. Nimmo, A. S. McEwen, T. Hurford, A. Barr Mlinar, L. Quick, W. Patterson, J. Soderblom (2016), "The Europa Imaging System (EIS): Investigating Europa's geology, ice shell, and current activity", 41st COSPAR Scientific Assembly: B0.3-3-16.

Vance, S. D., K. P. Hand, and R. T. Pappalardo (2016), "Geophysical controls of chemical disequilibria in Europa", Geophysical Research Letters, 43(10): 4871-4879.

Vu, T.H., R. Hodyss, M. Choukroun, and P. V. Johnson (2016), "Chemistry of frozen sodium magnesium-sulfate-chloride brines: implications for surface expression of Europa's ocean composition", The Astrophysical Journal Letters **816**: L26.

Waite, J. H. Jr., W.S. Lewis, B.A. Magee, J.I. Lunine, W.B. McKinnon, C.R. Glein, O. Mousis, D.T. Young, T. Brockwell, J. Westlake, M.-J. Nguyen, B.D. Teolis, H.B. Niemann, R.L. McNutt Jr., M. Perry, and W.-H. Ip (2009), "Liquid water on Enceladus from observations of ammonia and 40Ar in the plume", Nature **460**: 487–490

Walker, M. A. R. Rhoden , K. L. Craft , R. D. Lorenz , G. W. Patterson , C. R. German , M. V. Jakuba, C. McCarthy, V. Singh (2020), "What Ice Conditions Can a Tethered Probe Expect at Europa?" 51st LPSC, LPI, Abstract #2448.

Webb, A. (2016), "Design and fabrication of a Cryogenic Automated Test System (CATS)", 29th Space Simulation Conference, Institute of Environmental Sciences and Technology.

Westlake, J. H., R. L. McNutt, J. C. Kasper, A. W. Case, A. M. Rymer, M. L. Stevens, X. Jia, C. Paty, K. K. Khurana, M. G. Kivelson, J. A. Slavin, H. T. Smith, H. Korth, N. Krupp, E. Roussous, J. Saur (2016), "The Plasma Instrument for Magnetic Sounding (PIMS) for the Europa Mission", 3rd International Workshop on Instrumentation for Planetary Missions: 4037.

Wilcox, B. H., Carlton, J. A., Jenkins, J. M., & Porter, F. A. (2017), "A deep subsurface ice probe for Europa", In: Aerospace Conference, 2017 IEEE (pp. 1-13), IEEE.

Winebrenner, D. P., W. T. Elam, V. Miller *et al*. (2013), "A thermal ice-melt probe for exploration of Earth-analogs to Mars, Europa and Enceladus", In: 44th Lunar and Planetary Science Conference, Abstract #2986.

Wiscombe, W. J., and Warren, S. G. (1980), "A Model for the Spectral Albedo of Snow. I: Pure Snow", Journal of Atmospheric Sciences, **37**(12): 2712-2733.

Zahnle, K., J. L. Alvarellos, A. Dobrovolskis, P. Hamill (2008), "Secondary and sesquinary craters on Europa", Icarus **194**: 660–674.

Zacny, K., K. Luczek, A. Paz and M. Hedlund (2016), "Planetary Volatiles Extractor (PVEx) for In Situ Resource Utilization (ISRU)", 15th Biennial ASCE Conference on Engineering, Science.

Zimmerman, W., Bonitz, R. and Feldman, J., (2001), "Cryobot: an ice penetrating robotic vehicle for Mars and Europa", In Aerospace Conference, IEEE Proceedings, Vol. 1, pp. 1-311.

Zoet, L.K., B. Carpenter, M. Scuderi, R.B. Alley, S. Anandakrishnan, C. Marone, and M. Jackson (2013), "The effects of entrained debris on the basal sliding stability of a glacier", Journal of Geophysical Research: Earth Surface, **118**: 656-666.

Zolotov, M.Y., Kargel, J.S., (2009), "On the chemical composition of Europa's icy shell, Ocean, and underlying rocks." In: Pappalardo, R.T., McKinnon, W.B., Khurana, K. (Eds.), Europa. The University of Arizona Press, Tucson, 431–458.

Zolotov, M.Y., Shock, E.L., (2001), "Composition and stability of salts on the surface of Europa and their oceanic origin." Journal of Geophysical Research **106**: 32815–32827.

APPENDIX A

DESCRIPTION OF LAB FACILITIES AND INSTRUMENTATION

A.1 Ice Spectroscopy Lab (ISL) at Jet Propulsion Laboratory

Experimental ice research requires specific equipment and facilities to work at low temperatures, and special care to handle and characterize icy material without modifying its properties. At Dr. Murthy Gudipati's Ice Spectroscopy Laboratory (ISL) at JPL, I have developed state-of-the-art infrastructure for studying the spectral, optical-imaging, and compositional properties of ices under Europa's radiation conditions. This facility includes an ice deposition and sieving drybox with continuous N_2 purge, a high-vacuum chamber ($<10^{-9}$ mbar), a closed-cycle helium cryostat, UV-VIS-NIR reflection spectrometers, a remote microscope setup, and tunable electron gun sources (<100 keV) (Figure A.1). I have spent the past two years designing, fabricating, and calibrating instrumentation to enable the types of experiments described in this dissertation.

More broadly, ISL is equipped with experimental facility to carryout spectroscopic, photochemical, and analytical studies on organics, cryogenic ices, and minerals under radiation environment, including an organic synthesis laboratory to carryout synthesis of temperature, transportation, and atmospheric sensitive molecules. This enables us to understand the evolution of icy matter in the interstellar medium, in the solar system, and on Earth.

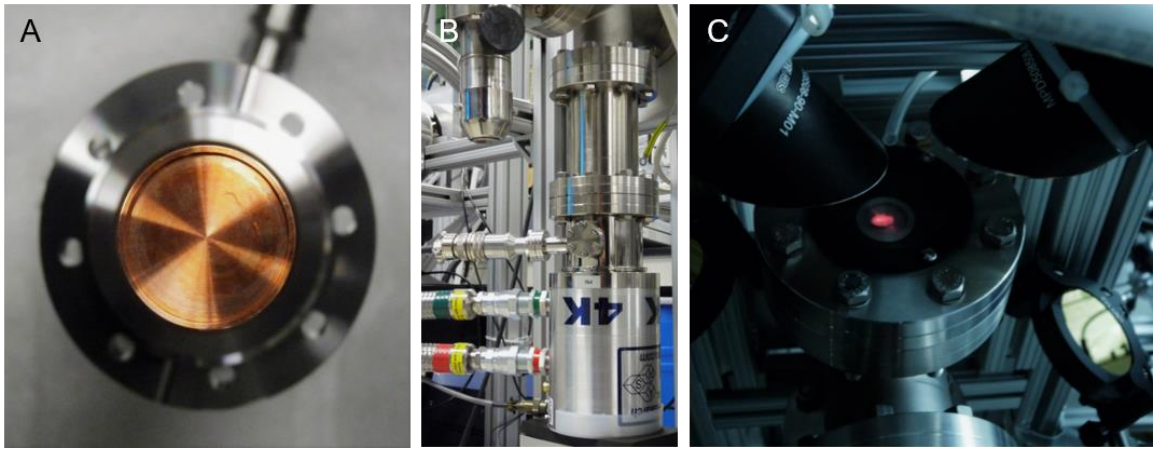

Figure A.1: Parts of the Apollo instrument at the "Ice Spectroscopy Lab" (ISL) at JPL. (A, B) 4.2 K closed-cycle helium cryostat is the heart of the experiments where ice samples are investigated between 10 and 250 K on a copper sample holder. This instrument includes (C) a reflection spectroscopy setup in the center. The setup includes a collection of five mirrors mounted around a KBr window. On the right, outside the frame is a FTIR Spectrometer used with an MCT detector to collect reflection-absorption spectra of ice samples. On top is a remote microscope with Zeiss digital camera to collect optical data.

Figure A.2: Biaxial cryogenic deformation apparatus at LDEO (pictured above) is used with LN to achieve cryogenic temperatures and simulate a broad range of velocities.

A.2 Rock and Ice Mechanics Laboratory, Lamont Doherty Earth Institute, Columbia University

Under the supervision of Dr. Christine McCarthy, and senior technician Ted Koczynski, I have modified the multi-purpose biaxial apparatus to use a liquid nitrogen-cooled cryostat and measure the mechanical properties of the ice-tether sample (Figure A.2). This apparatus has two separate servo-controlled hydraulic pistons capable of controlling biaxial load on a sample to great precision. The cryostat allows temperature-controlled testing for weeks at a time. We also built a custom, tensile strength testing and adhesion strength testing rig, using a set of radius arbors to house a tether during testing, while maintaining minimal gauge length.

The lab also includes a cryo-sample fabrication center, which includes a walk-in cold room (T = -17ºC), within which we have installed a dedicated band saw, arbor press, drill press, various saws and surface grinders for sample processing/handling, a microtome, and a Leica light microscope for sample characterization. Protocols were developed for sample preparation with the tether inside the ice. An LN-cooled Environmental Chamber was recently installed, and it can sustain accurate (± 0.01ºC) and stable (< ± 1ºC) programmable temperatures as low as -180ºC. The chamber has a relatively large interior volume (~m^3) and pass-through ports that will be used for functional performance testing of tethers while under the cold temperatures. Other equipment in the fabrication center includes a -45ºC chest freezer for short-term sample storage, a large LN-cooled dewar for long-term sample storage, a dry-ship dewar for sample transport, and an ultrasonic pulse testing instrument to measure P- and S-wave velocities and Young's modulus.

APPENDIX B

REFLECTION SPECTRA OF WATER ICE: SAMPLE DESCRIPTION

B.1 Mist Ice (MI)

Water ice deposited in LN at 77 K, placed in chamber at 100 K, cooled to 10 K, heated to 170 K, and cooled to 10 K. Grain size of 53 to 75 μm.

Table B.1: Sample Number vs Experimental Conditions for Mist Ice

Sample Number	Experimental Condition
Background	Background collected at 100 K
1	10 K: Ice after Placement
2	100 K: Ice after Heating
3	140 K: Ice after Heating
4	170 K: Ice after Heating
5	140 K: Re-cooled Ice
6	10 K: Re-cooled Ice

B.2 Freezer Ice (FI)

Water ice was deposited in freezer at 253 K, placed in chamber at 100 K, cooled to 10 K, heated to 150 K, and cooled to 10 K. Grain Size of 25 to 53 μm.

Table B.2: Sample Number vs Experimental Conditions for Freezer Ice

Sample Number	Experimental Condition
Background	Background collected at 100 K
1	100 K: Ice after Placement
2	90 K: Ice after Cooling
3	50 K: Ice after Cooling
4	10 K: Ice after Cooling
5	150 K: Ice after Heating
6	150 K: Ice after Heating, wait 30 minutes
7	10 K: Re-cooled Ice

B.3 Mist Ice (MI) Overnight

Water ice deposited in LN at 77 K, placed in chamber at 100 K, left for 72 hours, cooled to 10 K, heated to 150 K, and cooled to 10 K. Grain size of 25-53 μm.

Table B.3: Sample Number vs Experimental Conditions for Mist Ice Overnight

Sample Number	Experimental Condition
Background	Background collected at 100 K
1	100 K Placement
2	7 minutes
3	30 minutes
4	60 minutes
5	90 minutes
6	120 minutes
7	150 minutes
8	240 minutes
9	330 minutes
10	71 Hours
11	72 Hours
12	Cooled to 75 K
13	Cooled to 50 K
14	Cooled to 10 K
15	Heated to 50 K
16	Heated to 75 K
17	Heated to 125 K
18	Heated to 150 K
19	Re-cooled to 125 K
20	Re-cooled to 100 K
21	Re-cooled to 75 K
22	Re-cooled to 50 K
23	Re-cooled to 10 K
24	Re-cooled to 10 K